COUPLED HEAT AND MASS TRANSFER DURING CONDENSATION OF HIGH-TEMPERATURE-GLIDE ZEOTROPIC MIXTURES IN SMALL DIAMETER CHANNELS

A Dissertation
Presented to
The Academic Faculty

by

Brian Matthew Fronk

In Partial Fulfillment
of the Requirements for the Degree
Doctor of Philosophy in Mechanical Engineering

Georgia Institute of Technology
August 2014

COUPLED HEAT AND MASS TRANSFER DURING CONDENSATION OF HIGH-TEMPERATURE-GLIDE ZEOTROPIC MIXTURES IN SMALL DIAMETER CHANNELS

Approved by:

Dr. Srinivas Garimella, Advisor
G.W. Woodruff School of Mechanical Engineering
Georgia Institute of Technology

Dr. Thomas Fuller
School of Chemical and Biomolecular Engineering
Georgia Institute of Technology

Dr. S. Mostafa Ghiaasiaan
G.W. Woodruff School of Mechanical Engineering
Georgia Institute of Technology

Dr. Krista Walton
School of Chemical and Biomolecular Engineering
Georgia Institute of Technology

Dr. Yogendra Joshi
G.W. Woodruff School of Mechanical Engineering
Georgia Institute of Technology

Date Approved: May 14, 2014

To my wife, Theresa

ACKNOWLEDGEMENTS

First and foremost, I would like to thank my adviser, Dr. Srinivas Garimella for his support and guidance through my M.S., Ph.D. and in my general development as an engineer and a researcher. His advice and insights will be invaluable throughout the rest of my career.

I would also like to thank all of the past and present members of the Sustainable Thermal Systems Laboratory for their role in creating a fun and positive research environment. It has been a pleasure to work with such and intelligent and collegial group of people. In particular I would like to acknowledge my colleagues working in multi-phase heat and mass transfer, Dr. Brendon Keinath, Dr. Jeff Milkie, Dr. Anand Nagavarapu and Malcolm Macdonald for their willingness to answer questions, review my work, listen to my ideas, and offer advice. In addition, I would like to thank Adrienne Little, Chris Keinath and Alex Rattner for their technical and moral support throughout my time at Georgia Tech.

Finally, I would like to thank my Ph.D. committee members for their time, thoughtful comments, and feedback in the development of this dissertation.

TABLE OF CONTENTS

LIST OF TABLES

LIST OF FIGURES

LIST OF SYMBOLS AND ABBREVIATIONS

Symbols

A	Area (m^2), constant (-)
a	Regression coefficient (-)
AR	Aspect ratio (-)
B	Regression coefficient (-)
Bo	Bond number (-)
c	Regression coefficient (-)
C	Chisholm (1967) parameter (-), Concentration (kmol m^{-3})
Ca	Capillary number (-)
Co	Confinement number (-)
c_p	Specific heat (J kg^{-1} K^{-1})
D	Diameter (m)
D_{1-2}	Binary diffusion coefficient (m^2 s^{-1})
D_H	Hydraulic diameter (m)
E	Entrainment ratio (-)
f	Friction factor (-)
G	Mass flux (kg m^{-2} s^{-1})
g	Gravitational acceleration (m^2 s^{-1})
h	Specific enthalpy (kJ kg^{-1})
h_{fg}	Enthalpy of vaporization (kJ kg^{-1})
ID	Inner diameter (m)
j	Superficial velocity (m s^{-1})
j_G^*	Dimensionless gas velocity (-)
k	Thermal conductivity (W m^{-1} K^{-1})

L	Length (m) or Laplace constant (m)
$\dot{m}$	Mass flow rate (kg s^{-1})
m''	Condensing mass flux (kg m^{-2} s^{-1})
$\dot{N}$	Condensing molar flux (kmol m^{-2} s^{-1})
Nu	Nusselt number (-)
OD	Outer diameter
P	Pressure (kPa)
P_r	Reduced pressure (-)
Pr	Prandtl number (-)
q	Thermodynamic quality (-)
q''	Heat flux (W m^{-2})
$\dot{Q}$	Heat duty (W)
R	Thermal resistance (K W^{-1})
Ra	Rayleigh number (-)
r	Radius (m)
Re	Reynolds number (-)
Sc	Schmidt number
Sh	Sherwood number (-)
Su	Suratman number (-)
T	Temperature (°C)
T^+	Dimensionless temperature (-)
U	Velocity (m s^{-1})
$\bar{V}_{vj}$	Drift flux velocity (m s^{-1})
We	Weber number (-)

X	Martinelli (1949) parameter (-)
X_{tt}	Turbulent-turbulent Martinelli (1949) parameter (-)
x_{bulk}	Bulk mass fraction of ammonia
x_1	Liquid phase mass fraction of more volatile component (-)
$\tilde{x}_1$	Liquid phase mole fraction of more volatile component (-)
y_1	Vapor phase mass fraction of more volatile component (-)
$\tilde{y}_1$	Vapor phase mole fraction of more volatile component (-)
z	Ratio of volatile condensing flux to total flux (-)

Greek Letters

Λ	Ratio of sensible to total heat flux (Bell and Ghaly, 1973)
α	Heat transfer coefficient (W m^{-2} K^{-1})
α'	Apparent heat transfer coefficient (W m^{-2} K^{-1})
β	Mass transfer coefficient (m s^{-1}), Homogenous void fraction (-)
δ	Liquid film thickness (m)
ε	Void fraction (-)
Ξ	Mass transfer correction factor from Bird *et al.* (1960)
η	Vapor film thickness (m)
κ	Ackerman (1937) correction factor (-)
μ	Dynamic viscosity (kg m^{-1} s^{-1})
Φ	Two-phase multiplier (-)
ρ	Density (kg m^{-3})
θ	Liquid angle (rad)

σ	Surface tension (N m^{-1})
τ	Shear stress (N m^{-2})

Subscripts and Superscripts

1	More volatile component in binary mixture, state point 1
2	Less volatile component in binary mixture, state point 2
3	State point 3
4	State point 4
a	Acceleration, annular
ann	Annulus
amb	Ambient
avg	Average
b	Bulk
bub	Bubble point
C	Coolant
dew	Dew point
eq	Equilibrium
fr	Frictional
g	Gravitational
GC	Gas core
H	High temperature source
HT	Heat transfer
i	Interface, segment inlet
L	Liquid phase or low temperature source
LM	Log-mean

LO	Liquid only
λ	Latent
n-a	Non-annular
o	Segment outlet
pre	Pre-heater
post	Post-heater
H	High temperature source
mix	Mixture
red	Reducer
S,L	Sensible liquid load
S,V	Sensible vapor load
sat	Saturated
T	Total or turbulent
TP	Two-phase
UC	Unit cell
V	Vapor phase
VO	Vapor only
w	Wall
w,i	Inner wall
w,o	Outer wall

Abbreviations

AD	Average deviation
AAD	Absolute average deviation
CFC	Chloroflurocarbons

GWP	Global warming potential
HCFC	Hydrochlorofluorocarbons
LMTD	Log-mean temperature difference
ODP	Ozone depletion potential
ORC	Organic Rankine cycle

SUMMARY

Zeotropic mixtures exhibit a temperature glide between the dew and bubble points during condensation. This glide has the potential to increase system efficiency when matched to the thermal sink in power generation, chemical processing, and heating and cooling systems. Further improvements in energy efficiency can be realized by designing heat transfer components with mini- and microchannels. However, it has been shown that the concentration gradients arising from the changing composition of the vapor and liquid phases during condensation introduce additional mass transfer resistances, degrading the overall heat transfer. These effects are poorly understood for horizontal mini- and microchannel based devices.

A comprehensive investigation of the condensation of ammonia and high-temperature-glide zeotropic ammonia/water mixtures in small diameter channels was conducted. Condensation heat transfer and pressure drop experiments were conducted on ammonia and ammonia/water mixtures. Experiments on ammonia were conducted for varying tube diameters ($0.98 < D < 2.16$ mm), mass fluxes ($75 < G < 225$ kg m^{-2} s-1) and saturation conditions ($30 < T_{sat} < 60$°C). Zeotropic ammonia/water experiments were conducted for multiple tube diameters ($0.98 < D < 2.16$ mm), mass fluxes ($50 < G < 200$ kg m^{-2} s^{-1}) and bulk ammonia mass fractions (x_{bulk} = 0.8, 0.9 and > 0.96). An experimental an experimental methodology and data analysis procedure for evaluating the local condensation heat duty (for incremental Δq), condensation transfer coefficient (for pure ammonia), and apparent heat transfer coefficient (for zeotropic ammonia/water mixtures) and frictional pressure gradient with low uncertainties was developed. A heat transfer model for condensation of ammonia in mini/microchannels was developed.

Using the insights derived from the pure ammonia work, an improved zeotropic condenser design method for high-temperature-glide mixtures in small diameter channels, based on the non-equilibrium film theory, was introduced. The key features of the improved model were the consideration of annular and non-annular flow effects on liquid film transport, including condensate and vapor sensible cooling contributions, and accounting for mini/microchannel effects through the new liquid film correlation.

The findings of this study advance the understanding of microchannel condenser design for zeotropic fluid mixtures, in particular, those high temperature glides. High-temperature-glide mixtures including ammonia/water, hydrocarbons and others have important potential applications in thermally driven heating, cooling and power, as well as in the chemical process industry. By understanding the behavior of these mixtures in microchannel geometries, highly efficient, compact thermal conversion devices can be developed..

CHAPTER 1

INTRODUCTION

In condensing two-phase fluid mixtures, there is a strong coupling of momentum, heat, and mass transfer mechanisms. As the length scale of interest decreases, forces that were relatively unimportant at large scales increase in magnitude, changing the way in which the phenomena are coupled and should be modeled. Understanding the interactions between the momentum, heat, and mass transfer mechanisms at these small scales is essential for the continued development and optimization of advanced energy conversion systems for the transfer and conversion of heat and work. As global resources become increasingly constrained, improvements in the efficiency of energy conversion systems for producing power, heating, and/or cooling can yield significant energy and economic savings. Furthermore, the understanding of interphase transport of species and energy and within the liquid and vapor boundary layers at the microscale can readily be extended to gas absorption, separation processes, biological systems (*e.g.*, respiratory exchange, dialysis), and sensing applications. The present work aims to experimentally evaluate heat transfer and pressure drop in condensing mixtures, and to develop a method of modeling the coupled heat and mass transfer behavior in microchannels.

1.1 Motivation

One of the most important applications of condensation heat transfer is in thermodynamic cycles for the production of power, heating, and/or cooling. The Carnot cycle (Figure 1.1a), composed of four reversible processes, establishes the theoretical maximum efficiency for a cycle operating between two constant temperature reservoirs (T_H, and T_L). The isothermal condensation of a single-component fluid at a fixed saturation pressure

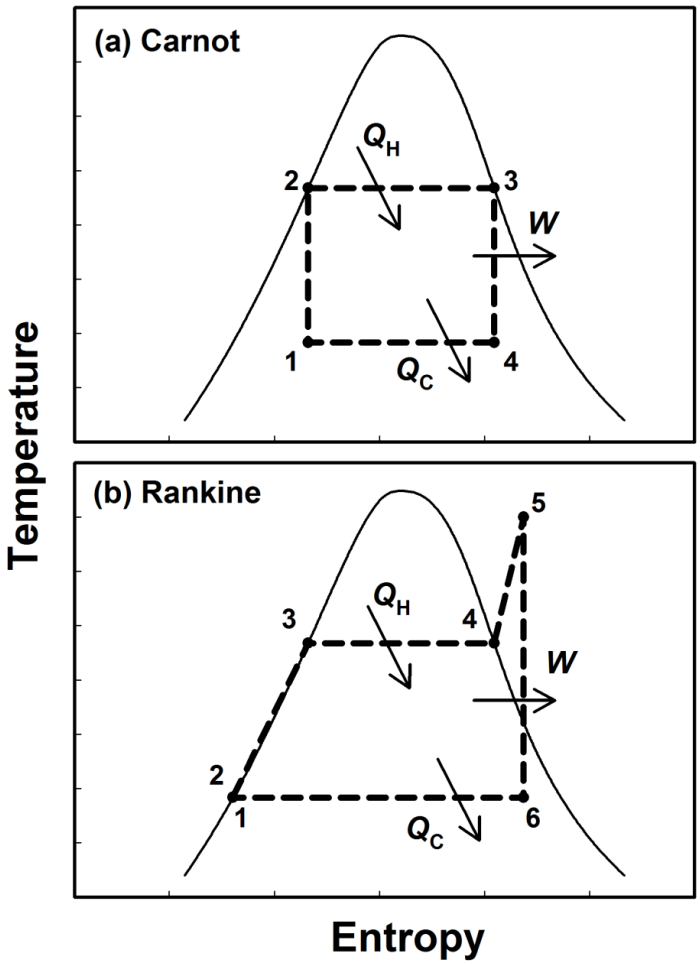

Figure 1.1: Temperature versus entropy diagram of (a) Carnot and (b) Rankine cycles

closely approximates the isothermal heat rejection process (3-4) of the Carnot cycle. In addition, the energy density of condensing fluids can be an order of magnitude higher than for the non-isothermal sensible heating of a single-phase fluid, reducing the required working fluid flow rate to transfer an equivalent amount of energy. However, several impracticalities exist in implementing a cycle as pictured in Figure 1.1a. Thus, the addition of fluid superheating in the evaporator and subcooling in the condenser yields the Rankine cycle (Figure 1.1b), the ideal vapor cycle for power generation.

In the Carnot cycle, the isothermal heat addition and rejection occur between a working fluid and a constant temperature source and sink at the same temperature (T_H and T_L, respectively). In practice, this would necessitate infinitely large heat exchangers and time scales. In reality, there is some finite temperature difference between the working fluid and the thermal reservoirs. Additionally, the heat sink/source may deviate significantly from the constant temperature assumption, such as in a gas-fired boiler or water-cooled condenser. Representative temperature profiles of a counterflow condenser are shown in Figure 1.2. As the temperature glide of the sink/source increases, the entropy generation in the heat exchangers increases, with the highest generation occurring at the regions corresponding to the maximum temperature difference. This has a deleterious effect on theoretical cycle efficiency. In the Lorenz cycle (Figure 1.3), the specific heat capacity of the working fluid is tuned such that the temperature glides between the working fluid and the source/sink are matched. Thus, a minimal temperature difference is maintained through the heat exchanger, minimizing entropy generation and improving cycle efficiency. Using a zeotropic fluid mixture as the working fluid, the composition can be varied to achieve a suitable glide, while still maintaining the high energy density characteristic of phase-change heat transfer.

An example of a successful implementation of the use of a condensing zeotropic fluid mixture is the Kalina cycle (Kalina, 1984) for power generation, which operates with a mixture of ammonia and water. The cycle has been shown theoretically to be particularly efficient for producing power from low-grade geothermal (Kalina and Leibowitz, 1989; Mlcak, 2002; DiPippo, 2004) and solar resources (Lolos and Rogdakis, 2009) compared to a conventional organic Rankine cycle (ORC). Several other cycles

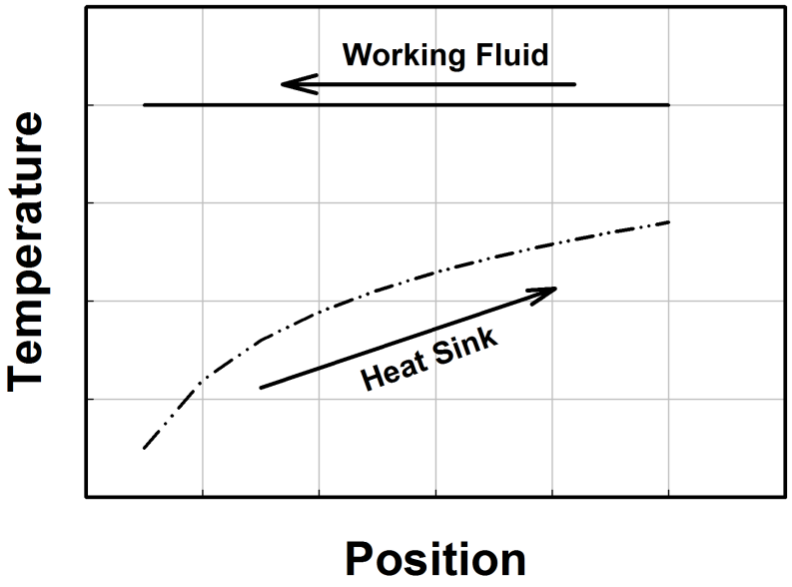

Figure 1.2: Representative condenser temperature profile

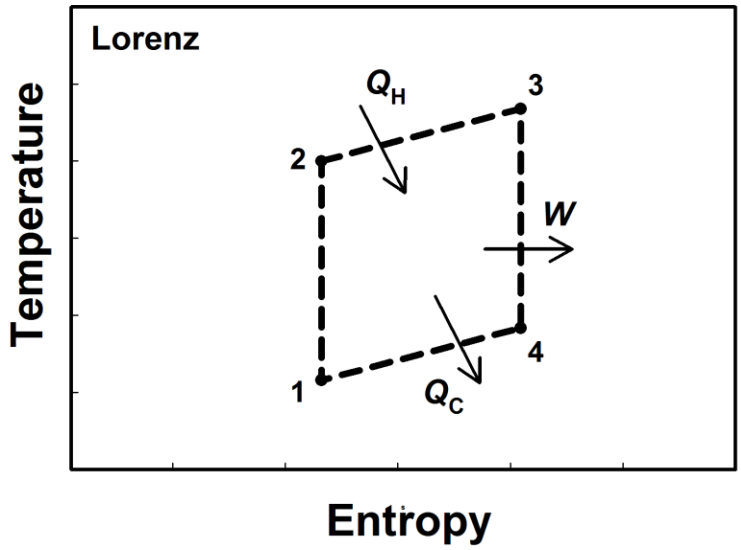

Figure 1.3: Lorenz cycle *T-s* diagram

that utilize phase-change mixtures for recovering low-grade thermal energy for power, cooling, and/or heating include absorption cycles, organic Rankine cycles, and vapor compression cycles. In the HVAC&R industry, continued restrictions on the use of chlorofluorocarbons (CFC) and hydrochlorofluorocarbons (HCFC) due to their high

ozone depletion potential (ODP) and/or global warming potential (GWP) has spurred the adaption of refrigerant mixtures that mitigate negative environmental impacts while maintaining good thermodynamic performance.

As energy prices increase, the higher costs of recovering lower grade thermal energy will become increasingly acceptable, and the use of fluid mixtures can be expected to increase. Miniaturization of the systems discussed above will open up new market opportunities including waste heat recovery in transportation applications and portable space-conditioning solutions. Also, miniaturization of components through the use of microchannel geometries will simultaneously increase heat transfer performance and reduce the working fluid inventory. Reduction of fluid inventory may increase acceptance of natural working fluids including toxic mixtures of ammonia/water and flammable mixtures of hydrocarbons. While it can readily be demonstrated that utilizing mixtures demonstrates theoretical gains in efficiency, adequate methods for accurately designing microchannel-based fluid-mixture components are not available. Extrapolation of modeling methodologies developed for larger tubes or single-component fluids may lead to drastically under- or over- designed components. It is therefore of great importance to understand and be able to model the interactions between the coupled momentum, heat, and mass transfer phenomena at the microscales.

1.2 Microchannel Condensation

A growing body of research that characterizes two-phase flow regimes, flow transitions, pressure drop, and heat transfer of single-component fluids in mini- and microchannels is available. A large fraction of these studies consists of observing flow regimes and measuring pressure drop for air/water mixtures. The experimental setup and operation is

simplified by using air/water mixtures at near atmospheric pressure; however, the significant property differences between air-water mixtures and typical refrigerants make extrapolation of air/water results to conditions of interest for boiling and condensation questionable. Another major thrust of two-phase mini- and microchannel research is in flow-boiling flow mechanisms, heat transfer, and pressure drop, with the electronics cooling industry being a primary driver. However, to achieve the goal of smaller heat transfer systems, it is also necessary to understand and accurately predict condensation heat transfer and pressure drop. The physical flow regimes and mechanisms of condensation in microchannels are expected to differ from flow boiling, as a thin liquid film is always likely to be present at the wall, and bubble nucleation and growth mechanisms do not apply to condensation. Additionally, heat rejection generally occurs at higher temperatures and thus higher reduced pressures than those typical of evaporation studies, where the properties of the saturated liquid and vapor phases become significantly different. Furthermore, accurately quantifying the small condensation heat duties and high heat transfer coefficients in microchannels is complicated by the inability to easily and accurately maintain and measure a constant heat flux as is commonly done in evaporation experiments with electrical heating. Thus, the development of experimental techniques to reduce uncertainties and accurately determine both heat transfer coefficients and frictional pressure gradients during condensation in small quality increments is of great importance.

The exact definitions of and demarcation between macro-, mini-, and microchannels remains nebulous. Rather than defining a hard cutoff between channel classifications, it can best be concluded that the difference between mini- and

microchannels and macro sized channels occurs when forces or phenomena generally not accounted for at the macro scale take on increasing importance. For two-phase flow, this is usually the increasing importance of surface tension forces and the decreasing influence of gravitational forces as channel size decreases. Kew and Cornwell (1997) relate the magnitudes of surface tension and gravitational forces through the Confinement number (microchannel effects exist when $Co > 0.5$), while Serizawa *et al.* (2002) relate the same forces through the Laplace constant (L), suggesting that microchannel effects exist when $L > D_h$. Both relations imply that microchannel effects will be observed in larger channels for fluids with larger surface tension. The microchannel transition diameter according to each criterion for representative fluids is shown in Table 1.1. The table shows that surface tension plays an important role over a wide range of channel diameters. However, defining microchannels in this manner is complicated by the general inconsistency in usage of terminology between academic literature and industry, which

Table 1.1: Comparison of microchannel classification criteria

			Transition Diameter (mm)	
	***P* (kPa)**	**T_{bub} (°C)**	**Co > 0.5**	**$L > D_H$**
R-134a	1500	55	1.32	0.66
R-404A	1500	32	1.20	0.60
Propane	1500	44	2.13	1.06
NH_3	1500	39	3.46	1.73
NH_3/H_2O (90/10)	1500	43	3.54	1.77
NH_3/H_2O (50/50)	1500	80	3.66	1.83
Water	1500	198	4.25	2.13

often refers to channels with $D_H < 1$ mm as microchannels.

1.3 Mixture Condensation

Condensation of fluid mixtures of interest can broadly be divided into three categories: mixtures with all components condensable and miscible in all concentrations (*i.e.* water and ammonia), mixtures with non-condensable components (*i.e.* water and air), and mixtures with all components condensable but immiscible in certain concentrations (*i.e.* water and hydrocarbons). The present study focuses on the first type of mixtures.

1.3.1 Mixture Classification

From the Gibbs phase rule, the thermodynamic properties of each phase in a two-phase mixture of *n* components are determined as a function of *n* independent properties (temperature/pressure and *n*-1 mass/mole fractions). Condensable mixtures can be classified based on the relationship between the concentrations of each component in each phase at equilibrium.

The focus of this study is on mixtures of ammonia and water, which at equilibrium have different compositions in the liquid and vapor phases. Figure 1.4 shows a plot of saturated vapor (dew point) and liquid (bubble point) temperature versus concentration of ammonia at a constant pressure for a binary mixture of ammonia/water. Generation of this plot requires knowledge of vapor/liquid equilibrium thermodynamics, details of which are outside the scope of this review. Throughout the present study, thermodynamic properties of the NH_3/H_2O mixtures were obtained from the correlations of Ibrahim and Klein (1993).

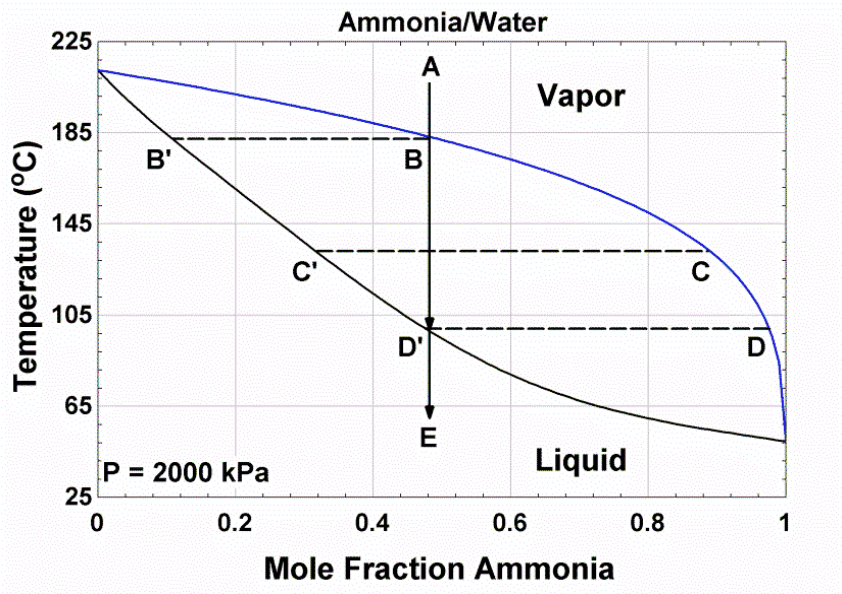

Figure 1.4: Ammonia/water phase diagram at *P* = 2000 kPa

Inspection of Figure 1.4 shows that at a given temperature, the concentration of the vapor and liquid are indeed different. It can also be inferred that as the mixture begins to condense, the concentration of the more volatile component in the vapor (in this case, ammonia) increases, and the dew point temperature decreases. Thus, unlike a single-component fluid, the condensation process is not isothermal. To further illustrate this, a representative condensation process is overlaid in Figure 1.4, assuming the entire system remains in equilibrium. Starting at point A, the mixture is a superheated vapor. Heat is removed until the dew point temperature is reached at point B, where the first drop of condensate formed has a composition of ammonia corresponding to point B' on the bubble point curve. The mixture is further condensed to the intermediate point represented by C and C', which correspond to the equilibrium concentration of ammonia in the vapor and liquid, respectively. The equilibrium temperature at this point is somewhere between the dew and bubble points. When the mixture is condensed down to the bubble temperature, the point D corresponds to the concentration of the last bubble of

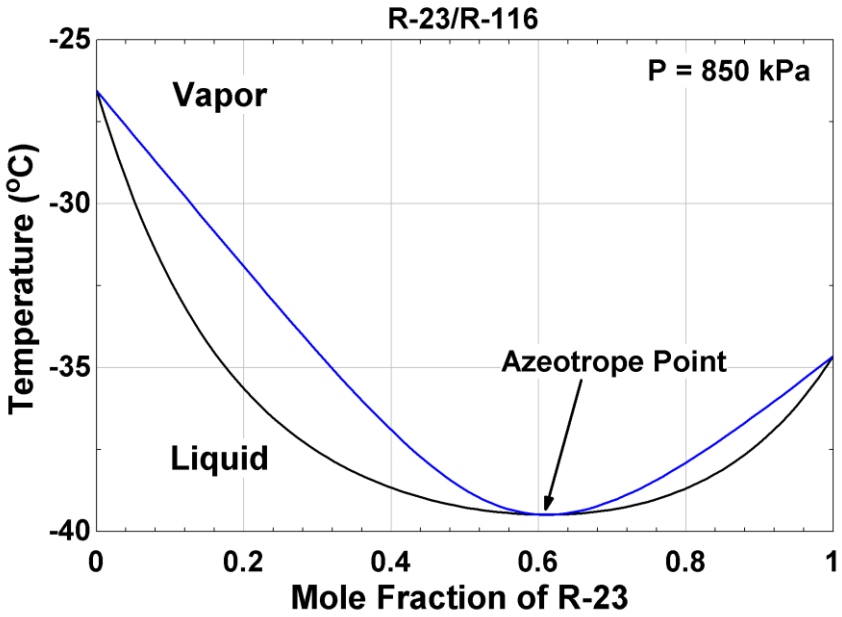

Figure 1.5: R-23/R-116 phase diagram with azeotrope point at *P* = 850 kPa

vapor condensed, while point D' corresponds to the concentration of the liquid being equal to the original bulk vapor concentration. By removing further heat, the mixture can be subcooled to point E, with the concentration unchanged. In general, the entire system will not remain at thermodynamic equilibrium, and the local concentrations and temperature at the interface will be different from the liquid and vapor bulk. This introduces several complications in the understanding and modeling of mixture condensation, which will be further discussed in the following section.

An azeotropic mixture has a constant boiling point that is different (*i.e.*, lower or higher) than that of any of the individual components. As the mixture boils or condenses, the composition of the vapor and liquid phase are equal. Thus, there is no temperature glide as the mixture condenses and the methods for predicting heat transfer for the condensation of single-component fluids are applicable. Azeotropic mixtures are usually binary mixtures; however, ternary azeotropes have been documented (Mohanraj *et al.*,

2011). Figure 1.5 shows the dew and bubble points versus composition for a mixture of R-23 and R-116. An azeotropic point can be seen at a molar concentration of R-23/R-116 of 40/60%.

For concentrations near the azeotropic point, the temperature glide is still very small. Fluid mixtures with concentrations corresponding to small temperature glides are commonly referred to as near-azeotropic mixtures, with in-tube condensation for such mixtures often modeled in the same way as for single-component fluids with reasonable accuracy. Azeotropic and near-azeotropic mixtures are not considered in the present study.

1.3.2 Heat and Mass Transfer Resistances in Mixtures

The condensation of a zeotropic mixture as discussed above corresponds to a situation in which the temperatures and concentrations of the vapor and liquid phases correspond to the thermodynamic equilibrium condition over the entire condensing process. In practice, this is not the case. Consider a binary zeotropic mixture condensing in a vertical channel, with heat rejected to a coolant in an outer annulus, shown schematically in Figure 1.6. The temperature and concentration profiles of the more volatile ($\tilde{y}_1$) component from the vapor bulk to the coolant are shown in the figure. As heat is removed from the system, the less volatile ($\tilde{y}_2$) component condenses more readily, resulting in a locally higher concentration of the more volatile component in the vapor near the interface. The local interface concentration is higher than in the bulk vapor. A review of Figure 1.4 shows that at a fixed pressure, a higher concentration of the more volatile component in the vapor will result in a lower local saturation temperature. Additionally, the resulting concentration gradient between the vapor interface and vapor bulk results in the back

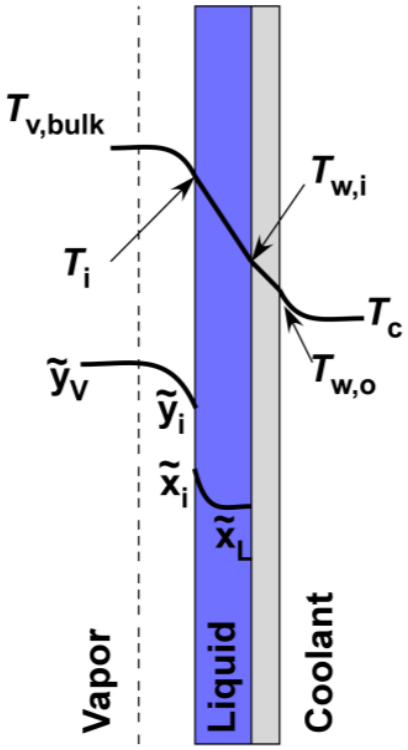

Figure 1.6: Schematic of zeotropic condensation process

diffusion of the volatile component towards the bulk and of the less volatile component towards the interface. A similar concentration gradient is set up in the liquid film. Thus, the interfacial concentration is governed by the combined effect of the rate of mass transfer in the vapor and liquid film and the rate of condensation. The condensation rate is directly related to the driving temperature difference from the interface to the coolant. Finally, the interface temperature is a function of the interfacial concentration; thus, the heat and mass transfer phenomena are strongly coupled.

A common assumption in modeling condensation of mixtures is that the vapor and liquid are in equilibrium at the interface (Colburn and Drew, 1937). This has been shown to yield extremely accurate results, although interfacial resistance ($T_{i,V} \neq T_{i,L}$) can become more significant for vapors condensing at very low pressures (Webb and

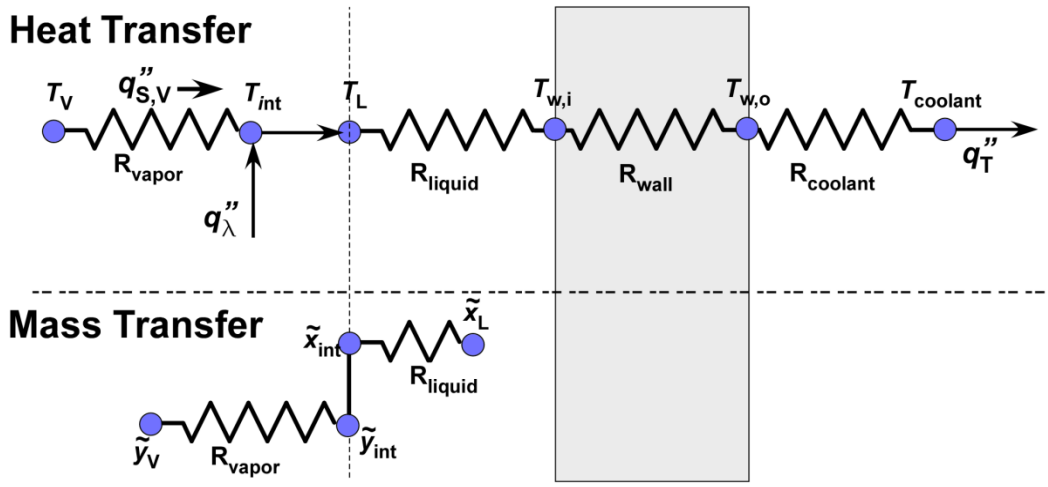

Figure 1.7: Liquid and vapor heat and mass transfer resistances

McNaught, 1980). However, assuming equilibrium, the interfacial temperature (T_i) can be determined from the interfacial concentration in either the liquid or the vapor ($\tilde{x}_i, \tilde{y}_i$), the local pressure, and knowledge of the vapor/liquid equilibrium properties. The interfacial concentrations are generally not known *a priori* and must be determined by considering the coupled heat and mass transfer in the vapor and liquid phases. Figure 1.7 shows a schematic of the heat and mass transfer resistances in the liquid and vapor.

The total heat duty rejected to the coolant is the sum of the latent heat of condensation and the sensible heat due to cooling of the bulk vapor and liquid film. Because a large fraction of the heat to be rejected is latent heat, it is desirable for the driving temperature difference across the condensate film (T_i - T_c) to be maximized. That is, it is preferable for T_i to be equal to T_v. This would be the case for infinitely fast mass transfer or for a single-component fluid. As the mass transfer resistance increases, the concentration of the volatile component at the interface increases and T_i approaches T_{bub} (as was shown in Figure 1.4), because the volatile component will readily condense at

this temperature. It should be noted that for mixtures with non-condensable components, the lower limit to the interface temperature is not established by these considerations as the concentration of the non-condensable component builds up at the interface. Therefore, poor mass transfer has a deleterious effect on heat transfer by reducing the driving temperature difference between the interface and the coolant.

Based on the above discussion, modeling the condensation heat duty in a multi-component mixture requires the ability to understand and predict the following:

- Mass transfer resistance in the vapor
- Sensible heat transfer resistance in the vapor
- Mass transfer resistance in the liquid film
- Sensible and latent heat transfer resistance in the liquid film
- Determination of interface temperature from interfacial composition and vapor-liquid equilibrium

1.4 Organization of Thesis

The remainder of this thesis is organized as follows:

- Chapter 2 presents an in-depth review of in-tube condensation heat transfer, pressure drop, and flow regime mapping for single- and multi-component fluids. The need for additional research and the objectives of the present study are also introduced here.

- Chapter 3 presents the experimental setup, instrumentation and procedures for the pure ammonia and zeotropic ammonia/water mixtures experiments.

- Chapter 4 presents the data analysis procedure and uncertainty analysis for determination of condensation heat duty, condensation heat transfer coefficient/apparent heat transfer coefficient, and frictional pressure gradient for the pure and zeotropic fluids.

- Chapter 5 details the experimental results and provides a comparison with existing correlations from the literature for pure ammonia.

- Chapter 6 details the experimental results and provides a comparison with existing correlations from the literature for zeotropic mixtures of ammonia and water.

- Chapter 7 presents the development of the flow regime-based ammonia condensation model and the development of coupled heat and mass transfer zeotropic condenser model, as well as a parametric investigation using this model for both ammonia and zeotropic ammonia/water mixtures.

- Chapter 8 provides conclusions from this study and recommendations for further research activities.

CHAPTER 2

PRIOR WORK

Internal forced condensation has been extensively studied due to its great importance in numerous industrial applications. However, there has been less research on condensation heat transfer and pressure drop at the microscale, and on condensation of zeotropic mixtures in both large and small diameter channels. The present study relies on the body of literature in both of these topics. Thus, studies on two-phase flow regimes, pressure drop and heat transfer during pure fluid condensation in microchannels, as well as work focused on condensing mixtures in tubes are reviewed in this chapter.

2.1 Microchannel Two-phase Flow

Understanding the prevailing two-phase flow regimes during condensation is critical for the development of mechanistic models for predicting heat transfer and pressure drop. Unlike two-phase flow in vertical tubes, stratification of the phases due to gravity can be important in horizontal and slightly inclined tubes. Two-phase flow patterns in horizontal channel have been extensively studied in large diameter tubes (D > 5 mm) for a variety of fluids (air/water, oil/gas, refrigerants, etc.) and operating conditions (adiabatic, condensing and evaporating flows). The results of these studies have shown that the mechanisms governing the flow transitions are a function of the relative importance of gravitational, inertial, viscous, and surface tension forces.

Flow regime maps, which plot the local flow regime as a function of relevant parameters (*e.g.*, superficial liquid/vapor velocities, dimensionless groups, etc.), have become useful tools for determining local flow regimes and transitions. Early empirical

flow maps for oil/gas and air/water flows include those of Baker (1954), Govier and Omer (1962) and Mandhane *et al.* (1974). Taitel and Dukler (1976) made one of the first attempts at defining flow regime transitions in horizontal and inclined tubes from a theoretical basis. They used a set of five dimensionless parameters which captured the effects of tube diameter, buoyancy and Kelvin-Helmholtz wave instabilities on the flow transitions. One drawback of the Taitel and Dukler (1976) map is that the transition criteria do not account for surface tension, which becomes increasing important in small diameter tubes.

Griffith and Lee (1964) observed air/water flows in small diameter tubes (D_H = 1 mm) and proposed that surface tension forces pull interfacial waves to the center of the tube during annular flow, eventually forming complete liquid bridges and resulting in liquid slug flow. Using this insight, Barnea *et al.* (1983) proposed a modification to the Taitel and Dukler (1976) map to account for surface tension for the transition from stratified flows to intermittent slug flow. Other air-water studies in small channels, such as those by Coleman and Garimella (1999) and Triplett *et al.* (1999) confirmed that the flow maps developed for large diameter channels (D_H > 10 mm) could not be extended to small diameter channels. Acknowledging the dominance of surface tension over gravity at small scales (D ~ 1 mm), Akbar *et al.* (2003) developed a simple phasic Weber number based flow map using the methodologies of Zhao and Rezkallah (1993) and Rezkallah (1996) for two-phase flow in microgravity. They divided the flow map into four zones: 1) surface tension dominated zone (bubbly and plug/slug regimes), 2) inertia-dominated zone #1 (annular and wavy annular regimes), 3) inertia dominated zone #2 (dispersed flow regime), and 4) transition zone, where inertial and surface tension forces are of

comparable magnitude. The map was based on data from multiple researchers on air/water flows with tube diameter ranging from 0.86 to 1.6 mm, superficial vapor velocities between 0.1 and 100 m s^{-1}, and superficial liquid velocities ranging from 0.003 to 20 m s^{-1}.

More recently, research has been conducted on two-phase flow regimes for condensing flows, with a focus on synthetic refrigerants (*e.g.*, R-134a, R-404A). As shown in Table 2.1, the fluid properties of refrigerants (including zeotropic NH_3/H_2O mixtures of 90% and 50% ammonia by mass) operating at typical condensing saturation pressures are significantly different than those of air/water. The relative magnitudes of the shear, gravity and surface tension forces are directly related to the fluid properties, and have an important role in determining flow regime transitions. Cavallini *et al.* (2002a) proposed a map for condensing HCFC, CFC and HFC fluids at reduced pressures of up to 0.75 in tubes with diameters ranging from 3 to 21 mm. El Hajal *et al.* (2003) presented a flow map for condensing refrigerants based on a previous map for flow boiling (Kattan *et al.*, 1998). The map was subsequently modified by Suliman *et al.* (2009) based on experiments with R134a at T_{sat} = 40°C, 75 < G < 300 kg m^{-2} s^{-1} and D =

Table 2.1: Comparison of properties

	P (kPa)	ρ_L/ρ_V	μ_V/μ_L	$\sigma \cdot 10^{-3}$ (N/m)	T_{bub} (°C)
Air/Water	101	845	48.2	38.1	-
R134a	1500	14	9.7	4.3	55
R-404A	1500	12.6	8.4	3.3	32
Ammonia	1500	50	15.6	15.8	39
NH_3/H_2O (90/10)	1500	74	16.4	18.9	43
NH_3/H_2O (50/50)	1500	99	6.3	25	80

8.38 mm.

Coleman and Garimella (2003) conducted one of the few studies for condensing flows in microchannels. Based on visualization of condensing R-134a (Coleman and Garimella, 2000), they developed empirical flow regime transition criteria as functions of mass flux, quality and tube size. The data encompassed circular (D = 4.91 mm) and rectangular channels ($0.67 < D_H < 4.8$ mm and $0.5 < AR < 2$) at mass fluxes ranging from 150 to 750 kg m^{-2} s^{-1}. They found that as the tube diameter decreased, the intermittent flow regime spanned a larger quality and mass flux region. Additionally, at the smallest tube diameters, transitions occurred directly from annular to intermittent flow, with no stratified wavy flow observed. Nema *et al.* (2014) used the data from Coleman and Garimella (2003) to develop a flow map based on dimensionless criteria to capture the combined effect of mass flux, quality, fluid properties and tube size.

Many empirical and semi-empirical flow maps have been developed for adiabatic and diabatic two-phase flows in a range of channel sizes. The fluids of interest in most of the regime classification studies to date have been air/water mixtures or synthetic refrigerants. The ammonia/water mixtures in the present investigation have properties that are between those of air/water and refrigerants. Classification of flow regimes and transitions remains highly subjective; however, the use of a flow map developed for conditions approximating those of the process of interest has been proven to improve pressure drop and heat transfer modeling (Cavallini *et al.*, 2002a; Thome *et al.*, 2003; Bandhauer *et al.*, 2006).

2.2 Microchannel Pressure Drop

The total two-phase, cross-section averaged, steady state pressure gradient in tubes is a sum of the contributions of the three terms in Eq. (2.1), as shown in Ghiaasiaan (2008).

$$\left(-\frac{\partial P}{\partial z}\right)=\underbrace{\left(-\frac{\partial P}{\partial z}\right)_{a}}_{\text{Term 1}}+\underbrace{\left(-\frac{\partial P}{\partial z}\right)_{fr}}_{\text{Term 2}}+\underbrace{\left(-\frac{\partial P}{\partial z}\right)_{g}}_{\text{Term3}} \tag{2.1}$$

The first term represents the pressure gradient caused by spatial mixture acceleration, the second term is the frictional pressure gradient, and the last term represents the hydrostatic pressure gradient.

Historically, two-phase frictional pressure drop in adiabatic and diabatic flows has been predicted using an empirical two-phase multiplier, which when multiplied by the appropriate single-phase frictional gradient (liquid, liquid-only, vapor, vapor-only) yields the two-phase pressure drop (Eq. (2.2)). The two-phase multiplier is empirical in nature and does not necessarily account for all physical phenomena. Large scatter in predictions can occur, particularly when models are applied outside the range of mass flux, tube size and fluid properties for which they were developed. In addition, the two-phase multiplier approach does not explicitly account for the local flow regime. As was discussed in the previous section, intermittent flow can occur over a large quality range in microchannels, which has significantly different pressure drop mechanisms than annular flow.

$$\left(-\frac{\partial P}{\partial z}\right)_{fr,TP}=\Phi_{LO}^{2}\left(-\frac{\partial P}{\partial z}\right)_{fr,LO} \tag{2.2}$$

For large tubes, Lockhart and Martinelli (1949) developed a correlation for adiabatic oil-gas flows. They found the two-phase multiplier to be a function of mass

flux, fluid properties and quality, but not explicitly of tube diameter. They defined a term *X*, referred to as the Martinelli parameter, as the square root of the ratio of the liquid/vapor frictional pressure gradients. They then graphically correlated the liquid and vapor two-phase multipliers as a function of the Martinelli parameter. Chisholm (1967) represented this relationship in an analytical form in Eq. (2.3), where the constant *C* is dependent on whether or not the liquid and vapor Reynolds numbers are turbulent, laminar or some combination of the two.

$$\Phi_L = \left(1 + \frac{C}{X} + \frac{1}{X^2}\right)^{1/2} \tag{2.3}$$

Other correlations for the two-phase multiplier have been developed by many other researchers (Martinelli and Nelson, 1948; Friedel, 1979; Beattie and Whalley, 1982; Cavallini *et al.*, 2002a) to account for different fluids, tube geometries and other parameters in large tubes ($D > 3$ mm). Two-phase pressure drop in small channels has also been extensively studied, with a primary focus on adiabatic air-water mixtures. There is limited research on pressure drops in condensing flows. Due to the prevalence of laminar flow and the importance of surface tension, correlations developed for large channels do not extrapolate well to the microscale. Excellent reviews of pressure drop research in microchannels can be found in Ghiaasiaan (2008) and Garimella (2014). Studies relevant to the experimental conditions of interest in the presented study are discussed here.

Mishima and Hibiki (1996) conducted adiabatic air/water pressure drop experiments in circular channels ($1 < D < 4$ mm) with vertical upward flow. They

observed local flow regimes using high-speed video recording techniques and measured void fraction with a neutron radiography technique. In addition, they determined frictional pressure loss from the measured pressure loss by neglecting any acceleration terms and subtracting the gravitational pressure loss. They found the value of the Chisholm parameter (*C*, in Eq. (2.3)) to decrease with decreasing tube diameter. They proposed a new correlation for *C*, shown in Eq. 2.4, where *D*, the tube diameter, is in mm. The new correlation predicts air/water data from several researchers with an average error of ±12%; however, when compared to two-phase saturated ammonia pressure drop data (Ungar and Cornwell, 1992) in circular horizontal tubes ($1.46 < D < 3.15$ mm), the error was ±25%. This indicates that the significant property variations of the different fluids are not completely accounted for.

$$C = 21\left(1 - \exp\left[-0.319 \cdot D\right]\right) \tag{2.4}$$

Lee and Lee (2001) also investigated air/water mixtures in horizontal, rectangular microchannels with high aspect ratio ($0.78 \le D_H \le 6.67$ mm; $5 \le AR \le 50$).They observed large deviations between the measured values of the two phase multiplier and those obtained by Eq. (2.4). They attributed the discrepancies to the fact that the Mishima and Hibiki (1996) correlation for Chisholm parameter did not account for liquid and vapor flow rates or the influence of surface tension. To capture these effects, they correlated the Chisholm parameter (Eq. (2.7)) as a function of the liquid-only Reynolds number, the Capillary number (Eq. (2.5)) and the ratio of gravity and surface tension forces (Eq. (2.6)), expected to be negligible for small, horizontal channels.

$$\psi = \frac{\mu_L j_{\text{slug}}}{\sigma} \tag{2.5}$$

$$\lambda = \frac{\mu_{\text{L}}^2}{\rho_{\text{L}} \sigma D_{\text{H}}} \tag{2.6}$$

$$C = A \cdot \lambda^q \cdot \psi^r \cdot \text{Re}_{\text{LO}}^s \tag{2.7}$$

The constants and the exponents for this correlation are evaluated differently for each combination of liquid and vapor Reynolds numbers. The *q* and *r* exponents are only greater than zero when both Reynolds numbers are in the laminar region, implying that the effect of surface tension becomes insignificant.

The considerably different properties of synthetic and natural refrigerants compared to air/water mixtures have led to a growing body of research on two-phase pressure drop of these fluids in mini- and microchannels. Cavallini, Del Col and co-workers (2005a; 2005b; 2006; 2009; 2010) have conducted numerous experimental studies on this subject. In 2005, they presented an empirical correlation, similar in form to the Friedel (1979) correlation, for frictional pressure gradient of annular refrigerant flow in minichannels. They attempted to account for liquid entrained in the vapor core through the entrainment ratio proposed by Paleev and Filippovich, (Eq. (2.8)).

$$\begin{aligned} E &= 0.015 + 0.44 \cdot \log\left(\left(\rho_{\text{GC}} / \rho_{\text{L}} \right) \cdot \left(\frac{\mu_{\text{L}} \cdot j_{\text{V}}}{\sigma} \right)^2 \cdot 10^4 \right) \\ \rho_{\text{GC}} &= \rho_{\text{V}} \left[1 + \left(1 - q\right) \cdot \frac{E}{q} \right] \end{aligned} \tag{2.8}$$

Data from several studies on condensation of refrigerants in mini- and microchannels were then correlated, resulting in the expression in Eq. (2.9) for the two-phase multiplier as a function of quality, fluid properties, and reduced pressure.

$$\Phi_{LO}^2 = Z + 3.595 \cdot F \cdot H \cdot (1-E)^W$$
$$Z = (1-q)^2 + q^2 \left(\frac{\rho_L}{\rho_V}\right) \cdot \left(\frac{\mu_V}{\mu_L}\right)^{0.2}$$
$$F = q^{0.9525} \cdot (1-q)^{0.414} \tag{2.9}$$
$$H = \left(\frac{\rho_L}{\rho_V}\right)^{1.132} \cdot \left(\frac{\mu_V}{\mu_L}\right)^{0.44} \left(1-\frac{\mu_V}{\mu_L}\right)^{3.542}$$
$$W = 1.398 \cdot P_r$$

They also investigated adiabatic frictional pressure drop in a rectangular multiport minichannel tubes (D_H = 1.4 mm, L = 1.13 m) for halogenated refrigerants R-134a and R-404A (2005a) and R-134a, R-236ea, and R-410A (2006). Data were obtained for mass fluxes from 200 to 1400 kg m^{-2} s^{-1} at a saturation temperature of 40°C. The refrigerants were selected to span a range of reduced pressures from high (P_R = 0.49 for R-410A), to medium (P_R = 0.25 for R-134a), to low (P_R = 0.14 for R-236ea). They found that most correlations were not able to predict the frictional gradient over the range of fluids and operating conditions for the multiport tube. However, they showed that the model given in Eqs. (2.8)-(2.9) was able to predict the data over the reduced pressure range from 0.2 to 0.5 satisfactorily. More recently, they have obtained additional data for R-134a (2009) and R-1234yf (2010) in a single circular channel with D = 0.96 mm at mass fluxes ranging from 200 to 1000 kg m^{-2} s^{-1}. They extended the above model (Cavallini *et al.*, 2005b) to account for surface roughness and non-shear dominated flow regimes (defined as j_V < 2.5) by modifying the calculation of the liquid-film friction factor.

The group of Thome and co-workers has also conducted numerous studies on two-phase pressure drop in adiabatic and evaporating flows through microchannels for synthetic and natural refrigerants. Ribatski *et al.* (2006) conducted a comprehensive review of heat transfer and pressure drop in microchannels ($0.05 < D_H < 3$ mm) for eight fluids at mass fluxes ranging from 23 to 6000 kg m^{-2} s^{-1} and vapor qualities up to 1. The studies reviewed included adiabatic and evaporation studies. They found that the correlation of Müller-Steinhagen and Heck (1986) developed for large channels predicted the data the best, followed by the method of Mishima and Hibiki (1996). However, even the best correlation predicted less than 50% of the data within ±30%. They noted particularly poor agreement at higher quality (> 0.6), where annular flow is expected to dominate. Revellin and Thome (2007) then conducted adiabatic pressure drop experiments with R134a and R245fa in circular microchannels ($0.509 < D_H < 0.790$ mm). They observed laminar, transition and turbulent zones when plotting two-phase friction factor vs. two-phase Reynolds number (using the two-phase viscosity model of McAdams *et al.* (1942)). They proposed a new correlation for two-phase friction factor as a function of two-phase Reynolds number. However, the correlations are specific to the tube diameters investigated and not easily extrapolated. Additionally, they note that there is still poor agreement in the transition and laminar regimes, which tend to correspond to the intermittent flow regime. Cioncolini *et al.* (2009) conducted a review of annular flow pressure drop data from micro to macro channel sizes ($0.52 < D_H < 25$ mm) for air/water and refrigerants flows. The method of Lombardi and Carsana (1992) was found to predict the data the best over the entire set of conditions, with a mean average deviation of 15.9% for macroscale tubes and 18.9% for the microscale tubes. They then proposed an

empirical correlation (Eq. (2.10)) as a function of vapor core Weber number and liquid Reynolds number. These dimensionless numbers are defined as a function of the fraction of liquid entrained in the core from the correlation of Oliemans *et al.* (1986).

$$\begin{aligned} f_{TP} &= 0.172 \cdot \mathrm{We}_{\mathrm{C}}^{-0.372} && \text{for Bo} \geq 4 \\ f_{TP} &= 0.0196 \cdot \mathrm{We}_{\mathrm{C}}^{-0.372} \cdot \mathrm{Re}_{l}^{0.318} && \text{for Bo} < 4 \end{aligned} \tag{2.10}$$

Agarwal and Garimella (2009) developed a multi-flow-regime based model for the pressure drop of condensing R134a in circular and non-circular microchannels (0.42 < D_{H} < 0.8 mm). Flow regimes were divided between intermittent, transition and annular flow based on the flow visualization studies of Coleman and Garimella (2003). The intermittent model extends the mechanistic model for the intermittent flow regime developed by Garimella *et al.* for circular (2005) and non-circular microchannels (2003). The model was based on the unit cell shown schematically in Figure 2.1. The total pressure drop in each unit cell is the sum of the pressure drop in the liquid slug, vapor bubble and transition between the two (Eq. (2.11)). Using the Armand (1946) void fraction correlation, it was shown that the velocity of the bubble is 1.2 times that of the

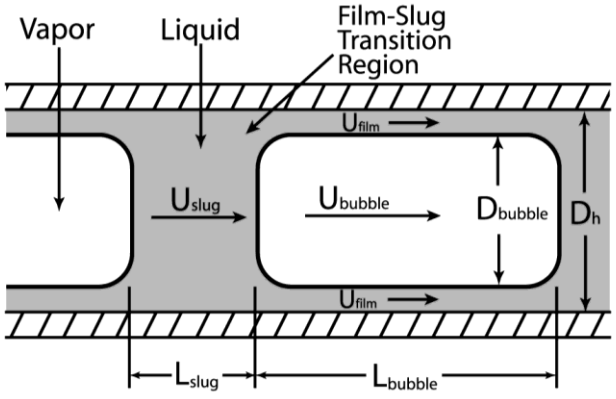

Figure 2.1: Schematic of intermittent unit cell from Garimella *et al.* (2002)

liquid slug. From this, the relative lengths of the bubble and slug were determined and a correlation for slug frequency was developed as a function of slug Reynolds number for circular and noncircular tubes.

$$\left(\frac{dP}{dz}\right)=\left(\frac{dP}{dz}\right)_{\substack{\text{film}\\\text{bubble}}}\left(\frac{L_{\text{bubble}}}{L_{\text{UC}}}\right)+\left(\frac{dP}{dz}\right)_{\text{slug}}\left(\frac{L_{\text{slug}}}{L_{\text{UC}}}\right)+\Delta P_{\text{transition}}\left(\frac{N_{\text{UC}}}{L}\right) \tag{2.11}$$

In the annular flow regime, the model of Garimella *et al.* (2005) was used as the starting point. The frictional pressure drop is related to the Darcy form of the interfacial friction factor as shown in Eq. (2.12), where the void fraction, ε, is calculated from the Baroczy (1965) model.

$$\frac{\Delta P}{L}=\frac{1}{2}\cdot f_i\frac{G^2\cdot q^2}{\rho_{\text{V}}\cdot\varepsilon^{2.5}}\cdot\frac{1}{D} \tag{2.12}$$

The interfacial friction factor (f_i) was then correlated to the liquid-phase Darcy friction factor (obtained using the Churchill (1977b) correlation), using the expression in Eq. (2.13), where X is the Martinelli parameter and ψ is the ratio of viscous to surface tension forces that was also used by Lee and Lee (2001).

$$\frac{f_i}{f_{\text{L}}}=A\cdot X^a\cdot\text{Re}_{\text{L}}^b\cdot\psi^c \tag{2.13}$$

The constant A and the exponents were then determined by regression for different tubes shapes. For points in the transition region, a double interpolation method between the two models was recommended. They found that over 80% of data for condensing R-134a flows were predicting within ±25%.

Chung and Kawaji (2004) used a similar mechanistic model for predicting pressure drop of N_2/water flows in circular microchannels ($0.05 < D < 0.53$ mm). In their experiments they accounted for fluid acceleration and inlet/outlet minor losses when determining the frictional pressure gradient, with a reported uncertainty of ±2 to ±7%. They observed predominantly intermittent plug/slug and annular flow. However, unlike the Garimella *et al.* (2005) model, they neglected mixing losses at the transitions between the bubble and slug regions. They theorized that the laminar characteristics of the flow under investigation would suppress mixing effects. They also assumed that the bubble and slug velocities were equal and that the bubble diameter was 90% of the tube diameter. Agarwal and Garimella (2014a) also built on the intermittent flow model of Garimella *et al.* (2005) for condensation of R-134a in multiple parallel rectangular microchannels ($0.1 < D_H < 0.4$ mm, $1 < AR < 4$). However, they found that the slug frequency model proposed in Garimella *et al.* (2005) did not predict the data well. A new slug frequency model that included additional property ratios and the influence of aspect ratio was introduced.

Using a large database of over 7,000 adiabatic and condensing frictional pressure drop results, Kim and Mudawar (2012) developed a general empirical two-phase pressure drop model for mini- and microchannels. The database was obtained from 36 sources and contained data for 17 working fluids, single and multiport circular, and rectangular channels with hydraulic diameter ranging from 0.0695 to 6.22 mm, mass flux from 4 to 8528 kg m^{-2} s^{-1} and reduced pressures ranging from 0.0052 to 0.91. The working fluids were predominantly synthetic refrigerants, with some limited data on natural working fluids (*e.g,* CO_2, ammonia, hydrocarbons.) They found that most existing pressure drop

models only predicted the data well for certain subsets of the database. Starting with the separated flow model of Lockhart-Martinelli, they developed new correlations for the Chisholm *C* parameter as a function of liquid Reynolds number and the vapor-only Suratman (also known as Laplace, Eq. (2.14)) number, which accounts for microchannel effects through the ratio of surface tension and momentum. The results are shown in Table 2.2.

$$\mathrm{Su}_{\mathrm{VO}} = \frac{\rho_{\mathrm{V}} \sigma D_{\mathrm{H}}}{\mu_{\mathrm{V}}^2} \tag{2.14}$$

For calculating the liquid and vapor friction factors necessary for the solution of the Lockhart-Martinelli approach, they recommend the following:

$$\begin{aligned} f &= \frac{16}{\mathrm{Re}} && \text{for } \mathrm{Re} < 2000 \\ f &= 0.079\,\mathrm{Re}^{-0.25} && \text{for } 2000 \le \mathrm{Re} < 20,000 \\ f &= 0.046\,\mathrm{Re}^{-0.2} && \text{for } \mathrm{Re} \ge 20,000 \end{aligned} \tag{2.15}$$

for laminar flow in rectangular channels:

$f\,\mathrm{Re} = 24\left(1 - 1.3553\beta + 1.9467\beta^2 - 1.7012\beta^3 + 0.9564\beta^4 - 0.2537\beta^5\right)$

$\beta =$ aspect ratio

Table 2.2: *C* parameter from Kim and Mudawar (2012) model

Liquid Regime	Vapor Regime	*C*
Laminar	Laminar	$C = 3\times10^{-5}\,\mathrm{Re}_{\mathrm{LO}}^{0.44}\,\mathrm{Su}_{\mathrm{VO}}^{0.50}\left(\frac{\rho_{\mathrm{L}}}{\rho_{\mathrm{V}}}\right)^{0.48}$
Laminar	Turbulent	$C = 0.0015\,\mathrm{Re}_{\mathrm{LO}}^{0.59}\,\mathrm{Su}_{\mathrm{VO}}^{0.19}\left(\frac{\rho_{\mathrm{L}}}{\rho_{\mathrm{V}}}\right)^{0.36}$
Turbulent	Laminar	$C = 8.7\times10^{-4}\,\mathrm{Re}_{\mathrm{LO}}^{0.17}\,\mathrm{Su}_{\mathrm{VO}}^{0.50}\left(\frac{\rho_{\mathrm{L}}}{\rho_{\mathrm{V}}}\right)^{0.14}$
Turbulent	Turbulent	$C = 0.39\,\mathrm{Re}_{\mathrm{LO}}^{0.03}\,\mathrm{Su}_{\mathrm{VO}}^{0.10}\left(\frac{\rho_{\mathrm{L}}}{\rho_{\mathrm{V}}}\right)^{0.35}$

Understanding the pressure drop at the microscale for condensing fluids is an important parameter for predicting the heat transfer coefficient, as discussed in the following section.

2.3 Microchannel Condensation Heat Transfer

The high heat transfer coefficients possible for condensing flows in microchannels have made this area increasingly popular for study. As with pressure drop, models developed for condensation heat transfer in large diameter tubes generally scale poorly to the microscale. Thus, there have been several experimental heat transfer studies used to develop empirical and semi-empirical models for predicting heat transfer coefficients in small diameter tubes. Unlike the present study, previous research has been almost exclusively conducted for pure fluids or azeotropic mixtures.

Dobson and Chato (1998) state that internal condensation in large diameter horizontal tubes can be divided into gravity controlled and vapor shear controlled regions. The gravity controlled region is characterized by the formation of condensate

around the top circumference, with liquid pooling and flowing axially along the bottom. Heat transfer in this regime is generally modeled with a Nusselt type analysis (Chato, 1962; Jaster and Kosky, 1976). However, this gravity controlled regime is not expected for the hydraulic diameters and mass fluxes in the present study, as shown in Section 2.1. Instead, the flow is expected to be primarily annular or intermittent, with heat transfer and pressure drop dominated by vapor shear.

Shear-dominated condensation in large diameter tubes has received much attention in the past, resulting in theoretical, semi-empirical and purely empirical correlations. The approaches taken to predict heat transfer can be divided into two categories: correlations developed with a boundary-layer approach (Traviss *et al.*, 1973; Cavallini *et al.*, 2002a; Cavallini *et al.*, 2005b; Agarwal *et al.*, 2010) and two-phase multiplier correlations (Shah, 1979; Dobson and Chato, 1998; Wang *et al.*, 2002; Koyama *et al.*, 2003; Thome *et al.*, 2003; Keinath, 2012).

In the boundary layer approach, appropriate for annular flow condensation, the liquid film is assumed to have characteristics similar to a turbulent boundary layer. The dimensionless liquid temperature (T^+) at the surface of the film is defined in terms of the liquid film properties, heat flux, wall shear stress and temperature difference across the liquid film. After using an appropriate relationship to find the film thickness, the dimensionless temperature is determined from the turbulent law of the wall temperature distributions and the wall shear stress determined from an appropriate correlation for the two-phase frictional pressure gradient. Finally, the heat transfer coefficient can be deduced, as shown in Eq. (2.16).

$$\alpha = \frac{\rho_L c_{p,L} \left(\tau_i / \rho_L\right)^{0.5}}{T^+} \tag{2.16}$$

A representative correlation for large tubes by Traviss *et al.*(1973) presents a relationship for the film thickness as a function of liquid Reynolds numbers, and uses the Lockhart and Martinelli (1949) correlation to determine the two-phase frictional pressure gradient. Their method is summarized in Eq. (2.17). The model was validated with condensation data for R-12 and R-22 in tubes with D = 8 mm at $161 \le G \le 1533$ kg m^{-2} s^{-1} and $25 \le T_{sat} \le 58$°C.

$$\mathrm{Nu} = \frac{0.15 \cdot \mathrm{Pr}_L \cdot \mathrm{Re}_L^{0.9}}{F_T}\left[\frac{1}{X_{tt}} + \frac{2.85}{X_{tt}^{0.476}}\right] \tag{2.17}$$

$$\text{where } F_T = \begin{cases} 5 \cdot \mathrm{Pr}_L + 5 \cdot \ln\left(1 + 5 \cdot \mathrm{Pr}_L\right) + 2.5 \cdot \ln\left(0.0031 \cdot \mathrm{Re}_L^{0.812}\right) & \mathrm{Re}_L > 1125 \\ 5 \cdot \mathrm{Pr}_L + 5 \cdot \ln\left[1 + \mathrm{Pr}_L \cdot \left(0.0964 \cdot \mathrm{Re}_L^{0.585} - 1\right)\right] & 50 < \mathrm{Re}_L < 1125 \\ 0.707 \cdot \mathrm{Pr}_L \cdot \mathrm{Re}_L^{0.5} & \mathrm{Re}_L < 50 \end{cases}$$

An example of an empirical two-phase multiplier correlation that has enjoyed widespread use is the Shah (1979) correlation and its subsequent modification (Shah, 2009). The correlation is simple to apply and yields good predictions for a range of tube sizes and fluids. In recent years, efforts have been made to develop and refine accurate heat transfer and pressure drop models that are valid over a range of tube sizes, mass fluxes and fluids, including experimental and analytical studies by Dobson and Chato (1998), Cavallini *et al.* (2002a) and Thome *et al.* (2003). In general, these studies have focused on round tubes with $D_H > 3$ mm.

Accurate measurements of condensation heat transfer in microchannels are needed to assess the applicability of the macroscale models to the microscale and for the development of new correlations. Obtaining accurate, repeatable results is made difficult by the small condensation heat duties, low mass flow rates, high heat transfer coefficients characteristic of microchannels, and the inability to easily apply and measure a constant heat flux. These difficulties are compounded when it is desired to measure heat transfer coefficients in small quality increments at high reduced pressures; where the associated h_{fg} and condensation heat duties are very small. Evaporation experiments can accurately measure and control electric resistance heaters to determine evaporation heat duty; however, no similar device exists for condensation. Some researchers (Baird *et al.*, 2003) have used thermoelectric coolers (TEC) to provide a fixed cooling load, with operation being controlled by an electrical power input, similar to electrical heaters. However, it has been shown that inconsistencies in TEC performance make them unreliable for use as actual heat flux measurement devices (Derby *et al.*, 2010). Thus, the condensing refrigerant must be coupled with a circulating coolant loop. However, it is desirable to maintain a high coolant mass flow rate and minimal difference in temperature ($T_{sat} - T_{coolant}$) across the test section to limit coolant side thermal resistance, which results in a high uncertainty of the measured heat duty. Other methods to determine the condensation heat duty more accurately include the use of thermopiles as heat flux sensors (Koyama *et al.*, 2003) and the thermal amplification technique proposed by Garimella and Bandhauer (2001).

As with the microchannel pressure drop, extensive reviews of condensation heat transfer experimental and modeling research in microchannels can be found in Garimella

(2006) and only studies relevant to the experimental conditions of interest in the current study are reviewed here.

Wang *et al.* (2002) and Koyama *et al.* (2003) both developed correlations based on mini- and microchannel condensation data for R-134a. The correlation of Wang *et al.* (2002) was developed from a boundary layer analysis, similar in form to the Traviss *et al.* (1973) correlation. It uses experimental data to correlate the vapor two-phase multiplier and the dimensionless boundary layer temperatures as a function of liquid Reynolds number, quality and the turbulent-turbulent Martinelli parameter, using R-134a condensation data in an extruded rectangular multi-port tube with D_H =1.46 mm. The final form of their annular regime correlation is shown in Eq. (2.18)

$$\mathrm{Nu} = 0.0274 \cdot \mathrm{Pr}_L \cdot \mathrm{Re}_L^{0.6792} \cdot q^{0.2208} \cdot \left(\frac{1.376 + 8 \cdot \left(X_{tt}^{1.655} \right)}{X_{tt}^{2}} \right)^{0.5} \tag{2.18}$$

Koyama *et al.* (2003) used a combination of the pressure drop correlations of Haraguchi *et al.* (1994b) and Mishima and Hibiki (1996), and concluded that the resulting model predicted the heat transfer coefficients well for R-134a data in extruded multi-port tubes with D_h = 0.80 and 1.11 mm. The resulting correlation considers contributions of both forced convection and gravity controlled condensation. However, the agreement is not explicitly quantified and the model generally appears to over predict heat transfer coefficient for both tube types.

Cavallini, Del Col and co-workers conducted experiments on the condensation heat transfer of halogenated refrigerants in concert with the pressure drop studies reviewed above (2005a; 2005b; 2006; 2010) in circular and rectangular channels with

hydraulic diameters less than 3 mm. Using the pressure drop model shown in Eqs. (2.8)-(2.9), they developed a model to predict heat transfer based on the momentum/heat transfer analogy (Cavallini *et al.*, 2005b). For condensation of R-134a and R-410A (Cavallini *et al.*, 2005a) at T_{sat} = 40°C, they found that existing correlations under predicted the data. In an update to the 2005 paper, they stated that the mini and microchannel model (2005b) could predict heat transfer of R-134a, R-410A and R-236ea in 1.4 mm rectangular channels satisfactorily, with a majority of the data within ±20%. In (2006), Cavallini *et al.* presented a new flow-regime based (ΔT dependent and independent flow regimes) model developed from an extensive database of condensation heat transfer data in tubes with D > 3 mm. Despite being comprised of data for large tubes, Del Col *et al.* found that the model predicted condensation data for R-1234yf in circular channels (D = 0.96 mm) within ±15%.

Bandhauer *et al.* (2006) and Agarwal *et al.* (2010) presented experimental results and new models for condensation of R134a in circular ($0.506 \leq D \leq 1.524$ mm) and non-circular ($0.424 \leq D_H \leq 0.839$ mm) channels, respectively. Data were obtained for mass fluxes ranging from 150 to 750 kg m^{-2} s^{-1}. To predict the shear-driven annular condensation heat transfer coefficient, they used an approach similar to Traviss *et al.* (1973), assuming a turbulent annular film. To account for microchannel effects, the pressure drop and interfacial shear stress were determined using the annular pressure drop models reviewed above in Eqs. (2.12)-(2.13). They found an absolute mean error of 16% for the non-circular channel model and 10% for the circular channels.

Agarwal and Garimella (2014b) conducted condensing R-134a heat transfer experiments in microchannels ($0.1 \leq D_H \leq 0.4$ mm) and developed a flow-regime-based

model for predicting condensation heat transfer. They treated the flow according to the unit cell shown previously in Figure 2.1. As with the Agarwal and Garimella (2014a) pressure drop model, they modeled the heat transfer in the vapor bubble and liquid slug region. The time-averaged heat transfer coefficient was then found to be a composite of the two, depending on the correlated slug length ratio (Eq. (2.19)). They found that for highly annular flows (high quality and mass flux), the liquid slug length is very small compared to the vapor bubble length and the heat transfer is dominated by that occurring across the thin annular film.

$$\alpha = \alpha_s \cdot \left(\frac{l_{slug}}{l_{slug} + l_{bubble}} \right) + \alpha_f \cdot \left(1 - \frac{l_{slug}}{l_{slug} + l_{bubble}} \right) \tag{2.19}$$

Wang and Rose (2005; 2011) developed a theoretical model for predicting heat transfer in horizontal microchannels with annular flow. The model accounts for the streamwise shear stress on the condensate film and the transverse pressure gradient due to surface tension. The transverse pressure gradient is particularly important in noncircular microchannels, where liquid is preferentially drawn to sharp corners resulting in local thinning of the condensate film and high heat transfer coefficients. This phenomenon is generally not accounted for in correlations developed for large diameter channels. Their analysis makes many of the same assumptions as the classic Nusselt analysis (*i.e.*, laminar condensate film, neglect inertial and convection terms in film), with the inclusion of the transverse shear and imposed pressure gradient. Closure to the model is provided through an empirical pressure drop prediction method. They identify a surface tension and viscosity dominated region where the heat transfer coefficient can be predicted via a simple Nusselt type correlation.

Keinath (2012) introduced a new multi-regime heat transfer model for condensing refrigerant in small channels (D < 3.05 mm). The model was based on data for condensing R-404A in circular mini/microchannel tubes (0.86 < D < 3.05 mm). The heat transfer models were developed using the Nema (2008) flow map and the microchannel void fraction model also presented in Keinath (2012). The wavy flow model was based on the previous model presented by Andresen (2007) and the annular flow model based on the Thome *et al.* (2003) annular film two-phase multiplier approach. The resulting heat transfer model predicted 93.6% of the data within ±25%.

Recently, Kim and Mudawar (2013) proposed a model for predicting annular and non-annular condensation in mini and microchannels, developed with the aid of a large database (4045 data points from 28 sources) of varying diameters (0.424 to 6.22), mass flux (53 to 1403 kg m^{-2} s^{-1}) and fluid types (17 fluids). They developed flow transition criteria as a function of the Soliman Weber number and turbulent-turbulent Martinelli parameter to indicate which model should be used. Based on the analysis of Traviss *et al.* (1973) and Dobson and Chato (1998), they showed that the functional form of the annular flow heat transfer coefficient could be expressed as:

$$\mathrm{Nu}_a = a\,\mathrm{Re}_L^b\,\mathrm{Pr}_L^c\,\frac{\Phi_V}{X_{tt}} \tag{2.20}$$

From a regression analysis, they found the constants to be $a = 0.048,\ b = 0.69,\ c = 0.34$, and the vapor two-phase multiplier was calculated from their pressure drop model, shown above (see Table 2.2). In the non-annular regime, they used the superposition approach of Churchill and Usagi (1974) between the annular

correlation and an empirical term as a function of the liquid Reynolds and vapor-only Suratman number.

$$Nu_{na} = \left[\left(Nu_a \right)^2 + \left(3.2 \times 10^{-7} \, Re_L^{-0.38} \, Su_{VO}^{1.39} \right)^2 \right]^{1/2} \tag{2.21}$$

Their model showed good agreement with the data, predicting 86.8% within 30% for an overall absolute average deviation of 16%.

Most of the studies on horizontal microchannel tube condensation reviewed above have focused on synthetic refrigerants common to the HVAC&R and automotive industry. There is little research on fluids comparable to those of the present study. There is some work with zeotropic mixtures in larger tubes, which will be discussed in the following two sections.

2.4 Mixtures Condensation Experiments

Compared to studies of single component fluid condensation in horizontal and vertical channels, there are few investigations on condensation of binary and multi-component mixtures, particularly of zeotropic mixtures. Of the available studies, there is often disagreement in the results from different investigators. This can be attributed to the inherent difficulties in performing condensation heat transfer experiments, coupled with the increased challenge of working with zeotropic mixtures. The following sections review some of these challenges, along with experimental approaches and results from mixture condensation studies of various fluids in vertical and horizontal channels. Several of the experimental studies reviewed here are used by other investigators to validate

mixture condensation heat and mass transfer models, which will be discussed in Section 2.5.

2.4.1 Challenges in Determining Heat Transfer Coefficient

Ideally, it is desirable to obtain condensation heat transfer coefficients for a wide range of operating conditions and at qualities ranging from 0 to 1. For a pure fluid, the local condensation heat transfer coefficient can be defined by Eq. (2.22).

$$q'' = \alpha \left(T_{\mathrm{b}} - T_{\mathrm{w,i}} \right) \tag{2.20}$$

Inspection of this equation reveals that three quantities (heat flux, bulk temperature and wall temperature) must be determined to calculate the local heat transfer coefficient. Determining the average condensation heat flux is subject to the difficulties discussed above, particularly for microchannels. In addition to the local heat flux, the inside wall temperature ($T_{\mathrm{w,i}}$) is required to calculate the local heat transfer coefficient. Many researchers (Eckels and Unruh, 1999; Philpott and Deans, 2004) either attach thermocouples to the outer tube surface or embed them in the wall of the tube containing the condensing mixture. Often multiple thermocouples distributed circumferentially are used, with the outer wall temperature assumed to be the average. The inner wall temperature can then be calculated from Eq. (2.23), assuming the thermal resistance of the tube is known.

$$q'' = \frac{\left(T_{\mathrm{w,i}} - T_{\mathrm{w,o}} \right)}{R_{\mathrm{w}}} \tag{2.21}$$

The bulk temperature (T_{b}) in Eq. (2.20) is usually assumed to be equal to the saturation temperature at the pressure under consideration in the tube for a single

component fluid. This is not always accurate for multi-component mixtures, because these fluids exhibit steep temperature glides and non-equilibrium effects. Furthermore, the temperature difference between the bulk fluid and the inner wall can be quite small because of the high local heat transfer coefficients found in condensing flows in microchannels. If there is large uncertainty in either the bulk or inner wall temperature, the corresponding measured value of heat transfer coefficient will not be very accurate.

In addition to direct measurement of the tube wall temperature, another commonly used method of determining heat transfer coefficient is through the use of the Wilson plot or modified Wilson plot method (Fernández-Seara *et al.*, 2007). With this method, the average condensation heat transfer coefficient can be determined from Eq. (2.24) (assuming a tube-in-tube condenser), where α_a is the heat transfer coefficient of the coolant in the annulus, R_w the thermal resistance of the wall, and α is the condensation heat transfer coefficient of interest.

$$\dot{Q} = \frac{\Delta T_{LM}}{UA} = \frac{\Delta T_{LM}}{\left(\frac{1}{\alpha_a \cdot A_o} + R_w + \frac{1}{\alpha \cdot A_i} \right)} \tag{2.22}$$

When applied to condensation experiments, the annulus heat transfer coefficient is generally correlated as a function of Reynolds number through some modification of the Wilson plot method, as detailed in Fernández-Seara *et al.* (2007). The total condensation heat duty can be calculated as before. The log-mean temperature can be calculated from the measured coolant inlet and outlet temperature and either the measured or calculated (from saturation pressure) condensing fluid temperature. The LMTD concept assumes that the specific heats of the fluids are constant and that the heat

transfer coefficients do not vary. Thus, for condensation of single components, this method is only accurate for small quality changes, where the condensation heat transfer coefficient variation is small and the effective specific heat of the condensing refrigerant is infinity. For zeotropic fluids, the temperature glide reduces the accuracy of the LMTD approach.

For both methods of calculating heat transfer coefficient, there is difficulty in defining what should be used as the bulk temperature (T_b) in Eq. (2.20) or (2.22). By inspecting Figure 1.7 in the previous section, it can be seen that the overall condensation heat transfer resistance (U_c) from the bulk vapor to the inside of the tube wall is a function of the heat transfer resistance in the vapor core and the liquid film, with driving temperature differences of (T_v-T_i) and (T_i-$T_{w,i}$), respectively. Therefore, the overall driving temperature difference in the condensing fluid is T_v-$T_{w,i}$. For a saturated single component fluid, it is generally assumed that there is no sensible heat transfer resistance in the vapor core and that the bulk temperature, the vapor core temperature, and the interface temperature are all equal to the fluid saturation temperature. However, defining T_b as the saturated temperature of a multi-component mixture assumes that both phases are in thermodynamic equilibrium, a situation that in general does not prevail. The *actual* liquid heat transfer coefficient for a zeotropic mixture should therefore be defined using the local interface (T_{int}) temperature. Unfortunately, measuring this temperature directly is difficult and many of the experimental studies reviewed in the following section report the *apparent* overall condensation heat transfer coefficient, defined in terms of the equilibrium saturation temperature. Tsotsas and Schlünder (1987) derived a relation between the real and apparent heat transfer coefficient as a function of the condensation

curve and other dimensionless groups. They showed that the ratio of the apparent to the real overall condensation heat transfer coefficient approached one with increasing heat flux for a given mixture. Thus, it can qualitatively be expected that the use of the saturation temperature will provide reasonable results at high heat fluxes. Using the equilibrium saturation temperature also facilitates comparison between different sets of experimental data. Finally, rather than comparing overall condensation heat transfer coefficients for different fluid mixtures and conditions, it is also possible to compare required heat transfer area to achieve a certain percentage of condensation.

Another difficulty in obtaining accurate zeotropic mixture heat transfer coefficients arises when attempting to use the UA-LMTD approach to determine the overall condensation heat transfer coefficient. As stated above, the LMTD method requires that both fluids have a constant specific heat. Figure 2.2 shows an equilibrium temperature versus enthalpy diagram for a 75/25 by mass mixture of ammonia/water for a quality ranging from 0 to 1. The figure shows a highly non-linear temperature glide,

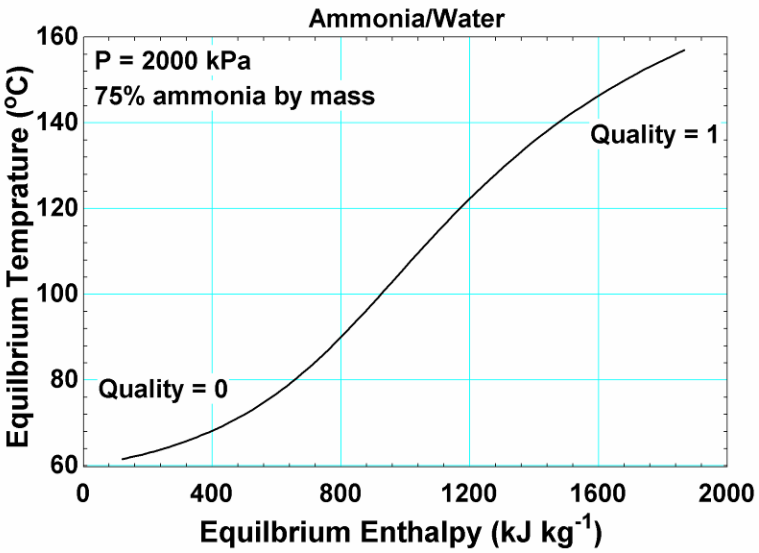

Figure 2.2: Equilibrium temperature versus enthalpy for 75/25 NH_3/H_2O mixture at constant P = 2000 kPa

which indicates a variable effective specific heat during the condensation process. Shao and Granryd (1998) discuss the error introduced by using the LMTD method to calculate condensation heat transfer coefficients with a non-constant specific heat. They show that the direction of the error is dependent on the shape of the temperature-enthalpy curve. For convex profiles, the calculated LMTD is lower than the real value, resulting in an over predicted heat transfer coefficient, with the opposite being true for concave profiles. It can be concluded that if the UA-LMTD method is applied for an experimental point with a sufficiently small quality change, the error induced by the variable effective specific heat would be small because the temperature-enthalpy curve would be approximately linear within that small quality range.

2.4.2 Mixture Condensation in Vertical Tubes

Investigations on the condensation of mixtures inside and outside vertical tubes date back further than studies on mixture condensation inside horizontal tubes, due to the prevalence of the geometry in process equipment (wetted wall towers, distillation columns, etc.) The studies reviewed in this section encompass a variety of conditions and fluid mixtures. A summary of all experimental studies in vertical tubes is presented in Table 2.3.

van Es and Heertjes (1956) conducted experiments with benzene and toluene in a vertical tube-in-tube condenser (ID = 88 mm, L = 1.08 m). Vapor generated from an electric boiler was introduced at the bottom of the inner tube, resulting in counter-flow between the vapor and gravity driven condensate film. Experiments were conducted with pure benzene, pure toluene and 43/57 and 72/28 by mass mixtures of benzene/toluene with vapor Reynolds number from 530 to 12,360 at various cooling fluid temperatures.

Temperature measurements were obtained at the inner tube wall and in the vapor core. The composition of the condensate at the condenser outlet was measured with a semi-micro boiling point apparatus (accuracy ±0.2%). The composition of the condensate was found to vary significantly for each case, indicating a widely differing percentage of the vapor being condensed. Rather than calculating a heat transfer coefficient, they reported the measured temperature difference between the vapor core and the wall versus vapor inlet molar flow rate. They then compared the data with the predictions of an analytical model with qualitative agreement (discussed below). While limited, these experimental results are some of the earliest reported for mixtures in vertical channels.

Onda *et al.* (1970) conducted a similar experiment, but extended the analysis to calculate a condensation heat transfer coefficient and mass transfer coefficients in the liquid and vapor phases. The experiments were conducted with steam and methanol in a vertical copper tube-in-tube condenser (ID = 21 mm, L = 0.33, 0.83, 1.33 and 1.83 m) with nominal mass fluxes ranging from 3 to 6 kg m^{-2} s^{-1} (Re_V from 5,000 to 11,000). The vapor and liquid were in counterflow. The temperatures of the vapor and condensate were measured at the inlet and outlet, and embedded thermocouples were used to measure the wall temperature. Vapor exiting the top of the test section was fully condensed in a separate heat exchanger and reintroduced as a constant flow liquid film at the top of the tube at a near-saturated condition. The flow rate and composition of the film at the bottom of the test section were measured. From this information, the latent heat rejected in the test section was calculated. As expected, the latent heat duty increased with increased vapor flow rate and increased temperature difference between the vapor and

tube wall. Neglecting the sensible cooling of the vapor, they reported the heat transfer coefficient of the liquid film, shown in Eq. (2.25).

$$\alpha_{\mathrm{L}} = \frac{q''_{\lambda}}{\left(T_{\mathrm{int}} - T_{\mathrm{w,i}}\right)} \tag{2.23}$$

The interface temperature (T_{int}) was determined by plotting the calculated latent heat at each mass flux versus the temperature difference between the bulk vapor and the wall temperature ($T_{\mathrm{v}} - T_{\mathrm{w,i}}$) and extrapolating the curve back (linear fit) to a latent heat of zero. At this point, it was assumed that there would be sensible cooling only and T_{v}-T_{int} was equal to the T_{v}-T_{w} at the zero latent heat flux condition. They claimed good agreement with the empirical model of Onda *et al.* (1968) for condensation number (Eq. (2.26)) as a function of Reynolds number developed for a single component fluid, although it is difficult to discern how well the model predicts the trends from the information presented.

$$N_{\mathrm{cond}} = \alpha_{\mathrm{cond}} \left(\frac{\mu_{\mathrm{L}}^2}{k_{\mathrm{L}}^3 \rho_{\mathrm{L}}^2 g} \right)^{1/3} \tag{2.24}$$

In their study, the calculated heat transfer coefficient is averaged over the entire test section and the interface temperature and heat flux are assumed to not change over the length of the test section, which will not be the case if the composition of the condensate or vapor changes significantly.

The high mass flux vapor and liquid heat transfer coefficients were calculated from Eqs. (2.27) and (2.28), respectively .

$$\dot{N}_{1,\mathrm{i}} = -\beta_{\mathrm{V}}^{*} \cdot \left(\tilde{y}_{1,\mathrm{i}} - \tilde{y}_{1} \right) + \dot{N}_{1,\mathrm{T}} \cdot \tilde{y}_{1,\mathrm{i}} \tag{2.25}$$

$$\dot{N}_{1,\mathrm{i}} = \beta_{\mathrm{L}}^{*} \cdot \left(\tilde{x}_{1,\mathrm{i}} - \tilde{x}_{1} \right) + \dot{N}_{1,\mathrm{T}} \cdot \tilde{x}_{1,\mathrm{i}} \tag{2.26}$$

The compositions at the interface were determined from the calculated interface temperature and the vapor/liquid equilibrium data for the mixture, while the condensing fluxes could be determined from the measured composition and flow rates. The vapor mass transfer coefficient was found to increase with an increase in vapor Reynolds number, while the liquid mass transfer coefficient was found to decrease with increasing condensation rate. For the vapor phase, they found that the film-theory analysis of Colburn-Drew (1937) agreed well with their data. In the liquid phase, they found that penetration theory could be used to predict the mass transfer coefficient with acceptable agreement. Unfortunately, no information on how the uncertainty of the experimental measurements affected the calculated heat and mass transfer coefficients was provided.

Hashimoto and Yanagi (1996) considered a vertical tube-in-tube condenser (ID = 25 mm, L = 3.0 m) with the vapor and liquid in a co-flow downward orientation. Zeotropic mixtures of methanol/ethanol, ethanol/water and ethanol/benzene with mass fractions of the volatile component varying from 0 to 1 and mass fluxes from 22 to 69 kg m^{-2} s^{-1} were considered. The saturation pressure ranged from 101 to 118 kPa, the average heat flux from 37 to 119 kW m^{-2}, and the condenser outlet quality from 0.01 to 0.43. Saturated vapor flowed from a liquid/vapor separator to the inlet of the test section, where the temperature, pressure and composition were measured by a gas chromatograph. Wall temperature measurements were made with K-type thermocouples embedded in the wall. The condensation heat duty was determined from an energy

balance on the coolant and a uniform heat flux was then assumed. Unlike the Onda *et al.* (1970) study, the measured heat duty included the latent and sensible contributions. The average liquid-film heat transfer coefficient was then calculated using Eq. (2.23) as before, using an average wall temperature and the measured average heat flux. The average interface temperature was determined by calculating the heat and mass transfer in the vapor phase from a Colburn-Drew (1937) type stagnant film analysis. Thus, it is expected that there will be a large uncertainty in the calculated value of T_i, as it relies on the validity of the vapor heat and mass transfer correlations used in the stagnant film model. Finally, the average liquid Nusselt number was defined by the calculated heat transfer coefficient, liquid film thermal conductivity, and the test section length.

The experimental values of average Nusselt number were compared with the calculated values from a modified version of an empirical formula of Fujii and Uehara (1973) developed for single-component fluid condensation. For the methanol/ethanol mixture, the experimental liquid-film Nusselt numbers were 0 to 20% lower than the predicted values. For ethanol and water, good agreement was observed at ethanol mole fractions greater than 0.8, which corresponded to an azeotropic region, while agreement outside this range was poor (experimental values up to six times greater than the predicted values). Finally, for ethanol/benzene, the experimental values were up to 30% higher than the predicted values. Because only the heat transfer resistance in the liquid film was considered, a model developed for single-component fluids would be expected to provide satisfactory results even for binary mixtures. Hashimoto and Yanagi (1996) speculate that dropwise condensation may occur and contribute to the higher than predicted liquid Nusselt numbers, despite the turbulent liquid film in a tube. It is also

possible that a large error was introduced to the experimental Nusselt number through the calculation of the interface temperature by the stagnant film model. This would also explain the good agreement of the model in the azeotropic region of the ethanol/water mixture, where the interface temperature should be equal to the measured bulk vapor temperature.

Panchal *et al.* (1997) conducted an experiment on the condensation of an ammonia/water mixture on the outside of the center tube (OD = 25.4 mm, L = 1.22 m) in a vertical tube-in-tube condenser. Experiments were conducted at ammonia compositions from 89 to 95% by mass, and saturation pressures from 911 to 942 kPa. Samples were taken at the end of each test run and the concentration of ammonia was determined by chemical titration. The condensation heat duty was determined from an energy balance on the coolant and the overall UA was determined from Eq. (2.22). The LMTD was calculated from the measured coolant inlet and outlet temperatures, and the dew and bubble point temperatures of the ammonia/water mixtures. For the reasons described above, the use of LMTD method, particularly for complete condensation of the highly zeotropic ammonia/water mixture, is not physically valid. However, Panchal *et al.* argue that the heat transfer coefficient calculated by this method can be compared to the pure ammonia heat transfer coefficient to gain an understanding of the impact of the mass transfer resistance. Thus, from the calculated UA, the combined heat transfer resistance in the tube wall and condensing mixture is calculated, with the coolant heat transfer coefficient calculated from the Wilson plot method. A degradation from 10 to 4 times at low (10 kW m^{-2}) and high (40 kW m^{-2}) heat fluxes, respectively, was observed compared

to heat transfer coefficients of pure ammonia obtained in the same experimental facility. The data were used to validate an analytical model detailed in the following section.

The previous studies were for binary mixtures in vertical channels where both components were condensable and miscible in all proportions. The heat and mass transfer behavior or multi-component mixtures, including those with non-condensable components is also of interest.

The combined evaporation and condensation of ternary mixture in an adiabatic vertical channel (ID = 25 mm, L = 0.61 m) was studied by Modine (1963), with the results reported in Krishna (1981). A liquid film consisting of a mixture of benzene and acetone was introduced at the top of the channel and vapor consisting of acetone, benzene and either nitrogen or helium flowed co-currently. The inlet temperature and composition of the vapor and liquid streams were measured at the inlet and outlet of the test section and the corresponding evaporation and condensation rates of each species were determined. Numerous test cases were run at varying inlet compositions, pressures ($119 \leq P \leq 155$ kPa), and gas flow rates ($2{,}000 \leq \mathrm{Re_V} \leq 9{,}600$). For most cases, it was observed that acetone condensed while benzene evaporated. Because the column was operated adiabatically, there was no heat transfer coefficient information obtained, however the detailed mass transfer data have been used by many researchers to validate multi-component condensation models (Furno *et al.*, 1986; Braun and Renz, 1996), as discussed below.

A multi-component mixture experiment specifically focused on condensation was conducted by Webb and Sardesai (1981) . Ternary mixtures of water, isopropyl alcohol

and either R-12 or nitrogen as the non-condensable component were considered. Experiments were conducted in a vertical test section (ID = 23 mm, L = 1 m) surrounded by a cooling water jacket. Vapor and condensate flowed downward co-currently. The mixture was partially condensed, where the condensable components were fully condensed after the test section and circulated with a pump, while the non-condensable component was separated and circulated with a blower. The temperature, composition and flow rate of the vapor and condensate were each measured at the condenser inlet and outlet. Embedded thermocouples in the tube wall measured temperature along the test section. Experiments were conducted at a constant pressure of 100 kPa, with molar compositions of the condensable components ranging from 10 to 60% and vapor Reynolds numbers ranging from 6,000 to 20,000 at the inlet. The heat duty calculated for the coolant and the gas/vapor mixture were reported ($1.0 \leq \dot{Q} \leq 1.4$ kW) and found to be in good agreement with one another. No attempt was made to define a heat transfer coefficient; rather, the measured heat duties and change in vapor and liquid compositions were used to validate an analytical multi-component condensation heat and mass transfer model.

2.4.3 Mixture Condensation in Horizontal Tubes

Many of the experimental studies on zeotropic mixture condensation in horizontal smooth and enhanced tubes have been driven by the needs of the HVAC&R industry. Thus, most of the reviewed studies investigate condensation of mixtures of synthetic (HFC, HCFC, CFC) and/or natural refrigerants (hydrocarbons, CO_2). A summary of experimental mixture condensation studies in horizontal tubes is presented in Table 2.4. Compared to vertical channels, horizontal tube investigations typically investigate

smaller diameter tubes (D < 25 mm) and higher mass flux conditions. While gravitational forces are significant in driving the falling-film condensate flow in vertical channels, the higher mass flux horizontal flows are dependent on pressure driven flow. Additionally, except at very low qualities, annular flow (thin liquid film distributed circumferentially) dominates the vertical geometry.

Table 2.3: Summary of experimental studies of condensation in vertical tubes

Study	Geometry	Fluid (% mass)	G (kg m^{-2} s^{-1})	P (kPa)	T_{glide} (K)	α Calculation
van Es and Heertjes (1956)	Vertical Tube Counter-flow ID = 88 mm	Benzene/Toluene 43/57 72/28	0.05 to 1.3	~100	5.4 to 6.2	-
Modine (1963)	Vertical Tube Co-flow ID = 25 mm	Benzene/Acetone/H_2 Benzene/Acetone/He	-	120 to 160	-	-
Onda *et al.* (1970)	Vertical Tube Counter-flow ID = 21 mm	Methanol/Water 0/100 → 100/0	3 to 6	~100	0 to 13	Measured ($T_{w,o}$) Measured (T_b)
Webb and Sardesai (1981)	Vertical Tube Co-flow ID = 23 mm	Water/ C_3H_8O /N_2 Water/C_3H_8O/R-12	-	100	-	-
Hashimoto and Yanagi (1996)	Vertical tube Co-flow ID = 25 mm	Methanol/Ethanol Ethanol/Water Ethanol/Benzene 0/100 → 100/0	22 to 69	100 to 120	0 to 1.6 0 to 11.2 0 to 5.4	Measured ($T_{w,o}$) Calculated (T_i)
Panchal *et al.* (1997)	Vertical Tube External OD = 25.4 mm	Ammonia/Water 89/11, 95/5	-	900	67 to 82	UA-LMTD method

As discussed above, as the refrigerant condenses in horizontal tubes, transitions from annular to stratified to intermittent/slug flow are observed (Traviss and Rohsenow, 1973; Taitel and Dukler, 1976; Tandon *et al.*, 1982; Coleman and Garimella, 1999, 2003). These flow regimes significantly change the heat and mass transfer processes and must be modeled using appropriate mechanistic idealizations.

Based on promising results from a computer simulation model of a vapor-compression refrigeration system using a zeotropic mixture of R-12 and R-114 (Launay, 1981), Stoecker and McCarthy (1984) conducted an experimental study of zeotropic heat pump performance. The experimental facility consisted of a complete heat pump powered by an open drive reciprocating compressor. Heat was rejected from the system through counterflow, water-coupled low and high temperature tube-in-tube horizontal condensers (ID = 25.4 mm), each with three passes (L = 3.12 m). Water and refrigerant temperature and pressure were measured at the inlet and outlet of each condenser pass. At the midsection of each pass, the tube wall and vapor core measurements were obtained from thermocouples attached to the outer wall of the test section and from thermocouples positioned in the center of the condensing mixture flow. Experiments were run with mass concentrations of R-114 ranging from 10 to 70% at varying mass fluxes to obtain a constant cooling load ($45 < G < 50$ kg m^{-2} s^{-1}) and a mixture inlet temperature of 34.2°C. Superheated vapor entered the high temperature condenser and the mixture left the low temperature condenser subcooled. Although an oil separator was installed, there was probably some fraction of lubricant that entered the condenser. The condensation heat duty was determined from an energy balance on the water side. The local heat flux at the center of each condenser pass was defined from the pass-average heat flux, measured

bulk refrigerant temperature ($T_{r,b}$), bulk water temperature ($T_{c,b}$), and the LMTD of the pass as shown in Eq. (2.29).

$$q'' = \frac{\bar{q}''\left(T_{r,b} - T_{c,b}\right)}{\Delta T_{LM}} \tag{2.27}$$

The local heat transfer coefficient was then calculated using Eq. (2.20), where the bulk and wall temperatures were both measured quantities. The uncertainties in the calculated heat duty and heat transfer coefficient were not reported.

The average measured heat transfer coefficients ranged from 0.8 to 2.8 kW m^{-2} K^{-1}. The variation in heat transfer coefficient with average pass quality was not reported. They found that as the concentration of R-114 increased, the average heat transfer coefficient decreased, reaching a minimum at around 50-60% mass concentration of R-114. The steepest degradation was observed as the R-114 concentration increased from 0 to 30%. These results imply that the mass transfer resistance in the zeotropic mixture degrades heat transfer worse than would be expected from a simple linear weighted average of the pure R-12 and R-114 heat transfer coefficients. Thus, the expected increased efficiency of the zeotropic heat pump system was less than that predicted by the computer model by approximately 6%.

Stoecker and Kornota (1985) continued the study of R-114/R-12 mixtures by developing a test facility for visual observation of the condensing flows in a horizontal glass tube-in-tube condenser, divided into 12 sections (ID = 12.7 mm, $L_{section}$ = 1.5 m). Experiments were conducted at mass concentrations of R-114 from 0 to 100%, at a nominal mass flux of 180 kg m^{-2} s^{-1} and an average heat flux between 4.22 and 4.5 kW m^{-}

[2]. They replaced the compressor with a positive displacement pump, eliminating any potential for contamination by the lubricant. They observed flow regime transitions from annular to stratified and slug flow as the mixture condensed, with no discernible variation in the locations of the transitions between flow regimes with varying mixture composition. DeGrush and Stoecker (1987) further advanced the study by measuring local heat transfer coefficients over the length of a horizontal, copper tube-in-tube condenser (ID = 12.7 mm, L = 19.8 m) while observing two-phase flow patterns in the same transparent condenser that was used by Stoecker and Kornota (1985). Their goal was to correlate the observed flow regimes in the transparent section with the measured heat transfer coefficients in the copper test section. The tube was instrumented in 8 locations (4 circumferential wall thermocouples and one vapor core thermocouple). Their goal was to correlate the observed flow regimes in the transparent section with the measured heat transfer coefficients in the copper test section condensation heat duty and local heat transfer coefficient were determined using the same method as used by Stoecker and McCarthy (1984). They reported heat transfer coefficients for each experimental condition as a function of condenser position, although not explicitly as a function of thermodynamic mass quality. They found an enhancement in heat transfer coefficient with increasing fraction of R-114 close to the condenser inlet (high quality, annular flow, as observed in the transparent condenser), with a maximum at a 50/50 mixture of R-114/R-12. In the stratified and slug-flow regimes, they found a strong degradation in heat transfer coefficient at concentrations of R-114 between 50 and 70%. Eight condensation heat transfer correlations developed for single component fluids were

evaluated, with a correlation by Tandon *et al.* (1985b) found to predict the data the best (97% of data within ±20%).

Tandon (1983) investigated the condensation of R-22/R-12 mixtures in a horizontal tube, with the results summarized in Tandon *et al.* (1986). The test section consisted of a water-cooled tube-in-tube condenser divided into three sections (ID = 10 mm, $L_{section}$ = 1 m). Condensation experiments were conducted at concentrations of 25, 50 and 75% by mass of R-22, at mass fluxes ranging from 170 to 530 kg m^{-2} s^{-1} and condensation temperatures ranging from 21 to 39°C. An average heat transfer coefficient for each condenser section was obtained from Eq. (2.20), using the measured average heat flux (coolant energy balance), mean tube-wall temperature, and refrigerant bulk temperature. The calculated heat transfer coefficients varied from 1.4 kW m^{-2} K^{-1} to over 3.0 kW m^{-2} K^{-1}. They observed that the average heat transfer coefficient was in general lower than the heat transfer coefficient for pure R-22 and higher than that for R-12 at a given mass flux. However, at low mass flux (< 200 kg m^{-2} s^{-1}), the 50/50 mixture average heat transfer coefficient was slightly higher than that for R-22, while at high mass flux (> 500 kg m^{-2} s^{-1}), the 75/25 mixture heat transfer coefficient was slightly lower than the R-12 heat transfer coefficient. The change in heat transfer coefficient was not found to be proportional to the change in R-22 concentration from 25 to 75%. Thus, the complex relationship of composition on heat transfer behavior was consistent with that observed by Stoecker and coworkers (1984; 1987) for R-114/R-12, a mixture with a higher temperature glide. It was concluded that definite trends could not be extracted from the average heat transfer data that they were able to obtain.

Doerr *et al.*(1994) contributed additional work on synthetic refrigerant mixtures, investigating the condensation of binary mixtures of R-125/R-32, R-134a/R-32 and ternary mixtures of R-32/R-125/R-134a and R-125/R-143a/R-134a at various compositions as potential replacements for R-22. The tests were conducted in horizontal copper tubes with OD = 3/8" (no wall thickness specified) and L = 3.67 m. Mass fluxes ranged from 125 to 375 kg m^{-2} s^{-1} and the average of the dew and bubble point temperatures was between 30 and 40°C. The average heat transfer coefficient was determined from the UA-LMTD method (Eq. (2.22)), where the water-side heat transfer coefficient was determined from the Wilson plot method and the heat duty was calculated from a water-side energy balance. Inlet and outlet temperatures of the refrigerant and water were measured with RTD probes with a reported accuracy of ±0.05 K. They reported a maximum uncertainty in heat transfer coefficient of ±8.3%; however, the errors introduced by the use of the LMTD concept were not addressed and may contribute significantly to the mixtures with higher temperature glides. All of the mixtures had a lower average heat transfer coefficient than R-22 when compared on an equal thermal capacity rate (equal $\dot{m} \cdot h_{fg}$) basis. At higher reduced pressures, the heat transfer coefficient was lower for all mixtures, as expected. Interestingly, the difference between the heat transfer coefficient of pure R-22 and the zeotropic mixtures was observed to decrease at higher reduced pressures.

Several studies by Shao and Granryd (1998; 2000b, a) investigated the condensation heat transfer and two-phase flow patterns of zeotropic refrigerant mixtures in horizontal tubes. They first conducted a detailed investigation (1998) on the condensation heat transfer and pressure drop of zeotropic mixtures of R-32/R-134a and

compared the results with the predictions of several existing correlations. The experimental facility consisted of water-coupled heat pump with compressor and oil separator. The condenser was a tube-in-tube heat exchanger divided into 10 segments (ID = 6 mm, $L_{segment}$ = 1 m), with the water and refrigerant temperature measured at each segment inlet and outlet with an estimated accuracy of ±0.05-0.1 K. Glass sight tubes (ID = 6 mm, L = 0.1 m) at the outlet of each test section allowed for visualization of the local flow regime. Experiments were conducted with pure R-32, R-134a, and three different mixtures (26.5, 55 and 74.5% by mass of R-32) at nominal mass fluxes ranging from 138 to 370 kg m^{-2} s^{-1}. The temperature glide varied from approximately 3 to 6°C. The average heat transfer coefficient for each test section was calculated using Eq. (2.20), where the average heat flux was calculated from the heat transfer area and an energy balance on the coolant. The average inner wall temperature was calculated by considering the measured average heat flux, measured coolant temperature and the calculated thermal resistance of the coolant (from a Dittus-Boelter type equation, which was assigned an optimistic uncertainty of ±5%) and the tube wall itself. The average mixture bulk temperature was assumed to be equal to the average equilibrium temperature in the test section, calculated using REFPROP and the measured pressure, composition and enthalpy balance from the previous condenser segment. A propagation of errors showed an uncertainty generally between ±10 and 15%. It is important to note that the equilibrium temperature is used for convenience, rather than the actual bulk vapor temperature. This study is one of the earlier studies to plot heat transfer coefficient as a function of average test section mass quality. For all fluids investigated, the heat transfer coefficient was highest at high qualities, and decreased with increasing liquid fraction. The heat transfer coefficient of

pure R-32 is higher than that of R-134a at all qualities and mass fluxes. Consistent with the observations of Stoecker and coworkers (1984; 1985), they observed a smaller degradation in measured heat transfer coefficient compared to an interpolated heat transfer coefficient of the pure fluids (weighted by composition) in turbulent annular flow compared to the stratified wavy flows. The highest deviation from the interpolated values was observed for mixtures with ~30% R-32. Shao and Granryd (1998) also compared mean heat transfer coefficients over the entire condenser, with the minimum heat transfer coefficient for varying mass flux and average temperature occurring at ~30% R-32 composition, with a degradation from the interpolated value of ~20% for G = 190 kg m^{-2} s^{-1} and ~16% for G = 300 kg m^{-2} s^{-1}.

Shao and Granryd (2000b, a) later extended their study to examine flow patterns and pressure drop for condensing pure fluids and azeotropic and zeotropic mixtures. The same experimental facility and mixtures of R-32/R-134a as before were used, as well as the near-azeotropic mixtures of R-404A and R-407C. Tests were conducted at mass fluxes ranging from 150 to 400 kg m^{-2} s^{-1} and an average saturation temperature of 30°C. The flow was observed in glass sight tubes between condensing sections. They observed three flow patterns (annular, wavy, slug), reporting difficulty in distinguishing between semi-annular and wavy flow. Qualitative agreement with the Tandon *et al.* (1982) flow map was reported for the near-azeotropic and zeotropic mixtures. The frictional pressure drop in each condensing section was calculated by accounting for the deceleration pressure gain, using the separated flow model and the Smith (1971) correlation for void fraction. A new empirical correlation for the two-phase multiplier as function of the

Martinelli parameter was proposed and found to predict the data well (within ±15%) for pure fluids and azeotropic, near-azeotropic and zeotropic mixtures.

As in many of the previous studies, Smit *et al.* (2002) conducted a study of condensation of HCFC refrigerant mixtures (R-22/R-142b) in a vapor compression heat pump system. The system was powered by a 10 kW reciprocating compressor with an oil separator. Only experimental runs with oil mass fractions less than 0.01 percent were used in the study. The test section consisted of the inner tube (ID = 8.11 mm) of a tube-in-tube condenser divided into eight sections (L = 1.6 m). A sight glass installed in between each test section allowed for visualization of the local flow pattern. Water and refrigerant temperature were measured at the inlet and outlet of each test section using calibrated RTDs (accuracy ±0.1°C). The refrigerant pressure drop was also measured for each condenser test section (accuracy ±0.05% of reading). The heat duty of each test section was calculated from a water-side energy balance, the average heat transfer coefficient from the UA-LMTD method, and the water-side annulus heat transfer coefficient was found using a modified Wilson plot method. They reported an average quality change of 10% across each test section; thus, the LMTD method may offer acceptable accuracy because the change in effective specific heat of the refrigerant mixture is small.

Experiments were conducted with mass fractions of R-22 from 50 to 100 percent in 10% increments at a nominal pressure of 2.43 MPa. The mass flux was varied from 40 to 800 kg m^{-2} s^{-1}, while the temperature glide for the mixture varied from 2.5 (90% R-22) to 6.5 K (50% R-22). The average heat transfer coefficient of each section was reported and ranged from 0.5 to more than 5 kW m^{-2} K^{-1}. Uncertainties in the calculated heat

transfer ranged from a minimum of ±4% to a maximum of ±20% at the lowest heat flux. They found that the heat transfer coefficient of pure R-22 was greater than that of any of the mixtures for all conditions. In general, it was found that heat transfer coefficients were degraded more for the mixtures at lower mass flux corresponding to stratified-wavy flow, than the mixtures at high mass flux, corresponding to annular flow. The average reduction in heat transfer coefficient for a 50/50 R-22/R-142b mixture was 25% when compared to pure R-22 in the stratified-wavy flow regime, while the average degradation was only 7% in the annular flow regime (quality > 0.7). This is similar to the observations of Stoecker and coworkers (1984; 1985) and Shao and Granryd (1998). At lower mass fluxes, the heat and mass transfer coefficients in the vapor phase are expected to be low, which may explain the observed results. Unfortunately, data for heat transfer coefficient of pure R-142b, which would have allowed a comparison of the degradation of the mixture heat transfer coefficient compared to an interpolated value of the two pure components, were not provided. They found that the heat transfer correlation of Dobson and Chato (1998), coupled with the correction method of Silver (1947) and Bell and Ghaly (1973) predicted the mixture heat transfer the best, with the deviations between -30 and +20%.

Condensation of a zeotropic mixture of R-125/R-236ea was studied by Cavallini *et al.* (2002b) The experiments were conducted in a tube-in-tube heat exchanger (ID = 8 mm , L = 2 m). Experiments were conducted at mass compositions of R-125/R-236ea of 30/70, 46/54 and 64/36 at pressures from 780 to 1420 kPa and mass fluxes from 400 to 750 kg m^{-2} s^{-1}. The temperature of the fluid mixture was measured with thermocouples at the inlet and outlet of the test section (accuracy ±0.05°C) and the mass flow rate was

measured using a Coriolis flow meter (accuracy ±0.4% measurement). The temperature change of the coolant was measured with a differential copper-constantan thermopile (accuracy ±0.03°C). The heat duty calculated from a coolant-side energy balance had a reported uncertainty of ±4.5%. For all tests, the vapor was superheated between 10 and 20 K. From the calculated heat duty, the outlet quality of the mixture was determined and found to vary between 0.25 and 0.99. Rather than calculating an average heat transfer coefficient, Cavallini *et al.* (2002b) presented the data as total heat duty versus outlet vapor quality for the different conditions, which was primarily for validating a condenser design model procedure, discussed in the following section.

A 50/50 mixture of propane (R-290) and butane (R-600) in a serpentine tube bank was investigated by Wen *et al.* (2006). The test condenser consisted of a water-coupled serpentine tube heat exchanger. The hydrocarbon mixture made eight serpentine passes (L = 0.46 m), with each pass consisting of three parallel tubes (ID = 2.46 mm). The flow between the water and refrigerant was cross-counterflow. The outer wall temperature of the tube carrying the mixture was measured with circumferentially distributed thermocouples at nine locations throughout the heat exchanger. The total condensation heat duty was determined from an energy balance on the water side and it was assumed that the heat flux was constant for the entire test section. The heat transfer coefficient was determined from Eq.(2.20), where the equilibrium temperature was used for the mixture bulk. The average quality for each tube pass was determined from an energy balance; however the calculation assumed that the heat flux was constant for all tubes. A maximum uncertainty in quality of ±4.2% was reported, although a detailed discussion of the errors introduced by using this approach was absent. Experiments were conducted for

mass fluxes ranging from 205 to 510 kg m^{-2} s^{-1} at a nominal heat flux of 5.2 kW m^{-2}. Heat transfer coefficients ranged from 6 to 13 kW m^{-2} K^{-1}, with a maximum reported uncertainty of ±4.9%. The data were compared with results of pure propane, butane and R-134a. The heat transfer coefficient results for the propane/butane mixture were approximately equal to the average of the pure components, indicating that there was not a significant mass transfer resistance for this mixture and composition. When comparing the data with several correlations developed for condensation of pure fluids in horizontal tubes, the Dobson and Chato (1998) correlation was found to replicate the data the best, with 100% of the data within ±20%.

Local heat transfer coefficients for condensing mixtures of CO_2 and Dimethyl Ether (DME) were measured by Afroz *et al.* (2008) in a vapor compression heat pump with a compressor and oil separator. The refrigerant was condensed in a horizontal tube (ID = 4.35 mm), which was divided into 12 sections (L = 0.3 m). The temperatures of the coolant and refrigerant were measured at the inlet and outlet of each test section with a reported accuracy of ±0.05 K. At the center of each test section, the outer wall temperature of the refrigerant tube was measured with four circumferentially distributed thermocouples. The heat duty of each section was determined from a coolant energy balance and the inner wall temperature was calculated from the measured outer wall temperature and the thermal resistance of the tube wall. Finally, the heat transfer coefficient was calculated from the average heat flux, the inner wall temperature, and the equilibrium temperature of the mixture at the test section inlet. The vapor/liquid equilibrium properties were determined from the Benedict-Webb-Rubin equation of state as shown in Miyara and Afroz (1971).

Experiments were conducted at a saturation temperature of 40°C, mass fluxes ranging from 200 to 500 kg m^{-2} s^{-1}, and CO_2 concentrations from 0 to 39%. The heat transfer coefficients of the mixtures were lower than those of pure DME, with heat transfer decreasing with increasing CO_2 fraction. This was attributed to the mass transfer resistance and the lower thermal conductivity of the mixture. Unlike many of the previous studies, the largest degradation was observed to occur at high qualities, which presumably correspond to the annular flow regime. Afroz *et al.* (2008) contend that mass transfer resistance for this mixture is lower at higher quality, where the vapor phase mass and heat transfer coefficients would be higher, leading to the observed results.

Table 2.4: Summary of experimental studies of condensation in horizontal smooth and enhanced tubes

Study	Geometry	Fluid (% mass)	G (kg m^{-2} s^{-1})	P (kPa)	$T_{sat,avg}$ (°C)	T_{glide} (K)	α Calculation
Stoecker and McCarthy (1984)	Horizontal Tube ID = 25.4 mm	R-12/R-114 30/70 → 90/10 *lubricant present	45 to 50	380 to 705	32	3.2 to 8.7	UA-LMTD method
Tandon *et al.* (1986)	Horizontal Tube ID = 10 mm	R-12/R-22	170 to 530	700 to 1400	-	0.4 to 2.6	Measured ($T_{w,o}$) Measured (T_b)
DeGrush and Stoecker (1987)	Horizontal Tube ID = 12.7 mm	R-12/R-114 0/100 → 100/0	180	280 to 890	-	0 to 8.7	UA-LMTD method
Doerr *et al.*(1994)	Horizontal Tube OD = 3/8"	R-125/R-32 (40/60) R-134a/R-32 (90/10, 75/25) R-32/R-125/R-134a (30/10/60) R-404a	125 to 375	-	30 to 40	0.22 to 4.5	UA-LMTD method
Shao and Granryd (1998)	Horizontal Tube ID = 6 mm	R-32/R-134a 26.5/33.5 → 74.5/25.5 *lubricant present	138 to 370	77 to 1,800	23 to 40	3 to 6	Measured ($T_{w,o}$) Equilibrium (T_b)
Cavallini *et al.* (2002b)	Horizontal Tube	R-125/R-236ea 30/70, 46/54, 64/36	400 to 750	780 to 1420	-	3.7 to 12.6	-
Smit *et al.* (2002)	Horizontal Tube ID = 8.11 mm	R-22/R-142b 50/50 → 100/0 *lubricant in system	40 to 800	2,430	40 to 58	0 to 4.6	UA-LMTD method
Wen et al. (2006).	Horizontal Serpentine Tube ID = 2.46 mm	Propane/Butane 50/50	205 to 510	718	40* (assumed nominal)	13	Measured (Tw,o) Equilibrium (Tb)
Afroz et al. (2008)	Horizontal Tube ID = 4.35 mm	CO2/Dimethyl Ether 0/100 → 39/61 *lubricant in system	200 to 500	885 to 2,130	40	0 to 32.6	Measured (Tw,o) Equilibrium (Tb)

Table 2.4: Summary of experimental studies of condensation in horizontal smooth and enhanced tubes - cont.

Study	Geometry	Fluid (% mass)	G (kg m^{-2} s^{-1})	P (kPa)	$T_{sat,avg}$ (°C)	T_{glide} (K)	α Calculation
Koyama et al. (1990)	Horizontal spiral groove tube IDnominal = 8.32 mm	R-22/R-114 0/100 → 100/0 *lubricant in system	130 to 360	290 to 1,500	35 to 60	0 to 8.5	Measured (Tw,o) Equilibrium (Tb)
Sami et al. (2000; 2000)	Horizontal microfinned tube IDroot = 8.7 mm	R-407C, R-507, R-408a, R-410a *lubricant in system	140 to 700	1,400 to 2,300	35 to 80	0 to 5.5	UA-LMTD method
Smit and Meyer (2002)	Horizontal microfinned tube IDroot =8.92 mm	R-22/R-142b 50/50 → 100/0 *lubricant in system	40 to 800	2,430	40 to 58	0 to 4.6	UA-LMTD method

2.5 Modeling Mixture Condensation Heat Transfer

Many different approaches have been taken to model the heat transfer of condensing mixtures for equipment design. The models can be used to determine the required condenser area to satisfy a given heat duty and to provide estimates of the composition of the vapor and condensate at the condenser outlet. This section reviews models that fall into four categories: 1) Models based on the conservation equations, 2) Non-equilibrium models based on film theory, 3) Equilibrium models, and 4) Empirical models. Many of the models reviewed here have been validated with data from the experimental studies described above.

2.5.1 Conservation Equation Models

There have been some attempts to model the condensation of mixtures by directly considering the coupled continuity, momentum, energy and species conservation equations. Sets of equations for the vapor and liquid phase are developed separately, and linked at the interface through continuity of flux, energy and vapor/liquid equilibrium. While theoretically rigorous, coupled non-linear equations are difficult to solve and use for design.

van Es and Heertjes (1956) and Sparrow and Marschall (1969) considered the conservation equations for condensation on a vertical surface. van Es and Heertjes (1956) consider condensation inside a vertical channel with vapor and liquid in counter flow, while the Sparrow and Marschall (1969) model was developed for condensation on an isothermal flat plate in an extensive environment. In both studies, the condensate film is assumed to remain laminar and the results of the Nusselt (1916) solution are used to model the flow and heat transfer.

van Es and Heertjes (1956) then developed a set of equations with the following assumptions: 1) condensation occurs as a film, 2) the liquid is completely miscible, 3) liquid flow is laminar, 4) vapor and liquid phase are in equilibrium at the interface, 5) the total molar concentration in each phase is constant, 6) the molar specific heat is constant, 7) properties in the film and vapor are constant, and 8) steady state. The total material balance, developed in cylindrical coordinates with molar units is expressed in Eq. (2.30). The species conservation equation for the more volatile component is given in Eq. (2.31) and an expression for conservation of energy is given in Eq. (2.32).

$$\frac{\partial\left(Cv_z\right)}{\partial z}+\frac{1}{r}\frac{\partial\left(rCv_r\right)}{\partial r}=0 \tag{2.28}$$

$$C\left(v_r\frac{\partial\tilde{y}_1}{\partial r}+v_z\frac{\partial\tilde{y}_1}{\partial z}\right)=\mathcal{D}\cdot C\left(\frac{1}{r}\frac{\partial\tilde{y}_1}{\partial r}+\frac{\partial^2\tilde{y}_1}{\partial r^2}+\frac{\partial^2\tilde{y}_1}{\partial z^2}\right) \tag{2.29}$$

$$C\cdot\tilde{c}_{\mathrm{p}}\left(v_r\frac{\partial\tilde{y}_1}{\partial r}+v_z\frac{\partial\tilde{y}_1}{\partial z}\right)=\lambda\left(\frac{1}{r}\frac{\partial T}{\partial r}+\frac{\partial^2 T}{\partial r^2}+\frac{\partial^2 T}{\partial z^2}\right) \tag{2.30}$$

They do not consider conservation of momentum, rather assuming that the molar fluxes in the *r* and *z* direction are known (from the bulk mass flow rate and condensation rate). Even for laminar flow, they state that no solution had been found at the time, although they recognize that the solution to the energy and species conservation equation will be the same if the Lewis number ($\alpha/\mathcal{D}$) is equal to one. They then extended the analysis to a situation with a turbulent vapor core. They assume that outside of a thin film near the condensate, no radial temperature concentration gradients exist and the developed equations can be applied to a thin viscous flow layer, where the relative

thickness of the diffusion and thermal layers are related as a function of $Le^{1/3}$. Finally, assuming the condensate layer is thin relative to the tube radius, Eqs. (2.29) and (2.30) can be simplified using boundary layer assumptions (neglecting temperature and concentration gradients in the *z* direction). The equations can then be integrated between 0 and some distance *r*, with the appropriate boundary conditions at the interface and vapor bulk. The results are identical to those originally given by Colburn and Drew (1937), detailed in the next section. With further rearrangement and some additional assumptions, they arrive at an equation for the average temperature difference between the vapor bulk and the wall. Their experimental results showed qualitative agreement with their expression; however, more detailed experiments would be necessary to quantitatively validate it.

Sparrow and Marschall (1969) developed a similar analysis for gravity driven condensation of a binary mixture on a isothermal plate and were able to obtain solutions through an iterative analysis. For the liquid film, the Nusselt (1916) solution is assumed. They assumed that the Nusselt (1916) solution could be applied to the liquid film, that the extensive vapor ambient was saturated, the liquid film remains well mixed, and that property variations within the film can be neglected. For the vapor boundary layer, they use the same boundary layer equations as van Es and Heertjes (1956), recast in Cartesian coordinates. Additionally, they introduce the momentum conservation equation including a free convection term that models buoyancy driven flow of the vapor. The boundary layer equations were transformed with a similarity variable and the Schmidt, Prandtl, and other dimensionless terms were evaluated at some reference temperature and pressure. The boundary conditions at the vapor-liquid interface are species concentrations specified

by vapor liquid equilibrium (= $f(T_i)$), conservation of mass and conservation of tangential velocity (no-slip assumed). An iterative solution to the problem is obtained using successive guesses of the interface temperature. They applied their solution to the case of methanol/water condensation with the difference between wall temperature and bulk vapor from 35 to a few degrees K. As the temperature difference increased (increased condensation rate), the buoyancy driven flow could effectively be neglected, simplifying the solution. The temperature difference for when this simplification was valid was shown to be a combination of the physical properties of the condensing species. Additionally, as the condensation rate increased, they found an increase in the concentration of the less volatile component (methanol) in the condensate, approaching that of the bulk vapor. With increasing condensation rate, they found a buildup of the more volatile component (methanol) at the interface, resulting in backflow of the more volatile component to the bulk and the less volatile (water) to the interface.

Tamir (1973) models a problem identical to that of Sparrow and Marschall (1969) with the approximate integral method, using the profiles developed by Rose (1969). As before, he found that buoyancy forces could be neglected at high condensation rates and the problem reduced to one dimension. Evaluating physical properties using the same techniques as Sparrow and Marschall, he obtains the condensation heat flux with iterative guesses of the interface temperature. For the case of a methanol/water mixture, he showed that the difference between the exact and integral solution method was around 10%, sufficient for use in design.

Kotake (1978) modeled the condensation of co-current and counter-current vapor/condensate in a vertical channel of varying cross sectional area using an

approximate integral analysis in the vapor core and the Nusselt model in the liquid film. The liquid film was driven by gravity and either assisted or retarded by the vapor shear, depending on flow orientation. In the vapor, the non-dimensional continuity, momentum, species and energy boundary layer equations were introduced. The vapor mixture was assumed to have a fully developed velocity profile and uniform temperature profile (at the saturation temperature) at the condenser inlet, and the wall was assumed to be maintained at a constant temperature. The liquid and vapor were coupled through the equality of velocity, heat flux and species conservation and vapor/liquid equilibrium at the interface. The coupled set of ODEs was solved by a finite difference method stepwise in the flow direction.

The model was applied to five different fluid mixtures and 3 channels cross section types (diffuser, nozzle, fixed); however, no comparisons with experiments were reported. Kotake (1978) found that the condensation rate and corresponding heat flux decreased rapidly in the developing region as the concentration boundary layer grew and the less-volatile component was depleted. After the minimum in condensation rate near the end of the developing region, transfer of the more volatile component towards the bulk and the less volatile component towards the interface results in an increase in condensation rate and heat flux. The film thickness was found to vary in the direction of gravity to the power of 0.15 to 0.3, depending on the channel, mixture and flow orientation.

Kim (1998) conducted a theoretical study of binary zeotropic mixtures with turbulent film condensation in horizontal tubes through an integral formulation of the continuity, momentum, energy and species equations in the liquid and vapor phase. The

model assumed annular flow, constant liquid and vapor properties, thermodynamic equilibrium at the interface, turbulent flow in the vapor core and liquid film, and fully developed velocity, temperature and concentration profiles. Turbulent profiles of velocity, temperature and concentration in the liquid film were based on the 1/7 power law and the boundary conditions, while uniform plug distributions of velocity, temperature, and concentration profile were assumed in the vapor core. The interfacial friction factor and shear stress was modeled from a correlation in Wallis (1969), while the friction factor at the wall was obtained from the Blasius (1913) correlation. The heat and mass flux at the interface were equated; where the diffusion mass transfer coefficient in the vapor was obtained from the heat and mass transfer analogy, while in the liquid film, it was determined as a function of a mass transfer enhancement factor, liquid film density, diffusivity, and film thickness. A total of 11 equations and 11 unknowns were solved by an explicit finite difference method, with discretization of the equations using the first-order forward-time and backward space-scheme results. Kim applied the solution to the experimental results from a study by Koyama *et al.* (1994) of R-22/R-114 in an *ID* = 7.9 mm tube with mass fluxes from ranging 170 to 283 kg m^{-2} s^{-1}. The experimental and predicted heat transfer coefficients were in good agreement. It was observed that there was a very small temperature difference between the vapor bulk and the interface, attributed to a high mass transfer coefficient in the vapor core. The total condensation flux was found to be nearly constant along the condenser length, although the composition of the condensing flux varied. Other trends were as expected, including increased heat transfer with higher mass flux and reduced heat transfer at low qualities (high liquid fraction).

The previous studies were developed with binary mixtures in mind. Braun and Renz (1996) analyzed the coupled heat and mass transfer of a multi-component mixture in a vertical channel with the two phases flowing co-currently. Sets of conservation equations were developed for the liquid and vapor; however, secondary effects (thermal diffusion, radiation, surface tension, etc.) were not considered. The vapor flow was assumed to be turbulent. The turbulent Prandtl and Schmidt numbers were assumed to be 0.9, and the turbulent viscosity was obtained from the k-ε model of Jones and Launder (1972). The diffusive mass flux (Eq. (2.33)) was modeled as a combination of molecular and turbulent diffusion using the generalized Fick's law, which captures diffusion due to concentration gradient (diagonal terms) and diffusion due to interaction with other species. The multi-component diffusion coefficients (*Djj* and D_{jk}) were derived from the Stefan-Maxwell equations as shown in Krishna and Standart (1979).

$$j_i'' = \underbrace{\underbrace{-\rho D_{jj}\frac{\partial y_j}{\partial r}}_{\text{diagonal term}} \underbrace{-\rho\sum_{\substack{k=1\\k\neq j}}^{n-1} D_{jk}\frac{\partial y_j}{\partial r}}_{\text{cross terms}}}_{\text{molecular diffusion}} - \underbrace{\frac{\mu_T}{Sc_T}\frac{\partial y_j}{\partial r}}_{\text{turbulent diffusion}} \tag{2.31}$$

They assumed that the condensate film was well mixed, laminar and could be described by Nusselt's theory. A computer code was developed to solve the differential equations for multi-component mixtures through a finite-difference method. The results were validated with several experimental data sets. Agreement within experimental uncertainty for species mass transfer rates with the data of Modine (1963) was reported. Good agreement was also observed with the condensation rate of isopropyl alcohol in the experiments of Webb and Sardesai (1981), while the rates for condensation of water were 15-25% too low, potentially due to inlet effects in the experimental system. The validated

model was then used to conduct numerical experiments near the point of osmotic diffusion, where the concentration profile of a particular species is at a local minimum. It was found that at higher Reynolds number, the osmotic diffusion point shifts from the viscous sub layer into the buffer layer.

2.5.2 Non-Equilibrium Models for Binary Mixtures

Use of the non-equilibrium film theory model has proven to be more practical for the design of condensers for mixtures than solution of the conservation equations. The term non-equilibrium refers to the fact that the composition and temperature at the vapor/liquid interface, where local equilibrium is assumed, is different from the bulk vapor and liquid composition and temperature. The methodology was first established by Colburn and Drew (1937) and then reframed by Price and Bell (1974) in a manner more appropriate for equipment design. The major assumptions in the method developed by Colburn and Drew are 1) film condensation, 2) condensate is miscible in all proportions, 3) vapor/liquid equilibrium occurs at the interface at system pressure and interface temperature, 4) the heat and mass transfer resistances in the vapor are confined to a thin film layer of thickness δ, 5) uniform temperature and concentration in the vapor outside of the thin film, and 6) all heat and mass transfer is in the direction perpendicular to the liquid film (neglect axial transport). A schematic that represents the modeled system was shown previously in Figure 1.6. While originally developed for binary mixtures, the model can be extended to multi-component mixtures with some effort. A summary of non-equilibrium models for binary and multi-component mixtures is shown in Table 2.5.

Colburn and Drew (1937) proposed that the molar flux of the more volatile component to the interface could be described by Eq. (2.34), where η is defined as the

fractional distance through the film and β_V is defined as the low-flux convective mass transfer coefficient.

$$\dot{N}_1 = \left(\dot{N}_1 + \dot{N}_2\right)\tilde{y}_1 + \beta_V \frac{d\tilde{y}_1}{d\eta} \tag{2.32}$$

By defining a variable *z* as the ratio between the condensing flux of the more volatile component and the total condensing flux, Eq. (2.32) can be integrated across the film thickness with the interface and bulk compositions as boundary conditions, resulting in an expression for total condensing flux (Eq. (2.35)). From a mass balance at the interface, a similar expression for mass transfer in the liquid phase can be derived.

$$\left(\dot{N}_1 + \dot{N}_2\right) = \dot{N}_T = \beta_V \ln\left(\frac{z - \tilde{y}_{1,i}}{z - \tilde{y}_{1,b}}\right) \tag{2.33}$$

As was shown in Figures 1.6 and 1.7 in the previous chapter, the total heat flux rejected to the coolant is a sum of the sensible heat from the vapor, the latent heat from the condensing species, and any sensible cooling of the liquid film. Colburn and Drew (1937) consider only the latent heat and sensible cooling of the vapor, neglecting the condensate sensible cooling. The latent heat flux is calculated using Eq. (2.36), where the enthalpy of vaporization of each species was evaluated at T_{int} and any heat of mixing was neglected.

$$q''_\lambda = \dot{N}_T \cdot z \cdot \tilde{h}_{fg,1} + \dot{N}_T \cdot (1-z) \cdot \tilde{h}_{fg,2} \tag{2.34}$$

The sensible heat flux from the vapor is shown in Eq. (2.37) where α_V is the zero-flux convective heat transfer coefficient in the vapor phase. As before, the expression can be integrated across the film thickness with the appropriate boundary conditions, with the results shown in Eq. (2.38).

$$q''_{S,V} = \left(\dot{N}_1 \cdot \tilde{c}_{p,1} + \dot{N}_2 \cdot \tilde{c}_{p,2}\right)\left(T - T_i\right) + \alpha_V \frac{dT}{d\eta} \tag{2.35}$$

$$q''_{S,V} = \frac{\left(\dot{N}_1 \cdot \tilde{c}_{p,1} + \dot{N}_2 \cdot \tilde{c}_{p,2}\right)\left(T_V - T_i\right)}{1 - \exp\left(-\left(\dot{N}_1 \cdot \tilde{c}_{p,1} + \dot{N}_2 \cdot \tilde{c}_{p,2}\right)/\alpha_V\right)} = \alpha_V \left(T_V - T_i\right)\frac{a}{1 - \exp\left(-a\right)}$$
$$a = \frac{\left(\dot{N}_1 \cdot \tilde{c}_{p,1} + \dot{N}_2 \cdot \tilde{c}_{p,2}\right)}{\alpha_V} \tag{2.36}$$

Eq. (2.36) is used to calculate the sensible heat conducted across the film and the sensible heat required for cooling the condensing flux from the bulk to the interface temperature. The term (a/(1-exp(-a)) appearing in Eq. (2.36) is identical to the Ackerman (1937) correction factor developed for heat transfer with a non-zero mass flux. The variable α_V is the zero-mass flux heat transfer coefficient, calculated assuming no mass transfer. Finally, the heat flux at that interface can be set equal to the overall heat transfer coefficient from the interface to the coolant (U_i) as shown in Eq. (2.39).

$$U_i\left(T_i - T_c\right) = q''_\lambda + q''_{S,V}$$
$$U_i = f\left(\alpha_L, \alpha_C, R_w\right) \tag{2.37}$$

The set of equations developed above requires knowledge of the individual zero-mass flux heat transfer coefficients for the vapor (α_V), condensate film (α_L) and coolant

(α_C), the thermal resistance of the tube wall, and the low-mass flux convective mass transfer coefficients in the liquid (β_L) and vapor (β_V) phase. The equations can then be solved simultaneously to find the interface temperature, composition of the liquid and vapor at the interface, and the ratio of the volatile component condensing flux to the total condensate flux (*z*). Colburn and Drew state that it is a reasonable assumption that the condensate film is perfectly mixed, that is $\beta_L = \infty$ and $\tilde{x}_i = \tilde{x}_L$. This eliminates one equation and one unknown. They then calculate the vapor heat and mass transfer coefficients from the Chilton-Colburn (1934) relation as a function of the vapor Reynolds number and assume U_i to be constant.

With the above assumptions, they considered a sample case for the condensation of methanol/water in a vertical channel at the onset of condensation with a composition equal to that of the condensing flux (function of *z*). As the temperature difference between the saturation point and the wall increases, the ratio of the more volatile component in the condensate increases and approaches the bulk initial concentration in the vapor. Additionally, as the temperature difference increases, there is an increased buildup of the more volatile component at the interface, which drives down the interface temperature. Thus, if only the equilibrium compositions of the condensate and vapor bulk are considered, serious errors can be introduced when estimating the required heat transfer area.

Price and Bell (1974) incorporated the Colburn and Drew equations into a computer program for condenser design. They used a piece-wise material and energy balance over the length of the condenser for a vertical counterflow tube-in-tube heat

exchanger (vapor and condensate in co-flow). In addition to the assumptions made by Colburn and Drew, they assumed isobaric condensation and a well-mixed condensate ($\beta_L = \infty$). The total heat duty rejected to the coolant in each segment was equal to the latent heat of condensation, sensible cooling of the condensing flux, sensible cooling of vapor bulk, and sensible cooling of the condensate. The vapor zero-flux heat transfer coefficient was calculated by either the Chilton and Colburn correlation (1934) or through a correlation (Eq. (2.40)) that attempted to capture the enhancement of the vapor heat transfer coefficient over a liquid film due to the disturbance of the boundary layer. This correlation was developed from a relation between the heat transfer coefficient and the frictional pressure gradient, where the two-phase frictional pressure gradient was estimated from the Martinelli-Nelson (1948) correlation.

$$\alpha_{V,TP} = \alpha_V \left[\left(\frac{dP}{dz} \right)_{f,TP} \Big/ \left(\frac{dP}{dz} \right)_{f,V} \right]^{0.445} \tag{2.38}$$

The condensate heat transfer coefficient was found from either the Nusselt (1916) equation for laminar flow, or the Colburn (1934) correlation for turbulent film condensation.

The system of equations for each segment and the energy and mass balances between each segment were calculated in an iterative fashion, where successive guesses for T_i and z were made until convergence was achieved. They then considered two test cases: (1) methanol/water condensation as in Colburn and Drew (1937), (2) *n*-butane/*n*-octane condensation inside vertical tubes (ID = 21.2 mm). For the methanol/water case, the results compared well with Colburn and Drew and they found little effect of the vapor

two-phase enhanced heat transfer coefficient (Eq. (2.38)) on composition and heat duty. Additionally, they found little vapor mass transfer resistance, as the largest temperature difference was between the interface and the coolant. For the *n*-butane/*n*-octane problem, they found an increased effect of the two-phase heat transfer coefficient and an increased importance of the vapor mass transfer resistance. Compared to the results from two approximate equilibrium methods (Ward, 1960; Bell and Ghaly, 1973), they found that their model resulted in a more conservative design (larger condenser heat transfer area). The equilibrium methods will be described in the following section.

Vuddagiri and Eubank (1998) modified the approach of Colburn and Drew by accounting for liquid-phase mass transfer and by introducing a modification to the Ackermann (1937) correction factor when calculating the vapor-phase sensible heat transfer. The vapor heat and mass transfer and condensate heat transfer coefficients were calculated as in Colburn and Drew (*i.e.*, Nusselt and Chilton and Colburn). The liquid-phase mass transfer coefficient was estimated from a correlation developed by Palen (1994) for falling-film evaporation of binary mixtures. Another difference from the original analysis was the inclusion of a modification to the Ackermann correction factor for calculating non-zero mass flux heat transfer in the vapor phase. The correction factor, shown in Eq. (2.36), assumed an ideal mixture, that is, the mixture specific heat was assumed equal to the weighted average of the individual molar specific heats. They state that the proposed correction improves accuracy for polar molecules. Three test cases were run with their model for methanol/water mixtures (70/30 methanol by mass) in a vertical wetted wall column at a mass flux of 10 kg m^{-2} s^{-1}, P = 0.1 MPa and cooling water temperature of 37°C. The assumed combined thermal resistance of the tube wall

and coolant was increased from Case 1 to Case 3. When comparing the results using the ideal and non-ideal correction factor, deviations near the entrance of the condenser, where condensation rates were high, were observed. However, for most of the condenser length, there was little deviation between the two models, which was attributed to the low system pressure (which tends to mitigate non-ideal fluid behavior) and the small fraction that the sensible cooling of the vapor contributed to the total heat load. Additionally, they compared the effect of a finite liquid mass transfer coefficient by comparing it to the perfect and no-mixing assumptions. For all three cases, the condensers that were designed assuming a finite mass transfer coefficient were on average 4.7% larger than those modeled with the perfectly mixed assumption, and 5.4% smaller than those modeled with the no-mixing assumption.

Lu and Lee (1994), Cavallini *et al.* (2002b) and Jin *et al.* (2003) all developed modifications of the Colburn and Drew non-equilibrium film model for the condensation of binary zeotropic refrigerant mixtures in horizontal tubes. Lu and Lee (1994) assumed negligible gravitational forces, annular flow with uniform film thickness, one dimensional vapor and condensate streams and negligible sensible cooling of the condensate. They modeled the condenser in a segmented fashion, with the inputs of each segment coupled to the outputs of the previous segment from energy and species balances. The vapor zero-flux heat transfer coefficient was found from the Gnielinski (1976) correlation for turbulent pipe flow and the vapor low-flux mass transfer coefficient from the Reynolds analogy. No Ackermann (1937) type correction to account for non-zero mass flux was used in calculating the vapor heat sensible heat transfer. The liquid-film heat transfer coefficient was calculated from the Shah (1979) correlation and

an estimate of mass transfer in the liquid phase was made from Fick's first law. Finally, the local frictional pressure gradient was calculated from the Friedel (1979) correlation. A total of 13 equations and unknowns for each segment were solved iteratively for guesses of T_i until convergence was achieved.

They compared the model with the annular flow condensation data of Kornota and Stoecker (1985) for R-114/R-12 with mass fractions of R-12 from 50 to 90%. The model inlet conditions were specified from the experiments and the local heat transfer coefficients were calculated from the heat flux and difference in temperature between the vapor bulk and wall. They reported an average heat transfer error of -5.6% with a maximum error of 8%, and an average pressure drop error of -3.2% with a maximum error of 33%. Additionally, they showed good agreement between the measured and calculated refrigerant vapor bulk temperature along the condenser tube.

Cavallini *et al.* (2002b) considered a counterflow, water-coupled tube-in-tube condenser. They used a segmented analysis and assumed that the fluid mixture at the inlet could either be saturated or superheated. In the superheated region, the local heat transfer coefficient was calculated using the Dittus and Boelter (Eq. (2.41)) equation until the local temperature is at the saturated condition.

$$\mathrm{Nu_V} = 0.023 \cdot \mathrm{Re_V^{0.8}} \cdot \mathrm{Pr_V}^{0.3} \tag{2.39}$$

They neglected sensible cooling of the condensate and assumed annular flow with a perfectly mixed condensate. The zero-flux heat transfer coefficient in the vapor core was calculated from the Dittus and Boelter equation and the low-flux vapor mass transfer coefficient was calculated using Eq. (2.42). The liquid film heat transfer coefficient was

found from the correlation of Cavallini and Zecchin (1974). Finally, pressure drop across each segment was determined using the Friedel (1979) correlation and the coolant heat transfer coefficient was found through measurements.

$$Sh_V = 0.023 \cdot Re_V^{0.8} \cdot Sc_V^{1/3} \tag{2.40}$$

They combined these equations into a model with unknowns of interface temperature and total condensing flux. For each segment, the local thermodynamic properties were calculated at the inlet temperature or the assumed interface temperature as appropriate. The equations were then solved simultaneously until convergence of heat flux for the local area was achieved. The composition of the vapor and condensate in the next segment was then determined from appropriate energy balances, and the pressure in the next segment was determined from the calculated pressure drop. The calculated heat duties from the condenser model were compared with the experimental data described previously for zeotropic mixtures of R-125/R-236ea. A total of 53 data points at three different compositions were compared, with a mean deviation of 8.7%.

The model of Jin *et al.* (2003), proposed for a horizontal tube-in-tube heat exchanger with annular flow, included mass transfer resistance in the liquid film, while neglecting sensible cooling of the vapor and condensate. Additionally, they modified the calculated low-flux mass transfer coefficients with the correction factor (Ξ) proposed by Bird *et al.* (1960), which accounts for the disturbance of the velocity profile near the interface at high rates of mass transfer, similar in form to the Ackermann correction factor for heat transfer.

$$\Xi_V = -\frac{\dot{N}_T}{\beta_V\left(e^{-\dot{N}_T/\beta_V} - 1\right)} \tag{2.41}$$

The vapor phase low-flux mass transfer coefficient was calculated from a correlation by Koyama *et al.* (1998), while the liquid low-flux mass transfer coefficient was obtained from the correlation of Lamourelle *et al.* (1972), developed for gas absorption processes. The liquid-film heat transfer coefficient was calculated using the empirical Shah (1979) correlation, while the local pressure drop was determined from the Haraguchi *et al.* (1994a) correlation developed for pure refrigerants in smooth tubes.

The model was solved in an iterative fashion and the results compared with data from Kogawa (1993) for condensing R-134a/R-123 mixtures in a horizontal smooth tube (*ID* = 8.4 mm). The model was run assuming perfectly mixed condensate, no mixing in the condensate, and with a mass transfer correction factor equal to one. Little difference was observed between the calculations with and without the mass transfer correction factor; however, the best agreement with the data was observed when the liquid mass transfer was accounted for. The perfectly mixed model predicted higher heat transfer coefficients than the measured values, while the no-mixing model predicted much lower heat transfer coefficients. The absolute mean deviation of the model compared to the data was 10.3%, and the maximum deviation of the model compared to a model assuming perfectly mixed condensate was 12.3%.

Panchal *et al.* (1997) applied the non-equilibrium analysis to condensation of ammonia/water on the outside of a vertical tube (*OD* = 25.4 mm), where the vapor-phase Reynolds number was generally less than 2000. They considered cases of perfect mixing

and no mixing of the condensate. The vapor heat transfer coefficient was found from the correlation of Chen *et al.* (reported in Knudsen and Katz (1958)), the vapor mass transfer coefficient was determined from a correlation in Sherwood *et al.* (1975) (with a correction for entrance effects) and the condensate heat transfer coefficient was calculated with the Chen *et al.* (1987) correlation. They compared the results of perfect and no-mixing to a case that assumed the mixture was at complete equilibrium. For all of the simulations, they found that the equilibrium assumption resulted in a condenser less than half the size of the perfect mixing assumption, consistent with the results of Price and Bell (1974). For the non-equilibrium cases, they found a steep drop in interface temperature near the condenser inlet as the mass transfer resistance in the vapor phase increases with decreasing vapor mass flow rate and the concentration of the more volatile component at the interface increases. When compared with their experiments, the data fell in between the perfect and zero-mixing predictions, more closely approaching the results of the perfect-mixing model.

Table 2.5: Summary of non-equilibrium model studies

		Heat Transfer Resistance		Mass Transfer Resistance	
Study	**Geometry**	α_L	α_V	β_L	β_V
Colburn and Drew (1937)	Vertical channel Vapor co-flow Binary mixture	Assumed constant value	Chilton and Colburn (1934) *with high flux correction	$\beta_L = 0$ $\beta_L = \infty$	Chilton and Colburn (1934) analogy
Price and Bell (1974)	Vertical channel Vapor co-flow Binary mixture	Nusselt (1916) Colburn (1934)	Chilton and Colburn (1934) Two-phase enhanced coefficient (Price and Bell, 1974) *with high flux correction	$\beta_L = \infty$	Chilton and Colburn (1934) analogy
Webb and Sardesai (1981)	Vertical channel Vapor co-flow Ternary mixture	Nusselt (1916)	*with high flux correction	$\beta_L = 0$ $\beta_L = \infty$	Effective diffusivity Toor (1964) Krishna and Standart (1976)
Taylor *et al.* (1986) and Furno *et al.* (1986)	Vertical channel Vapor co-flow Multi-component mixture	Nusselt (1916)	Chilton and Colburn (1934) *with high flux correction	$\beta_L = 0$ $\beta_L = \infty$	Effective diffusivity Toor (1964) Krishna and Standart (1976) Krishna (1982)
Jiang *et al.* (1997)	Vertical channel Vapor co-flow Multi-component	Butterworth (1983) Chen *et al.* (1987)	Chilton and Colburn (1934) *with high flux correction	$\beta_L = \infty$	Toor (1964) Stewart and Prober (1964)
Panchal *et al.* (1997)	Vertical tube (external) Binary mixture	Chen *et al.* (1987)	Chen *et al.* (reported in Knudsen and Katz (1958))	$\beta_L = 0$ $\beta_L = \infty$	Sherwood *et al.* (1975)
Vuddagiri and Eubank (1998)	Vertical channel Vapor co-flow Binary mixture	Nusselt (1916)	Chilton and Colburn (1934) * with non-ideal Ackermann high-flux correction	Palen (1994)	Chilton and Colburn (1934) analogy
Lu and Lee (1994)	Horizontal tube Annular flow Binary mixture	Shah (1979)	Gnielinski (1976)	Fick's Law	Reynolds heat and mass transfer analogy

Table 2.5: Summary of non-equilibrium model studies - cont.

		Heat Transfer Resistance		Mass Transfer Resistance	
Study	**Geometry**	α_L	α_V	β_L	β_V
Cavallini *et al.* (2002b)	Horizontal tube Annular flow Binary mixture	Cavallini and Zecchin (1974)	Dittus and Boelter	$\beta_L = \infty$	Sherwood correlation
Jin *et al.* (2003)	Horizontal tube Annular flow Binary mixture	Shah (1979)	Neglected	Koyama *et al.* (1998) *with high flux correction	Lamourelle *et al.*(1972) *with high flux correction

2.5.3 Non-Equilibrium Models for Multi-Component Mixtures

The primary complication in extending the non-equilibrium models developed previously to multi-component systems is modeling the mass transfer in the vapor. Unlike in binary mixture mass transfer, there is complex coupling between the concentration gradients of the multiple species. As detailed in a study by Smith and Taylor (1983), Taylor *et al.* (1986) and in the reference by Taylor and Krishna (1993), the vapor-phase mass transfer in the non-equilibrium film model can be evaluated using three methods 1) Effective diffusivity (neglecting any multi-component interaction effects), 2) Accounting for interaction effects (result implicit in species molar fluxes), and 3) Accounting for interaction effects (without *a priori* knowledge of molar fluxes).

The molar fluxes of the species using the effective diffusivity approach are calculated using Eq. (2.44), where the correction factor (Ξ_{eff}) is identical to that introduced earlier in Eq. (2.41) and the effective low-flux mass transfer coefficient is based on an effective diffusivity of the mixture and the flow conditions (Taylor *et al.*, 1986).

$$\dot{N}_{\text{V},j} = C_{\text{V}} \cdot \beta_{\text{eff}} \cdot \Xi_{\text{eff}} \cdot \left(\tilde{y}_{\text{V},j} - \tilde{y}_{\text{i},j} \right) \qquad j = 1, 2, ..., n \tag{2.42}$$

In the second method, the molar flux of each species is expressed in Eq. (2.45), where [β_{eff}] and [Ξ_{eff}] are matrices of low-flux mass transfer coefficients and correction factors for each species.

$$\left(\dot{N}_{\text{V}} \right) = C_{\text{V}} \left[\beta_{\text{eff}} \right] \left[\Xi_{\text{eff}} \right] \left(\tilde{y}_{\text{V}} - \tilde{y}_{\text{i}} \right) + \dot{N}_T \left(\tilde{y}_{\text{V}} \right) \tag{2.43}$$

The off-diagonal terms in the matrices are non-zero, thus the interactions of the concentration gradients of each species are captured. More information on the evaluation of these multi-component mass transfer coefficients can be found in Taylor and Krishna (1993). In general, the mass transfer coefficients depend on concentration, resulting in highly non-linear coupled equations. Stewart and Prober (1964) and Toor (1964) independently proposed a linearization method for solving the coupled equations that essentially neglects the variation of the mass transfer coefficient matrices with concentration. Krishna and Standart (1976) also proposed a method of solution based on the exact solution of the Maxwell-Stefan equations.

The molar fluxes of each species calculated using the third method are given in Eq. (2.46), where $[K_v]$ is a matrix of multi-component total mass transfer coefficients and ξ is a scalar correction factor. More information about calculating the matrix $[K_V]$ is given in Smith and Taylor (1983) and Taylor and Krishna (1993). Use of this method does not require a prior knowledge of the mass transfer rates.

$$\left(\dot{N}_{\mathrm{V}}\right) = C_{\mathrm{V}} \cdot \left[\mathrm{K}_{\mathrm{V}}\right] \cdot \zeta \cdot \left(\tilde{y}_{\mathrm{V}} - \tilde{y}_{\mathrm{i}}\right) \tag{2.44}$$

Webb and Sardesai (1981) developed a non-equilibrium film model for the condensation of ternary mixtures with one non-condensable component in a vertical tube. For the vapor-phase mass transfer, they considered the effective diffusivity model (Eq. (2.42)) and a model that accounted for interaction effects (Eq. (2.43)) with the flux evaluated from the linearization method of Toor (1964) or the exact solution of Krishna and Standart (1976). The multi-component mass transfer coefficients are functions of the binary mass transfer coefficients of the species, which were evaluated using the Chilton

and Colburn analogy, where the vapor-side heat transfer coefficient was calculated from Eq. (2.47).

$$\alpha_V = 0.039 \cdot \mathrm{Re}^{-0.24} \tag{2.45}$$

The liquid-film heat transfer coefficient was evaluated from Nusselt theory, where the perfectly mixed and unmixed condensate cases were considered. As in all the models, vapor/liquid equilibrium was assumed at the interface. These equations were applied in a segmented fashion, with energy and species balances specifying the conditions for the subsequent segment. The models were compared with data for water/isopropyl alcohol/N_2 and water/isopropyl alcohol/R-12. They found essentially no difference in the predictions of the two "interactive" vapor-phase mass transfer models (Toor, 1964; Krishna and Standart, 1976). Additionally, they found that the interactive models and the effective diffusivity approach predicted the total condensation rate within ±5% of one another. However, the interactive models were better able to predict the condensation rate of each species, thus they are better suited for a more detailed design and analysis. When considering mixed and unmixed condensate, they observed a negligible difference in the accuracy of the model. Finally they compared the predictions of the vapor temperature from the model with and without the Ackermann (1937) correction for vapor-phase heat transfer coefficient. It was found that omitting the Ackermann correction factor resulted in an overestimation of the vapor bulk temperature by 5 to 20%.

In the work of Taylor *et al.* (1986), a non-equilibrium film model was developed and evaluated for a range of different assumptions. For all variations of the model, heat transfer in the condensate was estimated using the Nusselt approach and the vapor-phase

low-flux heat transfer coefficient was approximated using the Chilton and Colburn (1934) correlation. Two different approaches to modeling vapor-phase mass transfer were used. The first was a film theory based approach, identical to those used in all of the other studies reviewed here. With this approach, the molar fluxes were calculated through both the effective diffusivity and "interactive" models. The second approach was to use the turbulent-eddy diffusivity model developed by Krishna (1982), which attempts to account for the molar flux of each species to the interface resulting from bulk turbulence and molecular diffusion. This model predicts that as the vapor Reynolds number increases, the importance of multi-component diffusion decreases and the transport is dominated by bulk turbulent transport. In the liquid phase, the condensate was assumed to be either completely mixed or unmixed.

A single system of equations was set up and solved simultaneously through the finite difference method. Four problems were considered: 1) methanol/water/air, 2) methanol/water/helium, 3) a straight-chain hydrocarbon mixture, and 4) a straight-chain hydrocarbon and hydrogen mixture. When comparing the film and turbulent model, there was little observed difference, and therefore, they concluded that the use of the simpler film model for design is unlikely to lead to significant discrepancies. However, when comparing the effective diffusivity model and the interactive models, they concluded that the effective diffusivity model was less accurate, resulting in a condenser 43% larger for the methanol/water/air problem when not accounting for multi-component mass transfer interaction effects. The use of either the perfectly mixed or unmixed condensate assumption was not important when a non-condensable gas was present (consistent with Webb and Sardesai (1981)).

Furno *et al.* (1986) used the model developed by Taylor *et al.* (1986) and compared it with experiments from Modine (1963) and Webb and Sardesai (1981). When compared to Modine's experiments, the model provided better agreement when multi-component interactions were considered in the vapor phase. Of the models that considered multi-component interactions, those based on a mass reference frame (constant mass density) performed slightly better than those based on a molar reference frame (constant molar density). Poor agreement with Modine's data was observed when no mixing of the condensate was assumed, while a perfectly mixed assumption provided significantly improved agreement. When compared to Webb and Sardesai's results, the interactive models again provided better agreement, although in this case, the molar reference models performed slightly better. Unlike the comparison to Modine's data, there was a negligible difference in agreement when using either the perfectly mixed or unmixed assumption. Thus, it could not be definitively concluded whether the molar or mass frame interactive models were superior, or what assumption of condensate mixing would provide better results for all conditions.

Jiang *et al.* (1997) developed a non-equilibrium film multi-component condensation model for simulating the performance of a cooling unit of an industrial polyethylene reactor system operating in condensation mode. A segmented approach was developed for vapor flowing downward in a vertical tube in a shell-and-tube heat exchanger cooled by water. Pressure drop in the tube was neglected and the liquid condensate was assumed to be completely mixed in each segment. The vapor-phase mass transfer coefficient was modeled using Eq. (2.43), assuming all components were condensable. The linearized solution method of Toor (1964) and Stewart and Prober

(1964) was used to evaluate the molar fluxes, with the multi-component mass transfer coefficients determined from estimates for the binary low-flux mass transfer coefficients of each species. The liquid-film heat transfer coefficient was calculated using the correlation of either Butterworth (1983) for shear stress controlled condensate flow or Chen *et al.* (1987) for laminar and turbulent condensate flow. The vapor-phase zero-flux heat transfer coefficient was determined using the Chilton and Colburn analogy. The highly nonlinear set of equations was solved numerically through a variety of computational methods. The model results were compared with data from an industrial source, predicting the outlet vapor bulk temperature with very good results. Additionally, the non-equilibrium model provided much better agreement with the data than the two equilibrium models that they compared to their results. Unfortunately, more detailed experimental data (heat duty, composition, etc.) were not available for comparison.

2.5.4 Equilibrium and Empirical Models

While more theoretically sound, the non-equilibrium method of condenser design for binary and multi-component mixtures can require substantially more computational resources. Calculation of the mass transfer in the vapor phase is particularly difficult due to high uncertainty in the mass transfer coefficients, particularly when multi-component interaction effects are considered. To overcome the challenge of modeling vapor phase mass transfer, a simplified calculation procedure was presented in similar studies by Silver (1947), Ward (1960) and Bell and Ghaly (1973). As stated in Bell and Ghaly (1973), the following assumptions underlie all of the studies reviewed in this section: 1) The liquid and vapor compositions are in equilibrium at the vapor bulk temperature, 2) Liquid and vapor enthalpies are those of the equilibrium phases at the vapor bulk

temperature, 3) Sensible heat is transferred from the bulk vapor to the interface by convective heat transfer, where the heat transfer coefficient is calculated for the given geometry assuming only vapor is present, using vapor bulk properties and vapor mass flux, and 4) The total latent heat of condensation and sensible heat of cooling of the condensate and vapor are transferred through the entire thickness of the condensate.

Unlike the non-equilibrium methods, where equilibrium only existed at the vapor/liquid interface, complete equilibrium is assumed in both phases. Due to this assumption, the calculation method is often referred to as the equilibrium model, or the Silver-Bell-Ghaly (SBG) model, named for those who first popularized it. However, the primary simplification is neglecting the mass transfer in the vapor phase. The argument provided by Bell and Ghaly (1973) is that calculating the sensible heat transfer coefficient in the vapor phase will result in a significant under prediction, because no two-phase enhancement effects are considered. The idea is that the additional resistance from mass transfer that is not calculated will be compensated for by underestimating the vapor zero-flux heat transfer coefficient.

Consider the idealized representation of multi-component condensation as presented by Bell and Ghaly (1973) in Figure 2.3. Note that only the heat fluxes are considered. The sensible heat removed from the vapor is defined in Eq. (2.48), while the total heat rejected to the coolant is defined in Eq. (2.49).

$$\frac{d\dot{Q}_{\mathrm{S,V}}}{dA} = \alpha_{\mathrm{V}} \left(T_{\mathrm{V}} - T_{\mathrm{i}} \right) \tag{2.46}$$

$$\frac{d\dot{Q}_{\mathrm{T}}}{dA} = \frac{d\dot{Q}_{\mathrm{S,V}} + d\dot{Q}_{\lambda} + d\dot{Q}_{\mathrm{S,L}}}{dA} = U_{\mathrm{i}}\left(T_{\mathrm{i}} - T_{\mathrm{C}}\right) \tag{2.47}$$

In Eq. (2.46), the zero-flux heat transfer coefficient is calculated from some correlation for vapor flow. In Eq. (2.47), the overall heat transfer coefficient is a function of the thermal resistance of the coolant (calculated from some known method), the tube wall and the condensate layer. The heat transfer coefficient of the condensate is calculated from a correlation for the geometry and flow regime of interest, using the bulk properties of the condensate. For true equilibrium, the temperature of the condensate, interface and vapor bulk would all be the same. However, if this were the case, there would be no sensible heat transfer from the vapor to the interface. Thus, despite the assumption of equilibrium composition in the vapor and liquid at the vapor bulk, it is assumed that the interface is at some unknown temperature T_{i}, less than the bulk vapor temperature. The unknown is eliminated by combining Eq. (2.46) and Eq. (2.47), yielding Eq. (2.50).

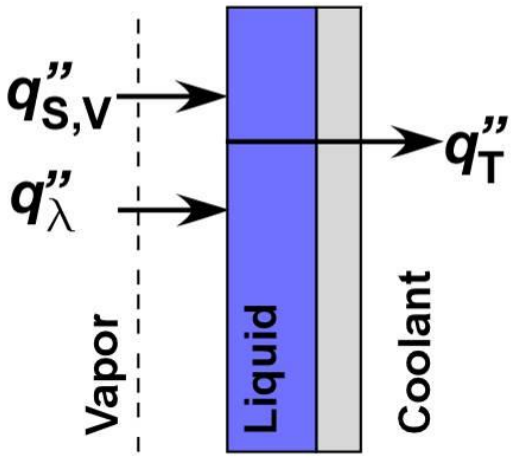

Figure 2.3: Schematic of heat fluxes considered by Silver (1947), Bell and Ghaly (1973)

$$\frac{d\dot{Q}_T}{dA} = U_i \left[T_V - \frac{1}{\alpha_V} \left(\frac{d\dot{Q}_{S,V}}{dA} \right) - T_c \right] \tag{2.48}$$

Bell and Ghaly (1973) then defined the ratio of the sensible heat flux to the total heat flux as Λ. Introducing this parameter into Eq. (2.48) and integrating over the desired total heat duty yields the expression for the total condenser area given in Eq. (2.51).

$$A = \int_0^{\dot{Q}_T} \frac{1 + \left(\frac{\Lambda \cdot U_i}{\alpha_V} \right)}{U_i \cdot \left(T_V - T_c \right)} \cdot d\dot{Q}_T \tag{2.49}$$

As the vapor sensible cooling approaches zero, Eq. (2.49) reduces to the expression expected for pure fluid condensation. Furthermore, as the ratio of sensible heat duty to total heat duty approaches one, the expression reduces to that for cooling of a vapor. Bell and Ghaly (1973) compared this model with a proprietary data set for condensation of steam/air and several hydrocarbon mixtures. The method calculated a condensation area from 1 to 2 times greater than the actual area, which they argued was desirable due to the resulting conservative designs.

The SBG approach has been used by many researchers to predict heat transfer in condensing fluid mixtures, including recently by Del Col *et al.* (2005) and Cavallini *et al.* (2006). The study of Del Col *et al.* (2005) was based on a flow regime map and heat transfer model developed by El Hajal *et al.* (2003) and Thome *et al.* (2003) for condensation of pure refrigerants in smooth horizontal tubes. The model considers the local flow regime (stratified, stratified-wavy, intermittent, annular and mist flow) and models the contribution of falling-film (Eq. (2.52)) and forced-convective condensation

heat transfer (Eq. (2.53)) to the overall local heat transfer coefficient. The two heat transfer coefficients are combined as a function of the calculated falling film angle, θ, shown in Eq. (2.54).

$$\alpha_{\mathrm{f}} = 0.728 \cdot \left[\frac{\rho_{\mathrm{L}} \cdot \left(\rho_{\mathrm{L}} - \rho_{\mathrm{V}}\right) \cdot g \cdot h_{\mathrm{fg}} \cdot k_{\mathrm{L}}^{3}}{\mu_{\mathrm{L}} \cdot D \cdot \left(T_{\mathrm{sat}} - T_{\mathrm{w,i}}\right)} \right]^{1/4} \tag{2.50}$$

$$\alpha_{\mathrm{c}} = 0.003 \cdot \mathrm{Re}_{\mathrm{L}}^{0.74} \cdot \mathrm{Pr}_{\mathrm{L}}^{0.5} \frac{k_{\mathrm{L}}}{\delta_{\mathrm{L}}} f_i \tag{2.51}$$

$$\alpha = \frac{\alpha_{\mathrm{f}} \cdot \theta + \left(2\pi - \theta\right) \cdot \alpha_{\mathrm{c}}}{2\pi} \tag{2.52}$$

Assuming the flow regime map is valid for fluid mixtures, Del Col *et al.* (2005) modified the Thome *et al.* (2003) model for convective and falling-film heat transfer coefficients according to the method of Bell and Ghaly (1973) as shown in Eq. (2.55) and Eq. (2.56) respectively.

$$\begin{aligned} \alpha_{\mathrm{c,m}} &= \left(\frac{1}{\alpha_{\mathrm{C}}} + R_{\mathrm{C}} \right)^{-1} \\ R_{\mathrm{C}} &= q \cdot c_{\mathrm{p,V}} \left(\frac{dT}{dh} \right) \frac{1}{\alpha_{\mathrm{V}} \cdot f_{\mathrm{i}}} \end{aligned} \tag{2.53}$$

$$\begin{aligned} \alpha_{\mathrm{f,m}} &= F_{\mathrm{M}} \left(\frac{1}{\alpha_{\mathrm{f}}} + R_{\mathrm{f}} \right)^{-1} \\ R_{\mathrm{f}} &= q \cdot c_{\mathrm{p,V}} \left(\frac{dT}{dh} \right) \frac{1}{\alpha_{\mathrm{V}}} \end{aligned} \tag{2.54}$$

For the convective heat transfer coefficient, the zero-flux vapor heat transfer coefficient is calculated from the Dittus and Boelter equation (Eq. (2.39)) and corrected with a interfacial friction factor, which they argued accounts for vapor-phase heat transfer area enhancement from surface waves. For the falling-film heat transfer correction they include the empirical term F_m, which accounts for non-equilibrium effects in the stratified regime (*i.e.,* the vapor and liquid are not in direct contact). The modified heat transfer coefficients are combined together as in the pure fluid model, depending on the local flow regime. The model was compared with condensation heat transfer results of ten different refrigerant mixtures with temperature glides between 3.5 and 22 K. The proposed method predicted 98% of refrigerant heat transfer data from Cavallini *et al.* within ±20%, and 70% of the data from other independent researchers within ±20%.

Cavallini *et al.* (2006) developed a simplified model for condensation of pure refrigerants in horizontal tubes (ID > 3 mm). The model was valid over a range of flow regimes, with heat transfer coefficients determined from curve fits of data from experiments with R-134a, R-125, R-32, R-410A and R-236ea. For zeotropic mixtures of refrigerants and hydrocarbons, the SBG approach was used to account for the sensible heat and mass transfer in the vapor phase, with the details presented in Cavallini *et al.* (2002a). The model was compared with several datasets. For R-407C, the SBG corrected model had an absolute average deviation of 21% for 250 data points, while for mixtures of R-125/R-236ea, the average absolute deviation was 22%. The reported agreement for mixtures of propane/*n*-butane and propane/isobutene was better, with an absolute average deviation of 7% for 659 data points.

Webb *et al.* (1996) report a comparison between the Colburn and Drew non-equilibrium design method and the equilibrium SBG method. In the equilibrium method, where the mixture is assumed to be saturated, the change in temperature with the change in bulk vapor composition ($dT_V/d\tilde{y}_{1,V}$) is tangent to the vapor/liquid equilibrium curve. In the non-equilibrium method, the change in vapor temperature is a function of the relative rates of heat and mass transfer in the vapor phase. They show that the slope $dT_V/d\tilde{y}_{1,V}$ is a function the vapor Lewis number ($\alpha_V/\mathcal{D}_{12}$). For Le greater than 1, the vapor temperature slope is greater than the slope of the condensation curve and the vapor bulk tends to be subcooled. In this case, the SBG method is deemed "unsafe" because it results in a higher than actual vapor-phase heat transfer coefficient and the condenser will be undersized. When Le < 1, the vapor tends to superheat and the SBG method can be considered "safe". They show that the equilibrium and non-equilibrium methods are only in agreement when Le is in the range of 0.6 to 0.8. Further, they theorize that the equilibrium method has shown good agreement with data because over the range of complete condensation, the vapor Lewis number can vary from greater than one to less than one, resulting in a compensatory effect over the length of condenser. To account for these differences, they proposed a new value of Λ_W, a further correction to the SBG method, which brings the non-equilibrium and equilibrium methods into better agreement.

The proposed correction factor does not require a film model analysis to be carried out, thus it still provides the advantage of reduced computational complexity. The predictions with the new factor are compared with data for benzene/nitrogen and toluene/nitrogen. Without the new correction factor, the equilibrium model resulted in a

40% and 80% error for condensation of benzene and toluene, respectively. When the new correction factor is applied, the model predicts data within 10 to 15%, consistent with the accuracy of the non-equilibrium method applied to the same data. It is not clear how the new factor performs when considering mixtures where both components are condensable.

An approach similar to the SBG method for modeling mixture condensation heat transfer was proposed by Granryd (1989) with the results most accessible in Shao and Granryd (1998). The model, shown in Eq. (2.57), corrected the condensation heat transfer coefficient calculated for a pure fluid with the mixture properties by attempting to account of local non-equilibrium in the gas (factor A_1) and liquid phase (factor A_2)

$$\frac{\alpha_{\text{mix}}}{\alpha_{\text{pure}}} = \frac{1}{1 + A_1 + A_2} \tag{2.55}$$

$$A_1 = q \cdot Z_1 \cdot \left(\frac{c_{\text{p,V}}}{c_{\text{p,eff}}} \right)_q \cdot \left(\frac{\alpha_{\text{pure}}}{\alpha_{\text{V}}} \right)_q \tag{2.56}$$
$$Z_1 = 1.1 \cdot q \left(1 - \exp\left[-10 \cdot (1 - q) \right] \right)$$

$$A_2 = q \cdot Z_2 \cdot \left(\frac{c_{\text{p,L}}}{c_{\text{p,eff}}} \right)_q \cdot \left(\frac{\alpha_{\text{pure}}}{\alpha_{\text{L}}} \right)_q \tag{2.57}$$
$$Z_2 = 0.9 (1 - q)$$

$$c_{\text{p,eff}} = \left(\frac{\partial T}{\partial h} \right)_{q,P} \tag{2.58}$$

The single component condensation heat transfer coefficient was calculated from an empirical correlation for annular flow of refrigerants in horizontal tubes by Tandon *et*

al. (1985b).The liquid and vapor heat transfer coefficients were calculated from the Dittus and Boelter equation based on the liquid or vapor Reynolds and Prandtl numbers. General agreement with the data of Shao and Granryd (1998) (within +20/-30%) and DeGrush and Stoecker (1987) (agreement not quantified) for condensation of refrigerant mixtures was reported.

Finally, many purely empirical models for condensation heat transfer of mixtures in tubes have been proposed. These correlations are generally validated for a specific set of mixtures and concentrations over a narrow range of operating conditions. They are not expected to be as widely applicable as the modeling methods described above. Tandon *et al.* (1986) proposed an empirical correlation (Eq. (2.61)) for predicting condensation heat transfer of R-22/R-12 mixtures inside a horizontal smooth tube.

$$\mathrm{Nu} = 2.82 \cdot \mathrm{Re}_{\mathrm{V}}^{0.146} \cdot \mathrm{Pr}_{\mathrm{L}}^{1/3} \cdot \left(\frac{h_{\mathrm{fg}}}{c_{\mathrm{p,L}} \left(T_{\mathrm{sat}} - T_{\mathrm{w,i}} \right)} \right)^{0.365} \tag{2.59}$$

The correlation was developed from least-square regression analysis of data in an *ID* = 10 mm tube. Similar empirical correlations were developed for condensation of R-22/R-114 in internally grooved horizontal tubes by Koyama *et al.* (1990), and for refrigerant mixture alternatives to R-22 in enhanced surface tubing by Sami and Grell (2000).

2.6 Summary and Need for Additional Work

Compared to condensation of pure fluids, condensation of zeotropic mixtures in horizontal channels remains relatively unexplored. Furthermore, most of the experimental work on binary and ternary mixtures has focused on large vertical channels, where the

condensate flow is more analogous to falling-film condensation on a vertical surface. In horizontal channels, the effects of gravity, interfacial shear and surface tension will affect the local flow regime and directly impact the momentum, heat and mass transfer mechanisms. As the channel size decreases to the order investigated in the current study (D ~ 1 mm), surface tension forces become increasingly important in governing the flow regime. Several researchers have shown that flow maps and heat transfer and pressure drop models developed for large tubes do not extrapolate well to small channels for pure fluids. Extrapolation is even worse when attempting to predict momentum, heat and mass transfer in fluids with vastly different properties than those for which the original work was developed for (*e.g.*, air/water models for refrigerants). In comparison to studies on microchannel effects for condensing pure fluids, the impact of channel diameter on condensing zeotropic mixtures has received little attention, particularly for horizontal channels.

A summary of the important experimental studies reviewed was provided in Tables 2.3 and 2.4. In the studies reviewed on primarily organic and natural working fluids in vertical tubes, experiments have been conducted on vapor in co-flow and counter-flow in tubes with inner diameters ranging from 21 to 88 mm. In horizontal tubes, many experiments have been conducted with mixtures of synthetic CFC, HCFC and HFC refrigerants, with a primary focus on HVAC&R applications. The horizontal tube sizes investigated vary from 2.45 mm to 25.4 mm and consist of both smooth and enhanced surfaces.

In the studies where heat transfer coefficients were calculated, either the UA-LMTD method or direct measurement/calculation of the local tube wall temperature,

fluid bulk temperature and heat flux were used. The experimental heat transfer coefficients were reported either as averages for the entire condensation process (quality change of 100%) or for some smaller average quality change. The quality changes investigated varied considerably from study to study. For studies that determined the heat transfer coefficient from wall and bulk fluid temperature difference, the definition of bulk temperature was inconsistent, with some studies assuming the equilibrium temperature and others attempting to directly measure the bulk temperature. Furthermore, several of the studies in horizontal tubes reported the presence of compressor lubricant in their test sections, which can confound the results.

Many of the studies, particularly those with mixtures of synthetic refrigerants, showed degradation in condensation heat transfer coefficient. Thus, when considering a weighted average of the heat transfer coefficients of the pure components, the measured heat transfer coefficient is lower for certain compositions. This implies that the additional mass transfer resistance in the vapor and liquid phases adversely affects the heat transfer. Additionally, most of the mixtures considered exhibit some temperature glide, ranging from near 0 K for the near-azeotropic mixtures to over 80 K for mixtures of ammonia and water. This leads to an additional sensible heat transfer resistance in the vapor phase, further reducing heat transfer. Moreover, for the ammonia/water mixtures investigated here, the heat of mixing is not insignificant and should be accounted for.

While there has been significant work on experimental evaluation of mixture condensation in channels, several gaps in understanding remain. Many of the binary and multi-component studies measured heat transfer coefficients over large quality increments, including complete condensation. For design of total and partial condensers,

as well as to better verify analytical models, it is important to be able to obtain heat transfer coefficients at varying quality in fine increments and varying operating conditions. This would allow better characterization of trends in local heat transfer, yielding a better fundamental understanding of the mixture condensation process. Many of the studies in horizontal tubes were conducted with mixtures of CFC, HCFC and HFC refrigerants, some with compressor lubricant present. While these are important for use in the HVAC&R industry, it would be illustrative to investigate heat transfer in different fluids with higher temperature glides and vastly different heat and mass transfer characteristics such as ammonia/water and hydrocarbon and hydrocarbon/refrigerant mixtures. It is also extremely important to isolate the effect of trace amounts of lubricant on the heat and mass transfer. In horizontal tubes, the flow undergoes many transitions as it is condensed. More work is needed to account for the effects of these transitions on multi-component condensation. Finally, as pressure to reduce fluid inventory and equipment size increases, investigations should be conducted in mini and microchannel geometries with binary and higher order mixtures.

In addition to the experimental work, four different categories of models for mixture condensation were reviewed. Nearly all of the models are developed for an idealized case of a cooled surface separated from the vapor by a liquid film with a smooth interface. This idealized model is most applicable to wetted wall vertical columns or for annular flow in horizontal tubes. With the increased focus on use of horizontal channels, more work is needed on understanding the conditions under which different flow regimes are present in two-phase fluid mixtures and the best methods to model the heat transfer and pressure drop using the modeling approaches reviewed in this study.

The models based on the conservation equations are the most theoretical and also most difficult to use in practice. Additionally, these models require specification of some condition such as interfacial friction factor to provide closure to the set of equations. This condition is usually found from some empirical or semi-empirical model. Further complications arise when attempting to consider deviations from ideal annular flow and when the vapor and/or liquid are turbulent. Application of the conservation equations to low mass flux flow in microchannels may have some promise as laminar flow will tend to dominate, simplifying the required model.

The non-equilibrium Colburn and Drew (1937) film model analysis has been used extensively in both vertical and horizontal geometries. It lends insight into the coupled heat and mass transfer processes, particularly in the vapor core, but so far, its application has been limited to annular type flow. The formulation of the film model, which was first introduced by Colburn and Drew (1937), provides a framework for addressing the heat and mass transfer problem. As can be seen, the methodology is only as accurate as the correlations used for determining the liquid and vapor mass and heat transfer coefficients and diffusivities. In the vapor phase, the mass transfer coefficient is usually determined from the Reynolds or Chilton-Colburn analogy from either a calculated heat transfer coefficient or interfacial friction factor. Further research on models for predicting heat and mass transfer coefficients in the vapor and liquid phases would greatly improve the accuracy of these types of model. Other items of particular interest include addressing the effect of a non-smooth interface, a condition that will be very prevalent in horizontal tube condensation. Additionally, for higher order mixtures, it is critical to be able to predict

the multi-component mass diffusivities and mass transfer coefficients in the vapor phase to more accurately account for multi-component interactions.

The equilibrium and empirical models reviewed here may be useful for design within narrow operating bands for specific fluids, but are not broadly applicable. Neither method captures the impact of mass transfer on the underlying heat transfer phenomena. Despite their narrow application, they are still frequently used in design due to their simplicity. Thus, more thorough experimental validation with various fluid mixtures, compositions and properties in different channel geometries should be conducted to extend their range of applicability.

2.7 Objectives of Present Study

From the above review of the pertinent literature, it is clear that there is no validated method for predicting zeotropic condensation of high-glide mixtures in small channels. Thus, the primary objective of the present study is the development of a model for the condensation of high-temperature-glide ammonia/water mixtures to enable the development of highly efficient, compact, thermal conversion devices. As channel size decreases, surface tension forces become increasingly important, affecting prevailing flow regimes and transitions (Triplett *et al.*, 1999; Serizawa *et al.*, 2002; Coleman and Garimella, 2003). Thus, models developed for predicting heat transfer and pressure drop of condensing flows in large channels do not extrapolate to small geometries. This work departs from the available literature by investigating the combined effects of coupled heat and mass transfer resistances in microscale geometries for condensing mixtures.

The objectives of the present study are to:

1. Develop an experimental methodology and data analysis procedure for evaluating the local condensation heat duty (for incremental Δq), condensation transfer coefficient (for pure ammonia), and apparent heat transfer coefficient (for zeotropic ammonia/water mixtures) with low uncertainties.

2. Conduct condensation heat transfer and pressure drop experiments with pure ammonia and ammonia/water mixtures of varying composition at multiple mass fluxes, vapor qualities, and tube diameters.

3. Develop and validate a flow mechanism-based model for predicting microscale condensation heat transfer of pure ammonia.

4. Develop and validate a zeotropic condenser design model based on film theory for predicting microscale condensation heat transfer and condensation heat duty by considering the coupled heat and mass transfer resistances for high-temperature-glide zeotropic mixtures.

CHAPTER 3

EXPERIMENTAL APPROACH

Condensation experiments on pure ammonia (NH_3) and zeotropic mixtures of ammonia and water (NH_3/H_2O) were conducted over a wide range of tube diameters ($0.98 \leq D \leq 2.16$ mm) and mass fluxes ($50 \leq G \leq 225$ kg m^{-2} s^{-1}). For pure NH_3, experiments were conducted at saturation temperatures ranging from 30 to 60°C ($0.10 \leq P_r \leq 0.23$), while the zeotropic mixture experiments were conducted at a single saturation pressure (P_{sat} = 1500 kPa) with a bulk mass fraction of 0.80, 0.90 and > 0.96 ammonia. As noted in Chapter 2, a significant challenge in microchannel condensation heat transfer experiments is accurately resolving very low condensation heat duties and very high heat transfer coefficients. In the present study, this challenge was overcome by decoupling the measurement of the heat transfer coefficient and heat duty through the use of accurately measured electric heat inputs, pre-heater, post-heater and test section energy balances, and a detailed analysis of the water-coupled test section. The formal data analysis is presented in Chapter 4. The general experimental approach was first presented by Agarwal and Garimella (2010), who developed a microchannel phase change experimental facility for the condensation of R-134a in rectangular, multiport microchannels (100 μm $\leq D_H \leq$ 160 μm; $30 \leq T_{sat} \leq 60$°C). The facility was subsequently used, with modifications, by Fronk and Garimella (2010) for CO_2 condensation experiments (100 μm $\leq D_H \leq$ 160 μm; $15 \leq T_{sat} \leq 25$°C) and Keinath (2012) for heat transfer, pressure drop, and flow visualization experiments on condensing R-404A ($0.508 \leq D \leq 1.55$ mm; $30 \leq T_{sat} \leq 60$°C). In the present study, the general operating principles are the same as in the previous investigations; however, the facility was completely

redesigned and rebuilt for compatibility with the working fluids under consideration and the desired operating conditions. The new test facility design, instrumentation, test section details, and experimental procedures are presented in the following sections.

3.1 Facility Design and Instrumentation

A schematic and photograph (prior to the installation of insulation and safety shield) of the condensation test facility are shown in Figures 3.1 and 3.2, respectively. The test

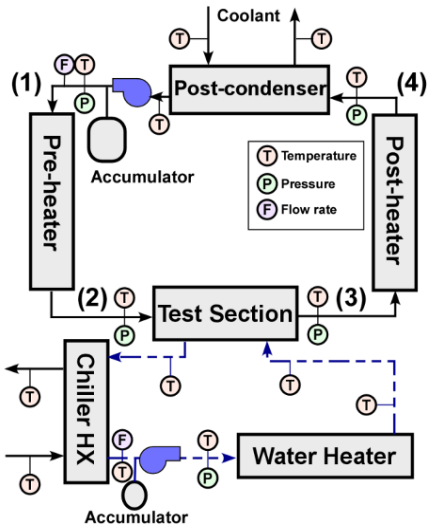

Figure 3.1: Experimental facility schematic

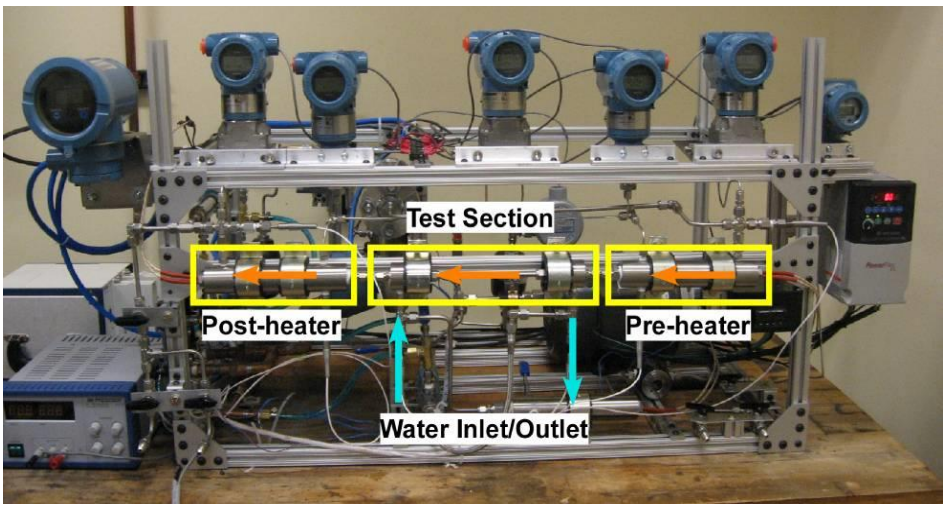

Figure 3.2: Photograph of experimental facility

facility is composed of two coupled, closed loops. The working fluid loop (shown with a solid line), nominally operates at a single pressure and includes the primary components of the pre-heater, test section, post-heater, post-condenser and working fluid pump. The condensation heat duty from the working fluid loop is rejected into the water loop (shown with dashed line) which includes the water pump, heater, the test section, and a chilled glycol-water coupled heat exchanger.

3.1.1 Working Fluid Loop Description

Due to material compatibility issues of NH_3 and NH_3/H_2O with copper and aluminum, all rigid wetted components were fabricated from stainless steel. All soft wetted components including seals, valve seats, etc., were also selected for material compatibility, with most components made of Teflon. The primary components in the working fluid loop are connected with seamless, stainless steel tubing with an outer diameter of 3.2 mm, wall thickness of 0.89 mm and pressure rating of 75 MPa. To minimize heat loss/gain from the system, all working fluid piping and components were insulated with low thermal conductivity (k = 0.042 W m^{-1} K^{-1}), rigid and wrap type fiberglass insulation with a minimum thickness of 25.4 mm.

As an introduction to the primary components of the working fluid loop, it is illustrative to proceed through the thermodynamic states (**1** to **4** in Figure 3.1). Starting at point **1**, subcooled NH_3 or zeotropic NH_3/H_2O mixture enters the pre-heater assembly, where it is partially evaporated using a measured electric input. The heater assembly is a custom designed, all stainless steel construction, fabricated by the Georgia Tech Research Institute (GTRI) machine shop. A cross sectional schematic (showing the heater installed) of the assembly is shown in Figure 3.3. The working fluid enters from the top through a

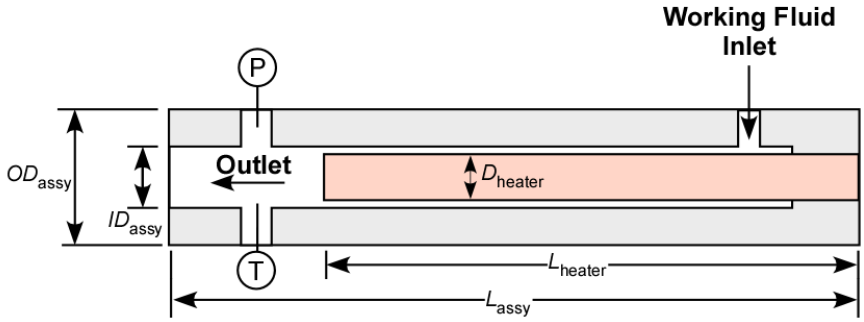

Figure 3.3: Schematic of heater housing assembly with installed cartridge heater

1/6”-27 NPT fitting, and is heated in the annulus formed between the cylindrical heating element and the assembly wall ($D_H \approx 5.2$ mm). The local pressure and temperature measurements are obtained in the mixing region at the outlet of the heater. The flow area is then further reduced and the fluid enters the adiabatic portion of the test section (state **2**).

The heating element is a single phase, 120V, 1000 W, cylindrical cartridge heater from Watlow (P/N: SE-10705). Detailed dimensions of the heater and assembly are provided in Table 3.1. The dimensions are important for determining the ambient losses from the heater assembly, discussed in Chapter 4. For material compatibility, the heater threaded connection is fabricated from stainless steel, welded to the heater body and pressure tested to 4,650 kPa. The heater power input is manually controlled using a variable voltage Variac device (0 to 120 V, 3 A max current) to achieve the desired test section inlet condition.

From the pre-heater, the working fluid flows through the test section (detailed in Chapter 3.2) and is partially condensed ($\Delta q_{avg} = 0.25$). At the test section outlet (state **3**), the working fluid enters the post-heater assembly. The assembly construction and post-

Table 3.1: Heater and heater housing assembly specifications

		Symbol	
Heater	Max Power (W)	-	1,000
	Length (mm)	L_{heater}	172
	Diameter (mm)	D_{heater}	12.7
Heater Housing Assembly	Outer diameter (mm)	OD_{assy}	38.1
	Inner diameter (mm)	ID_{assy}	17.9
	Length (mm)	L_{assy}	197
	Minimum insulation thickness (mm)	t_{ins}	25.4

heater specifications are identical to those of the pre-heater (Table 3.1). The heated mixture leaves the post-heater (state **4**), where the thermodynamic state is determined from the measured temperature and pressure (and bulk concentration for mixtures). The mixture is then completely condensed in the post-condenser section, which is composed of two stainless steel Exergy brand shell-and-tube heat exchangers connected in series. The condensing mixture flows on the tube-side, while a chilled glycol-water solution flows on the shell side of the heat exchanger. The chilled glycol-water solution is provided by a stand-alone recirculating chiller (Neslab Merlin M75, S/N: 109194014) with a nominal capacity of 2225 W and a temperature range of -15 to 35°C.

Finally, the subcooled fluid is pumped back to the pre-heater by a variable speed, stainless steel gear pump from Micropump (GAH-X21.P9FS.A). The pump gear set (X21) has a displacement of 0.017 mL rev^{-1}, with a maximum differential pressure of 5.2 bar. The maximum operating pressure of the pump head is 345 bar, and it is fitted with all Teflon seals for material compatibility. The pump head is magnetically coupled to a variable speed DC motor, controlled by a variable voltage DC power supply (B&K

Precision Corp, Model #1627A). Complete specifications of the pump, motor and voltage controller are provided in Table 3.2.

The working fluid loop pressure is maintained by the use of a rigid, 150 cubic centimeter stainless steel accumulator (Swagelok, P/N: 304L-HDF-150). The accumulator is isolated from the main loop by a Swagelok expansion and shutoff ball valve installed in series. There is no diaphragm or bladder in the rigid accumulator to adjust system pressure; rather, during operation, the valves are opened to meter working

Table 3.2: Working fluid pump, motor and power supply specifications

Micropump Pump Head (GAH-X21.P9FS.A)	
Displacement	0.017 mL rev^{-1}
Max differential pressure	5.2 bar
Max operating pressure	345 bar
Temperature range	-46 to 177°C
Maximum speed	8,000 RPM
Micropump DC Motor (306 A)	
Type	DC-Brush type permanent magnet A-mount
Speed	500 to 4,000 RPM
Max torque	0.21 N-m
Power	112 W/0.16 HP
Weight	1.14 kg
B&K Precision Corp DC power supply (1627A)	
Voltage range Max current	0 to 30 V 3 A

fluid in or out vessel depending on the operating condition of interest.

3.1.2 Water Loop Description

Like the working fluid loop, the water loop is primarily constructed of stainless steel tubing with an outer diameter of 3.2 mm, wall thickness of 0.89 mm and pressure rating of 75 MPa. The loop is insulated with low thermal conductivity (k = 0.042 W m^{-1} K^{-1}), rigid and wrap type fiberglass insulation with a minimum thickness of 25.4 mm. Depending on the desired system operating condition, the water loop can be operated above or below the ambient temperature. Thus, both a heater and a chilled glycol-coupled heat exchanger are included in the loop.

The water loop is operated at a very high flow rate (~ 5 L min^{-1}) to minimize the water-side thermal resistance and change in temperature in the test section. This leads to more accurate condensation heat transfer results and an approximately isothermal boundary condition for the condensing fluid. The water-side annulus hydraulic diameter in the test section (detailed below) is very small (0.7 to 2.6 mm), which leads to very high water-side heat transfer coefficients and a further decrease in the water-side resistance. However, the small flow area coupled with the high water flow rate requires the use of a large pump to drive the water loop and overcome the friction head. The pump head is a positive displacement gear pump from Micropump (Model GC-M25) with a displacement of 1.87 mL rev^{-1}. The maximum differential and operating pressures of the pump are 8.7 and 103 bar, respectively.

The pump is driven by a 3-phase AC motor (WEG P/N: 10022031). A variable frequency motor drive (Allen Bradley Power Flex 4) is used to operate the water-pump at

variable speeds to achieve the desired flow rates. Detailed specifications of the water pump, pump motor, and variable frequency drive are provided in Table 3.3.

Downstream of the pump, the water enters the water heater assembly. The heater assembly and heater specifications are the same as the pre- and post-heater (Figure 3.1 and Table 3.1), discussed above. However, here, the heat input is controlled automatically with a Watlow EZ-Zone (P/N: PM6C1CJ) PID temperature controller. A T-type thermocouple at the heater assembly outlet provides the set point. The PID controller and heater are coupled through a solid state relay (Watlow P/N: SSR-240-10A-DC1) with an output range of 24 to 240 VAC, and a max current of 10 A.

Table 3.3: Water pump, motor and drive specifications

Micropump Pump Head (GC-M25)	
Mount type	NEMA 56C
Displacement	1.82 mL rev^{-1}
Max differential pressure	8.7 bar
Max operating pressure	103 bar
Temperature range	-46 to 177°C
Maximum speed	6,000 RPM
WEG AC Motor (306 A)	
Voltage	3-Phase 208/230
Power	373 W/0.5 HP
Allen Bradley Power Flex 4 VFD (P/N: 22A-A9P6N103)	
Input	240 V 50/60 Hz 1-phase
Max current out	9.6 A
Max power out	3.0 HP/2.2 kW

Finally, after flowing through the test section, the water flows through a stainless steel Exergy brand shell-and-tube heat exchanger, that is coupled to a circulating glycol-water solution. The glycol-solution is conditioned by the same standalone chiller coupled to the post-condenser in the working fluid loop. Here, the glycol-water solution flows through the shell side, while the water flows through the tube side. The glycol flow rate through the heat exchanger is controlled manually with a Swagelok expansion valve. This valve, combined with the water heater outlet temperature controller, provides coarse and fine control over the water loop operating temperature.

During operation, the water loop is pressurized ($13.8 \leq P_{water} \leq 20.5$ bar) with a nitrogen diaphragm accumulator (Accumulators Inc., P/N: AM631003, maximum operation pressure of 21 MPa). Operating at elevated pressures allows experiments to be conducted at water temperatures greater than 100°C, and also minimizes the potential for pump cavitation due to the large loop pressure drop.

3.2 Test Section Design

The test section consists of a stainless steel counterflow tube-in-tube heat exchanger. A photograph and schematic of the test section are shown in Figures 3.4 and 3.5, respectively.

For all experiments, the water-side annulus is a thick-walled stainless steel tube with OD = 6.35 mm and a wall thickness of 1.245 mm, yielding an inner diameter of 3.86 mm. The working fluid flows through the inner tube, where three different test section diameters (0.98, 1.44, and 2.16 mm) are investigated. The two smaller diameter tubes are fabricated from SS 304 hypodermic tubes from Component Supply Company (P/N: HTX-18T (for D = 0.98 mm) and HTX-16X (for D = 1.44 mm)). The large tube (D =

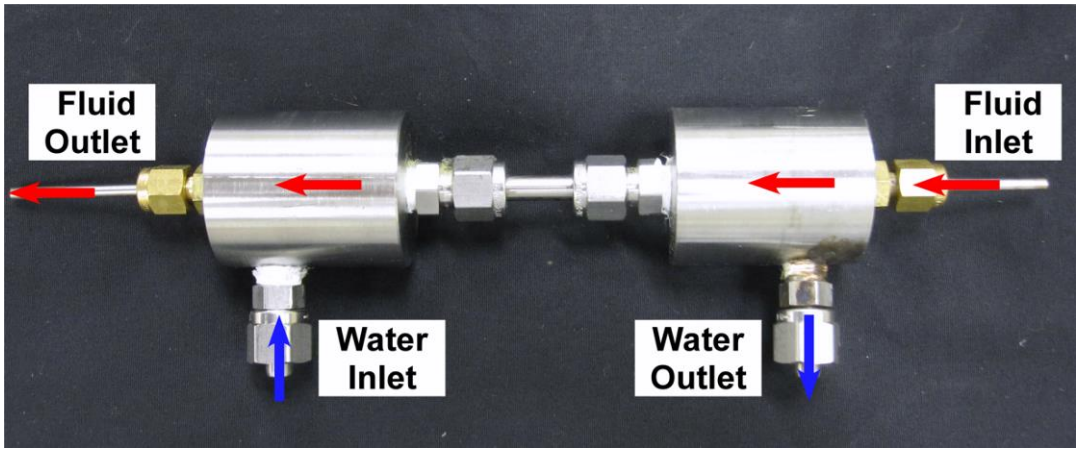

Figure 3.4: Representative test section photograph

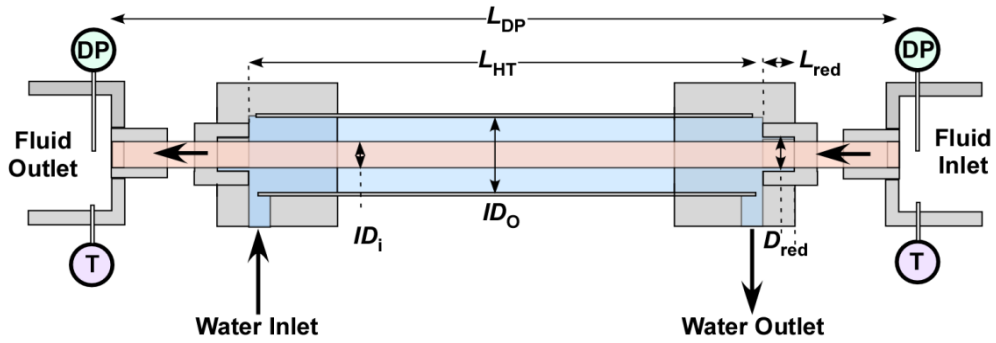

Figure 3.5: Test section schematic

2.16 mm) is standard SS 304 seamless tubing. As can be seen from Figure 3.5, two length dimensions in the test section are important. The overall test section length (L_{DP}) includes the adiabatic and condensing lengths, while the heat transfer length (L_{HT}) corresponds to only the water-coupled length. As will be shown in Chapter 4, L_{DP} is used for calculating pressure gradient and L_{HT} for calculating the condensation heat transfer coefficient. The adiabatic lengths at the entrance and exit allow for flow development and mixing, mitigating entrance and exit effects on the heat transfer process. Dimensional details of each test section investigated are shown in Table 3.4.

The inner and outer tubes are joined in the water-coupler assembly, with a schematic of the cross section shown in Figure 3.6. In the schematic, the coupling at the

Table 3.4: Test section dimensions

		Test Section Inner Diameter (mm)				
		Symbol	**0.98**	**1.44 (NH_3 only)**	**1.44 (NH_3/H_2O only)**	**2.16**
Inner Tube	Outer diameter (mm)	OD_i	1.27	1.651	1.651	3.175
	Inner diameter (mm)	ID_i, D	0.98	1.44	1.44	2.16
	Wall thickness (mm)	t_{wall}	0.145	0.108	0.108	0.508
	Inner tube total length (mm)	L_{DP}	248	381	248	248
	Heat transfer length (mm)	L_{HT}	127	249	127	127
	Reducer length (mm)	L_{red}	9.9	9.9	9.9	9.5
	Reducer diameter (mm)	ID_{red}	2.0	2.0	2.0	3.6
Outer Tube	Outer diameter (mm)	OD_O	6.35	6.35	6.35	6.35
	Inner diameter (mm)	ID_O	3.86	3.86	3.86	3.86
	Annulus length (mm)	L_{ann}	127	249	127	127
	Annulus hydraulic diameter (mm) (ID_o-OD_i)	$D_{H,ann}$	2.59	2.21	2.21	0.69
	Minimum Insulation Thickness (mm)	t_{ins}	63.5	63.5	63.5	63.5

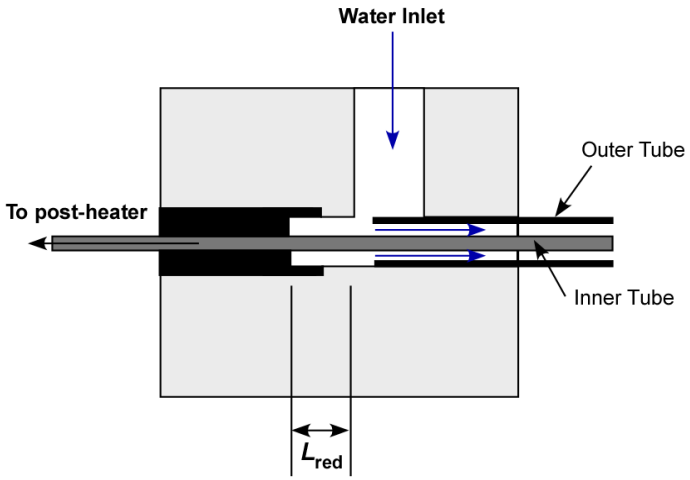

Figure 3.6: Cross section schematic of working fluid/water coupling assembly

water inlet/working fluid outlet is pictured. The assemblies were custom designed and fabricated from stainless steel by the GTRI machine shop. As can be seen from Figure 3.6, the custom design minimizes the stagnant or dead water zone due to the flow reducer. This so-called reducer length (L_{red}), represents an area of low heat transfer, and

must be accounted for when determining the condensation heat transfer coefficient (Andresen, 2007), as will be shown in Chapter 4.

3.3 Instrumentation and Data Acquisition

During the experiments, various temperature, pressures, flow rates and electric heat inputs are measured. The location of the temperature (13 total), absolute pressure (4 total), differential pressure (1 total) and flow rate (2 total) measurements were shown previously in Figure 3.1. By maintaining low measurement uncertainty, the overall uncertainty of the calculated heat duty, average quality, condensation heat transfer coefficient and two-phase frictional pressure gradient are minimized. Full details of the instrumentation used in the working fluid and water loops are provided in Table 3.5.

In the working fluid loop, the fluid temperatures at the test section inlet and outlet (states **2** and **3** in Figure 3.1) are measured with 4-wire platinum RTDs (JMS Inc., P/N: 3SSDNK3BZZ3(72)ZWTA) with an uncertainty of ±0.2°C. The other temperatures in the loop (pre-heater inlet, post-heater outlet, post-condenser-outlet and glycol-water post-condenser inlet/outlet) are measured using T-type thermocouples (Omega, P/N: TMQSS-062-6) with an uncertainty of ±0.5°C. For fluid compatibility, both the RTDs and thermocouples have stainless steel sheaths. The higher accuracy RTDs are selected for the test section inlet and outlet temperature as these variables have a more significant effect on the uncertainty of the calculated parameters. Absolute pressure measurements at the inlet and outlet of each heater assembly are obtained using Rosemount 3051 series transducers with a set span of 3,500 kPa (uncertainty: ± 2.625 kPa). Differential pressure between the test section inlet and outlet is measured with a Rosemount 3051 CD series transducer with an uncertainty of ±0.075 kPa. The working fluid mass flow rate is

measured using a high-accuracy Coriolis type mass flow meter (±0.25% of reading) installed for measurement of liquid-only flow. Finally, the pre- and post-heater power inputs are measured with Ohio Semitronics (P/N: GW5-10E) Watt meters, with an uncertainty of ±0.2% of the reading.

In the coupling fluid loop, the test section water inlet and outlet temperatures are also measured using 4-wire platinum RTDs, to minimize experimental uncertainty. The other loop temperatures (heater inlet/outlet, glycol-water inlet/outlet) are measured with

Table 3.5: Details of experimental facility instrumentation

Instrument	Location	Supplier	Model	Serial #	Uncertainty	Set Span
Pressure transducer	Pre-heater inlet	Rosemount	3051 CA4A22A1A M5	2036883	±2.625 kPa ±0.075% of span	0 to 3,500 kPa
Pressure transducer	Pre-heater outlet	Rosemount	3051 TA5A2B21A E5M5	0921022	±2.625 kPa ±0.075% of span	0 to 3,500 kPa
Pressure transducer	Post-heater inlet	Rosemount	3051 TA5A2B21A E5M5	0921024	±2.625 kPa ±0.075% of span	0 to 3,500 kPa
Pressure transducer	Post-heater outlet	Rosemount	3051 CA4A22A1A M5	2036884	±2.625 kPa ±0.075% of span	0 to 3,500 kPa
Pressure transducer	Water pump outlet	Rosemount	2088 A3M22A1M 7	138872	±6.9 kPa ±0.25% of span	0 to 2,760 kPa
Differential pressure transducer	Test Section Inlet/Outlet	Rosemount	3051 CD 4A22A1ADF MS	1719727	±0.075 kPa ±0.075% of span	0 to 100 kPa
4-wire platinum RTD	-	JMS Inc.	3SSDNK3BZ Z3(72)ZWTA	-	±0.2°C	-200 to 250°C
Thermocouple	-	Omega	TMQSS-062G-6	-	±0.5°C	0 to 350°C
Mass flow meter	Working fluid loop	Micromotion	CMF010 521N0BAEZ ZZ	12088639	±0.25%	0 to 50 g min^{-1}
Volumetric Flow Meter	Water loop	Omega	FTB-902/FLSC-62A	254551	±0.5%	0 to 300 gal hr^{-1}
Watt meter	Pre-heater	Ohio Semitronics	GW5-10E	11031821	±0.2%	0 to 1,000 W
Watt meter	Post-heater	Ohio Semitronics	GW5-10E	11031822	±0.2%	0 to 1,000 W

T-type thermocouples. The water loop pressure at the pump outlet is measured with a Rosemount 2088 series absolute pressure transducer (uncertainty ±6.9 kPa). The water volumetric flow is measured using a turbine type flow meter (Omega, P/N: FTB-902/FLSC-62A) with an uncertainty of ±0.5% of reading. The water heater input power is not used in any calculations and not directly recorded in the experiments.

3.3.1 Data Acquisition System

Data are acquired with a National Instruments SCXI modular data acquisition system. The system consists of SCXI-1000 chassis containing a 32-channel thermocouple/voltage input module (SCXI-1102 with SCXI-1303 terminal block) and a 16-channel RTD input module (SCXI-1503 with SCXI-1306 terminal block). The thermocouple/voltage terminal block (SCXI-1303) features a built-in cold reference junction for use in thermocouple measurements, while the RTD terminal block (SCXI-1306) features inputs for differential input signals and current excitation signals. The chassis and its submodules are connected to a PC through a National Instruments 16-bit PCMCIA acquisition card (P/N: DAQCard-6036E). Signals are read and manipulated using National Instruments LabVIEW version 8.6. A graphical interface is developed in LabVIEW to monitor instantaneous values and trends in all measured parameters.

3.4 Experimental Procedure and Safety

Experiments are conducted with pure ammonia and zeotropic mixtures of ammonia and water (x_{bulk} = 0.80, 0.90 and > 0.96 of NH_3). The charging and test procedures are slightly different depending on the working fluid of interest. Due to the moderate toxicity of both fluids, special safety precautions are taken during system charging, operation, shutdown and storage.

3.4.1 Charging Procedure

Prior to charging with either a pure fluid or zeotropic mixture, a dry nitrogen pressure test is conducted to ensure system integrity. The system is pressurized to approximately 3,500 kPa and allowed to come to equilibrium before the pressure measurements are recorded. If the system pressure is constant for a minimum of 24 hours (accounting for small pressure variation due to fluctuations in the ambient temperature), it is deemed satisfactory and the charging process proceeds. However, if the system exhibits indications of a leak, a combination of visual bubbling soap film, ultrasonic detection, and R-134a vapor charge and leak detection (United Refrigerants Inc., Model 69336) is used to isolate the problem.

Air and residual water are then evacuated from the facility using a 3 CFM rotary vane vacuum pump (J.B. Industries, Model DV-85N), with the vacuum pressure monitored with an analog gauge (Thermal Engineering Company, Model 14571). Due to the presence of water (liquid at ambient conditions) in the zeotropic mixtures, care is taken to flush out the system with nitrogen when making system modifications, changing system concentrations or switching between pure component and mixtures. Despite these precautions, residual water can accumulate in system and then in the vacuum oil, increasing the oil vapor pressure and limiting the lowest achievable vacuum. Thus, it is sometimes necessary to change the vacuum pump oil during the system evacuation process. Once a vacuum pressure less than 300 micron of mercury (< 40 Pa) is achieved, the pump is shutoff and removed from the system.

For pure ammonia experiments, a tank of anhydrous ammonia is connected to the system as shown in to Figure 3.7. To ensure a liquid charge, the vertical orientation in

Figure 3.7a is used if the tank has a dip tube installed, while the inclined orientation in Figure 3.7b is used for tanks without a dip tube. Prior to charging, the chilled glycol-water and coupling water loops are turned on and set to a sub-ambient temperature. This lowers the temperature of the working fluid loop and assists in condensing saturated vapor, ensuring enough mass of NH_3 is introduced. Finally, a mass of 150 to 200 grams of NH_3 is charged into the system, measured with a Wey-TEK refrigerant charging scale (P/N: 713-202-G1).

For zeotropic NH_3/H_2O mixtures, the charging procedure is somewhat different. Because the saturation pressure at ambient temperature for water is much lower than that of ammonia (2.5 versus 886 kPa at T_{sat} = 21°C), the water is introduced first, followed by the ammonia charge. After completing the same leak testing and vacuum process as described above, a stainless steel distilled water charging vessel is connected to the system. The glycol-water and coupling water loops are again turned on and set to a sub-ambient temperature to condense introduced vapor and to remove the heat liberated by

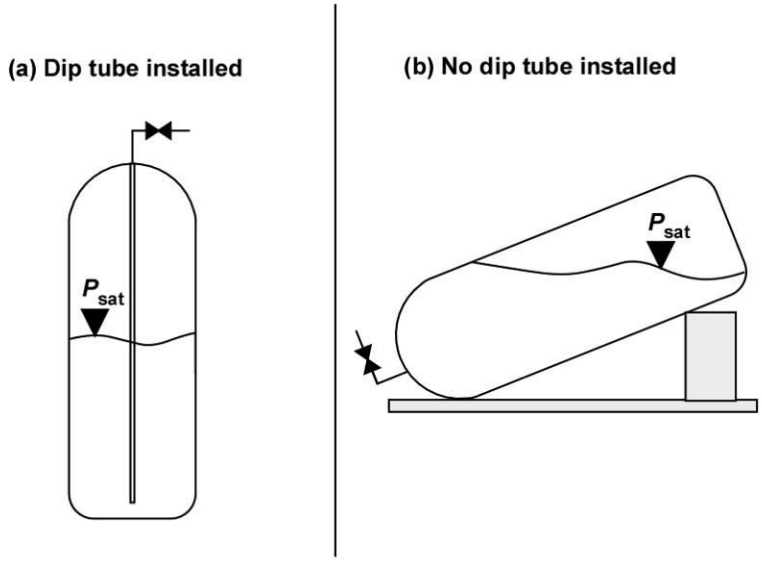

Figure 3.7: Schematic of charging procedure (a) with tank dip tube and (b) without dip tube installed

the mixing of water and ammonia. Then, depending on the desired bulk mass fraction, between 10 and 40 grams of liquid water are introduced into the system. The water tank is then removed and the ammonia cylinder attached as before (Figure 3.7). Finally, using the previously measured water mass charged, the required mass of ammonia is calculated from Eq. (3.1). As an example, for a desired bulk NH_3 mass fraction of $x_{bulk} = 0.80$, and an initial water charge of 40 g, the required ammonia mass charge is 160 g.

$$x_{bulk} = \frac{m_{NH_3}}{m_{NH_3} + m_{H_2O}} \tag{3.1}$$

3.4.2 Test Procedures

Prior to starting an experiment with either the pure fluid or zeotropic mixture, the presence of saturated liquid at the pump inlet is confirmed visually through inspection of the sight glass. The accumulator is fully opened to the system, and the glycol-water and closed water loops are both turned on and set to sub-ambient temperatures. As the system cools to sub-ambient temperatures, working fluid is drawn from the accumulator into the system. Once the glycol-water and closed water loop are operating stably, the working fluid pump is started. As the circulating working fluid temperature continues to decrease, more mass enters the working fluid loop, increasing the density and thus increasing the mass flow rate (for fixed speed positive displacement pump). Once an approximately steady state working fluid mass flow rate is achieved, the accumulator valves are closed and the coupling-water temperature is increased to the desired set point. Then, the pre- and post-heaters are energized and the power of each of them is increased in small increments (~ 5 W) until the desired test section inlet and post-heater outlet conditions is achieved. As additional power is added through the heaters, the system pressure tends to

increase. To maintain the system pressure, the operator can either 1) Meter working fluid mass into the accumulator, or 2) Decrease the set point of the chilled water-glycol solution. By controlling these two parameters, fine control over the system pressure is possible.

All data are reported in real-time in the LABView interface as instantaneous digital readouts and as graphs as a function of time. Once all values reach a constant value for a minimum of fifteen minutes, the system is assumed to be at steady state and data are captured at a rate of 100 Hz for a minimum period of five minutes. After the data capture is complete, a second set of data at the same conditions is obtained and compared with the first set to ensure that the system is truly stable. Each data point is then analyzed using *Engineering Equation Solver* software (Klein, 2012) to calculate the condensation heat duty, inlet and outlet quality, condensation heat transfer coefficient (for pure fluids), and to verify the bulk ammonia mass fraction (zeotropic mixtures). These analysis procedures are discussed in Chapter 4.

3.4.3 Safety Considerations

To mitigate concerns about working with ammonia and ammonia/water mixtures, several safety precautions are taken during system charging, operation, and storage. During charging, when the risk of a release of ammonia is greatest, the operator wears a full respirator that offers protection of the eyes, face and throat. The charged system is housed under a building chemical ventilation hood and surrounded by a sealed vinyl curtain at all times. The ventilation fan is run continuously, both during system operation and shutdown periods. This results in a negative pressure inside the sealed curtain area, directing any ammonia that may have leaked from the system to the outside of the

building through the vent and preventing it from entering the laboratory space. All system controls (valves, keypads, controllers, etc.) are accessible to the operator without having to open the curtain. Finally, when discharging the system, the ammonia or ammonia/water mixtures are vented into large volume containers of water, resulting in a dilute solution which could be safely disposed.

CHAPTER 4

DATA ANALYSIS

Condensation experiments on pure ammonia and zeotropic mixtures of ammonia and water were conducted at varying tube diameters, mass fluxes, saturation conditions and test section inlet quality using the approach described in the previous chapter. The nominal test matrices are shown in Tables 4.1 (ammonia) and 4.2 (zeotropic mixtures).

Using the measured temperatures, pressures, flow rates, and pre- and post-heater input power, several important parameters were calculated for the two fluid types. For ammonia, the following were determined from experimental measurements:

1. Inlet and outlet quality (q_{in}, q_{out})
2. Condensation heat duty ($\dot{Q}_{cond}$)
3. Average condensation heat transfer coefficient (α_{cond})
4. Frictional pressure gradient $(dP/dz)_f$

From the measured NH_3/H_2O variables, the following quantities were calculated:

1. Bulk ammonia mass fraction (x_{bulk})
2. Inlet and outlet quality (q_{in}, q_{out})
3. Condensation heat duty ($\dot{Q}_{cond}$)
4. Average *apparent* condensation heat transfer coefficient (α')

5. Frictional pressure gradient $(dP/dz)_f$

For both fluid categories, all data were analyzed using the *Engineering Equation Solver* (EES) platform (Klein, 2012). In addition, the uncertainties in each of the calculated parameters were determined using EES, assuming all measurements were uncorrelated and random (Taylor and Kuyatt, 1994). The heat transfer data analysis methods for pure ammonia are presented in Chapter 4.1, and those for zeotropic mixtures are presented in Chapter 4.2. A discussion of the frictional pressure gradient data analysis for both fluid types is presented in Chapter 4.3. Detailed discussions of the experimental results and uncertainties for ammonia and zeotropic mixtures are provided in Chapters 5 and 6, respectively.

Table 4.1: Matrix of ammonia experimental conditions

	Mass Flux (kg m^{-2} s^{-1})															
	75				**100**				**150**				**225**			
***D* (mm) / T_{sat} (°C)**	**30**	**40**	**50**	**60**	**30**	**40**	**50**	**60**	**30**	**40**	**50**	**60**	**30**	**40**	**50**	**60**
0.98 mm	X	X	X	X	X	X	X	X								
1.44 mm	X	X	X	X	X	X	X	X	X	X	X	X	X	X	X	X
2.16 mm	X		X	X	X	X	X	X								
	X = Data obtained															

Table 4.2: Matrix of ammonia/water experimental conditions

	Mass Flux (kg m^{-2} s^{-1})														
	50			**75**			**100**			**150**			**200**		
***D* (mm) / X_{bulk}**	**80**	**90**	**>96**	**80**	**90**	**>96**	**80**	**90**	**>96**	**80**	**90**	**>96**	**80**	**90**	**>96**
0.98 mm							X	X	X	X	X	X	X	X	X
1.44 mm				X	X	X	X	X	X	X	X	X	X	X	X
2.16 mm	X	X	X	X	X	X	X	X	X						
	X = Data obtained														

4.1 Pure Ammonia Data Analysis

In the ammonia analysis, the thermodynamic and transport properties of water, air, and ammonia were determined using thermophysical property functions embedded in the EES platform. For air, the thermodynamic properties were calculated from the equation of state of Lemmon *et al.* (2000), and the transport properties from correlations in Lemmon and Jacobsen (2004). Water properties were obtained using the *1995 Formulation for the Thermodynamic Properties of Ordinary Water Substances for General and Scientific Use*, issued by the International Association for the Properties of Water and Steam (IAPWS). For ammonia, the thermodynamic properties were determined from the

Table 4.3: Sample ammonia data point measured parameters

	Nominal Condition
Test Number	143
ID_i (mm)	1.44
OD_i (mm)	1.651
G (kg m^{-2} s^{-1})	150
T_{sat} (°C)	40
	Measured Value
T_1 (°C)	26.2
T_2 (°C)	40.4
T_3 (°C)	40.1
T_4 (°C)	53.7
$T_{w,in}$ (°C)	37.5
$T_{w,out}$ (°C)	37.3
T_{amb} (°C)	29.1
P_1 (kPa)	1570
P_2 (kPa)	1569
P_3 (kPa)	1561
P_4 (kPa)	1563
ΔP (kPa)	8.08
$\dot{m}$ (g min^{-1})	14.8
$\dot{Q}_{pre}$ (W)	142
$\dot{Q}_{post}$ (W)	204
$\dot{V}_{water}$ (gal hr^{-1})	72.4

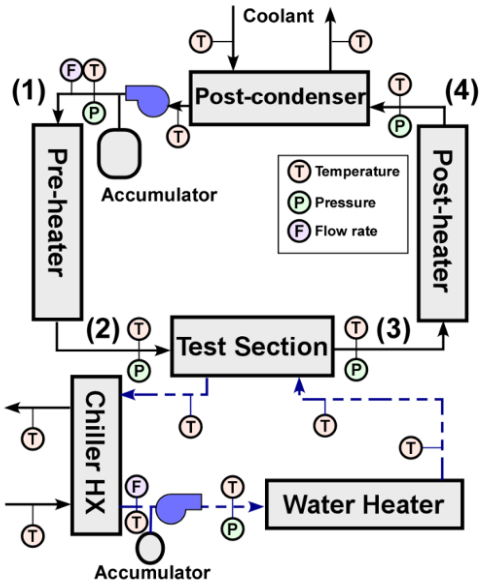

Figure 4.1: Experimental facility schematic

equation of state of Tilner-Roth *et al.* (1993), the viscosity from Fenghour, *et al.* (1995), the thermal conductivity from a modified version of the Tufeu *et al.* (1984) correlation, and the surface tension from Yaws (1999).

In the following sections, the basic analysis method for determining test section average quality, condensation heat duty, average condensation heat transfer coefficient, and the associated uncertainty in each of these quantities is presented. For illustrative purposes, an analysis of a sample data point at the conditions shown in Table 4.3 is presented along with the calculation procedure. A detailed step-by-step sample calculation for pure ammonia using this sample point is presented in Appendix A.

4.1.1 Ammonia Average Quality and Condensation Heat Duty

For reference, the test facility schematic is shown in Figure 4.1.

Starting at state **1**, the measured temperature and pressure were used to determine the specific enthalpy of the subcooled ammonia.

$$h_1 = f\left(T_1, P_1\right) = f\left(26.15\ ^{\circ}\text{C}, 1570\ \text{kPa}\right) = 323.4 \pm 0.95\ \text{kJ kg}^{-1} \tag{4.1}$$

In the pre-heater, electric power (Table 4.3) was added to the system, yielding a two-phase mixture at state **2**. From an energy balance on the pre-heater assembly, the specific enthalpy at the pre-heater outlet (h_2) was determined:

$$\begin{aligned} h_2 &= h_1 + \frac{\left(\dot{Q}_{\text{pre}} - \dot{Q}_{\text{pre,loss}}\right)}{\dot{m}} \\ 898 \pm 2.1\ \text{kJ kg}^{-1} &= 323\ \text{kJ kg}^{-1} + \frac{\left(142 - 0.2\right)\text{W}}{2.47 \cdot 10^{-4}\ \text{kg s}^{-1}} \end{aligned} \tag{4.2}$$

The energy balance in Eq. (4.2) includes an ambient heat loss term, $\dot{Q}_{\text{pre,loss}}$. Details for calculating the pre-and post-heater ambient heat losses are discussed in the following section. With h_2 and P_2 (measured) known, the test section inlet quality (q_2) was found as follows:

$$q_2 = f\left(h_2, P_2\right) = f\left(898\ \text{kJ kg}^{-1}, 1569\ \text{kPa}\right) = 0.46 \pm 0.002 \tag{4.3}$$

The ammonia then entered the test section and was partially condensed to state **3**. Here, the thermodynamic state was indeterminate with only the measured saturated temperature and pressure. Thus, the fluid was then evaporated in the post-heater to a superheated state **4**, with 10 to 20 K of superheat, depending on the specific test condition. Using the measured T_4 and P_4 of the superheated vapor, the specific enthalpy was determined as follows:

$$h_4 = f\left(T_4, P_4\right) = f\left(53.65\ ^{\circ}\text{C}, 1563\ \text{kPa}\right) = 1534 \pm 0.64\ \text{kJ kg}^{-1} \tag{4.4}$$

The specific enthalpy at state **3** was then determined from an energy balance on the post-heater (Eq. (4.5)). The test section outlet quality was determined from the calculated h3 and measured P3 (Eq. (4.6)).

$$h_3 = h_4 - \frac{\left(\dot{Q}_{\text{post}} - \dot{Q}_{\text{post,loss}}\right)}{\dot{m}}$$
$$710 \pm 3.2 \text{ kJ kg}^{-1} = 1534 \text{ kJ kg}^{-1} - \frac{(204 - 0.85)\text{ W}}{2.47 \cdot 10^{-4} \text{ kg s}^{-1}} \tag{4.5}$$

$$q_3 = f\left(h_3, P_3\right) = f\left(710 \text{ kJ kg}^{-1}, 1561 \text{ kPa}\right) = 0.29 \pm 0.003 \tag{4.6}$$

Finally, with the specific enthalpy at the test section inlet and outlet (h_2 and h_3) known, the condensation heat duty and the average quality were determined from Eqs. (4.7) and (4.8), respectively.

$$\dot{Q}_{\text{cond}} = \dot{m}\left(h_2 - h_3\right)$$
$$46.4 \pm 1.1 \text{ W} = \left(2.47 \cdot 10^{-4} \text{ kg s}^{-1}\right)\left(898.3 \text{ kJ kg}^{-1} - 710 \text{ kJ kg}^{-1}\right) \tag{4.7}$$

$$q_{\text{avg}} = \frac{q_2 + q_3}{2}$$
$$0.38 \pm 0.001 = \frac{0.46 + 0.29}{2} \tag{4.8}$$

For this sample point, the uncertainty in the condensation heat duty was less than 2.4% of the measured value. In general, the largest contribution to the uncertainty in the calculated condensation heat duty was the uncertainty in the measured mass flow rate, and the pre- and post-heater electric power. A complete summary of the procedure for calculating the thermodynamic states, condensation heat duty and average quality is

provided in Appendix A.1. Details of the uncertainty propagation analysis in calculating the ammonia condensation heat duty are presented in Appendix B.1.

4.1.2 Ambient Heat Loss/Gains

For determining the heat losses/gains, the coupled conduction, natural convection and radiation loss mechanisms (Eq. (4.9)) from the heater assemblies were considered. A schematic of the thermal resistance diagram used is shown in Figure 4.2.

$$\dot{Q}_{\text{pre,loss}} = \frac{T_{\text{pre,avg}} - T_{\text{amb}}}{R_{\text{tot}}}$$
$$0.2\ \text{W} = \frac{(33.27 - 29.1)\ ^{\circ}\text{C}}{21.28\ ^{\circ}\text{C W}^{-1}} \tag{4.9}$$

Here, $T_{\text{pre,avg}}$ is the average of the pre-heater ammonia inlet (T_1) and outlet temperature (T_2), and T_{amb} is the measured ambient temperature inside the safety shield area. As shown in Figure 4.2, the total thermal resistance (R_{tot}) consisted of the refrigerant convective resistance (R_{ref}), the heater assembly wall conduction resistance ($R_{\text{assy,wall}}$ Eq. (4.10)), heater assembly insulation conduction resistance (R_{ins}, Eq. (4.11)), and the

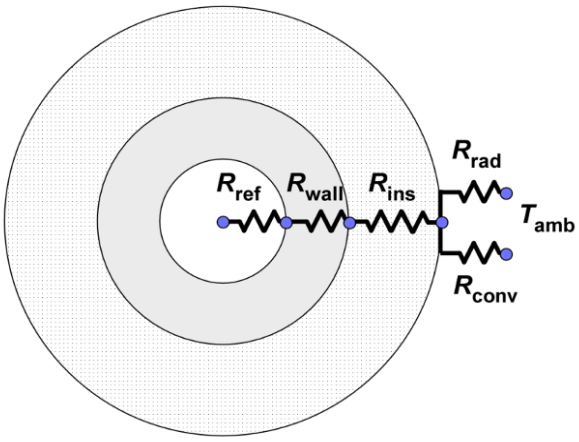

Figure 4.2: Resistance network for pre- and post-heater ambient heat loss analysis

parallel natural convection ($R_{assy,conv}$) and radiation ($R_{assy,rad}$) resistances (Eq. (4.12)) from the insulation surface. A constant refrigerant heat transfer coefficient of 10,000 W m^{-2} K^{-1} was assumed in calculating R_{ref}, which was insignificant compared to the other thermal resistances (*e.g.*, R_{ref} = 0.01 K W^{-1} versus R_{ins} = 18.29 K W^{-1}). The assembly wall and insulation conduction resistances were calculated using the standard approach for hollow cylinders:

$$R_{assy,wall} = \frac{\ln\left(OD_{assy}/ID_{assy}\right)}{2\pi L_{eff} k_{assy}}$$
$$0.047 \text{ K W}^{-1} = \frac{\ln\left(0.0381 \text{ m}/0.01786 \text{ m}\right)}{2\pi\left(0.1715 \text{ m}\right)\left(14.94 \text{ W m}^{-1} \text{ K}^{-1}\right)} \quad (4.10)$$

$$R_{ins} = \frac{\ln\left(\left[OD_{assy} + 2t_{ins}\right]/OD_{assy}\right)}{2\pi L_{eff} k_{ins}}$$
$$18.29 \text{ K W}^{-1} = \frac{\ln\left(\left[0.0381 \text{ m} + 2\cdot 0.025 \text{ m}\right]/0.0381 \text{ m}\right)}{2\pi\left(0.1715 \text{ m}\right)\left(0.043 \text{ W m}^{-1} \text{ K}^{-1}\right)} \quad (4.11)$$

Here, L_{eff} is the heat loss length between the temperature and pressure measurements at the heater assembly inlet and outlet. The other required geometric parameters of the heater assembly and insulation were presented in Chapter 3. The thermal conductivity of the stainless steel heater assembly and the fiberglass insulation were evaluated at the ambient temperature. At the surface, the natural convection and radiation thermal resistances were considered in parallel:

$$R_{\text{assy,surf}} = \left(\frac{1}{R_{\text{assy,conv}}} + \frac{1}{R_{\text{assy,rad}}} \right)^{-1}$$
$$2.93 \text{ K W}^{-1} = \left(\frac{1}{11.67 \text{ K W}^{-1}} + \frac{1}{3.91 \text{ K W}^{-1}} \right)^{-1} \quad (4.12)$$

Here, the natural convection from the surface was determined from the Churchill and Chu (1975) correlation for natural convection from a horizontal cylinder, and the radiation heat transfer coefficient was determined assuming an insulation emissivity of 0.8. Both the radiation and natural convective heat transfer coefficients were functions of the insulation surface temperature. This required that Eqs. (4.9) through (4.12) be solved in an iterative manner for each data point.

A conservative uncertainty of ±50% was assigned to the final calculated heat loss/gain. For pure ammonia, the calculated losses were very small (< 1% of condensation heat duty), with greater losses observed at higher saturation temperatures. For zeotropic mixtures, where the fluid operating temperature could be much higher than the ambient (ΔT > 100 K), the heat losses were of greater importance. A detailed, step-by-step calculation procedure for the ambient heat/loss gains is presented in Appendix A.2.

4.1.3 Ammonia Condensation Heat Transfer Coefficient

Once the ammonia condensation heat duty was calculated, the next step was to find the average condensation heat transfer coefficient using the UA-LMTD approach (Eq. (4.13)).

$$\dot{Q}_{\text{cond}} = UA \cdot \Delta T_{\text{LM}} \quad (4.13)$$

Table 4.4: Comparison of uncertainty of measured and calculated test section inlet and outlet temperatures

Nominal T_{sat} (°C)	P_{sat} (kPa)	Uncertainty of measured T	Uncertainty of calculated T
30	1167 ± 2.625	± 0.2 °C	± 0.076 °C
40	1555 ± 2.625	± 0.2 °C	± 0.061 °C
50	2033 ± 2.625	± 0.2 °C	± 0.050 °C
60	2614 ± 2.625	± 0.2 °C	±0.041 °C

The log-mean temperature difference (Eq. (4.14)) was calculated using the measured water inlet and outlet temperatures, and the saturated inlet and outlet ammonia temperatures calculated from the measured pressures (P_2 and P_3). The water-side flow rate was sufficiently high such that the change in measured water temperature was very small, for most cases, less than the experimental uncertainty. For the working fluid side, the calculated saturation temperature was used as it had a lower uncertainty than the measured temperature, as shown in Table 4.4.

As a check, the calculated $T_{sat}(P)$ and measured T were compared for each datapoint. For the sample point, the difference between the calculated and measured temperature was 0.08 and -0.07 K at the test section inlet and outlet, respectively. Both of these are within the experimental uncertainty, indicating good measurements and the absence of contaminants and noncondensables in the ammonia.

$$\Delta T_{LM} = \frac{\left[T_{sat}\left(P_2\right) - T_{w,o}\right] - \left[T_{sat}\left(P_3\right) - T_{w,i}\right]}{\ln\left[\frac{T_{sat}\left(P_2\right) - T_{w,o}}{T_{sat}\left(P_3\right) - T_{w,i}}\right]}$$
$$2.8 \pm 0.15 \text{ K} = \frac{\left[40.3 - 37.3\right] - \left[40.1 - 37.5\right]}{\ln\left[\frac{40.3 - 37.3}{40.1 - 37.5}\right]} \quad (4.14)$$

Using the calculated condensation heat duty and the log-mean temperature difference, the *UA*, or overall heat transfer conductance was calculated as follows:

$$UA = \frac{\dot{Q}_{\text{cond}}}{\Delta T_{\text{LM}}}$$
$$16.47 \pm 0.9 \text{ W K}^{-1} = \frac{46.43 \text{ W}}{2.8 \text{ K}} \tag{4.15}$$

The overall heat transfer conductance in the test section was an aggregate of the condensation (R_{cond}), tube wall (R_{wall}), and water (R_{water}) thermal resistances:

$$UA = \frac{1}{R_{\text{cond}} + R_{\text{wall}} + R_{\text{water}}} \tag{4.16}$$

By calculating the wall and water-side thermal resistances, the condensation thermal resistance and heat transfer coefficient was deduced. In Eq. (4.16), R_{wall} is the standard hollow cylinder resistance:

$$R_{\text{wall}} = \frac{\ln\left(\frac{\text{OD}_{\text{i}}}{\text{ID}_{\text{i}}}\right)}{2 \cdot \pi \cdot \left(L_{\text{ann}} + 2 \cdot L_{\text{red}}\right) \cdot k_{\text{wall}}}$$
$$R_{\text{wall}} = 0.006 \text{ K W}^{-1} \tag{4.17}$$

As shown in Figure 4.3, the water-side resistance was the composite of the resistance in the regions of forced (R_{ann}) convection in the annulus, and free convection (R_{red}) in the reducer sections.

$$\frac{1}{R_{\text{water}}} = \frac{1}{R_{\text{ann}}} + 2\frac{1}{R_{\text{red}}} \tag{4.18}$$

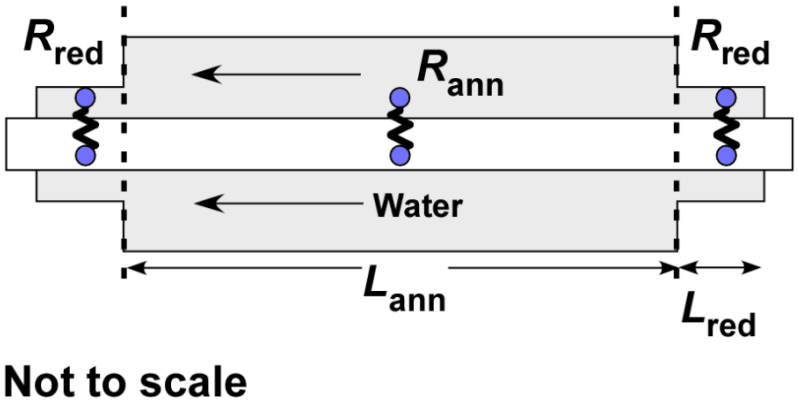

Figure 4.3: Schematic of parallel water-side thermal resistance in condensation test section

The heat transfer coefficient in the annulus was calculated from curve fits by Garimella and Christensen (1995) for the laminar and turbulent Nusselt numbers in annuli that were originally proposed by Kays and Leung (1963). The average water-side heat transfer coefficient for the D = 0.98, 1.44 and 2.16 mm test sections were 42.6, 46.7, and 49.0 kW m^{-2} K^{-1}, respectively. The primary difference in water-side heat transfer can be attributed to the changing annulus hydraulic diameter and water-side flow rate for the different tubes. For calculating the uncertainty in the condensation heat transfer coefficient, a conservative ±25% uncertainty was assigned to the annulus heat transfer coefficient. The annulus thermal resistance was then calculated from the following equation:

$$R_{ann} = \frac{1}{\alpha_{ann} \cdot \pi \cdot L_{ann} \cdot OD_i}$$

$$0.017 \text{ K W}^{-1} = \frac{1}{\left(45{,}311 \text{ W m}^{-2} \text{ K}^{-1}\right) \cdot \pi \cdot \left(0.2489 \text{ m}\right) \cdot \left(0.00165 \text{ m}\right)} \tag{4.19}$$

In the reducer section, the heat transfer coefficient was calculated using the correlation reported in Incropera and Dewitt (2002) for natural convection between two

horizontal, concentric cylinders (*i.e.*, the test section and the reducer). The correlation defined an expression for the effective thermal conductivity for the gap between the two cylinders as a function of the modified Rayleigh number (*Ra**, Eq. (4.20)) and the water Prandtl number. For *Ra** < 100, the problem was conduction dominated and k_{eff} was equal to the thermal conductivity of water.

$$Ra^* = \frac{\ln\left(\frac{D_{red}}{OD_i}\right)}{\left(OD_i^{-3/5} + D_{red}^{-3/5}\right)^5} \cdot \frac{Ra_L}{L_{red}^3} \tag{4.20}$$

For all data in the present study, *Ra** << 100 and $k_{eff} = k_{water}$, resulting in the reducer thermal resistance shown in Eq. (4.21).

$$\begin{aligned} R_{red} &= \frac{\ln\left(\frac{ID_{red}}{OD_i}\right)}{2 \cdot \pi \cdot L_{red} \cdot k_{eff}} \\ 4.9 \text{ K W}^{-1} &= \frac{\ln\left(\frac{2 \text{ mm}}{1.651 \text{ mm}}\right)}{2 \cdot \pi \cdot (0.009 \text{ m}) \cdot \left(0.63 \text{ W m}^{-1} \text{ K}^{-1}\right)} \end{aligned} \tag{4.21}$$

Using the calculated annulus and reducer resistances, the heat duty through the annulus portion is found to be 43.8 W (94% of total heat duty), with 2.6 W total transferred through the two reducer sections. The total water-side resistance was then calculated by considering the annulus and reducer thermal resistances in parallel, as defined in Eq. (4.22). For the sample data point, the water-side thermal resistance was 0.0169 ± 0.004 K W^{-1}. By maintaining a low water-side thermal resistance, the condensation thermal resistance was dominant, and was calculated from the following:

$$R_{\text{cond}} = \frac{\Delta T_{\text{LM}}}{\dot{Q}_{\text{cond}}} - R_{\text{wall}} - R_{\text{water}}$$
$$0.038 \pm 0.005 \text{ K W}^{-1} = \frac{2.8 \text{ K}}{46.4 \text{ W}} - \left(0.006 \text{ K W}^{-1}\right) - \left(0.0169 \text{ K W}^{-1}\right) \tag{4.22}$$

For the sample point, the resistance ratio ($R_{\text{cond}}/(R_{\text{water}} + R_{\text{wall}})$) is 1.7, ensuring that the condensation resistance dominates the heat transfer process. Thus, the condensation heat transfer coefficient was determined from the condensation thermal resistance, and the geometry of the test section:

$$\alpha_{\text{cond}} = \frac{1}{R_{\text{cond}} \cdot \pi \cdot \left(L_{\text{HT}} + 2L_{\text{red}}\right) \cdot D}$$
$$21{,}911 \pm 3{,}222 \text{ W m}^{-2} \text{ K}^{-1} = \frac{1}{\left(0.0376 \text{ K W}^{-1}\right) \cdot \pi \cdot \left(0.249 \text{ m} + 2 \cdot 0.009 \text{ m}\right) \cdot \left(0.00144 \text{ m}\right)} \tag{4.23}$$

Here, the uncertainty in the calculated condensation heat transfer coefficient was ±14.7% of the calculated value. The average uncertainties for the 0.98, 1.44, and 2.16 mm test sections were ±8.9%, ±15%, and ±20%, respectively. The primary contribution to the condensation heat transfer uncertainty was the ±25% uncertainty in the water-side heat transfer coefficient. A detailed, step-by-step calculation procedure for the condensation heat transfer coefficient is presented in Appendix A.3, and a detailed uncertainty propagation analysis of the average heat transfer coefficient in Appendix B.2.

4.2 Zeotropic Ammonia/Water Heat Transfer Analysis

The general data analysis procedure for the zeotropic ammonia/water mixtures is similar to that for pure ammonia, with some modifications to account for the mixture thermodynamics. Unlike pure ammonia, where the thermodynamic state could be fixed with two, independent, intensive properties, the binary mixture required a third property

(*i.e.*, bulk ammonia mass fraction) to completely define the thermodynamic state. Thermodynamic properties of the NH_3/H_2O mixtures were obtained from the correlations of Ibrahim and Klein (1993), while the vapor and liquid transport properties were from the correlations of Meacham (2002). The following section reviews the data analysis procedure for determining bulk ammonia mass fraction, test section average quality, condensation heat duty, apparent heat transfer coefficient, and the associated uncertainties of each. These equations are evaluated for a sample point corresponding to the test conditions shown in Table 4.5.

4.1.1 Mixture Concentration Verification

The first step in the mixture data analysis procedure was to verify the bulk mass fraction of ammonia. During charging, the masses of water and ammonia introduced into the system were measured, allowing the global system level mass fraction to be calculated. During operation, fluid was metered in and out of the rigid accumulator to maintain a constant saturation pressure, which could lead to small variations in the actual circulating mass fraction. Thus, the bulk mass fraction of ammonia for each data point was calculated from an energy balance on the pre- and post-heater assemblies:

$$\begin{gathered}\dot{Q}_{\text{pre}} - \dot{Q}_{\text{pre,loss}} = \dot{m}\left[h_2\left(T_2, P_2, x_{\text{bulk,pre}}\right) - h_1\left(T_1, P_1, x_{\text{bulk,pre}}\right)\right] \\ 219\text{ W} - 1.7\text{ W} = 1.58\cdot 10^{-4}\text{ kg s}^{-1}\left[h_2\left(101\text{ °C}, 1510\text{ kPa}, x_{\text{bulk,pre}}\right) - h_1\left(26.1\text{ °C}, 1510\text{ kPa}, x_{\text{bulk,pre}}\right)\right] \\ x_{\text{bulk,pre}} = 0.92 \pm 0.005\end{gathered} \tag{4.24}$$

$$\begin{gathered}\dot{Q}_{\text{post}} - \dot{Q}_{\text{post,loss}} = \dot{m}\left[h_4\left(T_4, P_4, x_{\text{bulk,post}}\right) - h_3\left(T_3, P_3, x_{\text{bulk,post}}\right)\right] \\ 113\text{ W} - 3.6\text{ W} = 1.58\cdot 10^{-4}\text{ kg s}^{-1}\left[h_4\left(146\text{ °C}, 1507\text{ kPa}, x_{\text{bulk,post}}\right) - h_3\left(57.4\text{ °C}, 1505\text{ kPa}, x_{\text{bulk,post}}\right)\right] \\ x_{\text{bulk,post}} = 0.91 \pm 0.002\end{gathered} \tag{4.25}$$

Table 4.5: Sample ammonia/water data point measured parameters

	Nominal Condition
Test Number	501
ID_i (mm)	1.44
OD_i (mm)	1.651
X_{bulk}	0.90
G (kg m^{-2} s^{-1})	100
P_{sat} (kPa)	1500
	Measured Value
T_1 (°C)	26.1
T_2 (°C)	101
T_3 (°C)	57.4
T_4 (°C)	146
$T_{w,in}$ (°C)	47.9
$T_{w,out}$ (°C)	48.4
T_{amb} (°C)	28.4
P_1 (kPa)	1510
P_2 (kPa)	1510
P_3 (kPa)	1507
P_4 (kPa)	1505
ΔP (kPa)	5.6
$\dot{m}$ (g min^{-1})	9.5
$\dot{Q}_{pre}$ (W)	219
$\dot{Q}_{post}$ (W)	113
$\dot{V}_{water}$ (gal hr^{-1})	74

In Eqs. (4.24) and (4.25), the temperatures, pressures, heater input power and mass flow rates were measured quantities. Heat losses from the pre- and post-heater assembly were calculated using the procedure described above (Section 4.1.2, Eqs. (4.9) - (4.12)). Thus, the only unknown in the two equations was the bulk mass fraction. For the sample point, the difference in the calculated mass fraction from the inlet to the outlet was 1.8%. For the remaining data analysis procedures in this section, the mass fraction calculated from the *post-heater* energy balance was used. The reason for this was that the average quality at the post-heater inlet (q_3) is lower for all data points than at the pre-heater outlet (q_2), because the fluid has been partially condensed. At higher qualities, the

slope of the temperature versus quality and/or mass fraction curve is very large. Thus, small errors in temperature measurement can yield large swings in calculated mass fraction. Therefore, the mass fraction calculated from the post-heater resulted in lower uncertainties. As a check on the quality of the data, the inlet and outlet calculated mass fractions were compared for every data point, with an average difference of less than 5%. A step-by-step calculation of the bulk mass fraction for the sample point is provided in Appendix A.4.

4.2.2 Mixture Average Quality and Condensation Heat Duty

Similar to pure ammonia, the test section inlet and outlet quality, and condensation heat duty were calculated from energy balances on the pre-heater, post-heater and test section itself. For reference, the state points referred to in this section correspond to the test section schematic shown previously in Figure 4.1. At state **1**, the enthalpy of the subcooled zeotropic mixture is found from the measured temperature, pressure and calculated bulk ammonia mass fraction (from Eq. (4.25)):

$$h_1 = f\left(T_1, P_1, x_{\text{bulk}}\right) = f\left(26.1\ ^{\circ}\text{C}, 1510\ \text{kPa}, 0.91\right) = 54.69 \pm 1.96\ \text{kJ kg}^{-1} \qquad (4.26)$$

The mixture was then partially evaporated in the pre-heater to state **2**, where the enthalpy was found from an energy balance:

$$h_2 = h_1 + \frac{\left(\dot{Q}_{\text{pre}} - \dot{Q}_{\text{pre,loss}}\right)}{\dot{m}}$$
$$1427 \pm 5.7\ \text{kJ kg}^{-1} = 54.7\ \text{kJ kg}^{-1} + \frac{\left(219 - 1.7\right)\text{W}}{1.58 \cdot 10^{-4}\ \text{kg s}^{-1}} \qquad (4.27)$$

Unlike a pure fluid, the specific enthalpy at state **2** could also be calculated as a function of the measured temperature, pressure and the calculated bulk mass fraction. For the sample point, the enthalpy calculated in this manner was 1399 ± 5.8 kJ kg^{-1}, a difference of -2%. The uncertainties of the two methods for the sample are comparable, with the enthalpy calculated from the energy balance method slightly better. However, at low qualities, where the change in temperature from the pre-heater inlet to outlet is much smaller (< 1 K), the uncertainty becomes greater for the enthalpy calculated from measured T, P, and x_{bulk}. Thus, the energy balance method in Eq. (4.27) was used for all zeotropic mixture data.

The quality at state **2** was then calculated from the measured pressure, calculated enthalpy and bulk mass fraction of ammonia:

$$q_2 = f\left(h_2, P_2, x_{\text{bulk}}\right) = f\left(1427 \text{ kJ kg}^{-1}, 1510 \text{ kPa}, 0.91\right) = 0.92 \pm 0.0018 \qquad (4.28)$$

The mixture was partially condensed in the test section and then heated in the post-heater, where the specific enthalpy at the outlet (h_4) was determined from the measured temperature, pressure and bulk concentration. Using the same energy balance as in the pure ammonia experiments, the specific enthalpy at state **3** (Eq. (4.29)), and then the condensation heat duty (Eq. (4.30)) were calculated as follows:

$$\begin{aligned} h_3 &= h_4 - \frac{\left(\dot{Q}_{\text{post}} - \dot{Q}_{\text{post,loss}}\right)}{\dot{m}} \\ 996 \pm 9 \text{ kJ kg}^{-1} &= 1690 \text{ kJ kg}^{-1} - \frac{\left(113.4 - 3.6\right)\text{W}}{1.58 \cdot 10^{-4} \text{ kg s}^{-1}} \end{aligned} \qquad (4.29)$$

$$\dot{Q}_{\text{cond}} = \dot{m}\left(h_2 - h_3\right)$$
$$68.2 \pm 2.1 \text{ W} = \left(1.583 \cdot 10^{-4} \text{ kg s}^{-1}\right)\left(1427 \text{ kJ kg}^{-1} - 996 \text{ kJ kg}^{-1}\right) \quad (4.30)$$

Using this method, the average uncertainty in the condensation heat duty for all data was ±4.15%. The primary contribution to the uncertainty in condensation heat duty was the uncertainty in the pre- and post-heater heat loss terms. The heat loss contributions were more significant for the zeotropic mixtures compared with those for pure ammonia, due to the much higher temperatures (> 100 °C for some points). A step-by-step calculation of the concentration for the sample point is provided in Appendix A.5 and an uncertainty propagation analysis in Appendix B.4.

4.2.3 Apparent Heat Transfer Coefficient

The final mixture parameter of interest was the apparent heat transfer coefficient (α'). Recall from Chapter 2 that because it is not possible to directly measure the interface temperature, the apparent heat transfer coefficient is defined using the mixture equilibrium temperature:

$$\alpha' = \frac{q''}{\left(T_{\text{eq}} - T_{\text{w,i}}\right)} \quad (4.31)$$

The apparent heat transfer coefficient is an aggregate of the coupled heat and mass transfer resistances, and is less useful from a fundamental modeling perspective. However, it is a useful metric for illustrating the degradation in heat transfer due to mixture effects. In the present experiments, the average apparent heat transfer coefficient was calculated from the UA-LMTD method, as above (Eq. (4.13)). The log-mean temperature difference was defined as:

$$\Delta T_{\mathrm{LM}} = \frac{\left[T_2\left(P_2, h_2, x_{\mathrm{bulk}}\right) - T_{\mathrm{w,o}}\right] - \left[T_3\left(P_3, h_3, x_{\mathrm{bulk}}\right) - T_{\mathrm{w,i}}\right]}{\ln\left[\dfrac{T_2\left(P_2, h_2, x_{\mathrm{bulk}}\right) - T_{\mathrm{w,o}}}{T_3\left(P_3, h_3, x_{\mathrm{bulk}}\right) - T_{\mathrm{w,i}}}\right]}$$
$$49.4\ \mathrm{K} = \frac{\left[103.1 - 47.8\right] - \left[91.8 - 47.5\right]}{\ln\left[\dfrac{103.1 - 47.8}{91.8 - 47.5}\right]} \tag{4.32}$$

Here, the mixture inlet and outlet temperatures were the equilibrium temperatures at the measured pressure, specific enthalpy and bulk ammonia mass fraction. The water inlet and outlet temperatures were the measured values. The mixture *UA* value was then calculated as:

$$UA = \frac{\dot{Q}_{\mathrm{cond}}}{\Delta T_{\mathrm{LM}}}$$
$$1.38\ \mathrm{W\ K^{-1}} = \frac{68.2\ \mathrm{W}}{49.4\ \mathrm{K}} \tag{4.33}$$

The mixture apparent thermal resistance was then found from the following:

$$R_{\mathrm{cond}} = \frac{\Delta T_{\mathrm{LM}}}{\dot{Q}_{\mathrm{cond}}} - R_{\mathrm{wall}} - R_{\mathrm{water}}$$
$$0.683\ \mathrm{K\ W^{-1}} = \frac{49.4\ \mathrm{K}}{68.2\ \mathrm{W}} - \left(0.011\ \mathrm{K\ W^{-1}}\right) - \left(0.030\ \mathrm{K\ W^{-1}}\right) \tag{4.34}$$

Here, R_{wall} and R_{water} were calculated in the same manner as in the pure ammonia analysis (Eqs. (4.17)-(4.21)). Finally, the mixture apparent heat transfer coefficient was calculated from R_{cond} and the geometry of the test section:

$$\alpha' = \frac{1}{R_{cond} \cdot \pi \cdot \left(L_{HT} + 2L_{red}\right) \cdot D}$$

$$2,231\ \text{W m}^{-2}\ \text{K}^{-1} = \frac{1}{\left(0.6833\ \text{K W}^{-1}\right) \cdot \pi \cdot \left(0.127\ \text{m} + 2 \cdot 0.009\ \text{m}\right) \cdot \left(0.00144\,\text{m}\right)} \tag{4.35}$$

4.3 Ammonia and Zeotropic Mixture Frictional Pressure Gradient Analysis

The final parameter of interest for both fluid types was the frictional pressure gradient. The measured pressure drop was a function of the frictional pressure drop, pressure change due to flow contractions and expansions at the test section inlet and outlet, and the pressure rise due to the changing momentum of the condensing flow:

$$\Delta P_{measured} = \Delta P_{fric} + \Delta P_{inlet} + \Delta P_{outlet} + \Delta P_{deceleration} \tag{4.36}$$

Thus, to isolate the frictional component, it is necessary to calculate the other parameters. The sample data point of pure ammonia detailed in Table 4.3 is used to illustrate the pressure gradient analysis procedure in this section. As shown in Figure 4.4, there were three flow contractions (labeled A, B, and C) at the test section inlet. At the outlet, the fluid expanded through the same geometry in the reverse order (*i.e.*, C→B→A). The diameter of each cross sectional area for the three different test sections is given in Table 4.6.

The three contraction losses at the test section inlet were calculated from the approach proposed by Hewitt *et al.* (1994):

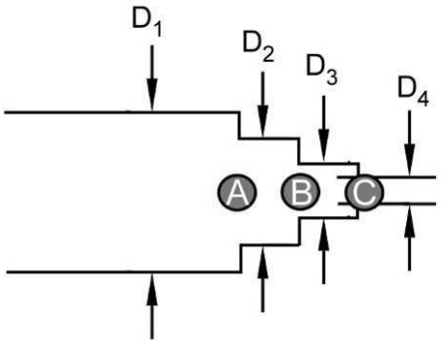

Figure 4.4: Schematic of test section inlet area contractions

Table 4.6: Expansion/contraction diameters for each test section

	Test Section Diameter (mm)		
	0.98	**1.44**	**2.16**
***D*1 (mm)**	17.8	17.8	17.8
***D*2 (mm)**	8.8	8.8	8.8
***D*3 (mm)**	3.2	3.2	3.2
***D*4 (mm)**	0.98	1.44	2.16

$$\Delta P_{\text{contraction}} = \frac{G^2}{\rho_{\text{L}}}\left(1 - A_{\text{ratio}}^2 + \left[\frac{1}{C_{\text{c}}} - 1\right]^2\right)\psi_{\text{H}}$$

where (4.37)

$$C_{\text{C}} = \frac{1}{0.639\left[1 - A_{\text{ratio}}\right]^{1/2} + 1}$$

$$\psi_{\text{H}} = 1 + \left(\frac{\rho_{\text{L}}}{\rho_{\text{V}}} - 1\right)q$$

Here, A_{ratio} is the ratio of the smaller area to the larger area, C_{C} is the contraction coefficient and ψ_{H} is the homogenous multiplier. The quality and liquid/vapor densities were evaluated at the pre-heater outlet. Using this approach, the calculated losses for each contraction are given below:

$$\begin{aligned} \Delta P_{\text{cont,A}} &= 0.41 \text{ Pa} \\ \Delta P_{\text{cont,B}} &= 24.5 \text{ Pa} \\ \Delta P_{\text{cont,C}} &= 581 \text{ Pa} \end{aligned} \tag{4.38}$$

Here, a positive value indicates a decrease in absolute pressure. Thus, the total inlet pressure drop due to minor losses was 0.605 kPa, or 7.5% of the measured pressure drop (8.08 kPa).

At the outlet of the test section, three flow expansions in series occur, from the test section to the reducer coupling (**C**, in Figure 4.4), from the reducer to a NPT coupling bushing (**B**), and from the bushing to the heater assembly (**A**), as shown previously in Figure 4.4. Each loss was modeled with the following equation suggested by Hewitt *et al.* (1994):

$$\Delta P_{\text{exp}} = -\frac{G^2 A_{\text{ratio}} \left(1 - A_{\text{ratio}}\right) \psi_{\text{s}}}{\rho_{\text{L}}}$$

where

$$\psi_{\text{s}} = 1 + \left(\frac{\rho_{\text{L}}}{\rho_{\text{V}}} - 1 \right) \left[0.25 \cdot q \left(1 - q\right) + q^2 \right] \tag{4.39}$$

Here, the A_{ratio} is the same as above, and ψ_{s} is the separated flow multiplier. The quality and liquid/vapor densities were evaluated at the post-heater inlet. The leading negative sign indicates that the absolute pressure increases in the expansions due to pressure recovery. The pressure recovery for each expansion is shown below

$$\begin{aligned}\Delta P_{\text{exp,C}} &= -47.6 \text{ Pa} \\ \Delta P_{\text{exp,B}} &= -1.39 \text{ Pa} \\ \Delta P_{\text{exp,A}} &= -0.03 \text{ Pa}\end{aligned} \tag{4.40}$$

Thus, the total pressure recovery at the outlet due to flow expansion is 0.05 kPa or 0.6% of the measured pressure drop. The final parameter calculated was the pressure recovery due to the momentum change of the condensing flow. The axial momentum balance on the separated flow derived in Carey (2008) was used:

$$\begin{aligned}\Delta P_{\text{deceleration}} &= G^2\left[\frac{q_3^2}{\rho_{\text{V},3}\cdot\varepsilon_3}+\frac{(1-q_3)^2}{\rho_{\text{L},3}\cdot(1-\varepsilon_3)}\right]-G^2\left[\frac{q_2^2}{\rho_{\text{V},2}\cdot\varepsilon_2}+\frac{(1-q_2)^2}{\rho_{\text{L},2}\cdot(1-\varepsilon_2)}\right] \\ \Delta P_{\text{deceleration}} &= -253 \text{ Pa}\end{aligned} \tag{4.41}$$

Here, the subscripts 2 and 3 refer to the quality, void fraction and phase density at the test section inlet and outlet, respectively. The negative sign in the calculated pressure change again indicates a pressure recovery due to the deceleration of the flow. The void fraction at the inlet and outlet was calculated using the Baroczy (1965) void fraction model (Eq. (4.42)).

$$\varepsilon = \left(1+\left(\frac{1-q}{q}\right)^{0.74}\left(\frac{\rho_{\text{V}}}{\rho_{\text{L}}}\right)^{0.65}\left(\frac{\mu_{\text{L}}}{\mu_{\text{V}}}\right)^{0.13}\right)^{-1} \tag{4.42}$$

The total minor loss was the sum of the expansion, contraction and momentum changes, which for the sample point was 0.302 kPa or 3.7% of the measured pressure drop. A conservative uncertainty of ±50% was assigned to each of the minor loss terms. The frictional pressure drop and gradient were then found from the following expression:

$$\Delta P_{\text{fric}} = \Delta P_{\text{exp}} - \Delta P_{\text{minor}}$$
$$7.78 \pm 0.338 \text{ kPa} = 8.08 \text{ kPa} - 0.302 \text{ kPa} \tag{4.43}$$

$$\left(\frac{dP}{dz}\right)_{\text{fric}} = \frac{\Delta P}{L_{\text{DP}}}$$
$$20.4 \pm 0.88 \text{ kPa m}^{-1} = \frac{7.78 \text{ kPa}}{0.381 \text{ m}} \tag{4.44}$$

Here, the uncertainty in frictional pressure gradient is ±4.3%, with the greatest contribution coming from the uncertainty assigned to the minor losses. A detailed step-by-step calculation of all of the minor losses is provided in Appendix A.6, and an uncertainty propagation analysis of the frictional pressure gradient in Appendix B.4.

CHAPTER 5

RESULTS AND DISCUSSION: PURE AMMONIA CONDENSATION

In this chapter, an overview of the experimental results on ammonia condensation is presented, followed by detailed condensation heat transfer and pressure drop results and a comparison of the results with models and correlations from the literature. A summary of the test conditions is presented in Table 5.1.

Overall, 301 data points were obtained. In the smallest test section, experiments were conducted at mass fluxes of 75 and 100 kg m^{-2} s^{-1}. At higher mass fluxes, the refrigerant pump was not able to provide the desired flow rate due to the increasing two-phase pressure drop, particularly at high vapor quality. Similarly, for the D = 2.16 mm tube, the highest mass fluxes and high qualities were not achievable due to a combination of pump flow and pressure differential limitations. Despite these limitations, sufficient data were obtained over a wide range of conditions to facilitate the analysis of the effects of tube diameter, mass flux, quality, and saturation temperature on ammonia condensation heat transfer and pressure drop.

For each data point, it was desired to obtain the local heat transfer coefficient and

Table 5.1: Summary of ammonia data

	Mass Flux (kg m^{-2} s^{-1})				**Number of Data Points**
	75	**100**	**150**	**225**	
0.98 mm	**X**	**X**			**110**
1.44 mm	**X**	**X**	**X**	**X**	**144**
2.16 mm	**X**	**X**			**47**

frictional pressure gradient at small quality increments with low uncertainty. Balancing these two requirements presented a significant challenge. Consider the expression for condensation heat duty (Eq. (5.1)).

$$\dot{Q}_{\text{cond}} = UA\Delta T_{\text{LM}} \tag{5.1}$$

As shown in Eq. (5.1), given an approximately constant experimental *UA* value, the heat duty and corresponding change in quality could only be reduced by decreasing the temperature difference between the water and the condensing fluid. However, as the temperature difference is decreased, the uncertainty in the calculated heat transfer coefficient increases due to measurement uncertainty in the refrigerant and water-side temperatures. Thus, a careful balance of small quality changes and temperature difference while maintaining reasonable uncertainty in the calculated heat transfer coefficient had to be maintained. For the pure ammonia experiments, the average closest approach temperature difference was 4.5 K, with a standard deviation of 1.3 K (minimum of 2.2 K and maximum of 10 K). This yielded an average quality change of 0.27 for all data, with a range from 0.06 to 0.5. Plots of the average quality and the calculated uncertainty for all data are shown as a function of tube diameter and saturation temperature in Figure 5.1.

The average uncertainty in the calculated average quality was very low, ±0.6%. For a given test section, the change in quality was greatest for the lowest mass flux, highest saturation temperature (due to smaller h_{fg}) and highest inlet quality (due to higher average heat transfer coefficient). As shown in Table 5.2, the change in quality was largest for the smallest tube. The average quality decreased with increasing tube diameter. Because an approximately equal approach temperature difference was

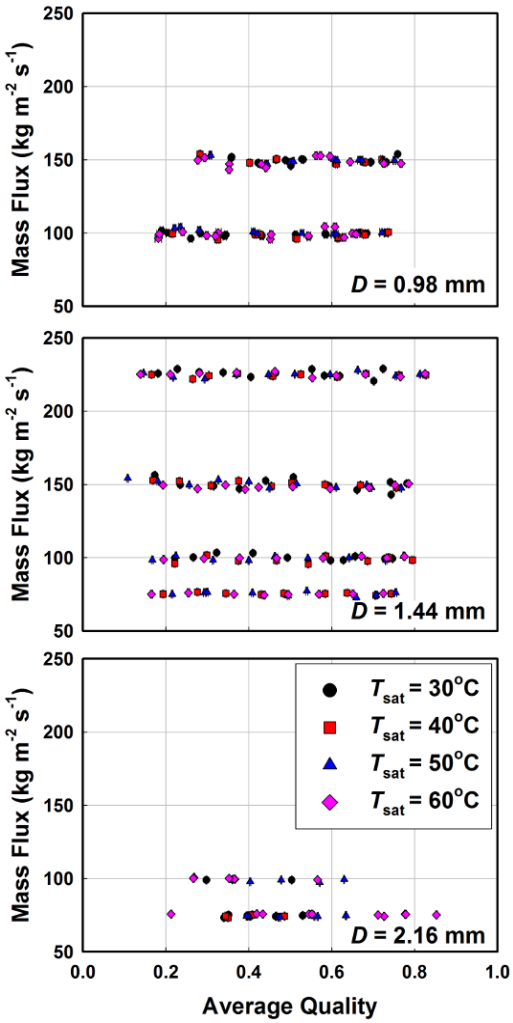

Figure 5.1: Average quality of ammonia condensation data

maintained for all three test sections, this can primarily be explained by the much larger heat transfer coefficients for the smallest tube.

The average test section heat duty for the 0.98, 1.44 and 2.16 mm test sections was 36.4 W, 57.6 W, and 35.6 W, respectively. For all ammonia data, the measured heat duty varied from 15 to 103 W. The average uncertainty in the calculated heat duties for all data was ±2.8%. This low uncertainty allowed for more accurate determination of the condensation heat transfer coefficient. Table 5.2 summarizes the average change in

Table 5.2: Summary of ammonia condensation heat duties and uncertainties

	Average Δq	Average Heat Duty (W)	Average $\dot{Q}_{cond}$ Uncertainty
0.98 mm	0.37	36.4	±3.1%
1.44 mm	0.25	57.6	±2.2%
2.16 mm	0.11	35.6	±4.2%
Total	**0.27**	**46.5**	**±2.8%**

quality, average condensation heat duty and heat flux, and average uncertainty in the calculated condensation heat duty.

5.1 Heat Transfer Results

The local heat transfer coefficient was determined for each point following the procedures outlined in Chapter 4. In this section, the results and trends are presented first, followed by a detailed discussion on the uncertainty in heat transfer coefficient. The local heat transfer coefficient data for all experiments are shown in Figure 5.2.

The average heat transfer coefficients for the 0.98, 1.44 and 2.16 mm test sections were 31.8, 24.0, and 8.1 kW m^{-2} K^{-1}, respectively. The average of all heat transfer coefficients was 24.5 kW m^{-2} K^{-1}, with a range from 4.2 to 55.4 kW m^{-2} K^{-1}. The general trends were consistent with previous investigations on condensation heat transfer in mini/microchannels (Bandhauer et al., 2006; Agarwal and Garimella, 2010; Keinath, 2012), and macro channels (Dobson and Chato, 1998; Cavallini et al., 2001). Thus, higher values of heat transfer coefficient were observed at higher qualities, higher mass flux, smaller tube diameters and lower saturation temperature .

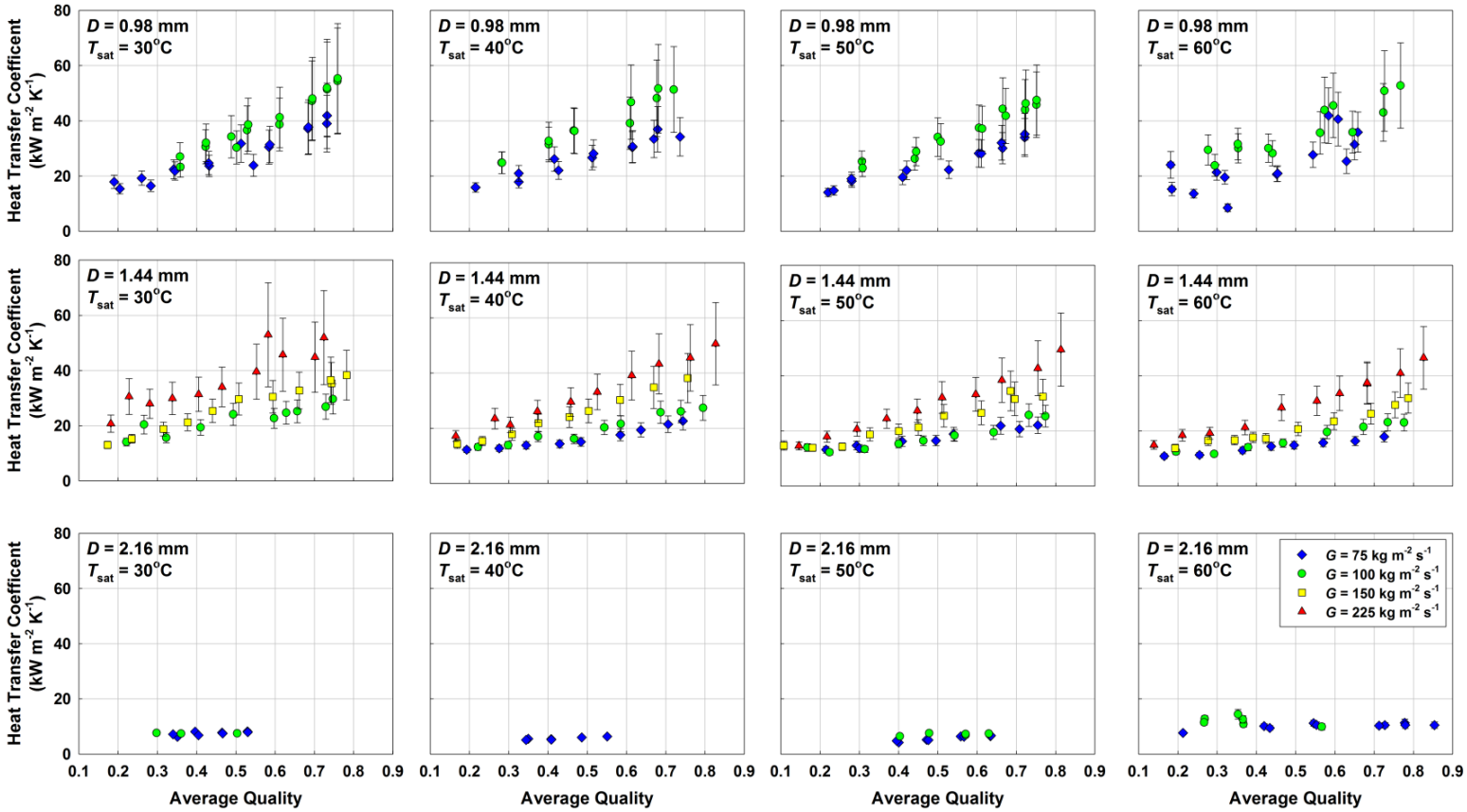

Figure 5.2: Ammonia condensation heat transfer data

5.1.1 Uncertainty and resistance ratio

One of the most challenging aspects of the present investigation was measuring very high condensation heat transfer coefficients with low uncertainty. Recall from Chapter 4 that the condensation resistance was found from the following equation:

$$R_{cond} = \frac{\Delta T_{LM}}{\dot{Q}_{cond}} - R_{wall} - R_{water} \tag{5.2}$$

Thus, high resolution of the condensation heat transfer coefficient required that the dominant thermal resistance was due to condensation. The relative importance of the condensation resistance to the combined water and wall thermal resistances can be expressed as the resistance R_{atio}:

$$R_{ratio} = \frac{R_{cond}}{R_{wall} + R_{water}} \tag{5.3}$$

For very high resistance ratios, the condensation resistance governs the overall heat transfer, and thus, can be resolved with low uncertainty. A summary of the resistance ratios and heat transfer coefficient uncertainties as functions tube diameter and saturation temperature is shown in Table 5.3 and graphically in Figure 5.3.

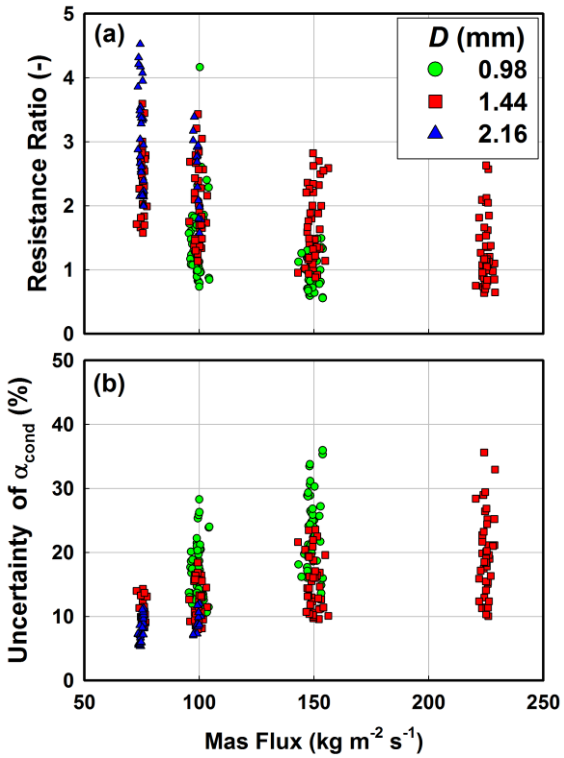

Figure 5.3: Summary of (a) resistance ratio and (b) uncertainty in condensation heat transfer coefficient

The resistance ratio and uncertainty are clearly inversely proportional. The resistance ratio is larger at higher saturation temperatures, lower mass fluxes and larger tube diameters (due to lower condensation heat transfer resistance). Thus, these points have the lowest uncertainty. The highest uncertainties are at points with high mass flux, low saturation temperature and very high quality. In the present study, the average resistance ratio was 1.75, and the average uncertainty in heat transfer coefficient uncertainty was ±15.9%, with a maximum and minimum of ±5.3% and ±35.9%.

5.1.2 Effect of Mass Flux and Quality

Figure 5.4 shows the effect of mass flux and average quality on heat transfer coefficient for a given tube diameter (D = 1.44 mm) and saturation temperature (T_{sat} = 40°C).

Table 5.3: Average resistance ratio and uncertainty in heat transfer coefficient

D (mm)	T_{sat} (°C)	Average R_{ratio}	Average α_{cond} (kW m^{-2} K^{-1})	Average α_{cond} Uncertainty (%)
0.98 mm	30	1.02	33.6	±22.5
	40	1.15	31.8	±19.8
	50	1.24	30.8	±18.7
	60	1.37	30.6	±19.2
1.44 mm	30	1.31	29.0	±19.3
	40	1.72	23.9	±15.1
	50	1.90	22.4	±14.0
	60	2.10	21.6	±12.7
2.16 mm	30	2.78	7.5	±7.9
	40	3.6	6.0	±7.2
	50	3.8	6.2	±6.4
	60	2.11	10.8	±9.9
TOTAL	-	**1.75**	**24.4**	**±15.9**

For all data, a higher mass flux yields a higher heat transfer coefficient. The mass flux effect is more pronounced at higher average qualities. As an example, consider the

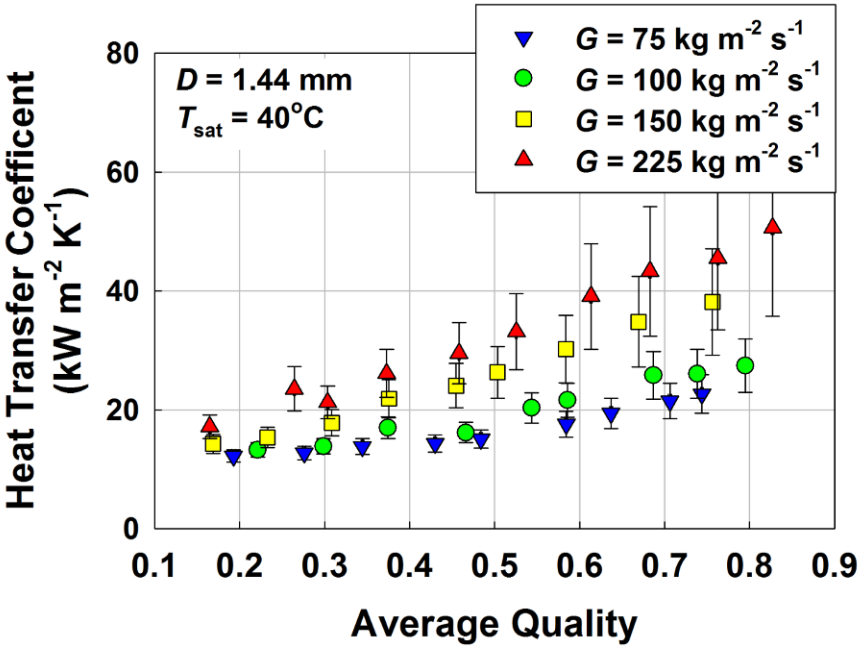

Figure 5.4: Effect of mass flux and quality on ammonia condensation heat transfer coefficient for D = 1.44 mm, T_{sat} = 40°C

four data points with an average quality of approximately 0.3 in Figure 5.4. Starting with the lowest mass flux (G = 75 kg m^{-2} s^{-1}), increasing the nominal mass flux to 133%, 200% and 300% of this value yields values of heat transfer coefficient of 108%, 140%, and 167% of the nominal, respectively. Contrast this for data with an average quality of approximately 0.75, where the same increases in mass flux yield heat transfer coefficients that are 115%, 169%, and 200% of nominal. At high quality, the condensation process is shear dominated, and increases in the mass flux yield higher vapor core velocities, increasing interfacial shear and thinning the condensate film, thereby resulting in increasing heat transfer coefficient. However, for the largest tube, gravity effects are of increased importance, and thus the effect of increased vapor shear is somewhat lower. This effect can be seen in Figure 5.5.

Here, there is essentially no change in the heat transfer coefficient as the mass

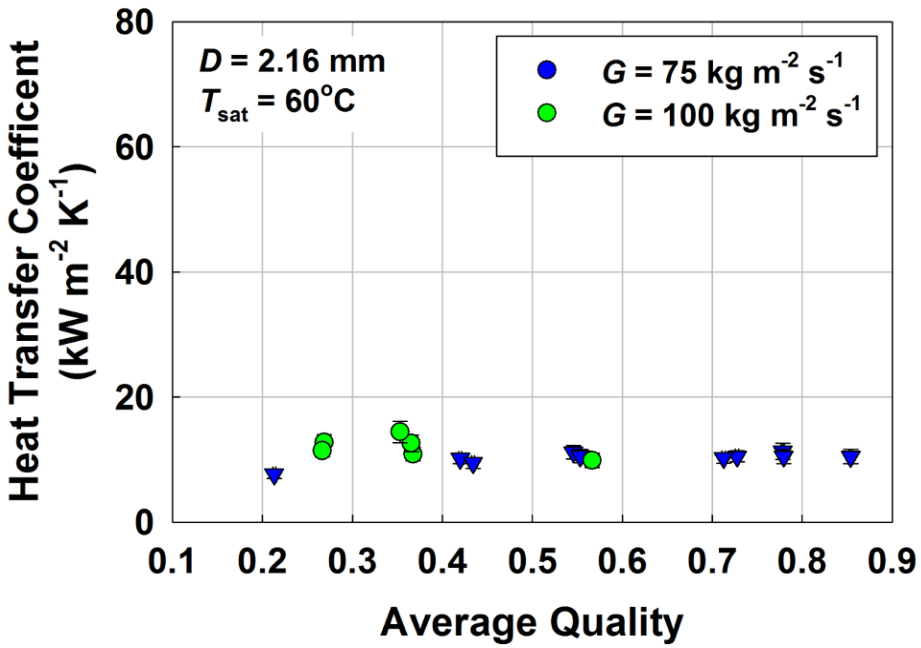

Figure 5.5: Effect of mass flux and quality on ammonia condensation heat transfer coefficient for D = 2.16 mm, T_{sat} = 60°C

flux is increased from 75 to 100 kg m^{-2} s^{-1}. Furthermore, there is very little increase in the heat transfer coefficient with increasing quality. This same behavior was observed by Dobson and Chato (1998) for condensation for a near-azeotropic mixture of R-32/R-125 in a similarly sized tube (D = 3.14 mm) at mass fluxes from 75 to 150 kg m^{-2} s^{-1}. For these points, they stated that vapor shear forces were relatively less important, as the flow is expected to be a combination of wavy and wavy-annular type flow. In this regime, the heat transfer is controlled predominantly by gravity driven condensation. Thus, the effect of flow regime must be accounted for in the development of a heat transfer model.

5.1.3 Effect of Tube Diameter and Saturation Temperature

The effects of tube diameter and saturation temperature on condensation heat transfer

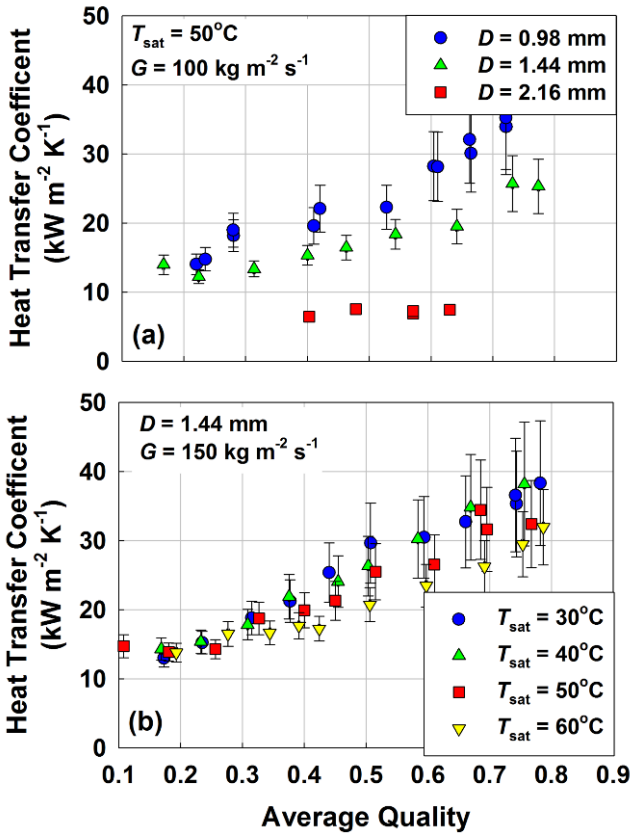

Figure 5.6: Effect of (a) diameter and (b) saturation temperature on ammonia condensation heat transfer coefficient

coefficient are shown in Figures 5.6a and 5.6b, respectively. A clear trend of increasing heat transfer coefficient with decreasing diameter was observed for all data.

For the range of reduced pressures investigated here ($0.10 < P_r < 0.23$), the effect of saturation temperature is within the experimental uncertainty for most points. Still, the general trend shows slightly higher heat transfer coefficients at lower saturation temperatures. There are several different mechanisms that contribute to this. As shown in Table 5.4, the enthalpy of vaporization, phase properties and surface tension change as the saturation temperature increases (*e.g.*, liquid-vapor density ratio and surface tension decrease by 60% and 34%, respectively, for a 30 K increase in saturation temperature).

For non-annular flow regimes, gravity driven film condensation becomes increasingly important. The result of the Nusselt (1916) laminar film analysis for condensation on a flat plate can be used to illustrate the influence of fluid properties on heat transfer coefficient:

$$h = \frac{k_L}{\delta} = \left(\frac{\rho_L \left(\rho_L - \rho_V \right) g h_{fg} k_L^3}{4 \mu_L x \left(T_{sat} - T_w \right)} \right)^{1/4} \tag{5.4}$$

Using Eq. (5.4) as a basis, the heat transfer coefficient is expected to increase with

Table 5.4: Saturated ammonia properties

T_{sat}	P_r (-)	h_{fg} (kJ kg^{-1})	ρ_L/ρ_V	μ_L/μ_V	σ (N m^{-1})
30°C	0.10	1144	65.7	12.6	0.0186
40°C	0.14	1099	48.2	11.0	0.0164
50°C	0.18	1051	35.7	9.7	0.0143
60°C	0.23	997	26.6	8.6	0.0122

increasing liquid thermal conductivity, enthalpy of vaporization, and liquid-vapor phase density ratio as the saturation temperature decreases.

In the annular regime, the condensation heat transfer mechanism is shear dominated. Thus, a decrease in T_{sat} yields larger differences in the vapor and liquid densities and viscosities. This results in larger differences in phase velocities and higher interfacial shear, increasing the heat transfer coefficient. The effects of saturation temperature on condensation heat transfer in both flow regimes are expected to be more pronounced across larger ranges of reduced pressure.

5.2 Heat Transfer Comparison with Literature

The heat transfer results were compared with various macro, mini, and microchannel condensation heat transfer models and correlations from the literature, shown in Table 5.5 and previously introduced in Chapter 2.

5.2.1 Flow Regime Predictions

It is well established that flow morphology has a significant influence on condensation heat transfer mechanisms. To that end, many different maps for predicting two-phase

Table 5.5: Evaluated condensation heat transfer models

Study	Channel Size	Flow Regimes
Bandhauer *et al.* (2006)	Mini/Micro	Annular
Shah (2009)	Mini/Micro	Annular
Keinath (2012)	Mini/Micro	Annular
Kim and Mudawar (2013)	Mini/Micro	Multi-regime
Traviss *et al.* (1973)	Macro	Annular
Shah (1979)	Macro	Annular
Dobson and Chato (1998)	Macro	Multi-regime
Thome *et al.* (2003)	Macro	Multi-regime
Cavallini *et al.* (2006)	Macro	Multi-regime

flow regimes and transitions have been introduced and were reviewed in Chapter 2. In the present study, there was no direct observation of the prevailing flow regime. Rather, as discussed above, the dominant heat transfer mechanism can be qualitatively inferred from the operating conditions, tube diameters, and trends in the heat transfer data. As observed from the trends of heat transfer coefficient with mass flux in Figures 5.2 and 5.3, non-annular flow appears to be more prevalent than annular flow for the largest tube diameter under investigation.

The models of Dobson and Chato (1998), Thome *et al.* (2003), Cavallini *et al.* (2006), and Kim and Mudawar (2013) considered the effect of flow regime on the heat transfer mechanisms. The percentage of the data for each different tube predicted to be either annular or non-annular flow is shown in Table 5.6.

From a qualitative comparison of the flow regime predictions with the observed trends in the heat transfer data, the Cavallini *et al.* (2006) flow transition criterion appears to be the most realistic, namely that annular flow is predicted to dominate for the D = 0.98 mm and 1.44 mm tubes, and that non-annular flow takes on increasing importance

Table 5.6: Percentage of data predicted in annular and non-annular flow regime

Study	0.98 mm		1.44 mm		2.16 mm	
	A **(%)**	***N-A*** **(%)**	***A*** **(%)**	***N-A*** **(%)**	***A*** **(%)**	***N-A*** **(%)**
Dobson and Chato (1998)	83	17	74	26	44	56
Thome *et al.* (2003)	0	100	21	79	0	100
Cavallini *et al.* (2006)	100	0	96	4	80	20
Kim and Mudawar (2013)	69	31	72	28	63	37
***A* = annular flow; *N-A* = non-annular flow**						

for the largest tube (D = 2.16 mm).

5.2.2 Heat Transfer Results

The heat transfer models were compared based on the average deviation (AD, Eq. (5.5)) and the absolute average deviation (AAD, Eq.(5.6)).

$$\mathrm{AD} = \frac{100\%}{n}\sum_{i=1}^{n}\frac{\alpha_{\mathrm{mod}} - \alpha_{\mathrm{exp}}}{\alpha_{\mathrm{exp}}} \tag{5.5}$$

$$\mathrm{ADD} = \frac{100\%}{n}\sum_{i=1}^{n}\left|\frac{\alpha_{\mathrm{mod}} - \alpha_{\mathrm{exp}}}{\alpha_{\mathrm{exp}}}\right| \tag{5.6}$$

The absolute average deviation provides an indication of the bias of the model. For instance, a model with a very high degree of scatter could have a very low AD (for equal positive and negative errors). However, the same model would have a very large AAD. A summary of the AD and AAD for all the models and correlations is shown in Table 5.7. A graphical representation of the agreement of the six best performing models is shown in Figure 5.7.

Table 5.7: Comparison of measured versus predicted heat transfer coefficient

Study	AD (%)	AAD (%)
Bandhauer *et al.* (2006)	-23	38
Shah (2009)	-66	66
Keinath (2012)	-1.0	32
Kim and Mudawar (2013)	-33	44
Traviss *et al.* (1973)	-20	36
Shah (1979; 2013)	-38	45
Dobson and Chato (1998)	-17	37
Thome *et al.* (2003)	-23	44
Cavallini *et al.* (2006)	-38	46

From the table and the figure, it is clear that all of the models under predict a large percentage of the data, except for some data from the D = 2.16 mm tube. Of the evaluated models, the microchannel correlation of Keinath (2012) has both the lowest AAD and AD. In his annular model, a two-phase film heat transfer multiplier is introduced as a function of the phase velocities. These quantities were determined using a drift-flux based void fraction model developed from flow visualization of R-404A in mini/microchannels. Despite the large property difference between ammonia and R-404A, the use of a void fraction model developed from microchannel data appears to improve the predictive accuracy.

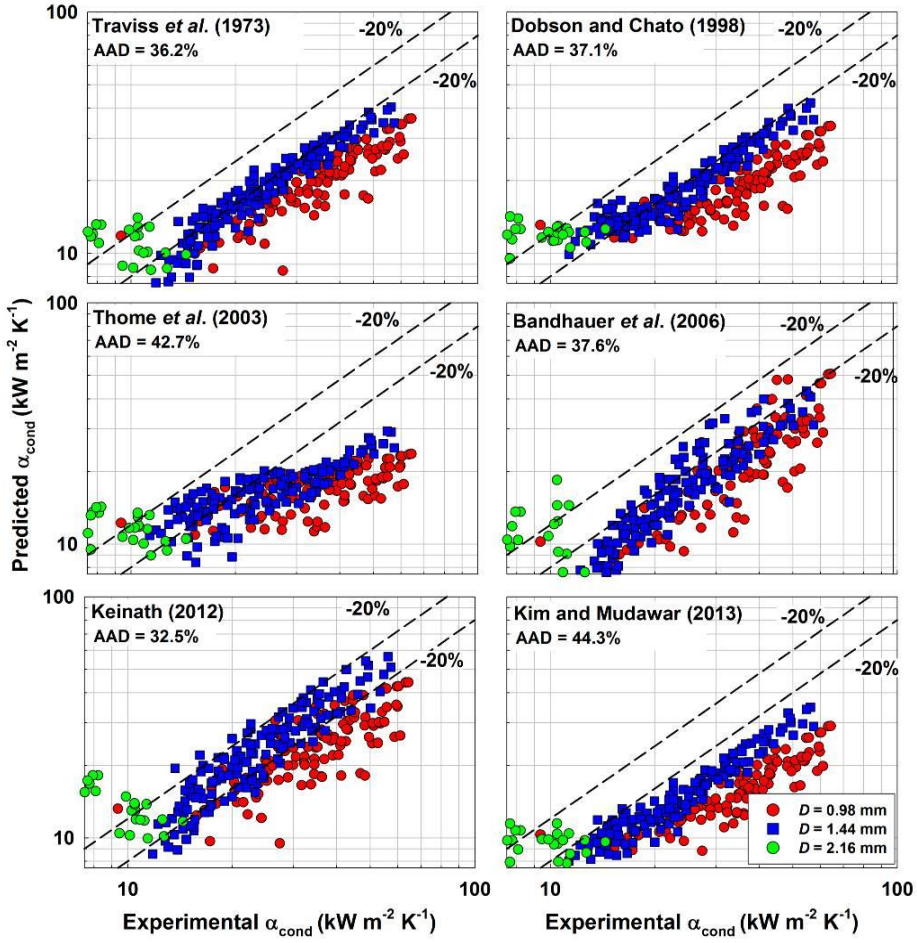

Figure 5.7: Comparison of ammonia condensation heat transfer data with literature correlations

Table 5.8: Absolute average deviation for annular and non-annular flow

Study	0.98 mm		1.44 mm		2.16 mm	
	A **(AAD)**	***N-A*** **(AAD)**	***A*** **(AAD)**	***N-A*** **(AAD)** -	***A*** **(AAD)**	***N-A*** **(AAD)**
Dobson and Chato (1998)	48%	31%	26%	9.5%	55	73
Thome *et al.* (2003)	-	49%	47%	27%	-	64%
Cavallini *et al.* (2006)	57%	-	41%	50%	33%	41%
Kim and Mudawar (2013)	57%	48%	40%	31%	33%	58%
***A* = annular flow; *N-A* = non-annular flow**						

Interestingly, the agreement of the models developed for mini/micro and macro scale channels were not significantly different, with AAD ranging from 32 to 46% (excluding the Shah (2009) microchannel model). In fact, the Shah (2009) model, developed for mini and microchannel applications, exhibited the poorest overall agreement. In addition, the multi-regime models did not offer a significant improvement in overall predictive capability. A breakdown of the agreement by predicted flow regime and tube diameter for these four models is shown in Table 5.8.

Here again, there is no clear trend in the agreement between different flow regimes. The poor predictive capabilities of the condensation models and the variation between each of the models are not surprising. Su *et al.* (2009) showed that many heat transfer models developed for R-134a had exhibited good agreement with one another when applied to R-134a in a microchannel. However, when they were applied to ammonia in the same tube, they exhibited wide scatter with one another. An example case is shown in Figure 5.8.

Thus, while the models examined here may show good agreement when applied to the fluids for which they were developed (*i.e.*, synthetic refrigerants), they do not

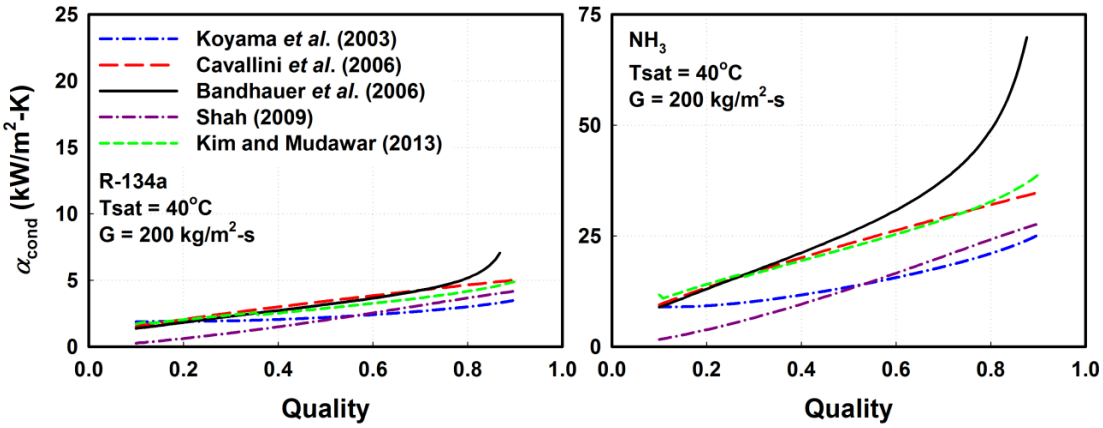

Figure 5.8: Comparison of predictions of mini/microchannel condensation heat transfer models for R-134a and ammonia

extrapolate well to the new fluid and geometry of interest here. As a reference, at a saturation temperature of 50°C, the liquid-vapor density ratio, surface tension, liquid thermal conductivity and enthalpy of vaporization are 2.2, 2.9, 5.9, and 6.9 times greater for ammonia than R-134a, respectively. These large property differences potentially explain the poor applicability of models developed for R-134a and other synthetic refrigerants to ammonia.

5.3 Pressure Drop Results

Condensation pressure drop data were obtained concurrently with the heat transfer data reported above. The pressure drop data and observed trends are reported first, followed by a comparison of the data with the literature. A complete summary of the pressure drop results for different saturation temperatures, tube diameters, mass fluxes, and qualities is shown in Figure 5.9.

The trends in pressure drop closely mirror the observed trends in heat transfer coefficient. An increase in mass flux and quality yields higher pressure drops, as shown in Figure 5.10 for D = 1.44 mm and T_{sat} = 40°C.

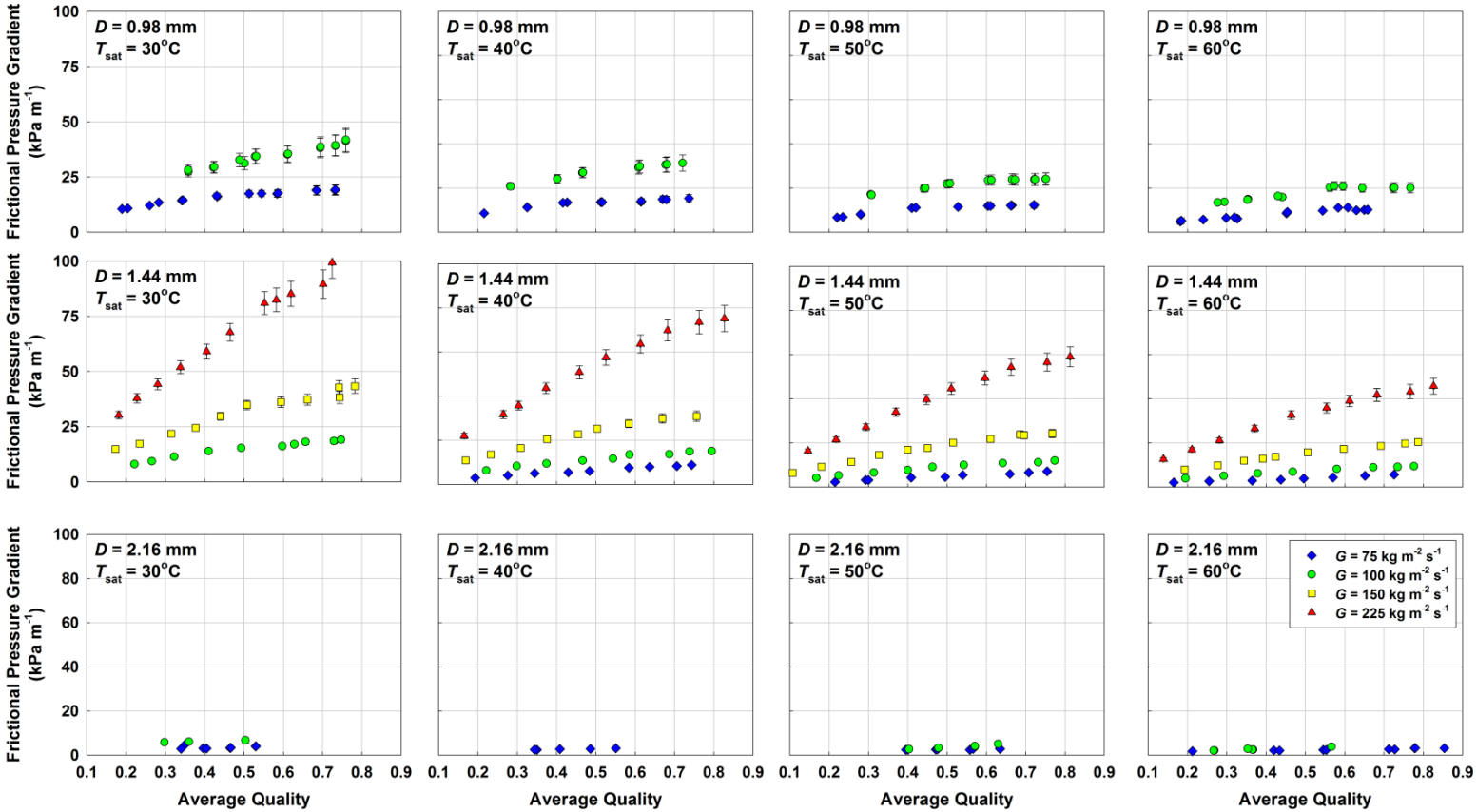

Figure 5.9: Ammonia condensation frictional pressure gradient data

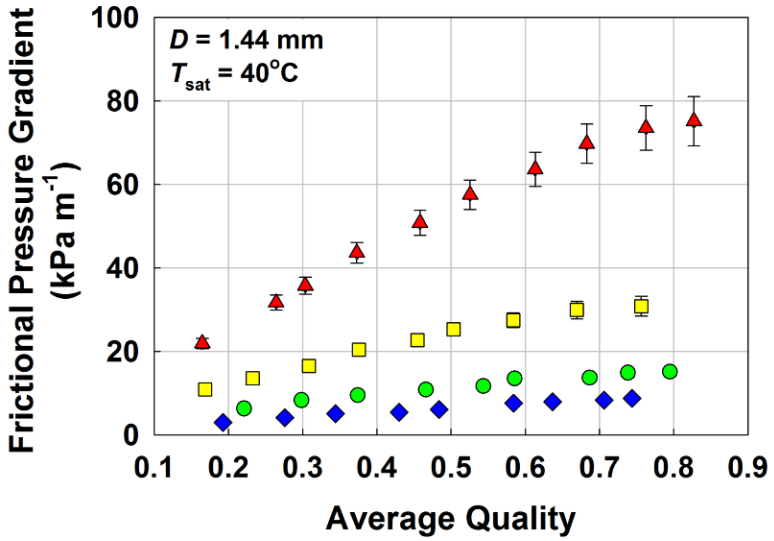

Figure 5.10: Effect of mass flux and quality on ammonia condensation frictional pressure gradient for D = 1.44 mm, T_{sat} = 40°C

The effect of increasing mass flux at a fixed quality is comparable over the entire range of quality. As an example, for a quality of 0.3, for changes in nominal mass flux from 75 kg m^{-2} s^{-1} to 133%, 200% and 300%, respectively, the resulting pressure gradients were 203%, 406% and 880% of the nominal value. Similarly, for an average quality of 0.7, the resulting pressure gradient was 169%, 352% and 837% of the nominal for the same change in mass flux. This trend is different from that observed for heat transfer coefficient, where the effect of mass flux was less pronounced at lower qualities. This can be explained by considering that for heat transfer, the underlying condensation mechanisms change at low qualities (from shear to gravity dominated).

However, for pressure drop, the underlying mechanism is less sensitive to the expected change in flow morphology from annular to wavy flow. As shown in Garimella *et al.* 2005, a change in the trend of pressure drop is observed as the flow transitions from annular and disperse-wave to intermittent flow. In this regime, the vapor phase is no longer continuous, but rather separated by liquid slugs. In this type of flow,

the pressure gradient is a combination of bubble and slug shear contributions, as well as pressure losses associated with the flow area changes of the liquid film at the leading and trailing edges of vapor bubbles. Due to the different pressure drop mechanisms, Garimella *et al.* (2002) and Agarwal (2006) each developed pressure drop models specifically for intermittent flow. In the present study, a more pronounced change in observed pressure drop with quality (*i.e.*, liquid fraction), mass flux and tube diameter would be expected if significant intermittent flow were present. Thus, the pressure drop results further validate the assumption that the flow is primarily annular, and annular/wavy and wavy type flow.

At the same quality and mass flux, the pressure gradient is larger for smaller tubes and at lower saturation pressures. These effects are illustrated in Figure 5.11. Here, the trends are the same as for the heat transfer coefficient. As discussed previously, at lower saturation temperature, the ratios of saturated liquid/vapor density and viscosity increase, yielding more significant interfacial shear effects and an increase in frictional pressure gradient.

5.3.1 Uncertainty in Pressure Gradient

In Chapter 4 it was shown that the frictional pressure drop could be calculated as follows:

$$\Delta P_{fric} = \Delta P_{measured} - \Delta P_{inlet} - \Delta P_{outlet} - \Delta P_{deccleration} \tag{5.7}$$

The uncertainty in the measured pressure drop was very low (±0.075% of span or ±0.075 kPa). Thus, the primary contribution to the uncertainty in the frictional pressure drop was the ±50% uncertainty assigned to the calculated inlet, outlet and deceleration pressure changes. Figure 5.12 shows the percent uncertainty in the frictional gradient,

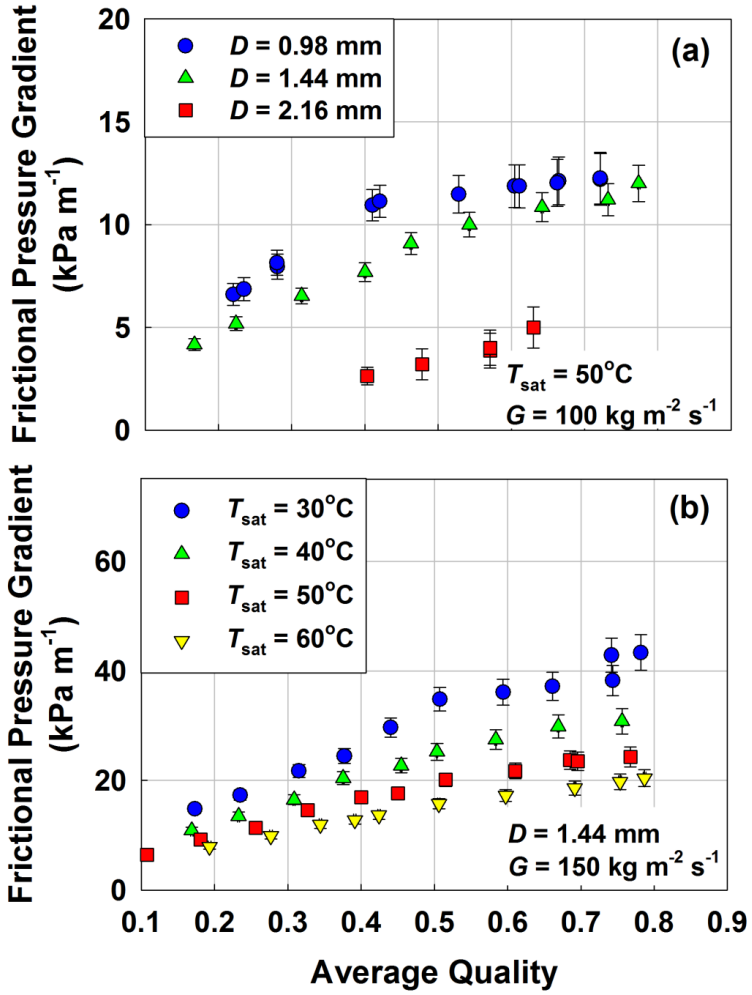

Figure 5.11: Effect of (a) diameter and (b) saturation temperature on ammonia condensation frictional pressure gradient

and the ratio of the calculated frictional pressure gradient to the measured pressure gradient, as a function of tube diameter and mass flux.

The average uncertainty in the calculated frictional pressure gradient was ±9.5%, with a minimum of ±5% and a maximum of ±23%. The average uncertainty for the 0.98, 1.44 and 2.16 mm tubes was ±8.9%, ±6.5%, and ±20.2%, respectively. The uncertainty was largest for the 2.16 mm tube. This was due to small mass flux and large diameter, which resulted in small measured pressure drop.

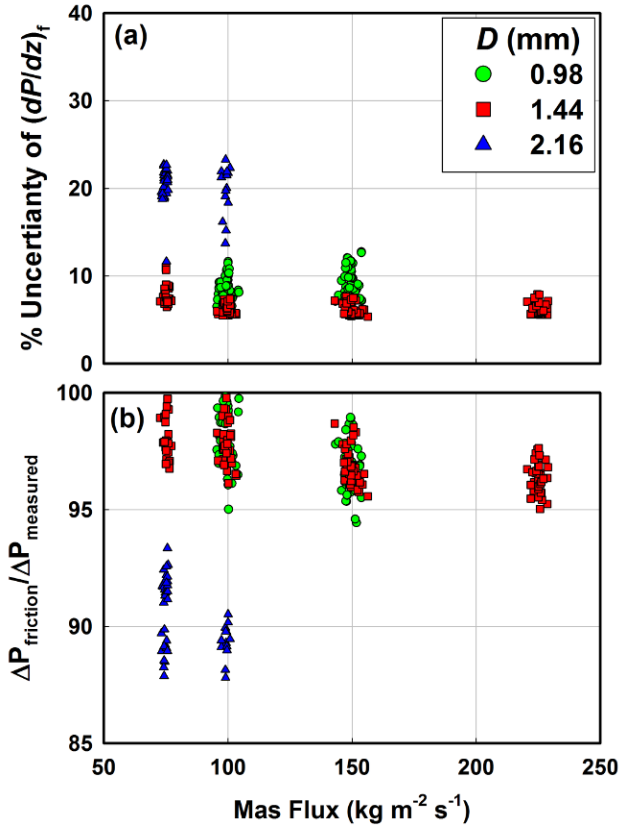

Figure 5.12: (a) Uncertainty in frictional pressure gradient and (b) ratio of calculated frictional pressure prop to total measured pressure drop

Because the magnitude of the minor losses and deceleration pressure change for each tube were approximately the same, they accounted for a larger percentage of the total pressure drop for the D = 2.16 mm tube (as shown in Figure 5.12), resulting in larger uncertainty in the frictional pressure drop. From this reasoning, it may be expected that the 0.98 mm tube would have the lowest uncertainty because the frictional contribution to pressure drop is dominant. However, the pressure drop length was 1.5 times greater for the 1.44 mm tube, and experiments were conducted at larger mass fluxes which increased the frictional component in the data, yielding slightly lower average uncertainty.

5.4 Pressure Drop Comparison with Literature

The calculated frictional pressure gradient data were compared with pressure drop models developed for adiabatic and condensing flows in macro and mini/channels, as shown in Table 5.9. An introduction to the underlying assumptions of these models was provided in Chapter 2.

The pressure drop models were compared based on the average deviation (AD, Eq. (5.5)) and the absolute average deviation (AAD, Eq.(5.6)). The results are shown graphically in Figure 5.13 and in Table 5.10 as a function of tube diameter.

Of the models considered, the Friedel (1979) macrochannel and the Kim and Mudawar (2012) microchannel condensation correlations predicted the data most accurately. Both of these correlations were developed using a large range of data from varying tube diameters, mass fluxes and saturation conditions. Interestingly, as can be seen from Table 5.7, the Friedel (1979) correlation exhibited the best agreement for all three tube diameters. The microchannel models of Mishima and Hibiki (1996) (developed for smaller channels and with air/water mixtures) exhibited the poorest overall agreement. The Garimella *et al.* (2005) microchannel condensation model was

Table 5.9: Evaluated pressure drop models

Study	Channel Size	Boundary Condition
Mishima and Hibiki (1996)	Mini/Micro	Adiabatic
Garimella *et al.* (2005)	Mini/Micro	Condensation
Keinath (2012)	Mini/Micro	Condensation
Kim and Mudawar (2012)	Mini/Micro	Condensation
Lockhart and Martinelli (1949)	Macro	Adiabatic
Friedel (1979)	Macro	Adiabatic

developed using R-134a data. Here, the model predicted the general trend of the ammonia pressure drop well, but the data were under predicted overall. This again illustrates the difficulty in extrapolating correlations outside their original range of applicability.

5.5 Ammonia Results Summary

The ability to accurately measure ammonia heat transfer coefficient and frictional pressure drop for small channels ($0.98 < D < 2.16$ mm) and range of mass fluxes ($50 < G < 225$ kg m^{-2} s^{-1}) and saturation temperatures was demonstrated in this chapter. The

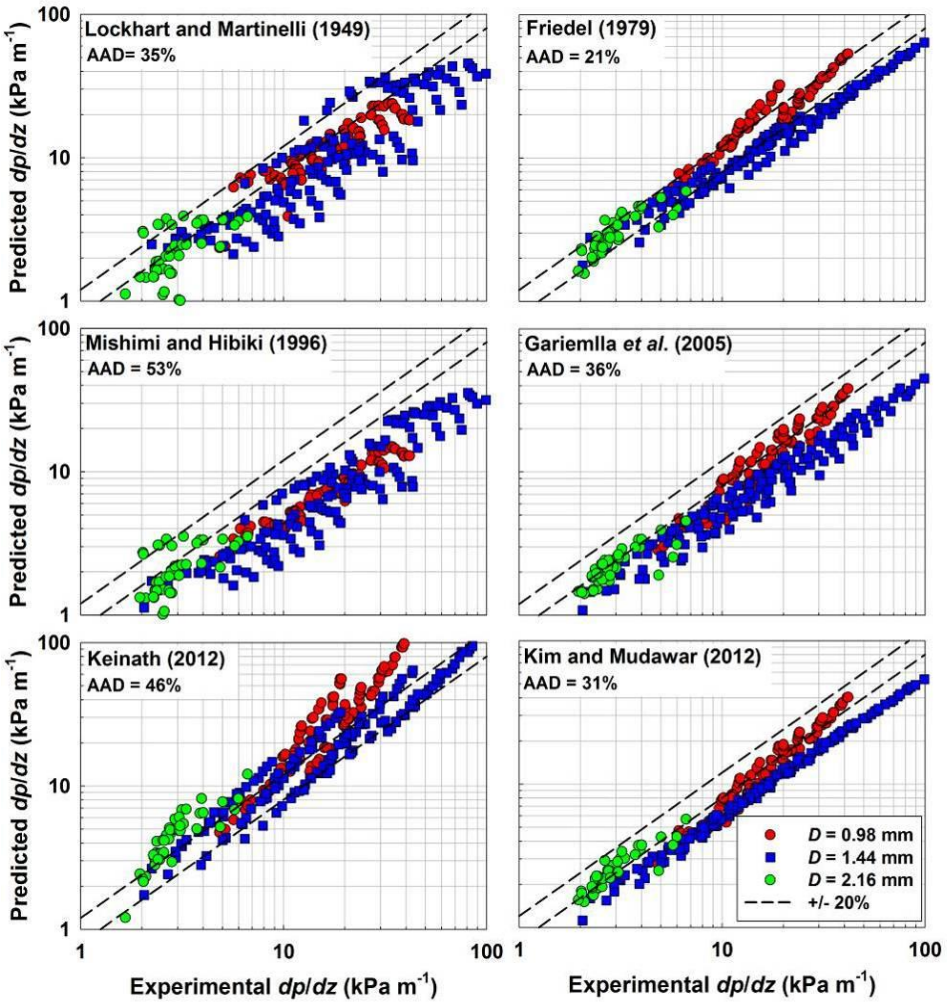

Figure 5.13: Comparison of ammonia condensation frictional pressure gradient data with literature correlations

Table 5.10: Pressure drop model agreement

	Absolute Average Deviation (AAD)			
Study	**0.98 mm**	**1.44 mm**	**2.16 mm**	**Total**
Mishima and Hibiki (1996)	56%	55%	37%	53%
Garimella *et al.* (2005)	25%	48%	25%	36%
Keinath (2012)	69%	23%	55%	46%
Kim and Mudawar (2012)	23%	40 %	17%	31%
Lockhart and Martinelli (1949)	29%	40%	34%	35%
Friedel (1979)	20%	25%	14%	21%

measured heat transfer coefficients ranged from 4 to 55 kW m^{-2} K^{-1} with an average uncertainty of ±15.9%, and a maximum of ±35.9%. The dependence of pressure drop and heat transfer on quality and mass flux was consistent with previous investigations; however, it was shown that existing heat transfer models were not able to accurately predict the results. The Keinath (2012) correlation exhibited the best agreement, with a mean absolute percentage error of 32.5%. The coupled effects of ammonia properties and microscale geometry are outside the applicable range of most condensation heat transfer models. The available pressure drop correlations showed better agreement, with the simple Friedel (1979) correlation predicting the data the best.

To improve the predicative capabilities for design of ammonia condensers, a new, flow-regime based heat transfer model accounting for ammonia properties and microchannel effects is introduced in Chapter 7. In addition to enabling more accurate design of ammonia based components, the model can be applied within the non-equilibrium framework to predict the liquid-film heat transfer coefficient of condensing ammonia/water zeotropic mixtures, as will also be shown in Chapter 7.

CHAPTER 6

RESULTS AND DISCUSSION: ZEOTROPIC MIXTURE CONDENSATION

In this chapter, an overview of the zeotropic ammonia/water condensation experimental results is presented, followed by a detailed discussion of the condensation heat transfer and pressure drop results and a comparison of the results with predictions of models and correlations from the literature. A summary of the zeotropic mixture test conditions is presented in Table 6.1.

Overall, 438 data points were obtained at mass fluxes ranging from 50 to 200 kg m^{-2} s^{-1}, and bulk ammonia mass fraction (x_{bulk}) ranging from 0.80 to > 0.96. For data in the > 0.96 category, the calculated bulk mass fraction of ammonia ranged from 0.96 to 0.98. All data were obtained at a nominal saturation pressure of 1500 kPa, with an average deviation of ±3.2% from the nominal. As with the pure ammonia data, the lowest mass flux for the D = 0.98 mm and the highest mass fluxes for the D = 2.16 mm were limited by pump, heater input and/or mass flow meter operational limits. For each data point, the bulk ammonia mass fraction, condensation heat duty, apparent heat

Table 6.1: Summary of zeotropic mixture data

	Mass Flux (kg m^{-2} s^{-1})					**Number of Data Points**
	50	**75**	**100**	**150**	**200**	
0.98 mm			**X**	**X**	**X**	**153**
1.44 mm		**X**	**X**	**X**	**X**	**138**
2.16 mm	**X**	**X**	**X**			**147**

transfer coefficient, and frictional pressure gradient were calculated according to the procedures detailed in Chapter 4.

6.1 Bulk Ammonia Mass Fraction Results

As outlined in Chapters 3 and 4, the system was initially charged with the appropriate mass of ammonia and water to achieve the desired nominal bulk mass fraction. During operation, zeotropic mixture mass was metered in and out of a rigid accumulator to control system pressure, which could cause small local shifts in the actual circulating bulk mass fraction. To account for this, the local mass fraction was calculated using both a pre- and post-heater energy balance for each data point. As also detailed in Chapter 4, due to lower overall uncertainty, the value obtained from the post-heater energy balance was used in subsequent analysis. Table 6.2 shows the average percentage deviation of the calculated bulk ammonia mass fraction value from the nominal condition, and the average percent difference between $x_{bulk,pre}$ and $x_{bulk,post}$ for each tube diameter. The average uncertainty in the calculated x_{bulk} is also reported.

The experimental uncertainty in the bulk ammonia mass fraction was very small, with an average of less than ±0.6% of the calculated value. The primary contribution to the uncertainty was the test section outlet mixture temperature and the uncertainty in the

Table 6.2: Summary of zeotropic mixture bulk mass fraction (x_{bulk}) and uncertainty

	Average Deviation from Nominal	Average Percent Difference of $x_{bulk,pre}$ and $x_{bulk,post}$	Average Uncertainty
0.98 mm	2.7%	6.7%	±0.6%
1.44 mm	1.9%	4.3%	±0.5%
2.16 mm	2.6%	5.3%	±0.7%
Total	**2.5%**	**5.5%**	±0.6%

heat loss of the post-heater.

6.2 Mixture Heat Duty and Average Quality

Unlike for pure ammonia, the zeotropic mixture exhibited a strong temperature glide during condensation. Because the water-side change in temperature was negligible, there was a potential for a temperature "pinch" between the mixture outlet temperature and the water inlet temperature, resulting in inactive heat transfer area as the temperature difference between the two fluids became negligible. This pinch could be avoided by reducing the water-side temperature. However, this resulted in a larger average driving temperature difference, which yielded greater heat duty and change in quality. Thus, a careful balance of maintaining an adequate temperature difference without significant pinch points and minimizing the average quality change was necessary. For the mixture experiments, the average closest approach temperature difference between the water and ammonia/water mixture was 8.2, 6.3, and 5.6 K for the x_{bulk} = 0.8, 0.9 and > 0.96 points, respectively. The average temperature glide (*i.e.*, the difference between the mixture inlet and outlet temperature) change in quality and uncertainty in quality for each data point are shown in Table 6.3. The average quality with calculated uncertainty as a function of tube diameter, ammonia mass fraction, and mass flux is shown in Figure 6.1.

Table 6.3: Summary of average temperature glide, change in quality and average quality uncertainty

x_{bulk}	$\Delta T_{glide,\ avg}$ (K)	Δq_{avg}	q_{avg} Uncertainty
0.80	35.6	0.32	±2.3%
0.90	23.1	0.27	±1.4%
> 0.96	7.0	0.27	±1.3%
Total	**26.3**	0.28	±1.7%

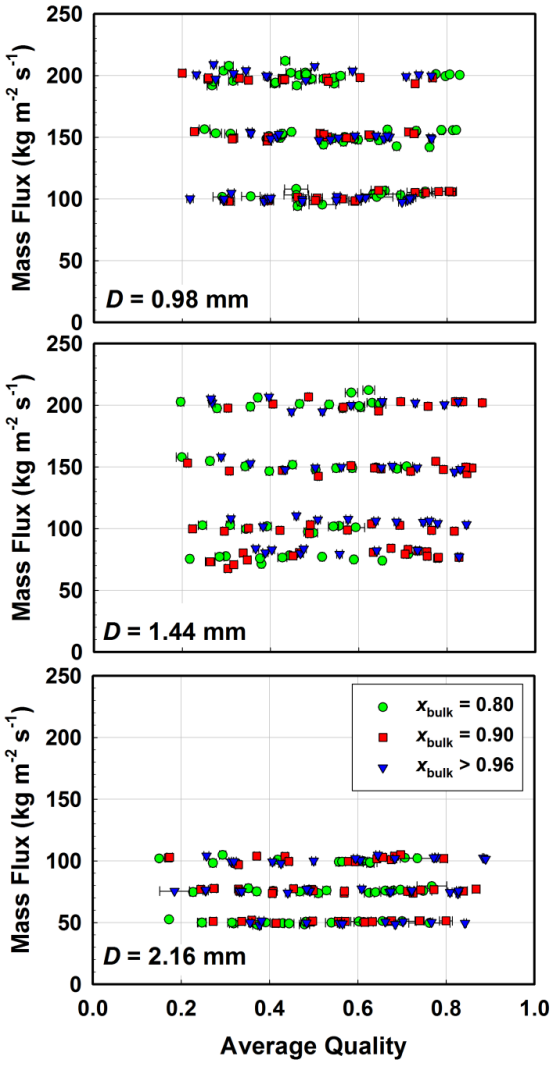

Figure 6.1: Average quality of zeotropic mixture data

As seen from Table 6.3, the uncertainty in the average test section quality is low (±1.7%). However, the uncertainty is slightly larger than it was for pure ammonia (*i.e.*, ±1.7% versus ±0.6%), due to the additional uncertainty in calculating the bulk mass fraction. From Table 6.3, it is also observed that the average temperature glide decreases with increasing bulk ammonia mass fraction. For reference, a plot of equilibrium temperature for each bulk mass fraction versus quality at a constant pressure of 1500 kPa is shown in Figure 6.2. As can be seen from the figure, as the mass fraction of ammonia

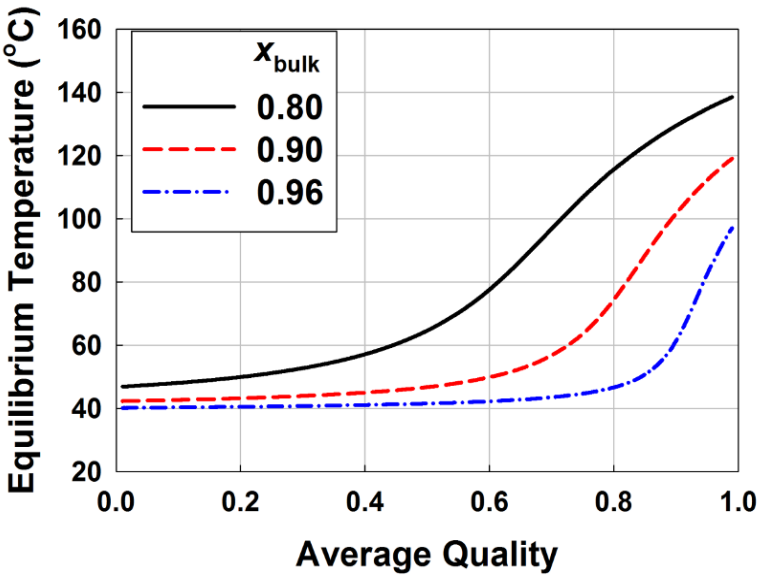

Figure 6.2: Equilibrium mixture temperature versus quality at *P* = 1500 kPa

is increased, the temperature glide is confined to a narrower quality range. Because data are collected over the entire quality range, the average temperature glide achieved for the high ammonia mass fraction points is smaller.

The average test section heat duty for the 0.98, 1.44 and 2.16 mm test sections was 61 W, 84.5 W, and 85 W, respectively. The average uncertainty in the calculated heat duties for all data was ±4.2%. This low uncertainty allowed for an accurate determination of the apparent condensation heat transfer coefficient, as well as an accurate basis for comparison of the film model described in the following chapter. Figure 6.3 summarizes the average condensation heat duty, and the average uncertainty in the calculated condensation heat duty.

6.3 Mixture Apparent Heat Transfer Coefficient

The mixture apparent heat transfer coefficient was calculated for every data point, according to the procedures described in Chapter 4. The calculated parameter is due to an aggregate of the heat and mass transfer resistances. In this section, the apparent heat

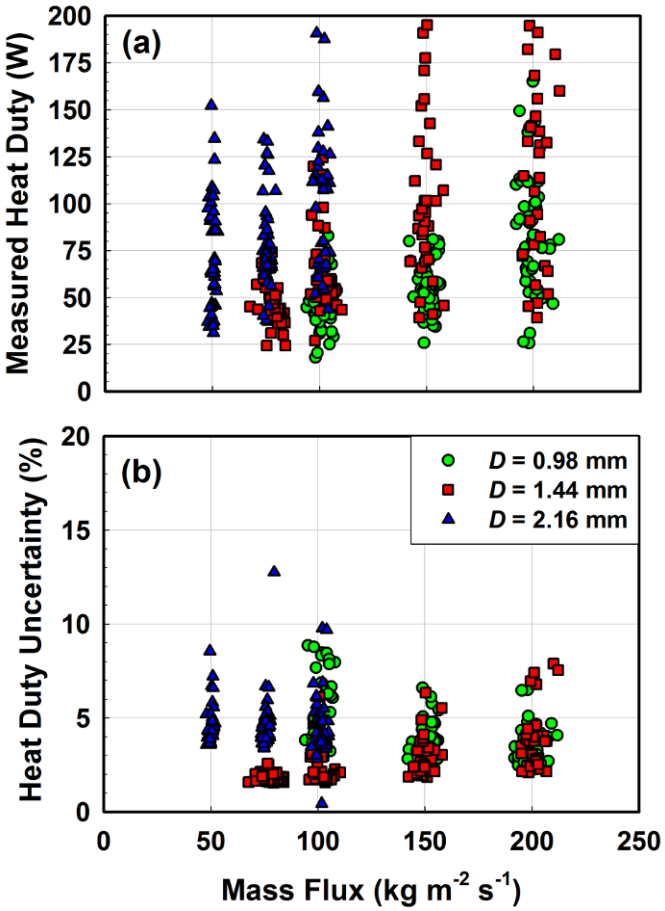

Figure 6.3: Summary of (a) average condensation heat duty and (b) heat duty uncertainty

transfer coefficient is presented for all data, and then compared with heat transfer coefficients for pure ammonia at similar conditions and correlations from the literature using the equilibrium Silver-Bell-Ghaly approach to approximate the additional mixture resistance. Figure 6.4 shows the apparent heat transfer coefficient as a function of tube diameter, mass flux, and bulk mass fraction of ammonia.

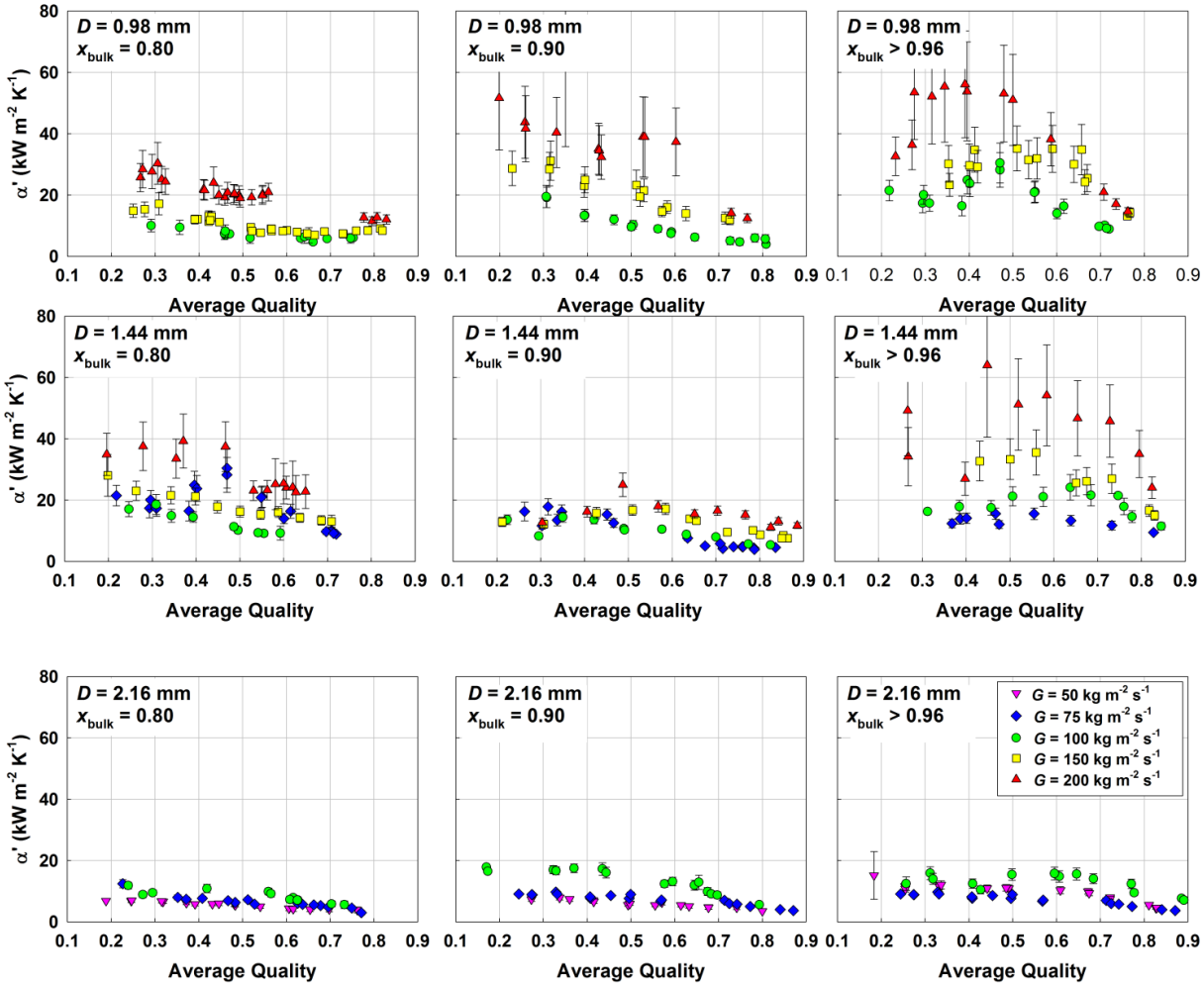

Figure 6.4: Zeotropic mixture condensation apparent heat transfer data

Some interesting trends are immediately evident. Unlike the pure ammonia data, the apparent heat transfer coefficient does not increase with increasing quality. Rather, a local maximum or a continuous gradual decrease in apparent heat transfer coefficient is observed with increasing quality, depending on the conditions. This behavior can be attributed to two effects: 1) the reduction of the interface saturation temperature below the equilibrium temperature due to mass transfer resistance and 2) the change in liquid-film heat transfer coefficient with quality. If there were no mixture effects, it would be expected that the heat transfer coefficient increase at higher qualities (consistent with pure ammonia results), due to a thinner liquid film and increased vapor/liquid shear, enhancing transport across the film. However, this region of favorable liquid-film heat transfer coefficient is negated due to mass transfer resistance effects, which result in a vapor/liquid interface temperature lower than the equilibrium saturation temperature, degrading heat transfer. Consider again Figure 6.3, which shows the zeotropic mixture equilibrium temperature as a function of quality for each mass fraction. At higher quality, the slope of the equilibrium temperature is greatest. Physically, this can be attributed to the condensation of the mostly less volatile water at high qualities. At lower qualities, most of the water has condensed, and the ammonia-water mixture increases in concentration toward pure ammonia, leading to much smaller mixture effects. The combination of high liquid-film heat transfer coefficient and large mass transfer effects at high quality, and low liquid-film heat transfer and low mass transfer effects at low quality result in the fairly flat apparent heat transfer coefficient profiles that are observed here, particularly at lower mass flux and larger tube diameter (where liquid-film heat transfer coefficients are smaller). This effect is more clearly illustrated in Figure 6.5, which

compares the ammonia condensation heat transfer coefficient at T_{sat} = 40°C and the apparent heat transfer coefficient of the zeotropic mixture with x_{bulk} = 0.90 in a D = 1.44 mm tube. For reference, the equilibrium temperature of the zeotropic mixture is plotted as a function of quality.

It can be seen that for the mixture, a maximum apparent heat transfer coefficient is reached at about a quality of 0.55. This peak corresponds well with the change in slope of the T_{eq} versus quality line. In this region, for an equivalent change in quality, the temperature glide increases sharply, indicating a large change in phase concentration that results in significant desuperheating-like behavior of the vapor. The relatively poor gas-phase sensible heat transfer mechanism, coupled with the vapor and liquid phase mass transfer resistances, can potentially explain the observed degradation in Figures 6.4 and

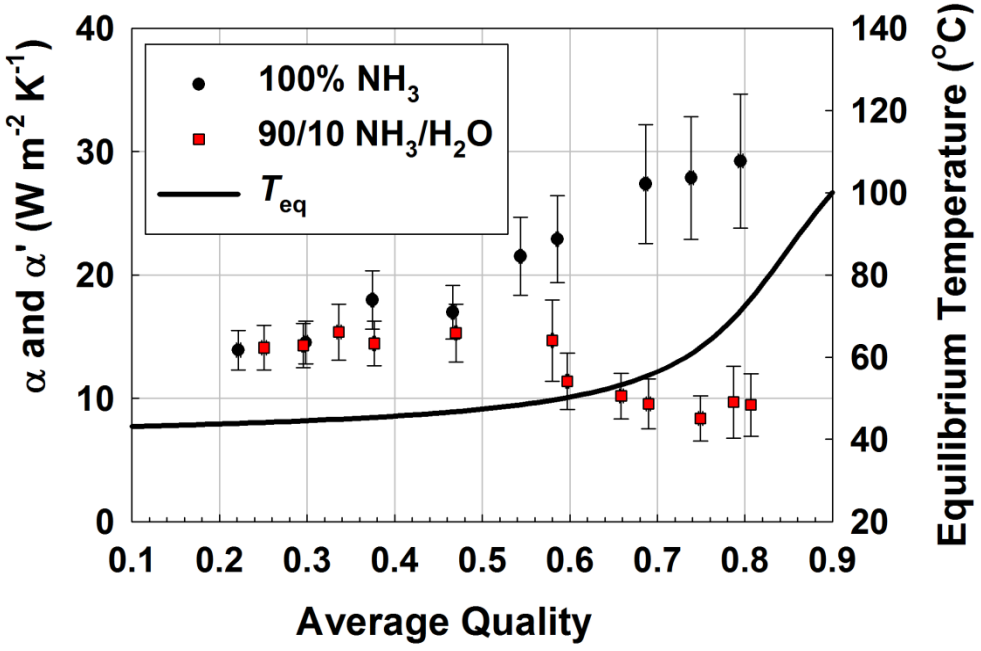

Figure 6.5: Comparison of pure ammonia and zeotropic ammonia condensation heat transfer coefficients for D = 1.44 mm and G = 100 kg m^{-2} s^{-1}

6.5.

The trends of increasing apparent heat transfer coefficient with increasing mass flux and decreasing tube diameter are similar to those observed for the pure ammonia case. This can be attributed to the higher liquid-film heat transfer coefficient at these conditions.

6.3.1 Uncertainty and Resistance Ratios

For the pure ammonia experiments, maintaining a low uncertainty in the calculated heat transfer coefficient was difficult due to the very high expected coefficients (up to 55 kW m^{-2} K^{-1}). Due to the zeotropic mixture degradation, the average values of apparent heat transfer coefficient are much lower (α'_{avg} = 15 kW m^{-2} K^{-1}). This resulted in much larger apparent resistance ratios for the mixture, as seen in Figure 6.6. Here, the average

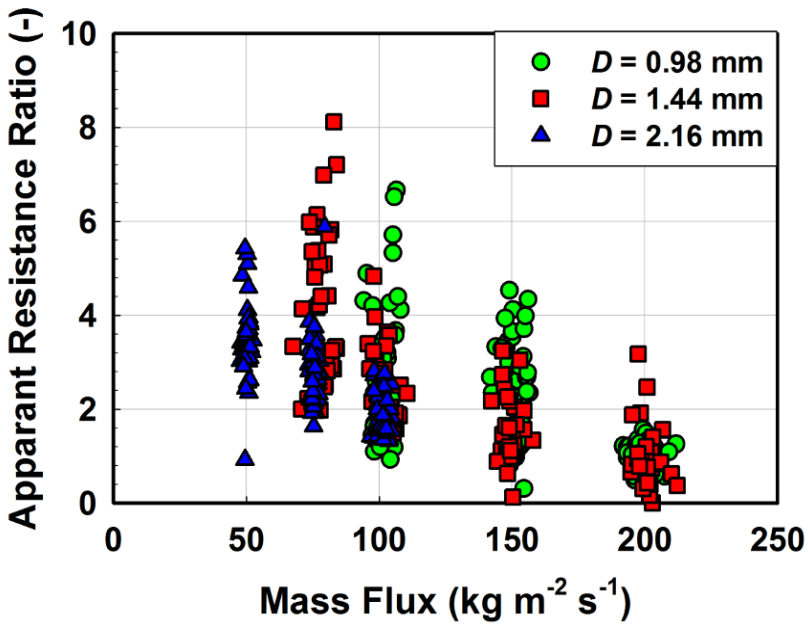

Figure 6.6: Summary of apparent heat resistance ratio for zeotropic mixtures

resistance ratio is 3.4, compared to an average of 1.75 for pure ammonia.

From the figure, the lowest resistance ratios occur at high mass flux (*i.e.*, regions of high liquid-film transfer coefficient), with most of the values of resistance ratio well above 1. Thus, while it was still important to maintain a low water-side thermal resistance, the primary contribution to the apparent heat transfer coefficient uncertainty was the uncertainty in the measured heat duty and the bulk mass fraction of ammonia. The average uncertainty of the apparent heat transfer coefficient for the 0.98, 1.44 and 2.16 mm tubes was 17.6, 13.9, and 11.4%, respectively. The lower uncertainty at the largest tube can be attributed to the smallest liquid-film heat transfer coefficients, resulting in a larger resistance ratio.

6.4 Apparent Heat Transfer Coefficient Comparison with Literature

The apparent heat transfer coefficient data were compared with various macro and mini/microchannel condensation heat transfer correlations. Each correlation used for comparison utilized the equilibrium Bell and Ghaly (1973) approximate mixture resistance:

$$R_{\text{mix}} = \left(\frac{\dot{Q}_{\text{S,V}}}{\dot{Q}_{\text{T}}} \right) \left(\frac{1}{\alpha_{\text{V}}} \right) \tag{6.1}$$

In Eq. (6.1), the vapor-phase heat transfer coefficient is calculated from the Churchill (1977b) correlation. The condensation correlations and the Bell and Ghaly (1973) method were both introduced in Chapter 2. The macro and mini/microchannel condensation correlations considered here were the same as those considered for pure ammonia in Chapter 4. The results from the best performing models are shown

graphically in Figure 6.7, while a summary of average deviation (AD) and absolute average deviation (AAD) is shown in Table 6.4. For comparison, the AAD for pure ammonia is also shown

The figure and table show that all the models under predict the data. In addition, all models using the mixture correction exhibit poorer overall agreement than the

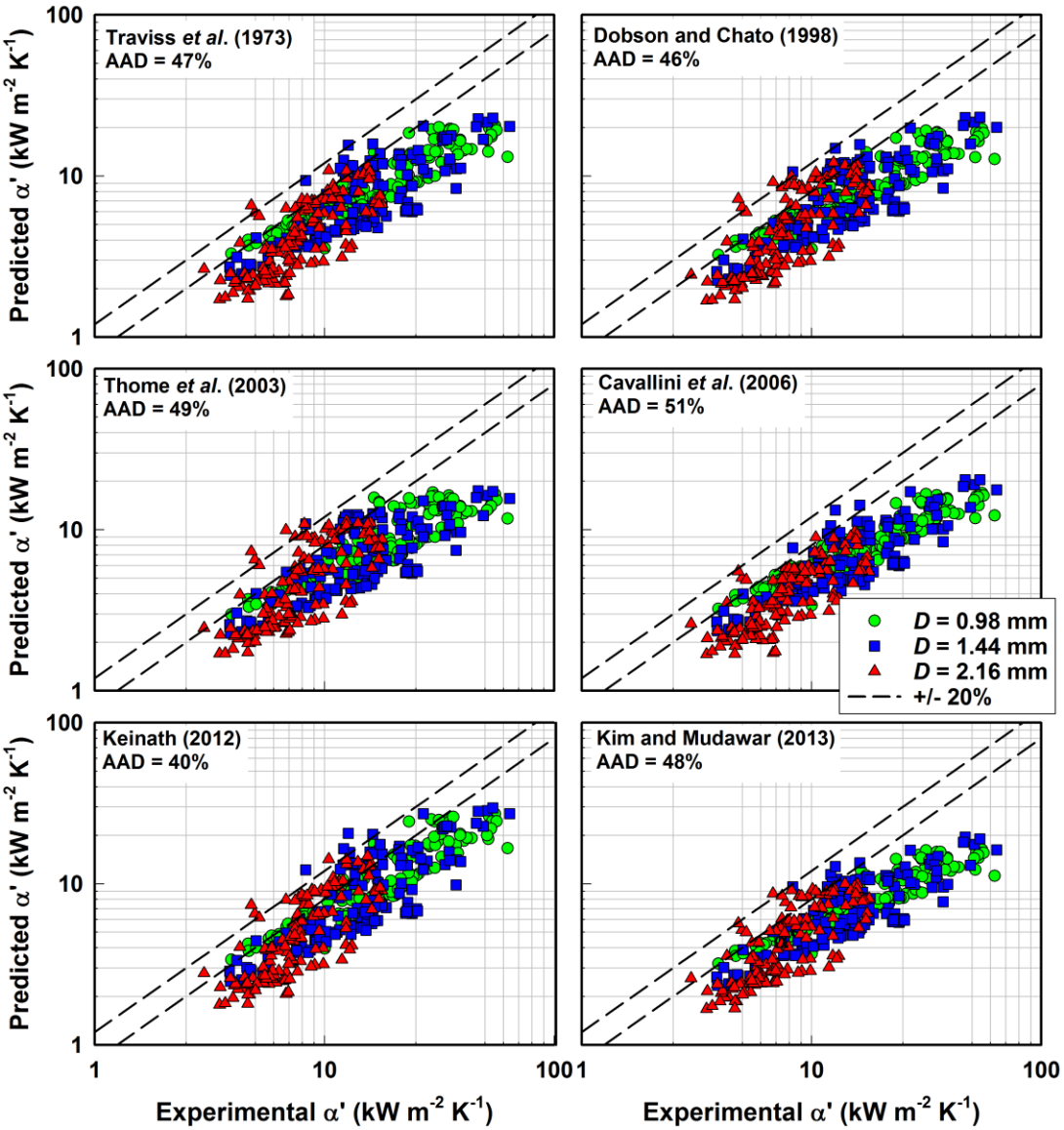

Figure 6.7: Comparison of zeotropic apparent heat transfer coefficient data with literature correlations using Silver-Bell-Ghaly correction factor

uncorrected models for pure ammonia, indicating the additional complication of accounting for mass transfer effects through the approximate equilibrium approach. Of the evaluated models, the Keinath (2012) model predicts the data best. It is interesting to note that this model also predicted the pure ammonia data the best (see Table 6.4).

This consistent agreement suggests that while mass transfer effects are important for the zeotropic mixture condensation, the underlying liquid film heat transfer mechanisms are similar between ammonia and ammonia/water mixtures. However, for the case of zeotropic mixtures, it appears that the mixture resistance (Eq. (6.1)) is overestimated, resulting in poorer agreement than for pure ammonia (AAD = 40% versus 32%). This over prediction of apparent mixture resistance can potentially be attributed to the very large temperature glide of NH_3/H_2O mixtures, which leads to a very large effective resistance. Still, the similarity in trend of liquid-phase heat transfer between pure ammonia and mixtures will be used in the development of a non-equilibrium film model in the following chapter.

Table 6.4: Comparison of measured versus predicted apparent heat transfer coefficient

	Zeotropic Mixtures		**100% NH_3**
Study	**AD (%)**	**AAD (%)**	**AAD (%)**
Shah (2009)	-65	66	66
Keinath (2012)	-38	40	32
Kim and Mudawar (2013)	-47	48	44
Traviss *et al.* (1973)	-46	47	36
Shah (1979)	-52	52	45
Dobson and Chato (1998)	-45	46	37
Thome *et al.* (2003)	-47	49	44
Cavallini *et al.* (2006)	-51	51	46

6.5 Mixture Pressure Drop Experimental Results

Frictional pressure gradients for zeotropic mixtures were measured at the same time as heat duty and apparent heat transfer coefficient. The results for all tubes, mass flux, and bulk ammonia concentrations are shown in Figure 6.8. The results are consistent with the trends for quality, mass flux, and tube diameter observed in the condensing ammonia data (Chapter 5.3). The effect of changing bulk ammonia mass fraction is shown in Figure 6.9. As the bulk mass fraction of ammonia decreases, the pressure gradient slightly increases at a given mass flux, tube diameter, and quality. However, this effect is less pronounced than the effect of changing tube diameter and mass flux. The slight change in pressure drop can be attributed to changing properties of the fluid, namely surface tension, liquid-vapor density ratio, and liquid-vapor viscosity ratio (see Table 6.5). It should be noted that the properties in Table 6.5 are evaluated for saturated liquid at a quality of 0 and vapor at quality of 1. At a given point during condensation, the actual liquid and vapor properties will be different, due to varying composition of each phase. The properties in Table 6.5 are the bounding values. As the bulk fraction of water is increased at a fixed pressure, the value of the liquid-vapor density ratio increases, which yields larger differences in phase velocities and higher interfacial shear, increasing frictional pressure gradient compared to pure ammonia.

Figure 6.10 shows the percent uncertainty of the frictional gradient as a function of mass flux and tube diameter, as well as the ratio of calculated frictional pressure gradient drop to measured pressure gradient. Here the data for the largest tube and lowest mass flux (D = 2.16, G = 50 kg m^{-2} s^{-1}) are excluded, as the measured pressure drop is extremely low, resulting in very large uncertainties .

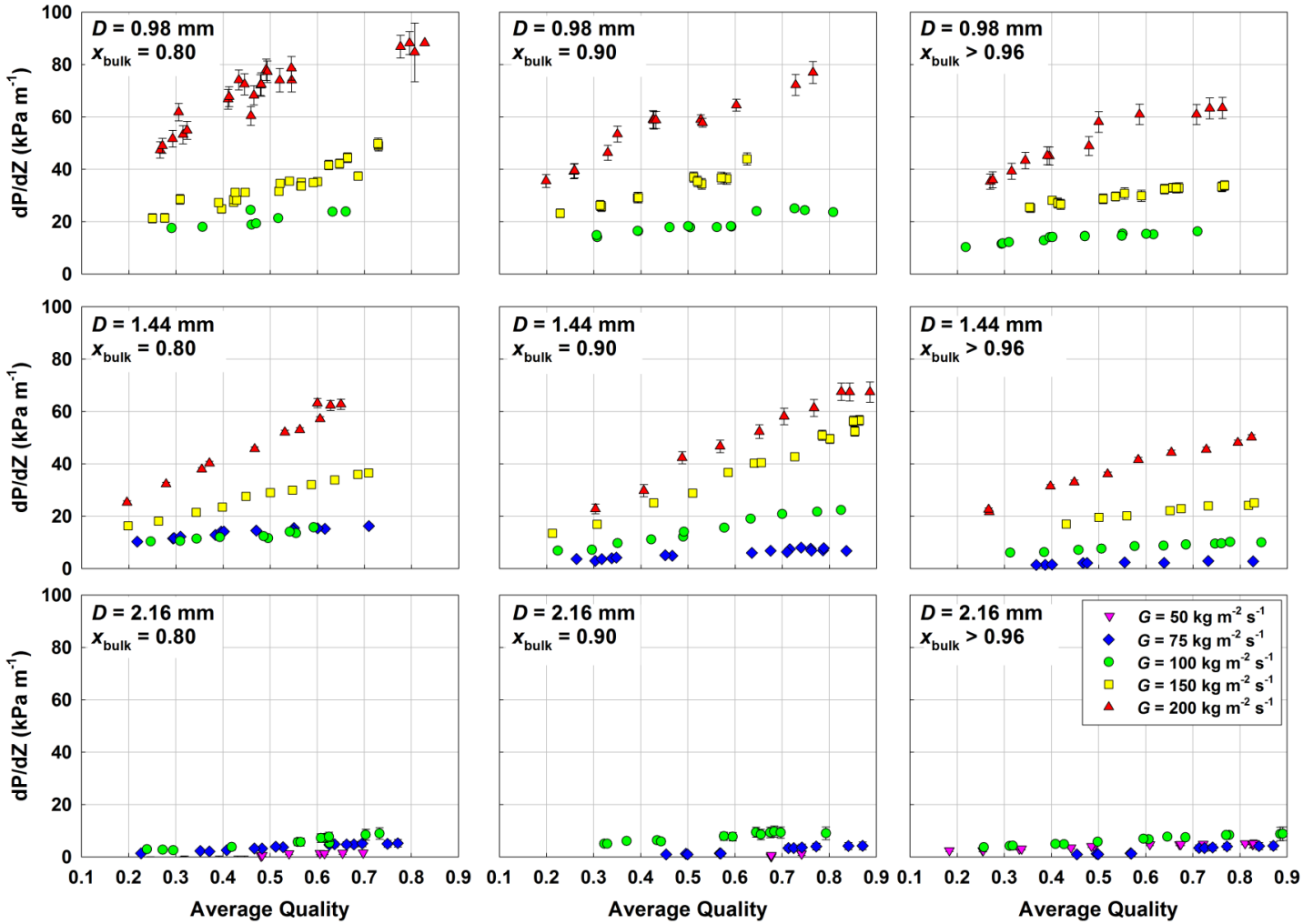

Figure 6.8: Zeotropic mixture condensation pressure drop data

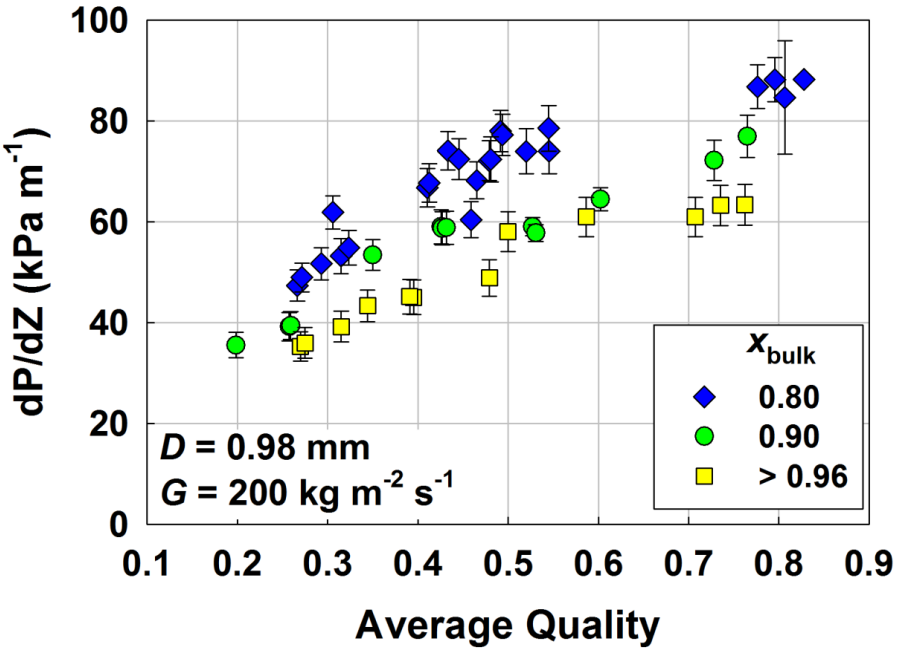

Figure 6.9: Effect of ammonia bulk mass fraction on zeotropic mixture frictional pressure gradient for D = 0.98 mm, G = 200 kg m^{-2} s^{-1}

Table 6.5: Comparison of saturated properties of ammonia and zeotropic ammonia mixtures

	P_{sat} = 1500 kPa				
x_{bulk}	ΔT_{glide}	h_{fg} (kJ kg^{-1})	ρ_L/ρ_V	μ_L/μ_V	σ (N m^{-1})
0.80	93	1705	82.8	11.3	0.0211
0.90	78	1501	74.0	9.5	0.0190
0.96	60	1349	66.8	10.9	0.0172
1.0	0	1099	48.2	11.0	0.0164

The average uncertainty in the calculated frictional gradient was ±9.5% (excluding D = 2.16, G = 50 kg m^{-2} s^{-1} data). The average uncertainty for each tube for the 0.98, 1.44 and 2.16 mm tubes was ±5.8%, ±4.5%, and ±23.5%, respectively. The average uncertainty was lowest for the D = 1.44 mm tube because the highest mass fluxes (G = 200 kg m^{-2} s^{-1}), and thus very high frictional losses, were possible in this test section. Due to the very low frictional pressure drop in the largest tube, the minor losses

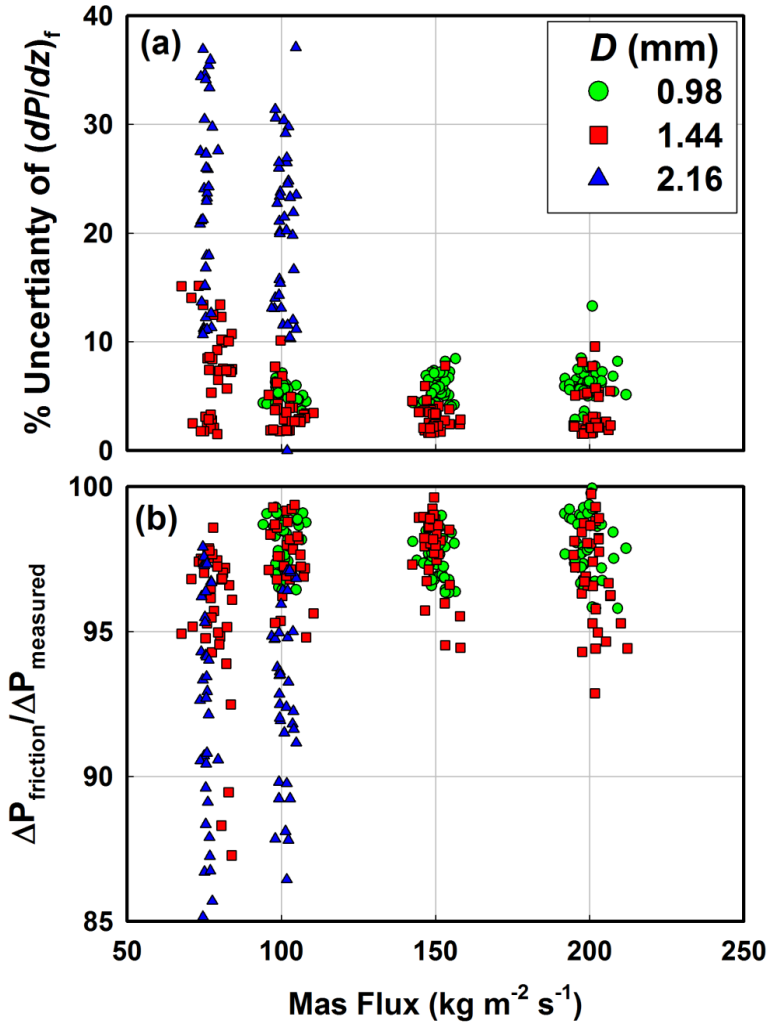

Figure 6.10: (a) Uncertainty of frictional pressure gradient and (b) ratio of calculated frictional pressure drop to total measured pressure drop

accounted for a much greater percentage of the measured value, resulting in significantly greater uncertainty.

6.6 Mixture Pressure Drop Comparison with Literature

The calculated condensing mixture frictional pressure gradient was compared with the pressure drop models used in Chapter 5 for pure ammonia (see Table 5.9 in Chapter 5). These models were previously introduced in Chapter 4. The results are tabulated in Table 6.6 as a function of tube diameter and shown graphically in Figure 6.11. The overall agreement of the correlations with pure ammonia is also included for reference in Table 6.6.

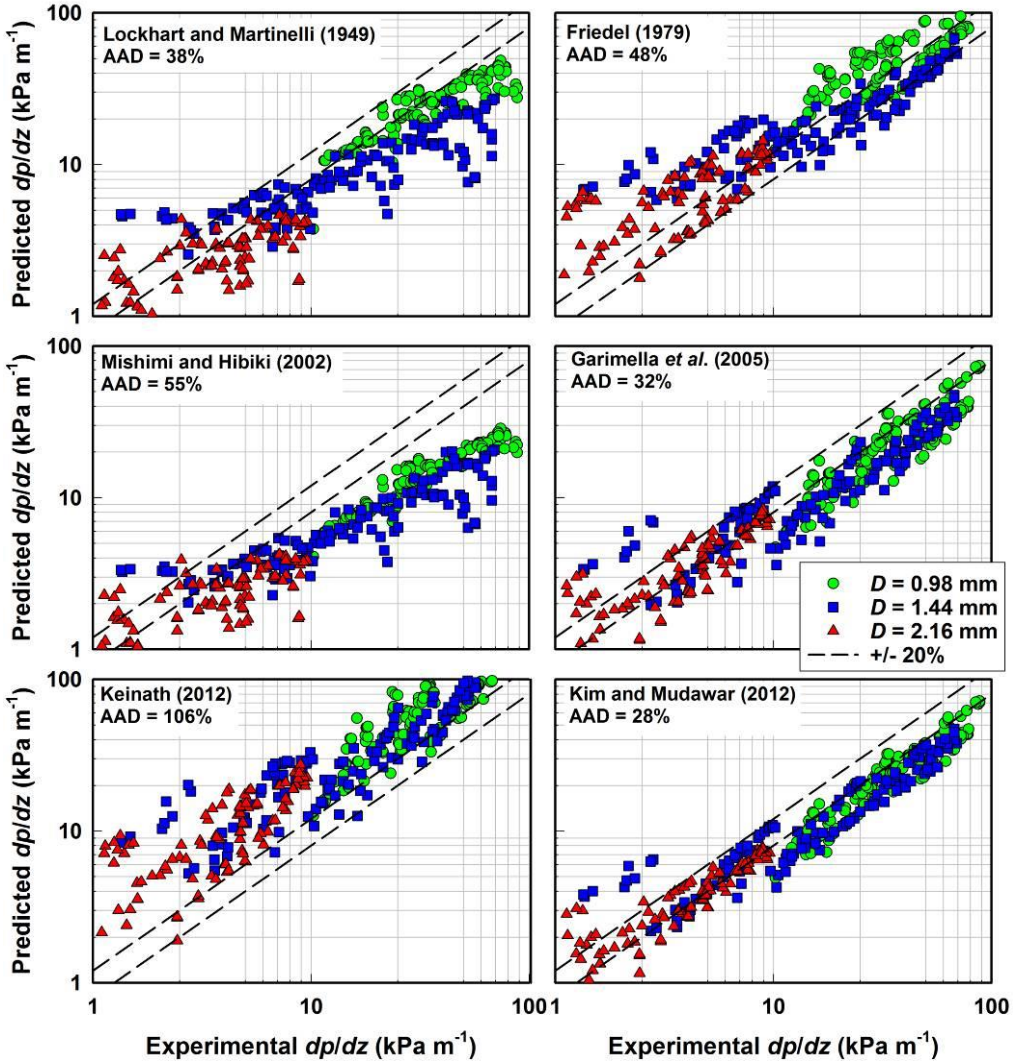

Figure 6.11: Comparison of zeotropic mixture condensation frictional pressure gradient data with literature correlations

Table 6.6: Pressure drop model agreement with mixture data

Study	Mean Average Percentage Error (AAD)				
	0.98 mm	1.44 mm	2.16 mm	Total	NH_3 Total
Mishima and Hibiki (1996)	56%	58%	46%	55%	53%
Garimella *et al.* (2005)	34%	35%	24%	32%	36%
Keinath (2012)	97%	97%	136%	106%	46%
Kim and Mudawar (2012)	31%	31%	20%	28%	31%
Lockhart and Martinelli (1949)	29%	46%	42%	38%	35%
Friedel (1979)	45%	49%	50%	48%	21%

In general, the models exhibit larger scatter with the mixture data compared with the pure ammonia data. One potential cause of this is the significant change in liquid and vapor properties as the fluid condenses. The poorest agreement overall was with the Mishima and Hibiki (1996) correlation. The poor agreement was consistent between the zeotropic mixtures and pure ammonia. The models that provided the best agreement for both mixtures and pure ammonia were the Garimella *et al.* (2005) and the Kim and Mudawar (2012) models. Both of these models were developed specifically for mini and microchannels, highlighting the importance of tube size on the underlying two-phase pressure drop mechanisms. Furthermore, these two models exhibited the best and most consistent agreement over the range of tube diameters under investigation. Interestingly, the Friedel model, which agreed with the pure ammonia data very well, exhibited relatively poor agreement here (AAD = 48%). Here, the effects of different properties, as well as the strongly varying properties as a function of quality, probably resulted in the poor performance of the empirical model.

6.7 Zeotropic Mixture Results

In this chapter, the ability to accurately calculate mixture bulk mass fraction, condensation heat duty, apparent heat transfer coefficient and frictional pressure drop was demonstrated. The dependence of pressure drop on quality and mass flux was consistent with the pure ammonia data. Of the models considered, the mini- and microchannel condensation pressure drop models of Kim and Mudawar (2012) and Garimella *et al.* (2005) predicted the data best.

The apparent heat transfer coefficient showed a different trend from the pure ammonia heat transfer coefficient, with strong degradation observed in quality ranges with large temperature glides. At low quality ranges (*i.e.*, low temperature glides and smaller mixture effects), the pure ammonia heat transfer coefficient and zeotropic mixture apparent heat transfer coefficient were in good agreement (see Figure 6.5). This implies that the underlying transport through the condensate film of the latent and sensible loads is similar between the pure ammonia and the mixtures. This is further justified by the consistent agreement with literature correlations for both fluid types, where the Keinath (2012) model predicted the ammonia and mixture data best (AAD = 32 and 40% for NH_3 and NH_3/H_2O)**.** Because the liquid-film heat transfer coefficient is similar, the degradation in heat transfer for the mixtures can primarily be attributed to the combined mixtures effects of mass transfer resistances and sensible loads. These insights are used in Chapter 7 to guide the development of a non-equilibrium film model for mixture condensation.

CHAPTER 7

PURE COMPONENT AND ZEOTROPIC MIXTURE CONDENSATION MODELING

The results presented in Chapters 5 and 6 illustrate that accurate models and design methods for ammonia or zeotropic ammonia/water microchannel condensers are not available. Existing empirical and semi-empirical design methods were developed for fluids with widely different properties, different flow conditions, and different tube geometries. In this chapter, a new correlation for condensation of ammonia in microchannels is introduced, followed by a design method for high-temperature-glide, zeotropic mixture condensers. Both the ammonia and zeotropic models are compared with data, and assessed under varying conditions and geometries. For the zeotropic model, the effects of different simplifying assumptions on the accuracy of the design method are evaluated. Finally, a summary of the implementation of the pure and mixture models is provided at the end of the chapter, with a sample calculation of each model provided in Appendix C.

7.1 Ammonia Mini/Microchannel Condensation Heat Transfer Correlation

In Chapter 5, it was demonstrated that correlations developed for pure fluid condensation in both macro and mini/microchannels could not accurately predict the ammonia data over the range of diameters and mass fluxes of interest. Of the evaluated literature models, the Keinath (2012) annular correlation predicted the data the best with a mean absolute percentage error of 32%. However, the trends in the data showed qualitative evidence of both annular and non-annular condensation, with non-annular condensation more predominant in the largest tubes at the lowest mass fluxes. Thus, starting with the

Keinath (2012) annular model as a basis, an improved multi-regime correlation for predicting ammonia mini/microchannel condensation heat transfer was developed. This model was then used in the development of a design method for zeotropic mixture condensation, described in the Section 7.3.

7.1.1 Ammonia Flow Regime Transition

A simple mechanism for determining the transition between annular and non-annular flow was necessary for model development. Because direct flow visualization of the condensing flow was not obtained, an existing transition criterion that qualitatively predicted the trends was used. For simplicity, the transition criterion defined by Cavallini *et al.* (2002a) as a function of the dimensionless gas velocity (j_G^*) was used, defined in Eq. (7.1).

$$\begin{aligned} &\text{Annular flow} && j_G^* > 2.5 \\ &\text{Non-annular flow} && j_G^* \le 2.5 \end{aligned} \tag{7.1}$$

where

$$j_{\mathrm{G}}^* = \frac{G \cdot q}{\sqrt{D \cdot g \cdot \rho_{\mathrm{V}} \cdot \left(\rho_{\mathrm{L}} - \rho_{\mathrm{V}}\right)}}$$

This criterion was developed based on an aggregate of the horizontal condensation flow transition criteria of Breber *et al.* (1980), Sardesai *et al.* (1981), Tandon *et al.* (1982) and Dobson and Chato (1998). Cavallini *et al.* (2002a) then showed that the criterion was able to predict data for condensation of halogenated refrigerants in tubes with D = 8 mm well. More recently, the criterion was used to accurately predict data on condensing R-404A and R-410A in mini/microchannels by Andresen (2007). It should be noted that the criterion in Eq. (7.1) is for horizontal tubes only. For downward

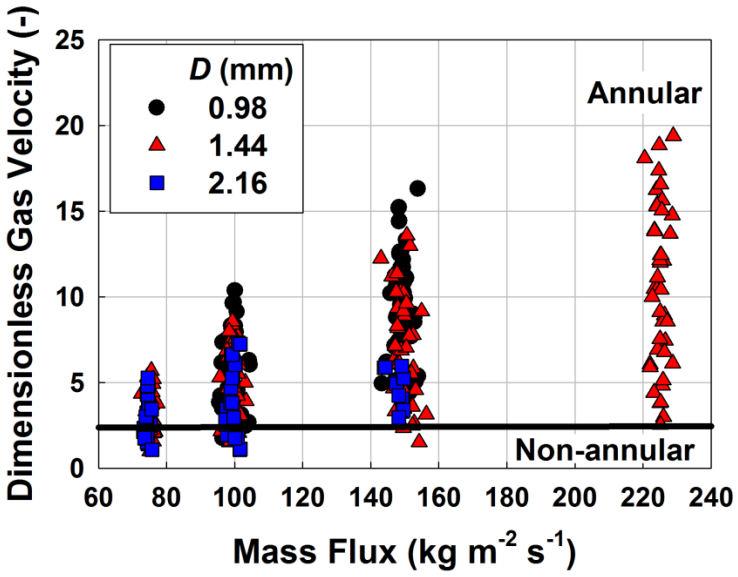

Figure 7.1: Ammonia flow transition criterion

or upward flow in vertical tubes, the gravity driven stratified wavy regime is not expected to be present. Depending on the flow orientation (*i.e.*, upward or downward), the expected flow regimes for vertical tubes include annular, churn, plug/slug and bubbly type flows (Hewitt and Roberts, 1969). Thus, different flow regime transition criteria would be necessary to apply the model developed here to vertical flows. Furthermore, because gravity may affect the circumferential distribution of the liquid film in the annular regime, verification of the applicability of the annular model developed here for vertical tubes is necessary.

Figure 7.1 shows the ammonia data evaluated using this criterion as a function of the dimensionless gas velocity, mass flux and tube diameter. Consistent with the observations of the heat transfer measurements, most of the non-annular flow points correspond to the largest tube diameters and lowest mass fluxes.

7.1.2 Model Development: Pure Ammonia, Annular Flow

The annular flow model is based on the two-phase multiplier approach of Thome *et al.* (2003) and Keinath (2012). The model is based on the schematic representation of annular flow shown in Figure 7.2.Here, the liquid film is assumed to be uniform with thickness δ and no liquid entrainment. Unlike the previous studies, the definition of Nusselt number is based on the tube diameter rather than the film thickness, as follows:

$$\mathrm{Nu_a} = \frac{\alpha D}{k_\mathrm{L}} = 0.023 \cdot \mathrm{Re_{LO}^{0.8}} \cdot \mathrm{Pr_L^{0.4}} \cdot \Phi \tag{7.2}$$

The two-phase multiplier, Φ, accounts for the enhancement in heat transfer over liquid-only flow due to vapor-liquid interfacial roughness arising from phase momentum differences. To capture these effects, the form of the two-phase multiplier is similar to that proposed by Thome *et al.* (2003):

$$\Phi = \left(1 + a \left(\frac{U_\mathrm{V}}{U_\mathrm{L}} \right)^b f_\mathrm{i}^c \right) \tag{7.3}$$

where

$$f_\mathrm{i} = \frac{\left(\rho_\mathrm{L} - \rho_\mathrm{V} \right) \cdot g \cdot \delta^2}{\sigma}$$

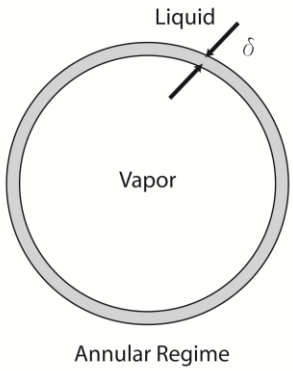

Figure 7.2: Annular flow schematic

Here, U_V and U_L are the phase velocities, and δ is the film thickness calculated from an appropriate void fraction model, described below. The term f_i accounts for the contribution of Taylor instabilities in the liquid film to the generation of interfacial waves and thus, additional heat transfer enhancement, as proposed by Thome *et al.* (2003). A regression analysis using the data predicted to be in the annular flow regime yields values of 0.27, 0.21, and -0.46, for *a*, *b* and *c*, respectively. Thus, the annular regime correlation is as follows:

$$\mathrm{Nu}_a = \frac{\alpha D}{k_L} = 0.023 \cdot \mathrm{Re}_{LO}^{0.8} \cdot \mathrm{Pr}_L^{0.4} \cdot \left(1 + 0.27 \left(\frac{U_V}{U_L} \right)^{0.21} f_i^{-0.46} \right) \tag{7.4}$$

As quality tends towards zero, the condensate film becomes very thick, and the two-phase multiplier approaches unity, yielding the liquid-only heat transfer coefficient. Thus, the model is physically consistent at the saturated liquid limit. To evaluate Eq. (7.4) , it is necessary to determine the phase velocities and film thickness. Assuming the geometry in Figure 7.2 (*i.e.*, uniform film thickness with no entrainment), the phase velocities and film thickness can be calculated as follows:

$$\frac{U_V}{U_L} = \left(\frac{q}{1-q} \right) \left(\frac{\rho_L}{\rho_V} \right) \left(\frac{1-\varepsilon}{\varepsilon} \right) \tag{7.5}$$

$$\delta = \frac{1}{2} \left(D - D_i \right) = \frac{D}{2} \left(1 - \sqrt{\varepsilon} \right) \tag{7.6}$$

Here, ε is the void fraction calculated using the drift-flux model of Keinath (2012).

$$\varepsilon = \frac{\beta}{1+\bar{V}_{\mathrm{vj}}/j} \tag{7.7}$$

Here, $\bar{V}_{\mathrm{vj}}$ is the vapor drift velocity, found as a function of the Martinelli parameter (X, Eq. (7.9)) and liquid Capillary ($\mathrm{Ca_L}$, Eq. (7.10)) number:

$$\bar{V}_{\mathrm{vj}} = 0.336 \cdot X^{0.25} \cdot \mathrm{Ca}_{\mathrm{L}}^{0.154} \left(\sqrt{\frac{\rho_{\mathrm{L}}}{\rho_{\mathrm{V}}}} - 1 \right)^{0.81} j \tag{7.8}$$

$$X = \sqrt{\frac{\left(dP/dz\right)_{\mathrm{L}}}{\left(dP/dz\right)_{\mathrm{V}}}} \tag{7.9}$$

$$\mathrm{Ca}_{\mathrm{L}} = \frac{\mu_{\mathrm{L}} \cdot \left(1-q\right) \cdot G}{\rho_{\mathrm{L}} \cdot \sigma} \tag{7.10}$$

In Eq. (7.9), the phase frictional pressure gradients were calculated using the Fanning friction factor, with the Blasisus (1913) correlation used for $\mathrm{Re} \geq 2000$:

$$f = \begin{cases} \dfrac{16}{\mathrm{Re}} & \text{for } \mathrm{Re} < 2000 \\ 0.079\,\mathrm{Re}^{-0.25} & \text{for } \mathrm{Re} \geq 2000 \end{cases} \tag{7.11}$$

The Keinath (2012) void fraction model was developed from high-speed visualization of condensing flows of R-404A in channels similar to those in the current study ($0.508 < D < 3.0$). By using a model developed for mini/microchannel condensing flows, a more accurate prediction of both film thickness and phase velocity is expected.

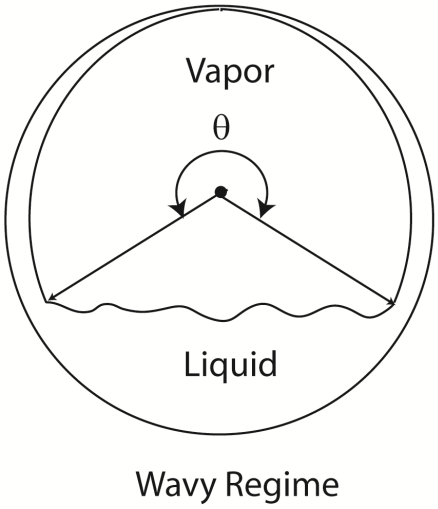

Figure 7.3: Wavy flow schematic

7.1.3 Model Development: Pure Ammonia, Non-Annular Flow

For data where $j_G^* \leq 2.5$, non-annular flow is expected to prevail. Figure 7.3 shows an idealized schematic of pure wavy flow, where thin-film condensation occurs on the top of the tube and convective heat transfer occurs through the stratified liquid pool.

As observed in the condensation flow visualization studies of Coleman and Garimella (2003) and Keinath (2012), pure wavy flow occurs over a narrow range of conditions in mini/microchannels. Thus, in the non-annular regime, a combination of annular (Figure 7.2) and wavy type flow (Figure 7.3) is expected. To account for these combined effects, Cavallini *et al.* (2006) proposed a weighted contribution of gravity and shear driven terms:

$$\mathrm{Nu}_{\mathrm{n\text{-}a}} = \left[\mathrm{Nu}_{\mathrm{a}} \left(\frac{j_{\mathrm{T}}}{j_{\mathrm{G}}^*} \right)^{0.8} - \mathrm{Nu}_{\mathrm{wavy}} \right] \left(\frac{j_{\mathrm{G}}^*}{j_{\mathrm{T}}} \right) + \mathrm{Nu}_{\mathrm{wavy}} \tag{7.12}$$

Here j_{T} is the transition gas velocity, or $j_{\mathrm{T}} = 2.5$ in the present study. The annular Nusselt number ($\mathrm{Nu_a}$) is calculated using the correlation in Eq. (7.4), above. For the wavy

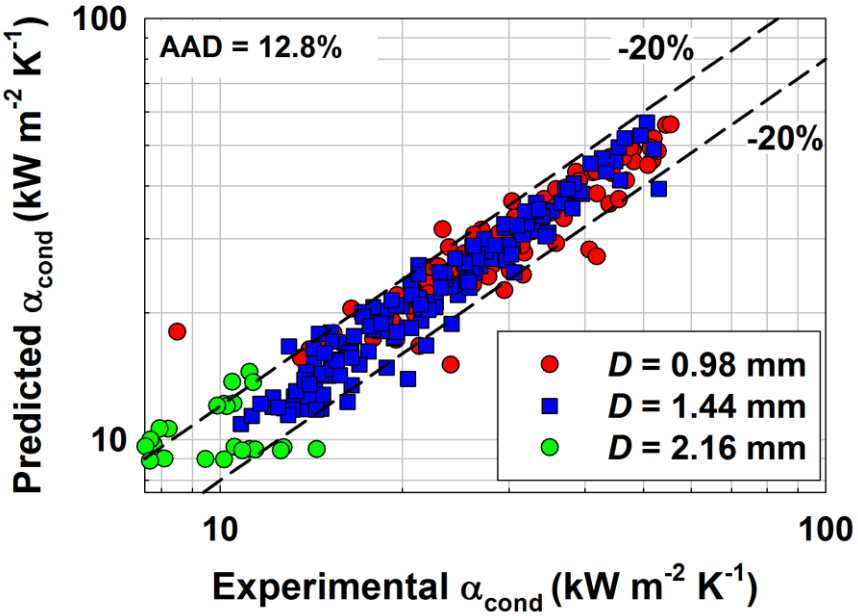

Figure 7.4: Comparison of predicted versus measured ammonia condensation heat transfer coefficient

Nusselt number, the semi-empirical correlation of Cavallini *et al.* (2006) is used (Eq. (7.13)):

$$\begin{aligned}
\mathrm{Nu}_{\mathrm{wavy}} &= \left[\left(1+0.741\left[\frac{1-q}{q}\right]^{0.3321}\right)^{-1}\mathrm{Nu}_{\mathrm{film}}+\mathrm{Nu}_{\mathrm{pool}}\right] \\
\mathrm{Nu}_{\mathrm{film}} &= \left(\frac{D}{k_{\mathrm{L}}}\right)0.725\left(\frac{k_{\mathrm{L}}^{3}\rho_{\mathrm{L}}\left(\rho_{\mathrm{L}}-\rho_{\mathrm{V}}\right)gh_{\mathrm{fg}}}{\mu_{\mathrm{L}}D\left(T_{\mathrm{sat}}-T_{\mathrm{wall}}\right)}\right)^{0.25} \\
\mathrm{Nu}_{\mathrm{pool}} &= 0.023\,\mathrm{Re}_{\mathrm{LO}}^{0.8}\,\mathrm{Pr}_{\mathrm{L}}^{0.4}\left(1-x^{0.087}\right)
\end{aligned} \tag{7.13}$$

This correlation includes contributions due to falling film ($\mathrm{Nu}_{\mathrm{film}}$) condensation and convective heat transfer in the liquid pool ($\mathrm{Nu}_{\mathrm{pool}}$).

7.2 Evaluation of Ammonia Model

The absolute average deviation (AAD) for all data is 12.9%. Overall, 88% of the data are predicted within ±25%. The predicted versus actual condensation heat transfer

coefficients as a function of tube diameter are shown in Figure 7.4. It should be noted that in Figure 7.4, the model is evaluated at the measured test section *average* quality and compared to the measured test section *average* heat transfer coefficient. In fact, the test section quality and heat transfer coefficient change with position within the test section. To understand the effect of using an average quality, the required length of a tube-in-tube test section for complete condensation is calculated using the heat transfer correlation developed here for quality segments from ranging from 0.01 to 0.25.

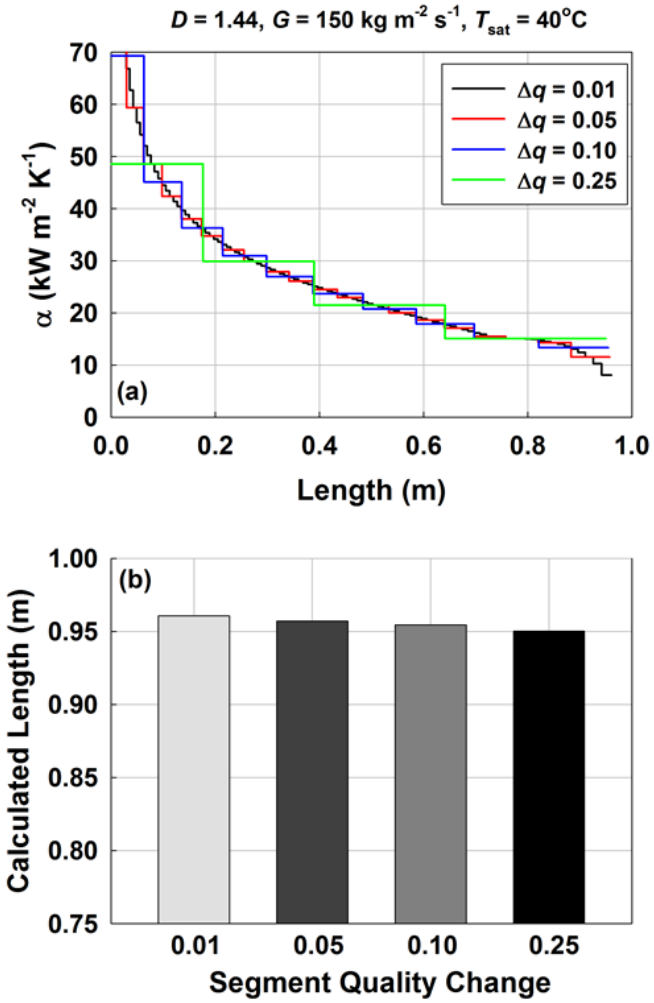

Figure 7.5: (a) Predicted heat transfer coefficient versus length and (b) total predicted length versus segment quality change

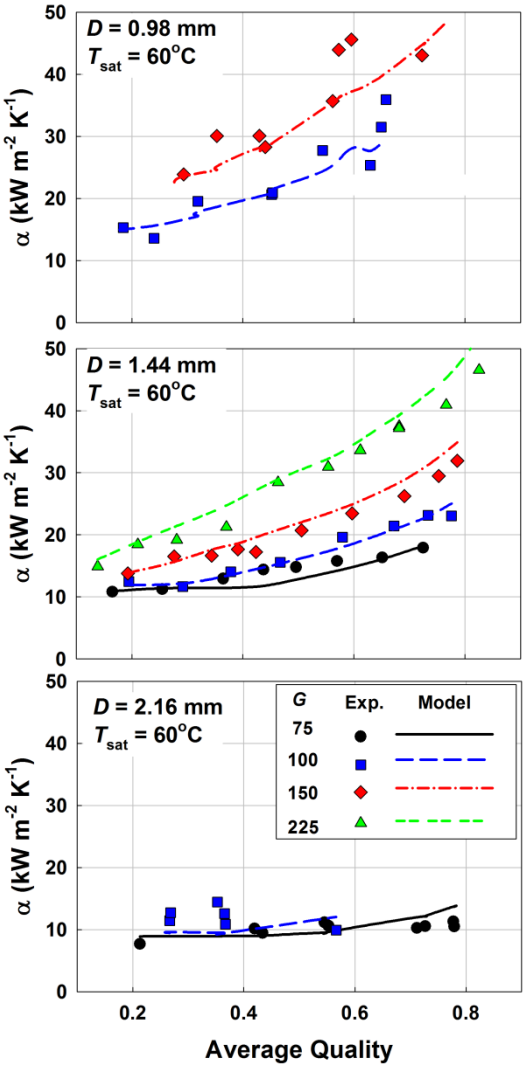

Figure 7.6: Comparison of trends of predicted versus measured ammonia condensation heat transfer coefficient

The inlet conditions to the D = 1.44 mm test section are saturated ammonia vapor (q = 1) at T_{sat} = 40°C and G = 150 kg m^{-2} s^{-1} with a constant coolant temperature of 35°C. Starting with the specified inlet conditions, a 1-D heat transfer analysis was conducted for discrete nodes, where the local heat transfer coefficient was determined from the correlation described above at the local quality, and the required length of each segment was determined. Figure 7.5a shows a plot of predicted heat transfer coefficient as a

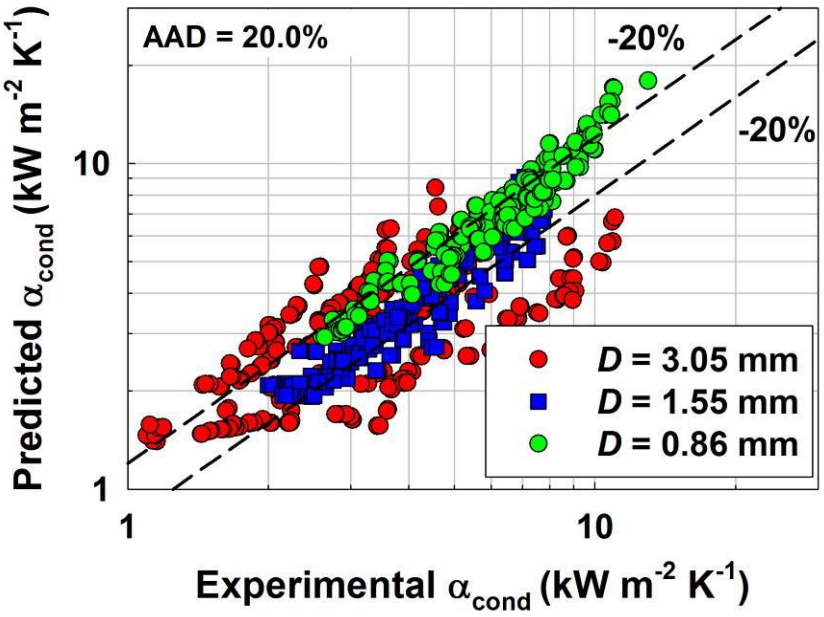

Figure 7.7: Comparison of predicted versus measured R-404A condensation heat transfer coefficient from Keinath (2012)

function of position for each chosen quality decrement, while Figure 7.5b shows the calculated total condenser length for each case. A 1.1% smaller condenser is predicted for a segment quality decrement of 0.25 compared to a decrement of 0.01.

Thus, comparison of the heat transfer coefficient predicted by the correlation at the average experimental test section quality to the average measured heat transfer coefficient for the test section provides a valid assessment of the predictive capability of the correlation. This is further illustrated by comparing model trends with data overlaid as a function of quality and tube diameter in Figure 7.6 for a saturation temperature of T_{sat} = 60°C. Data are indicated with solid symbols, while model predictions are shown as lines. The model is able to predict the observed trends with quality, tube diameter and mass flux well. In addition, there is no discontinuity as the flow regime transitions from non-annular to annular flow regimes. More detailed discussion of the model trends is presented in the following section.

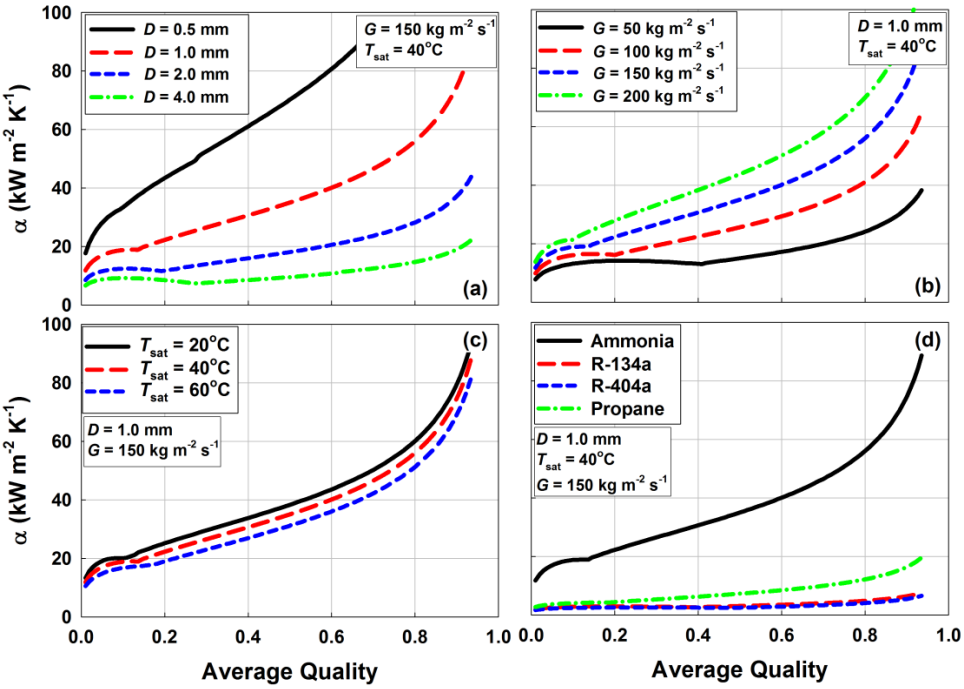

Figure 7.8: Evaluation of model trends for different (a) tube diameter, (b) mass flux, (c) saturation temperature, and (d) fluid type

The predictions of this correlation were then compared with data from Keinath (2012) for condensing R-404A in circular microchannels ($0.86 < D < 3.05$ mm) at varying mass fluxes ($200 < G < 800$ kg m^{-2} s^{-1}) and saturation temperatures ($30 < T_{sat} < 60$°C). The measured versus predicted heat transfer coefficient as a function of tube diameter is shown in Figure 7.7.

The model exhibited an AAD of 20% with 70% of the data predicted within 25%. Thus, the model is able to predict well the condensation heat transfer of a fluid with significantly different properties in similar mini/microchannel geometries. The agreement is particularly good for the two smallest channels, with a AAD of 17% and 12.8% for the 0.86 and 1.55 mm channels, respectively, indicating that microchannel effects are predicted well. It should be noted that the R-404A data in Figure 7.7 were not used in the regression analysis for developing the annular flow model.

Table 7.1: Fluid properties at T_{sat} = 40°C

	P_r (-)	h_{fg} (kJ kg^{-1})	ρ_L/ρ_V	k_L (W m^{-1} K^{-1})	σ (N m^{-1})
Ammonia	0.14	1099	48.2	0.443	0.016
R-134a	0.25	163	22.9	0.076	0.006
R-404A	0.49	121	9.5	0.063	0.002
Propane	0.32	307	15.5	0.088	0.005

To better illustrate the model trends, Figure 7.8 shows predicted heat transfer coefficients at varying (a) diameters (b) mass fluxes (c) saturation conditions, and (d) fluid type.

All trends are consistent with the data and the discussion provided in Chapter 5. In the top left figure (a), the effect of diameter at a fixed mass flux is clearly illustrated, with significantly increasing heat transfer coefficient at smaller tube diameter. In addition, the transition to non-annular flow occurs at a higher quality as the tube diameter increases, consistent with the experimental data. Likewise, in the top right figure (b), the transition to non-annular flow occurs at increasing quality at the lowest mass fluxes. Again, this is consistent with experimental results and physically, the larger inertial forces at higher mass flux limit the influence of gravity to cases with larger liquid fractions. The dependence on saturation temperature (c) for the range considered is small. This was reflected in the experimental results, and can be attributed to the relatively narrow range of reduced pressures to which the saturation temperatures correspond ($0.08 < P_r < 0.23$). Finally, the much larger condensation heat transfer coefficients of ammonia for equivalent diameter, saturation temperature and mass flux compared to other working fluids can be seen in the bottom right figure (d). The much higher heat transfer coefficient can be attributed to the superior transport properties of ammonia, shown in

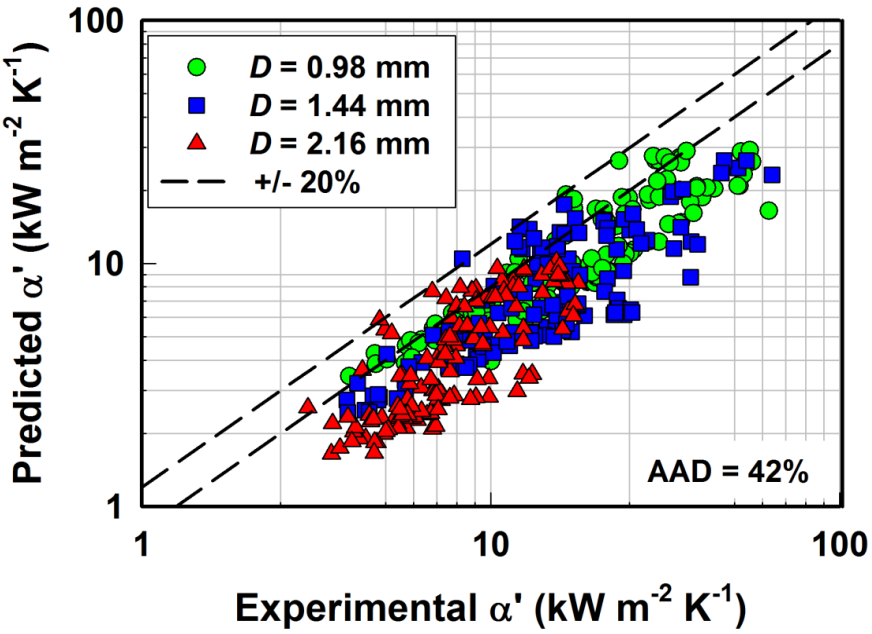

Figure 7.9: Comparison of predicted zeotropic mixture apparent heat transfer coefficient with measured value

Table 7.1. In particular, the liquid thermal conductivity and enthalpy of vaporization are much higher.

7.3 Design Method: Zeotropic Ammonia-Water Mixtures, Non-Equilibrium Film

As presented in Chapter 2, zeotropic mixture condensation can be modeled either by direct solution of the conservation equations, via the simplified equilibrium method (*i.e.*, Silver-Bell-Ghaly correction factor) or through the non-equilibrium film theory framework. For mini/microchannel flows, direct solution of the conservation equations is difficult due to the complex flow morphology (*i.e.*, annular versus non-annular flow, presence of surface waves, etc.). Furthermore, the high computational cost of such a solution makes it cost-prohibitive for design processes. Thus, the equilibrium and non-equilibrium methods are the two most commonly used approaches for zeotropic condenser design.

In Chapter 6, it was shown that the equilibrium method under predicted the measured apparent zeotropic heat transfer coefficient when applied to several common condensation models in the literature. Part of this poor agreement was attributed to the poor predictive capability of the underlying condensation models due to the significantly different properties of ammonia and ammonia/water mixtures. To assess the importance of the predicative capability of the underlying condensation heat transfer model, the zeotropic data are compared in Figure 7.9 with the new model developed above (Eqs. (7.4) and (7.12)), using the Silver-Bell-Ghaly correction (Eq. (7.14)).

$$R_{\text{mix}} = \left(\frac{\dot{Q}_{\text{S,V}}}{\dot{Q}_{\text{T}}} \right) \left(\frac{1}{\alpha_{\text{V}}} \right) \tag{7.14}$$

The equilibrium method using the improved liquid-phase heat transfer coefficient still under predicts all of the data, with a AAD of 42%. This significant deviation can be attributed to the very large temperature glide of this zeotropic mixture, which leads to large sensible heat load; increasing the apparent mixture resistance term in Eq. (7.14). The results here indicate that the equilibrium model cannot adequately predict the mixture effects of the high-temperature-glide ammonia/water mixture, even when using a validated liquid-phase heat transfer coefficient model as the basis.

Thus, an improved non-equilibrium model was developed. As discussed in Chapter 2, the non-equilibrium film theory framework has been used by several researches for designing zeotropic condensers. The film theory considers the coupled temperature and mass transfer gradients in each phase (shown schematically in Figure

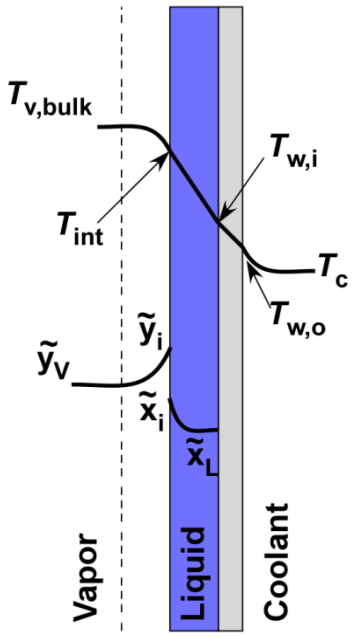

Figure 7.10: Non-equilibrium film theory schematic

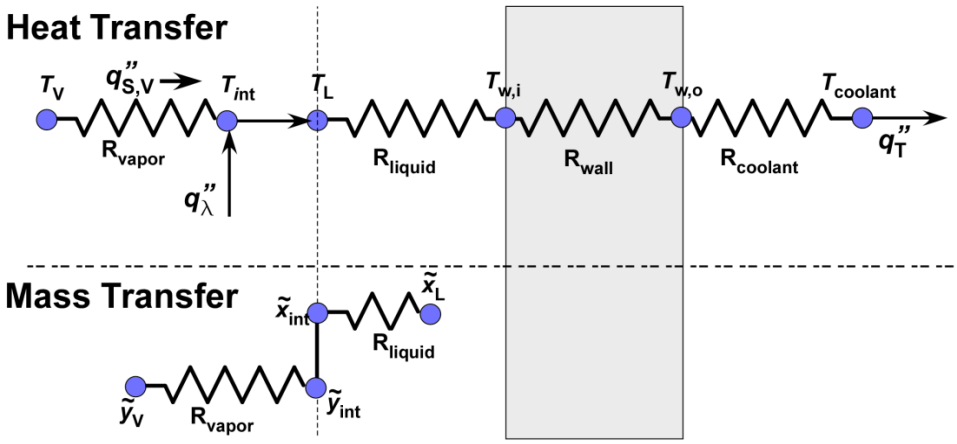

Figure 7.11: Schematic of non-equilibrium film theory heat and mass transfer resistances

7.10), yielding the overall heat and mass transfer resistance network shown in Figure 7.11.

By evaluating each of the thermal and mass transfer resistances in Figure 7.11, either the total condensation load or the required condenser area can be determined.

Solution of the coupled resistances requires an iterative procedure, such as the one proposed by Price and Bell (1974). To ease the computational demands, previous investigations have relied on several simplifying assumptions, including:

1. Annular flow only
2. Laminar condensate film
3. Neglect sensible cooling of condensate
4. Neglect sensible cooling of vapor phase
5. Well mixed liquid film (no liquid-phase mass transfer resistance)

In the proposed model, assumptions 1 through 4 are removed, while assumption 5 is demonstrated to be valid for the fluids, flow conditions and geometries of interest here. To account for the temperature glide and changing thermophysical properties of the zeotropic mixture, the test section is divided into discrete segments. The local heat duty of each segment is calculated, and the outlet conditions (*i.e.*, phase temperature, concentrations) are used as the inlet conditions for the subsequent segment. The basic procedure for calculating the condensation heat duty for a segment with a known heat transfer area and inlet conditions is outlined in the following steps. A representative segment is shown in Figure 7.12, with the calculated values for important liquid and vapor temperatures, mass fractions and mass flow rates. For illustrative purposes, sample values for a data point with D = 0.98 mm, x_{bulk} = 0.90 and G = 100 kg m^{-2} s^{-1} are shown. For this data point, the total condenser length is 0.13 m, which is divided into eight segments. The sample values reported here are for the 2nd segment. The complete sample

calculations for this point are provided in Appendix C. The intermediate sample values reported for each step were determined from the results of the iterative solution of the entire system of equations, but are reported with the introduction of each equation for illustrative purposes.

7.3.1 Vapor-Phase Sensible Heat Transfer

The sensible heat transfer of the vapor phase was determined from the following equation:

$$\dot{Q}_{S,V} = \frac{\alpha_V \cdot \kappa \cdot \Delta T_{LM,V}}{\pi \cdot D \cdot L_{seg}} \tag{7.15}$$

Here, α_V is the vapor phase heat transfer coefficient, κ is the Ackerman (1937) correction factor and $\Delta T_{LM,V}$ is the log-mean temperature difference between the vapor phase and the liquid interface. The vapor-phase heat transfer coefficient was calculated using the Churchill (1977a) correlation (Eqs. (7.16) and (7.17)), which accounts for

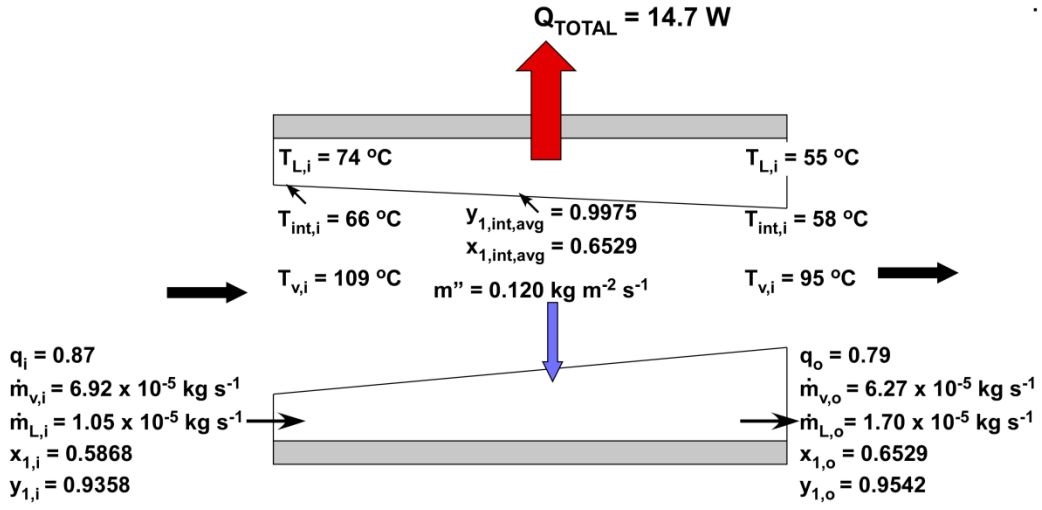

Figure 7.12: Schematic of zeotropic condenser segment

laminar, transition and turbulent flow regimes. In the calculation of the vapor-phase friction factor (Eq. (7.17)), a smooth surface is assumed (*i.e.*, $\varepsilon = 0$) . While in reality interfacial roughness is expected, a reliable estimate of this value is not possible from the present data. However, the enhancement of heat transfer due to interface roughness is captured in the liquid-phase heat transfer coefficient correlation, as introduced above. It will be shown in the following section that the uncertainty due to these assumptions in the overall calculated heat load is negligible. For the sample point, the calculated vapor-phase heat transfer coefficient was 906 W m^{-2} K^{-1}.

$$\mathrm{Nu_V} = \left(4.364^{10} + \left(\frac{exp\left(\frac{2200 - \mathrm{Re_V}}{365} \right)}{4.364^2} + \frac{1}{\left(6.3 + 0.079 \cdot \left(\frac{f_V}{8} \right)^{0.5} \cdot \mathrm{Re_V} \cdot \frac{\mathrm{Pr_V}}{\left(1 + \mathrm{Pr_V}^{0.8} \right)^{5/6}} \right)^2} \right)^{-5} \right)^{1/10} \tag{7.16}$$

$$f_V = 8 \cdot \left(\left(\frac{8}{\mathrm{Re_V}} \right)^{12} + \frac{1}{\left(\left(2.457 \cdot ln\left(\frac{1}{\left(7/\mathrm{Re_V} \right)^{0.9} + \left(0.27 \cdot \varepsilon \right)} \right) \right)^{16} + \left(37530/\mathrm{Re_V} \right)^{16} \right)^{1.5}} \right)^{1/12} \tag{7.17}$$

The Ackerman (1937) correction factor (Eq. (7.18)) accounts for the effect of non-zero mass flux on the transport of thermal energy, and is a function of the condensing flux, vapor specific heat and vapor-phase heat transfer coefficient. For the sample point, the value of κ was 1.17.

$$\kappa = \frac{a}{1-\exp(-a)}$$

where

$$a = \frac{m'' \cdot c_{P,V}}{\alpha_V} \tag{7.18}$$

Finally, the vapor-phase log-mean temperature difference is a function of the segment inlet and outlet vapor phase and interface temperatures. These temperatures are found through the iterative solution method, with an LMTD of 39.7 K for the sample point.

$$\Delta T_{LM,V} = \frac{\left(T_{v,i} - T_{int,i}\right) - \left(T_{v,o} - T_{int,o}\right)}{\ln\left(\frac{T_{v,i} - T_{int,i}}{T_{v,o} - T_{int,o}}\right)} \tag{7.19}$$

Closure to the vapor-phase sensible heat transfer is accomplished through a vapor-phase energy balance, as shown below:

$$\dot{Q}_{S,V} = \dot{m} \cdot q_{avg} \cdot c_{P,V} \cdot \left(T_{V,i} - T_{V,o}\right) \tag{7.20}$$

For the sample point, the calculated vapor sensible heat load was 2.3 W, with a change in vapor bulk temperature from the segment inlet to the outlet from 109 to 95.1°C, and a change in quality from 0.87 to 0.79.

7.3.2 Vapor-Phase Mass Transfer and Condensing Flux

In a binary mixture, the condensing flux contains two components designated 1 (ammonia) and 2 (water) in the following equations. As discussed in Chapter 2, the total

condensing flux with the film theory assumptions can be determined by the following equation:

$$\dot{N}_{\mathrm{T}} = \dot{N}_1 + \dot{N}_2 = \beta_{\mathrm{V}} \cdot C_{\mathrm{T,V}} \cdot \ln\left(\frac{z - \tilde{y}_{1,\mathrm{int,avg}}}{z - \tilde{y}_{1,\mathrm{avg}}}\right) \tag{7.21}$$

Here, $\tilde{y}_{1,\mathrm{int,avg}}$ and $\tilde{y}_{1,\mathrm{avg}}$ are the vapor interface and bulk mole fractions, respectively. The parameter *z* is defined in Eq. (7.22), and the vapor-phase mass transfer coefficient is found using the Chilton-Colburn heat and mass (1934) transfer analogy, as shown in Eq. (7.23).

$$z = \frac{\dot{N}_1}{\dot{N}_{\mathrm{T}}} \tag{7.22}$$

$$\begin{aligned} \mathrm{Sh}_{\mathrm{V}} &= \mathrm{Nu}_{\mathrm{V}}\left(\frac{\mathrm{Sc}_{\mathrm{V}}}{\mathrm{Pr}_{\mathrm{V}}}\right)^{1/3} \\ \beta_{\mathrm{V}} &= \frac{\mathrm{Sh}_{\mathrm{V}} D_{1-2}}{D} \end{aligned} \tag{7.23}$$

For the sample point, the vapor-phase interface and bulk mole fractions were 0.9976 and 0.9479, respectively, and the vapor-phase mass transfer coefficient was 0.06 m s^{-1}. From the iterative solution, the total condensing flux was found to be 0.0069 kmol s^{-1} m^{-2}, or 0.120 kg s^{-1} m^{-2} on a mass basis. The value of *z* was 0.768.

7.3.3 Liquid-Phase and Overall Heat Transfer

With the condensing flux and sensible cooling of the vapor determined, the liquid-phase and overall heat transfer could be calculated. From Figure 7.11, it can be seen that the vapor sensible load and latent load due to condensation are transported through the liquid

film. It is also assumed that the entire condensate subcooling heat load is transported through the entire film thickness. This yields the following expression for total segment heat load:

$$\dot{Q}_{\mathrm{T}} = \frac{\Delta T_{\mathrm{LM,int}}}{R_{\mathrm{L}} + R_{\mathrm{wall}} + R_{\mathrm{water}}} \tag{7.24}$$

The parameter $\Delta T_{\mathrm{LM,int}}$ is the log-mean temperature difference between the liquid interface temperature and the coolant. To facilitate comparison with the experiments, the coolant was assumed to maintain a constant temperature for the sample case, and the inlet and outlet interface temperatures were 66.4 and 58.2°C, respectively, yielding an interface LMTD of 15.9 K. When the model is applied to other flow orientations (*i.e.*, counterflow or co-flow), as well as different coupling fluid flow rates and properties, the coolant temperature should be incremented based on the calculated segment heat duty. For the sample condenser, the construction was identical to that of the tube-in-tube test section (see Chapter 3). Thus, the wall thermal resistance was found using Eq. (7.25), the water-side thermal resistance was found from Eq. (7.26), and the liquid-phase thermal resistance from Eq. (7.27).

$$R_{\mathrm{wall}} = \frac{\ln\left(OD_{\mathrm{i}}/ID_{\mathrm{i}}\right)}{2\pi \cdot k_{\mathrm{tube}} \cdot L_{\mathrm{seg}}} \tag{7.25}$$

$$R_{\mathrm{water}} = \frac{1}{\alpha_{\mathrm{water}} \cdot \pi \cdot OD_{\mathrm{i}} \cdot L_{\mathrm{seg}}} \tag{7.26}$$

$$R_{\mathrm{L}} = \frac{1}{\alpha_{\mathrm{L}} \cdot \pi \cdot ID_{\mathrm{i}} \cdot L_{\mathrm{seg}}} \tag{7.27}$$

The water-side heat transfer coefficient (α_{water} = 46,000 W m^{-2} K^{-1}) was found from the single-phase annulus correlation of Garimella and Christensen (1995), while the liquid-phase heat transfer coefficient (α_L = 30,030 W m^{-2} K^{-1}) was calculated from the ammonia condensation model developed in the previous section. The use of a model validated for similar fluid properties and tube geometric for predicting the liquid-film heat transfer was very important for improving the predictive capability of the film theory framework, as will be further discussed below. For the sample point, R_{wall} was 0.169 K W^{-1}, R_{water} was 0.30 K W^{-1}, and R_L was 0.62 K W^{-1}. The total heat duty for the segment from the iterative solution was 14.7 W. The new liquid-phase heat transfer coefficient was dependent on the local flow regime, with the criterion of Eq. (7.1) used to delineate annular and non-annular mechanisms. As the fluid properties and flow conditions of the zeotropic mixture and pure ammonia were similar, the transition criterion was expected to apply well. Furthermore, previous investigations by Tandon *et al*. (1985a), Shah and Granryd (2000b) and Del Col et al. (2005) have shown that flow regime transitions developed for pure fluids and azeotropic mixtures have extrapolated well for zeotropic mixtures. For condensation conditions of interest, the transitions are governed by the relative importance of shear, gravity and surface tension forces, as determined by the fluid properties and the flow conditions. For sufficiently low flow rates or for very thin films, there is the potential for mixture-specific mechanisms such as surface tension driven thermocapillary flow, or solutal capillary flow to affect the condensate flow. However, these effects are considered to be insignificant compared to the hydrodynamic forces in the present investigation.

7.3.4 Phase Species and Energy Balance and Interface Condition

To provide closure to the above set of equations, as well as account for the sensible cooling of the condensate and vapor phases, energy and species balances for each phase were derived. In addition, the interface condition was coupled to vapor-liquid equilibrium data for the ammonia/water mixture under consideration. This allowed the interfacial temperatures and the coupled interfacial vapor/liquid concentrations to be determined. The segment mass (Eq. (7.28)) and species (Eq. (7.29)) balance for the vapor and liquid phases were determined as follows:

$$\begin{aligned} \dot{m}_{\mathrm{L,O}} &= \underbrace{\dot{m}_{\mathrm{L,i}}}_{\text{Mass flow liquid in}} + \underbrace{m_1^{''} \cdot A}_{\text{Mass Flow NH}_3\text{ condensed in}} + \underbrace{m_2^{''} \cdot A}_{\text{Mass Flow H}_2\text{O condensed in}} \\ \dot{m}_{\mathrm{V,O}} &= \underbrace{\dot{m}_{\mathrm{V,i}}}_{\text{Mass flow vapor in}} - \underbrace{m_1^{''} \cdot A}_{\text{Mass Flow NH}_3\text{ condensed in}} - \underbrace{m_2^{''} \cdot A}_{\text{Mass Flow H}_2\text{O condensed in}} \end{aligned} \tag{7.28}$$

$$\begin{aligned} x_{1,\mathrm{O}} \dot{m}_{\mathrm{L,O}} &= \underbrace{x_{1,\mathrm{i}} \cdot \dot{m}_{\mathrm{L,i}}}_{\text{Mass Flow NH}_3\text{ in}} + \underbrace{m_1^{''} \cdot A}_{\text{Mass Flow NH}_3\text{ condensed in}} \\ y_{1,\mathrm{O}} \dot{m}_{\mathrm{V,O}} &= \underbrace{y_{1,\mathrm{i}} \cdot \dot{m}_{\mathrm{V,i}}}_{\text{Mass Flow NH}_3\text{ in}} - \underbrace{m_{11}^{''} \cdot A}_{\text{Mass Flow NH}_3\text{ condensed out}} \end{aligned} \tag{7.29}$$

Here, $\dot{m}_{\mathrm{V,i}} / \dot{m}_{\mathrm{V,O}}$ and $\dot{m}_{\mathrm{L,i}} / \dot{m}_{\mathrm{L,O}}$ are the vapor and liquid mass flow rates at the segment inlet/outlet, and $x_{1,\mathrm{O}}$ and $y_{1,\mathrm{O}}$ are the liquid and vapor mass fractions of ammonia at the segment inlet/outlet ($x_{1,\mathrm{i}}$ = 0.5868, $x_{1,\mathrm{O}}$ = 0.6529, $y_{1,\mathrm{i}}$ = 0.9358, and $y_{1,\mathrm{O}}$ = 0.9542 for the sample point). An overall phase energy balance was then defined as:

$$\begin{aligned} \dot{m} \cdot h_{\mathrm{out,T}} &= \dot{m}_{\mathrm{V,O}} h_{\mathrm{V,O}} + \dot{m}_{\mathrm{L,O}} h_{\mathrm{L,O}} \\ h_{\mathrm{out,T}} &= h_{\mathrm{in,T}} - \frac{\dot{Q}_T}{\dot{m}} \end{aligned} \tag{7.30}$$

Here, $h_{\text{in,T}}$ and $h_{\text{out,T}}$ were the total mixture inlet and outlet enthalpies, and $\dot{Q}_T$ is the total segment heat duty. The vapor- and liquid- phase outlet enthalpies (with sample value) were defined as follows:

$$\begin{aligned} h_{\text{V,O}} &= f\left(P, T_{\text{V,O}}, y_{1,\text{O}}\right) = \ 1491 \text{ kJ/kg} \\ h_{\text{L,O}} &= f\left(P, T_{\text{L,O}}, x_{1,\text{O}}\right) = \ 55.3 \text{ kJ/kg} \end{aligned} \tag{7.31}$$

Here, the vapor outlet temperature was calculated from Eq. (7.20), and the bulk liquid film outlet temperature was calculated using Eq. (7.32).

$$T_{\text{L,o}} = T_{\text{wall,o}} + \frac{1}{3}\left(T_{\text{int,o}} - T_{\text{wall,o}}\right) \tag{7.32}$$

When used in the Nusselt (1916) laminar solution, this film reference temperature was shown by Minkowycz and Sparrow (1966) to accurately match numerical solutions with non-constant properties. An alternative reference temperature can be derived by assuming a linear temperature profile and a laminar film. However, condensation flow visualization studies by Coleman and Garimella (2003) and Keinath (2012) suggest that even for small channels (D < 3 mm), the liquid film is highly agitated over a wide range of conditions, and a linear profile is not likely in practice. Wither either assumption, by using a bulk liquid temperature ($T_{\text{L,o}}$ = 54.8°C) rather than the interface temperature ($T_{\text{int,o}}$ = 58.2°C), the effect of condensate subcooling is including in the overall heat duty. The importance of this parameter is highlighted in the following section.

Because the film is assumed to be well mixed from a mass transfer perspective, the average liquid interface mass fraction is equal to the average bulk mass fraction of the liquid:

$$x_{\text{int,avg}} = x_{1,\text{avg}} = 0.65 \text{ (well mixed film)} \tag{7.33}$$

With this assumption, the interface temperature and vapor interface mass fraction can be determined by assuming thermodynamic equilibrium at the interface:

$$\begin{aligned} T_{\text{int,avg}} &= f\left(P, q = 0, x_{1,\text{int,avg}} = 0.65\right) = 58.2^{\circ}\text{C} \\ y_{1,\text{int,avg}} &= f\left(P, q = 1, T_{\text{int,avg}} = 58.6^{\circ}\text{C}\right) = 0.9975 \end{aligned} \tag{7.34}$$

The system of equations was then completely defined and an iterative solution could be found. The calculated outlet temperature and mass fractions of each phase were used as the inlet conditions for the subsequent segment. Each segment was solved and the overall heat duty was determined. For the sample case the total heat duty for all eight segments was 56.7 W.

7.4 Evaluation of Non-Equilibrium Model

The model discussed above was used to predict the heat duty of the test section for the

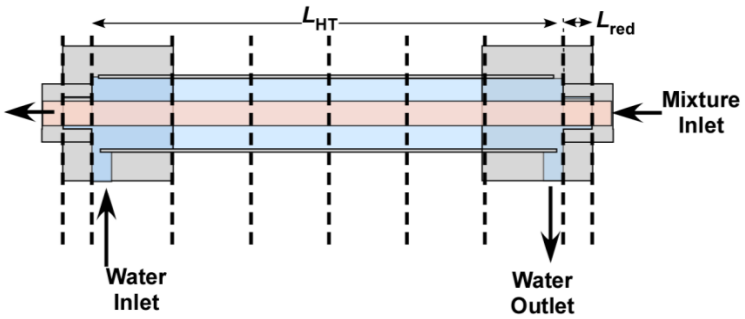

Figure 7.13: Schematic of segmented test section

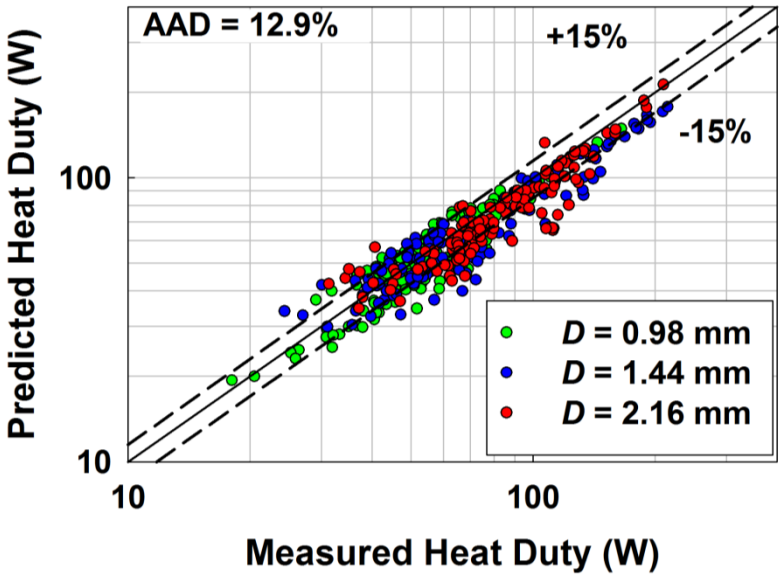

Figure 7.14: Predicted versus measured zeotropic condensation heat duty

Table 7.2: Predictive capability of improved zeotropic condenser model

***D* (mm)**	**AAD (%)**	**AD (%)**
0.98	11.9	-3.4
1.44	14.3	-9.0
2.16	12.5	-8.2
ALL	12.9	-6.7
x_{bulk}	**AAD (%)**	**AD (%)**
0.80	11.9	-4.7
0.90	11.6	-5.4
> 0.96	15.5	-10.8

different experimental conditions. The calculated value of heat duty was then compared with the measured value to assess the predictive capability of the model. The test section was segmented as shown in Figure 7.13.

A segment sensitivity analysis was performed at several different inlet conditions, with less than a 0.5% change in calculated heat duty by increasing from 8 to 9 segments. As shown, the annulus was divided into equal length regions, and the water-side heat transfer coefficient was calculated using the Garimella and Christensen (1995) annulus

heat transfer coefficient. Each reducer region was treated as an individual segment, and the water-side heat transfer coefficient for those regions was calculated using the effective thermal conductivity model discussed previously in Chapter 4. The predicted versus measured test section heat duties are shown in Figure 7.14. A breakdown of AD and AAD by tube diameter and bulk ammonia mass fraction is provided in Table 7.2.

Overall the model provides good agreement with the data, with an AAD of 12.9%. Furthermore, as evidenced by Table 7.2, the agreement is consistent over a range of tube diameters and bulk fractions of ammonia. To assess the utility of comparing measured versus predicted heat duty; it is illustrative to compare the contribution of the apparent mixture thermal resistance to the condensation heat duty. The apparent mixture resistance is calculated using Eq. (7.35).

$$R'_{\text{mix}} = \frac{\Delta T_{\text{LM}}}{\dot{Q}_{\text{cond}}} - R_{\text{wall}} - R_{\text{water}} \tag{7.35}$$

Here, the LMTD is calculated using the coolant temperature and the calculated mixture inlet and outlet equilibrium temperatures. It should be noted that the apparent mixture thermal resistance is not a physical quantity, but rather an aggregate of the heat and mass transfer resistances for each data point. Recall from the results in Chapter 6 that very low experimental values of water-side and tube wall thermal resistance were maintained (*i.e.*, average apparent resistance ratio of 3.4 for the zeotropic mixture) to ensure that small changes in the apparent mixture resistance were reflected in the measured condensation heat duty. For reference, the apparent resistance ratio for all data as a function of mass flux is shown in Figure 7.15.

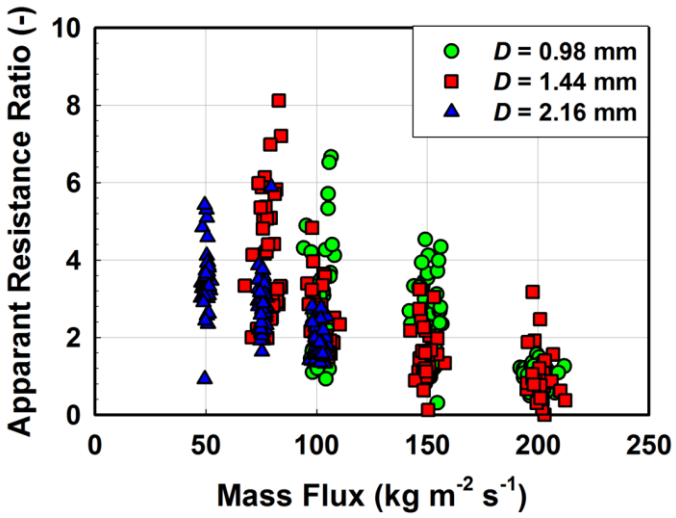

Figure 7.15: Apparent resistance ratio versus mass flux

Thus, in the present work, comparison of heat duty for assessing the predictive capability of the model is an effective and more meaningful metric than comparison of the non-physical apparent heat transfer coefficient. For data in which the coolant thermal resistance is larger than the apparent mixture resistance, comparison of measured versus

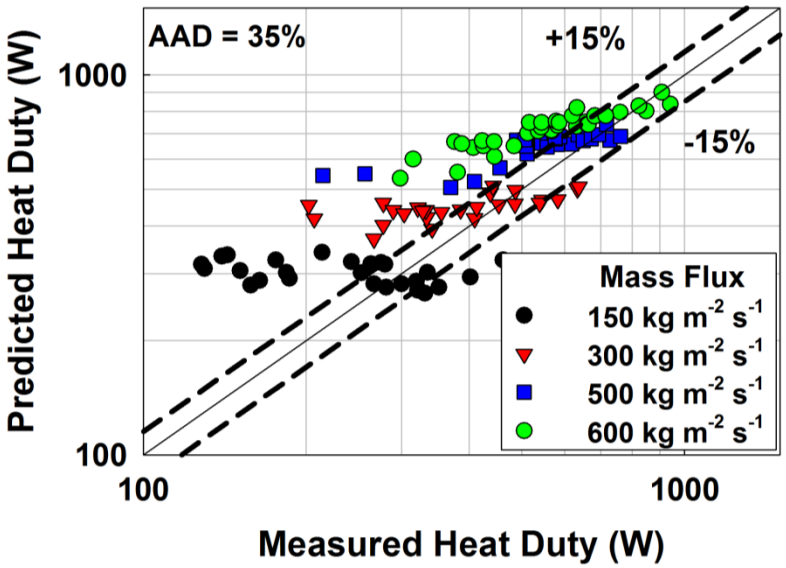

Figure 7.16: Comparison of predicted versus measured heat duty for R-245fa/*n*-pentane data of Milkie (2014)

predicted heat duty would be a less reliable indicator of model validity.

7.4.1 Comparison of Model to Data of Milkie (2014)

The model was compared with the results of Milkie (2014) to assess the applicability of the improved non-equilibrium approach for mixtures, operating conditions and tube diameters outside of the range for which the model was developed, Milkie (2014) conducted condensation experiments with mixtures of R-245fa and *n*-pentane in a 7.75 mm tube, which is much larger than the diameters investigated in the present study. Experiments were conducted at mass fluxes ranging from 150 to 600 kg m^{-2} s^{-1}, at a bulk mass fraction of R-245fa of 45%, and at bubble point temperatures ranging from 30 to 80°C ($0.05 < P_r < 0.21$). As was done for data from the present study, the predicted mixture condensation heat duty is plotted versus the experimental value as a function of mass flux in Figure 7.16.

The data are generally over predicted, with an AAD of 35% and AD of 30%. The results suggest that the liquid-phase heat transfer coefficient is over predicted by the present model, yielding higher predicted condensation heat duties. The deviation is

Table 7.3: Comparison of thermophysical properties of R-245/*n*-pentane and NH_3/H_2O zeotropic mixtures

k	NH_3/H_2O 80/10 (mass)	NH_3/H_2O 90/10 (mass)	R-245fa/*n*-pentane 45/55 (mass)
P_{sat} (kPa)	1500	1500	151
T_{bub} (°C)	139	120	40
T_{glide} (K)	93	78	7.6
h_{fg} (kJ kg^{-1})	1705	1501	284
ρ_L/ρ_V	83	74	142
k_L (W m^{-1} K^{-1})	0.47	0.46	0.10
$c_{p,L}$ (kJ kg^{-1} K^{-1})	4.8	4.9	1.9
σ (N m^{-1})	0.021	0.019	0.016

particularly high for the G = 150 and 300 kg m^{-2} s^{-1} cases. Here, the transition criterion of Eq. (7.1) predicts generally wavy flow only, with a weaker dependence of heat transfer coefficient on quality. A comparison of the relevant thermophysical properties of ammonia-water mixtures, operating temperatures and temperature glides, and the corresponding values for the R-245fa/n-pentane mixture studied by Milkie (2014) is provided in Table 7.3. Based on the large differences between the operating temperatures and the thermophysical properties of the two fluid mixtures, it appears that the flow transition criterion, as well as the individual species liquid-phase heat transfer correlations, may not extrapolate well to tube diameters, fluid properties and mass fluxes dramatically different from those of the present study. A more general liquid-phase heat transfer coefficient model would improve the overall performance of the proposed improved liquid-film model. In addition, the sensible contributions due to cooling of the vapor (average of 0.3% of total, with a maximum of 1%) and liquid condensate (average of 4.2% of total heat load, with a maximum of 7.4%) are much less important for the R-245fa/*n*-pentane mixture, compared to that of NH_3/H_2O in the present study (as discussed below). This can be attributed to the lower temperature glide of the R-245fa/*n*-pentane mixture (< 15 K), compared to 60 to 90 K for NH_3/H_2O, as well as the lower average liquid phase specific heat. The decreased importance of accounting for the sensible cooling for the R-245fa/*n*-pentane mixture increases the importance of the liquid-phase heat transfer coefficient for predicting the overall condensation duty. A detailed discussion of the importance of the sensible cooling in the present study is provided in the following sections (7.4.3 and 7.4.4).

7.4.2 Effect of Liquid-Phase Heat Transfer Coefficient Model

One of the new contributions of the proposed model is the use of a multi-regime ammonia mini/microchannel model (introduced in Chapter 7.2) for predicting the liquid-phase heat transfer coefficient. While the film theory is a theoretically rigorous method of framing the zeotropic condensation problem, it relies on underlying models for liquid and vapor heat and mass transfer for the results. In particular, the liquid-phase heat transfer coefficient is extremely important for reliably predicting the condensation heat duty, as the entire heat load is transported through the liquid phase across a small temperature difference ($T_{int} - T_{wall}$). To assess the improvement of using the new ammonia mini/microchannel model, the zeotropic design procedure outlined in Section 7.3 was followed using the following pure component condensation heat transfer correlation as

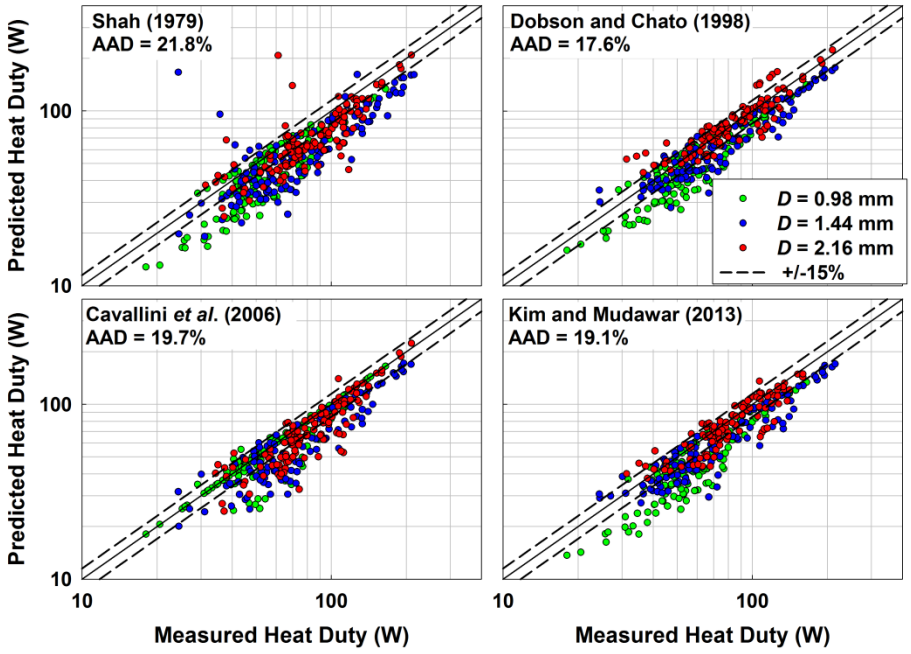

Figure 7.17: Predicted versus measured zeotropic condensation heat duty with different liquid film heat transfer coefficient models from literature

inputs:

- Shah (1979)
- Dobson and Chato (1998)
- Cavallini *et al.* (2006)
- Kim and Mudawar (2013)

A comparison of the predicted versus measured heat duty using each model within the film theory framework is shown in Figure 7.17.

Compared to the proposed model, the Shah (1979), Dobson and Chato (1998), Cavallini *et al.* (2006), and Kim and Mudawar (2013) all had worse agreement. Of the four considered models, the Dobson and Chato (1998) model performed the best, with an AAD of 17.6% (compared to an AAD of 12.9% for proposed model). It should be noted that the Dobson and Chato (1998) correlation was also shown to predict the pure ammonia data the best (AAD = 37%) compared to the other three. This further reinforces the importance of accurately predicting the underlying liquid film heat transfer, and its strong influence on the overall predicted condensation heat transfer coefficient.

7.4.3 Effect of Vapor-Phase Heat Transfer Coefficient

The vapor-phase heat transfer coefficient is also required for closure to the film-theory model developed above. In the proposed model, a correlation (Churchill, 1977a) for predicting single-phase convective heat transfer in the laminar, transition and turbulent regimes was used. To assess the importance of the vapor-phase heat transfer coefficient to the overall heat transfer, the calculated relative vapor, liquid, wall and coolant thermal

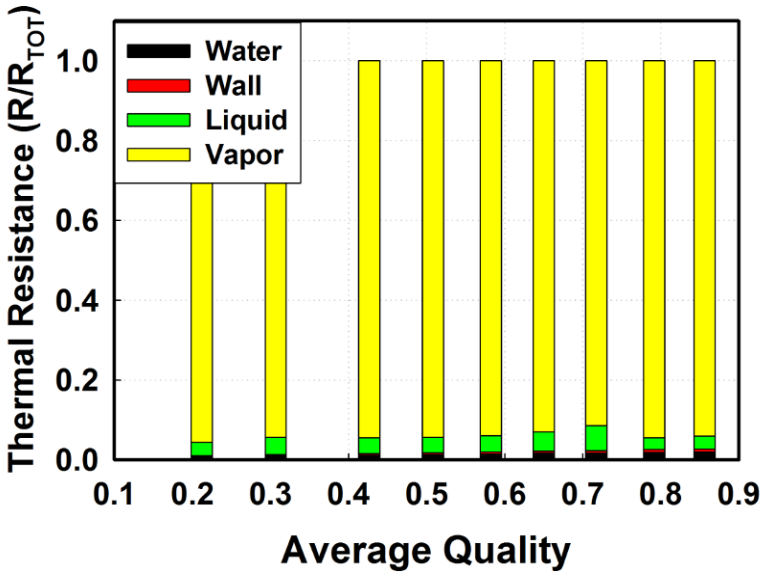

Figure 7.18: Calculated normalized thermal resistance of vapor, liquid, wall and coolant

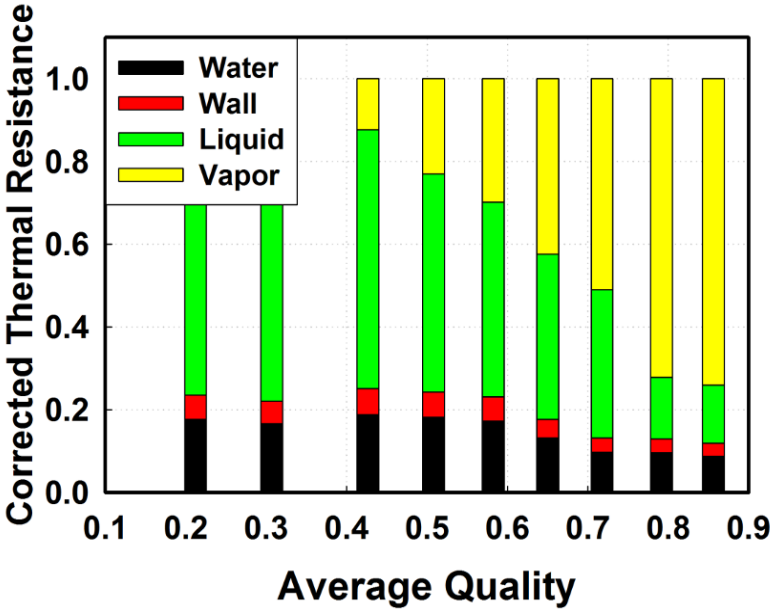

Figure 7.19: Calculated normalized thermal resistance of vapor, liquid, wall and coolant corrected with vapor sensible to total heat ratio

resistances are shown as a function of quality for a point with G = 150 kg m^{-2} s^{-1}, x_{bulk} = 0.90 and D = 1.44 mm in Figure 7.18.

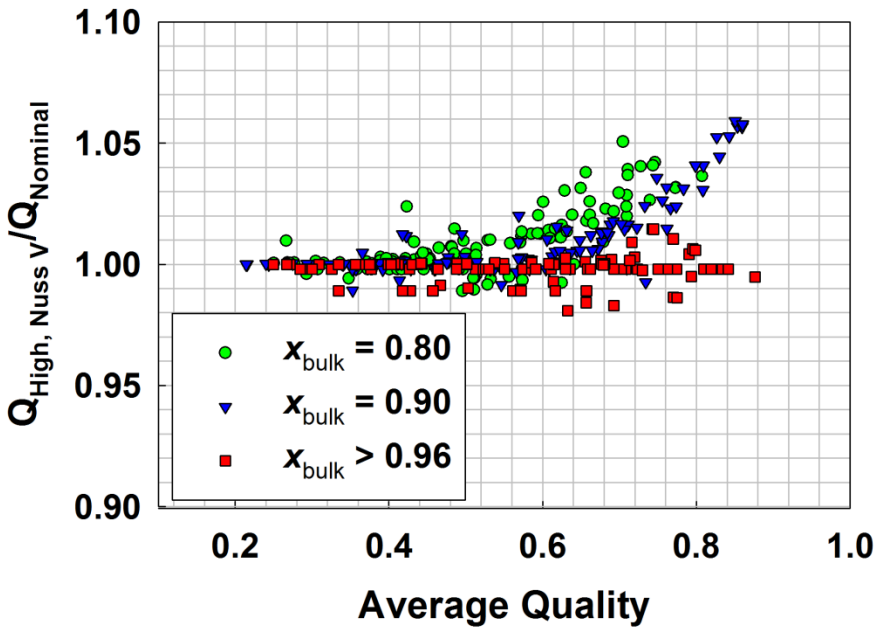

Figure 7.20: Effect of increased vapor Nusselt number on predicted zeotropic condensation heat duty

For every point, the vapor-phase thermal resistance is dominant, due to the poorer transport properties in the vapor versus liquid phase and coolant. However, the vapor-phase heat transfer coefficient governs only the vapor sensible load (see Eq. (7.15)), which is generally small compared to the total heat load transported through the liquid film. Figure 7.19 shows the normalized resistances again, this time with a correction factor of $q''_{S,V}/q''_{T}$ applied to the vapor-phase thermal resistance. With this correction, the vapor-phase thermal resistance only becomes significant above a certain threshold of $q''_{S,V}/q''_{T}$.

This effect can clearly be seen in Figure 7.20, which plots the ratio of the predicted heat duty assuming a vapor-phase Nusselt number 25% **greater** than nominal to the predicted heat duty assuming the nominal vapor-phase Nusselt number versus average test section quality.

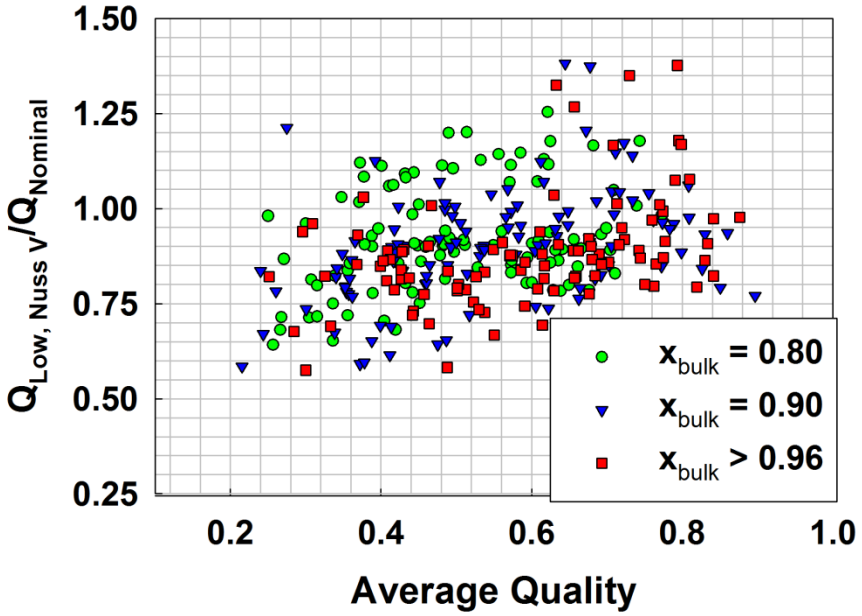

Figure 7.21: Effect of decreased vapor Nusselt number on predicted zeotropic condensation heat duty

Using the 25% greater vapor-phase Nusselt number, the agreement with experiments is on par with the nominal condition, with a AAD of 13.3% versus 12.9%, However, as can be seen in the figure, at higher qualities, the predicted heat duty for the high vapor-phase heat transfer coefficient is greater than the nominal. As Figure 7.20 also shows, the deviation from the nominal prediction occurs at progressively lower qualities as the mass fraction of bulk ammonia decreases. This is consistent with the increasing temperature glide, and the corresponding increase in vapor sensible heat load at lower bulk ammonia mass fraction (see Chapter 6).

As a final investigation of the influence of vapor-phase heat transfer coefficient on the proposed model's accuracy, the other case where the vapor-phase Nusselt number was 25% **less** than nominal was investigated. The results of the predicted versus measured heat duty are shown in Figure 7.21. Overall, the AAD is greater for the low

Table 7.4: Predictive capability of nominal model and model neglecting condensate sensible cooling

x_{bulk}	Neglect Condensate Subcooling AAD (%)	Nominal AAD (%)
0.80	15.4	11.9
0.90	13.9	11.6
> 0.96	14.6	15.5

Nusselt number case (14.3% versus 12.9% for the baseline). In addition, as shown in Figure 7.19, there is much greater scatter observed in the low vapor Nusselt number data compared to the high Nusselt number data (Figure 7.20). In addition, most of the data are under predicted. The results of the model at the extreme cases of ±25% vapor-phase Nusselt number suggest that the nominal proposed vapor-phase correlation predicts the data the best.

7.4.4 Effect of Condensate Subcooling

To assess the importance of condensate subcooling, the model developed in Chapter 7.2 was compared with each data point with condensate subcooling neglected (*i.e.*, liquid bulk temperature was equal to interface temperature). This led to an increase in overall AAD from 12.9 to 14.6%. Table 7.4 shows a breakdown of the model agreement as a function of bulk mass fraction of ammonia with and without condensate subcooling accounted for.

The deviation between the two approaches is greatest for x_{bulk} = 0.8. Here, the temperature glide is the largest; and the subcooling is expected to be a more significant contribution to the total heat load. The agreement between the two models is almost the same for x_{bulk} > 0.96, where the sensible cooling of the condensate is expected to be less

significant. Clearly, as the mass fraction of ammonia decreases, it is important to consider the condensate subcooling.

7.4.5 Example of Model Predictions

Using the validated model, it is useful to assess some predicted trends in condensing zeotropic mixture phase concentrations, temperatures and heat loads. Two sample data points were evaluated, both with D = 0.98 mm, G = 100 kg m^{-2} s^{-1} and x_{bulk} = 0.80. The average quality for sample point (a) was 0.3 and for sample point (b) was 0.7. Figure 7.22 shows the calculated vapor bulk (y_1) and vapor interface ($y_{1,int}$) mass fraction of ammonia for the two points as a function of position within the condenser.

The mass transfer effects can be clearly observed for the high quality point (b). Here, the condensation of less volatile water leads to an accumulation of more volatile ammonia at the interface. This accumulation leads to a decrease in the local saturation temperature and the back diffusion of ammonia to the vapor bulk, coupling the heat and mass transfer. For the low quality point (a), most of the water has been condensed, and the concentration gradient between the vapor bulk and interface is smaller, decreasing the importance of mass transfer effects. The influence of these parameters on the calculated interface temperature can be seen for the same two points in Figure 7.23.

Here, the calculated vapor bulk, interface, equilibrium, and coolant temperatures are plotted as a function of position within the condenser. For the low quality point (a), the temperature difference between the interface and mixture thermodynamic equilibrium temperature is very small. Here again, most of the water has condensed and the vapor is primarily ammonia (as evidenced by Figure 7.22), decreasing the influence of mixture effects. However, at the high quality point, the temperature difference between the

calculated interface and the equilibrium temperature is very large, upwards of 20 to 30 K. Here, the mixture effects are significant, and the high-temperature glide of the mixture is of great importance. Attempting to design a condenser using the equilibrium temperature rather than the calculated interface temperature in this region would result in a significantly undersized condenser. The final effect of a high-temperature-glide mixture can be seen in Figure 7.24, which shows the relative contributions of vapor sensible cooling, liquid sensible cooling and latent heat of condensation for the same two points.

Most existing models neglect entirely the liquid subcooling. In the previous section, improved predictive capability was shown when this contribution was considered. Figure 7.24 shows that for certain conditions (*i.e.*, high quality, high-temperature-glide regions in Figure 7.24a), the liquid sensible cooling can account for up to 50-60% of the local heat flux. From the low quality (b) plot, it can be seen that the contribution of the sensible loads is very low near the end of condensation, where the temperature glide is minimal. Thus, for low-temperature-glide mixtures, it may be a more reasonable assumption to neglect the sensible load contribution. However, for high-temperature-glide mixtures, this can introduce undesirable errors.

7.5 Model Summary

In this chapter, a multi-regime correlation for predicting mini/microchannel ammonia condensation heat transfer was developed. The model was validated with experimental data and showed a significantly improved predictive capability compared to models and correlations developed for different classes of fluids and channel geometries. Using the correlation for pure ammonia condensation developed here, an improved film theory based method for zeotropic condenser design was introduced and analyzed. The method

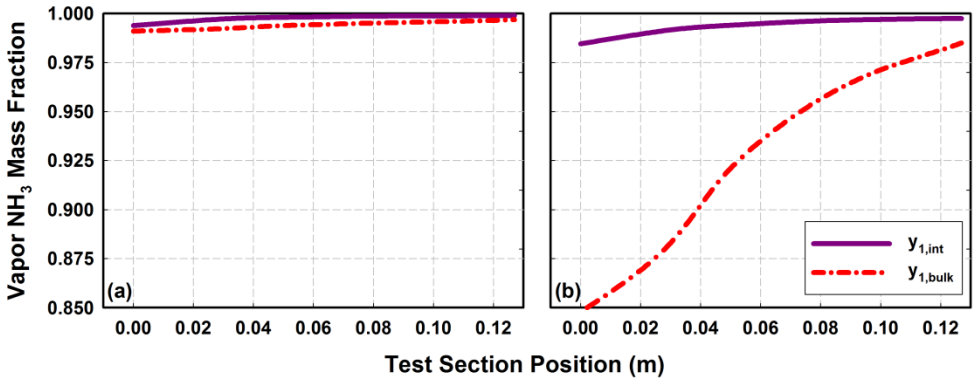

Figure 7.22: Calculated vapor bulk and vapor interface ammonia mass fraction at (a) q_{avg} = 0.3 and (b) q_{avg} = 0.7 for x_{bulk} = 0.80

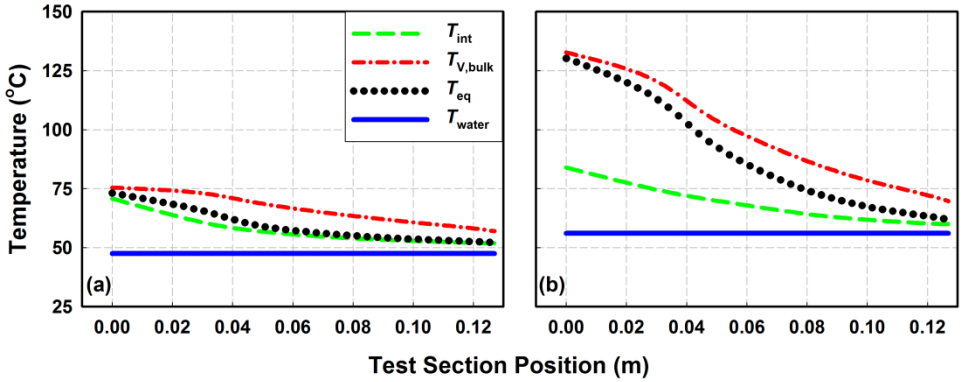

Figure 7.23: Calculated vapor bulk, interface and equilibrium temperature at (a) q_{avg} = 0.3 and (b) q_{avg} = 0.7 for x_{bulk} = 0.80

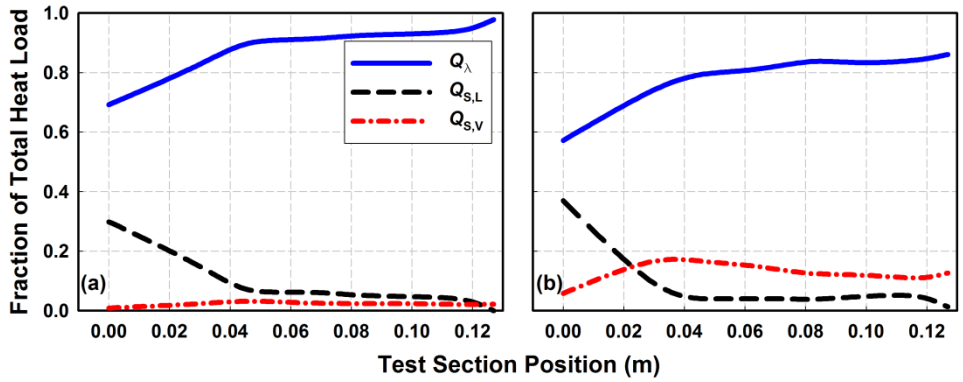

Figure 7.24: Relative contribution of sensible vapor cooling, sensible liquid cooling and latent heat at (a) q_{avg} = 0.3 and (b) q_{avg} = 0.7 for x_{bulk} = 0.80

was validated for high-temperature-glide ammonia-water mixtures in small diameter channels. The key features of the improved model were considering annular and non-annular flow effects on liquid film transport, including condensate and vapor sensible

cooling contributions, and accounting for mini/microchannel effects through the new liquid-film correlation. A full sample implementation of both the pure component correlation and the zeotropic condenser model is provided in Appendix C.

CHAPTER 8

CONCLUSIONS AND RECOMMENDATIONS

A comprehensive investigation of the condensation of ammonia and high-temperature-glide zeotropic ammonia/water mixtures in small diameter channels was conducted. Condensation heat transfer and pressure drop experiments were conducted on ammonia and ammonia/water mixtures. Data for pure ammonia were obtained for varying tube diameters ($0.98 < D < 2.16$ mm), mass fluxes ($75 < G < 225$ kg m^{-2} s^{-1}), and saturation conditions ($30 < T_{sat} < 60$°C). Experiments on zeotropic ammonia/water mixtures were conducted for multiple tube diameters ($0.98 < D < 2.16$ mm), mass fluxes ($50 < G < 200$ kg m^{-2} s^{-1}), and bulk ammonia mass fractions ($x_{bulk} = 0.8$, 0.9 and > 0.96).

An experimental methodology and data analysis procedure for evaluating the local condensation heat duty (for incremental Δq), condensation transfer coefficient (for pure ammonia), and apparent heat transfer coefficient (for zeotropic ammonia/water mixtures) and frictional pressure gradient with low uncertainties was developed. For pure ammonia, existing pressure drop models showed fair agreement with the data, with the simple Friedel (1979) correlation predicting the data the best (AAD = 21%). For the zeotropic ammonia/water mixtures, the dependence of pressure drop on quality and mass flux was consistent with the pure ammonia data. Overall, the mini- and microchannel condensation pressure drop models of Kim and Mudawar (2012) and Garimella *et al.* (2005) predicted the ammonia and ammonia/water data the best.

Ammonia heat transfer coefficients ranged from 4 to 55 kW m^{-2} K^{-1}, with an average uncertainty of ±15.9%. The dependence of pressure drop and heat transfer on

quality and mass flux was consistent with previous investigations; however, it was shown that heat transfer models in the literature that were developed for both macro and mini/microchannels were not able to accurately predict the results. The Keinath (2012) correlation exhibited the best agreement, with an absolute average deviation (AAD) of 32.5%. For zeotropic mixtures, the apparent heat transfer coefficient showed a different trend from the pure ammonia heat transfer coefficient, with strong degradation observed in quality ranges with large temperature glides. At low quality ranges (*i.e.*, low temperature glides and smaller mixture effects), the pure ammonia heat transfer coefficient and zeotropic mixture apparent heat transfer coefficient were in good agreement. The similarity between the underlying liquid film transport of ammonia and ammonia/water mixtures is further justified by the consistent agreement with literature correlations for both fluid types, where the Keinath (2012) model predicted the ammonia and mixture data best (AAD = 32 and 40% for NH_3 and NH_3/H_2O, respectively)**.**

A condensation heat transfer model was developed for ammonia in mini/microchannels. The model considered both annular and non-annular condensation mechanisms, using the simple transition criterion of Cavallini *et al.* (2002a) to delineate the two regimes. In the annular regime, a two-phase multiplier model based on the approach of Thome *et al.* (2003) and Keinath (2012) was used. The model was validated with experimental data and showed a significantly improved predictive capability (AAD = 12.8% for all ammonia data) compared to models and correlation developed for different classes of fluids and channel geometries.

Using the insights derived from the pure ammonia work, an improved zeotropic condenser design method for high-temperature-glide mixtures in small channels, based

on the non-equilibrium film theory, was introduced. The key features of the improved model were the consideration of annular and non-annular flow effects on liquid film transport, including condensate and vapor sensible cooling contributions, and accounting for mini/microchannel effects through the new liquid film correlation. When compared with data, the model predicted measured condensation heat duty with an AAD of 12.9%. Agreement was consistent for the entire range of tube diameters and bulk ammonia mass fractions. Furthermore, it was demonstrated that the liquid-film heat transfer coefficient was the most important input to the film theory framework.

The findings of this study advance the understanding of microchannel zeotropic condenser design, particularly in relation to the use of high-temperature-glide mixtures. High-temperature glide mixtures including ammonia/water, hydrocarbons and others have important potential applications in thermally driven heating, cooling and power systems, as well as in the chemical process industry. By understanding the behavior of these mixtures in microchannel geometries, highly efficient, compact thermal conversion devices can be developed.

8.1 Recommendations for Future Work

There are several additional opportunities for continued work in the area of condensation of zeotropic mixtures, summarized here:

- While the present investigation focused on relatively low mass fluxes compared to those considered in other studies in the literature, the mass flux requirements of compact equipment may be even lower ($G < 10$ kg m^{-2} s^{-1}). At this very low flow rate, flow morphology and transport are expected to differ from what was inferred in the present study. Thus, the intermittent flow regime is expected to become more

important, which may dramatically alter the coupled heat and mass transfer processes due to the change in interfacial heat transfer area and local compositions in the vapor bubbles and liquid slugs.

- The focus of the present study was on binary mixtures. To achieve a better tailoring of the working fluid temperature glide, the use of higher order mixtures may be required. Additional work should be focused on understanding condensation of these multi-component mixtures, particularly at very low mass fluxes in small geometries. Here, multi-component mass transfer effects in the vapor-phase may play a more prominent role in the overall condensation process.
- The present study considered a mixture of fully condensable components. Further study on understanding the effect of non-condensables on zeotropic mixture condensation should be conducted.
- In the present study, the mixture condensation heat duty was directly measured and mass transfer effects inferred from the data. As work expands to multi-component mixtures of both condensable and non-condensable components, direct characterization of mass transfer behavior by measuring phase composition during the condensation process would allow the heat transfer and mass transfer mechanisms to be measured separately, enabling the development of more robust heat and mass transfer models.
- It was not possible to quantitatively determine the influence of flow structure on the underlying heat and mass transfer mechanisms. In future studies, directly visualize the condensing flow under representative operating conditions while simultaneously measuring condensation heat duty and mass transfer. This would facilitate the

validation of existing flow regime maps, as well as quantify the effect of flow regime on both heat and mass transfer.

APPENDIX A

DATA POINT SAMPLE CALCULATIONS

Representative analyses for an ammonia and ammonia/water data point are presented in this Appendix. For ammonia, the test section condensation heat duty and average quality (Table A.1), ambient heat loss (Table A.2) condensation heat transfer coefficient (Table A.3), and frictional pressure gradient (Table A.6) analyses are presented. For the zeotropic ammonia/water mixtures, analyses of bulk ammonia mass fraction verification (Table A.4) and zeotropic condensation heat duty (Table A.5) are presented. Each analysis corresponds to the data and figures introduced in Chapter 4.

Table A.1: NH_3 test section condensation heat duty and average quality calculation

Sample Calculation: NH_3 , D = 1.44 mm, T_{sat} = 40, G = 150 kg m^{-2} s^{-1}, TestID: 143		
Inputs	**Equations**	**Results**
Calculation of Condensation Heat Duty $\dot{Q}_{cond}$		
$T_1 = 26.15$ °C (measured) $P_1 = 1570$ kPa (measured)	$T_{sat,1} = f(P_1)$ $\Delta T_{sub} = T_{sat,1} - T_1$ $h_1 = f(T_1, P_1)$ (subcooled)	$T_{sat,1} = 40.34$°C $\Delta T_{sub} = 14.2$ K $h_1 = 323.4$ kJ kg^{-1}
$h_1 = 323.4$ kJ kg^{-1} $\dot{Q}_{pre} = 142$ W (measured) $\dot{Q}_{pre,loss} = 0.2$ W (see Table A.2) $\dot{m} = 2.46\times10^{-4}$ kg/s (measured)	$h_2 = \frac{\dot{Q}_{pre} - \dot{Q}_{pre,loss}}{\dot{m}} + h_1$	$h_2 = 898.3$ kJ kg^{-1}
$T_4 = 53.7$ °C (measured) $P_4 = 1563$ kPa (measured)	$T_{sat,4} = f(P_4)$ $\Delta T_{sup} = T_4 - T_{sat,4}$ $h_4 = f(T_4, P_4)$ (superheated)	$T_{sat,4} = 40.18$°C $\Delta T_{sup} = 13.5$ K $h_4 = 1534$ kJ kg^{-1}
$h_4 = 1534$ kJ kg^{-1} $\dot{Q}_{post} = 204.2$ W (measured) $\dot{Q}_{post,loss} = 0.85$ W (see Table A.2) $\dot{m} = 2.46\times10^{-4}$ kg/s (measured)	$h_3 = h_4 - \frac{\dot{Q}_{post} - \dot{Q}_{post,loss}}{\dot{m}}$	$h_3 = 710$ kJ kg^{-1}

Table A.1: NH_3 test section condensation heat duty and average quality calculation – cont.

Sample Calculation: NH_3 , D = 1.44 mm, T_{sat} = 40, G = 150 kg m^{-2} s^{-1}, TestID: 143		
Inputs	**Equations**	**Results**
$h_2 = 898.3$ kJ kg^{-1} $h_3 = 710$ kJ kg^{-1} $\dot{m} = 2.46\times10^{-4}$ kg/s (measured)	$\dot{Q}_{cond} = \dot{m}(h_2 - h_3)$	$\dot{Q}_{cond} = 46.43$ W
Calculation of Average Test Section Quality q_{avg}		
$h_2 = 898.3$ kJ kg^{-1} $P_2 = 1569$ kPa (measured)	$q_2 = f(h_2, P_2)$	$q_2 = 0.461$
$h_3 = 710$ kJ kg^{-1} $P_3 = 1561$ kPa (measured)	$q_3 = f(h_3, P_3)$	$q_3 = 0.290$
$q_2 = 0.461$ $q_3 = 0.290$	$q_{avg} = \frac{q_2 + q_3}{2}$	$q_{avg} = 0.376$

Table A.2: NH_3 test section heat loss sample calculation

Sample Calculation: NH_3 , D = 1.44 mm, T_{sat} = 40, G = 150 kg m^{-2} s^{-1}, TestID: 143		
Inputs	**Equations**	**Results**
Calculation of Pre-heater Ambient Heat Loss $\dot{Q}_{pre,loss}$		
Material = Stainless AISI304 T_{amb} = 29.1 °C (measured)	$k_{assy} = f(\text{Material}, T_{amb})$	k_{assy} = 14.94 W m^{-1} K^{-1}
T_1 = 26.15 °C (measured) T_2 = 40.39 °C (measured)	$T_{ref,avg} = \frac{T_1 + T_2}{2}$	$T_{ref,avg}$ = 33.3° C
α_{ref} = 10000 W m^{-2} K^{-1} (assumed) ID_{assy} = 0.0179 m L_{eff} = 0.1715 m	$R_{ref} = \frac{1}{\pi \cdot L_{eff} \cdot ID_{assy} \cdot \alpha_{ref}}$	R_{ref} = 0.01 K W^{-1}
OD_{assy} = 0.0381 m ID_{assy} = 0.0179 m L_{eff} = 0.1715 m k_{assy} = 14.94 W m^{-1} K^{-1}	$R_{assy,wall} = \frac{\ln(OD_{assy}/ID_{assy})}{2\pi L_{eff} k_{assy}}$	$R_{assy,wall}$ = 0.047 K W^{-1}
OD_{assy} = 0.0381 m t_{ins} = 0.025 m L_{eff} = 0.1715 m k_{ins} = 0.043 W m^{-1} K^{-1}	$R_{ins} = \frac{\ln([OD_{assy} + 2t_{ins}]/OD_{assy})}{2\pi L_{eff} k_{ins}}$	R_{ins} = 18.29 W K^{-1}
T_{amb} = 29.1° C (measured) $T_{ins,surf}$ = 29.7° C (solved iteratively)	$T_{air,film} = \frac{T_{amb} + T_{ins,surf}}{2}$	$T_{air,film}$ = 29.39° C
$T_{air,film}$ = 29.39° C P_{amb} = 101 kPa (assumed)	Air properties= $f(T_{air,film}, P_{amb})$	β = 0.00332 K^{-1} c_p = 1.007 kJ kg^{-1} K^{-1} k = 0.02657 W m^{-1} K^{-1} ν = 1.604×10^{-5} m^2 s^{-1} ρ = 1.163 kg m^{-3} Pr = 0.707
T_{amb} = 29.1° C (measured) $T_{ins,surf}$ = 29.7° C (solved iteratively) OD_{ins} = 0.0889 m β = 0.00332 K^{-1} ν = 1.604×10^{-5} m^2 s^{-1} Pr = 0.707	$Ra_{air} = \frac{g \cdot (T_{amb} - T_{ins,surf}) \cdot Pr \cdot \beta \cdot OD_{ins}^3}{\nu^2}$	Ra_{air} = 36036

Table A.2: NH_3 test section heat loss sample calculation – cont.

Sample Calculation: NH_3 , D = 1.44 mm, T_{sat} = 40, G = 150 kg m^{-2} s^{-1}, TestID: 143		
Inputs	**Equations**	**Results**
$k = 0.02657$ W m^{-1} K^{-1} $\Pr = 0.707$ $\mathrm{Ra}_{air} = 36036$ $\mathrm{OD}_{ins} = 0.0889$ m $L_{eff} = 0.1715$ m	Churchill and Chu (1975) $\mathrm{Nu}_{air} = \left(0.6 + \frac{0.387 \cdot \mathrm{Ra}_{air}^{1/6}}{\left(1+\left(0.559/\Pr\right)^{9/16}\right)^{8/27}} \right)^2$ $\alpha_{conv,air} = \frac{\mathrm{Nu}_{air} \cdot k}{\mathrm{OD}_{ins}}$ $R_{assy,conv} = \frac{1}{\pi \cdot L_{eff} \cdot \mathrm{OD}_{ins} \cdot \alpha_{conv,air}}$	$\mathrm{Nu}_{air} = 5.98$ $\alpha_{conv,air} = 1.78$ W m^{-2} K^{-1} $R_{assy,conv} = 11.67$ K W^{-1}
$T_{amb} = 29.1^{o}$C (measured) $T_{ins,surf} = 29.7^{o}$C (solved iteratively) $\varepsilon = 0.85$ (assumed) $\mathrm{OD}_{ins} = 0.0889$ m $L_{eff} = 0.1715$ m	$\alpha_{rad,air} = \sigma \cdot \varepsilon \cdot \left(T_{ins,surf}^2 + T_{amb}^2\right)\left(T_{ins,surf} + T_{amb}\right)$ $R_{assy,rad} = \frac{1}{\pi \cdot L_{eff} \cdot \mathrm{OD}_{ins} \cdot \alpha_{rad,air}}$	$\alpha_{rad,air} = 5.34$ W m^{-2} K^{-1} $R_{assy,rad} = 3.91$ K W^{-1}
$R_{assy,conv} = 11.67$ K W^{-1} $R_{assy,rad} = 3.91$ K W^{-1}	$R_{assy,surf} = \left(\frac{1}{R_{assy,conv}} + \frac{1}{R_{assy,rad}} \right)^{-1}$	$R_{assy,surf} = 2.93$ K W^{-1}
$R_{ref} = 0.01$ K W^{-1} $R_{assy,wall} = 0.047$ K W^{-1} $R_{ins} = 18.29$ K W^{-1} $R_{assy,surf} = 2.93$ K W^{-1} $T_{amb} = 29.1^{o}$C (measured) $T_{ref,avg} = 33.3^{o}$C	$\dot{Q}_{pre,loss} = \frac{T_{ref,avg} - T_{amb}}{R_{ref} + R_{assy,wall} + R_{ins} + R_{assy,surf}}$	$\dot{Q}_{pre,loss} = 0.2$ W
Calculation of Post-heater Ambient Heat Loss $\dot{Q}_{post,loss}$		
Material = Stainless AISI304 $T_{amb} = 29.1\ ^{o}$C (measured)	$k_{assy} = f\left(\text{Material}, T_{amb}\right)$	$k_{assy} = 14.94$ W m^{-1} K^{-1}
$T_3 = 40.05\ ^{o}$C (measured) $T_4 = 53.65\ ^{o}$C (measured)	$T_{ref,avg} = \frac{T_3 + T_4}{2}$	$T_{ref,avg} = 46.85^{o}$C
$\alpha_{ref} = 10000$ W m^{-2} K^{-1} (assumed) $\mathrm{ID}_{assy} = 0.0179$ m $L_{eff} = 0.1715$ m	$R_{ref} = \frac{1}{\pi \cdot L_{eff} \cdot \mathrm{ID}_{assy} \cdot \alpha_{ref}}$	$R_{ref} = 0.01$ K W^{-1}
$\mathrm{OD}_{assy} = 0.0381$ m $\mathrm{ID}_{assy} = 0.0179$ m $L_{eff} = 0.1715$ m $k_{assy} = 14.94$ W m^{-1} K^{-1}	$R_{assy,wall} = \frac{\ln\left(\mathrm{OD}_{assy}/\mathrm{ID}_{assy}\right)}{2\pi L_{eff} k_{assy}}$	$R_{assy,wall} = 0.047$ K W^{-1}

Table A.2: NH_3 test section heat loss sample calculation – cont.

Sample Calculation: NH_3 , D = 1.44 mm, T_{sat} = 40, G = 150 kg m^{-2} s^{-1}, TestID: 143		
Inputs	**Equations**	**Results**
$\mathrm{OD}_{assy} = 0.0381$ m $t_{ins} = 0.025$ m $L_{eff} = 0.1715$ m $k_{ins} = 0.043$ W m^{-1} K^{-1}	$R_{ins} = \frac{\ln\left(\left[\mathrm{OD}_{assy} + 2t_{ins}\right]/\mathrm{OD}_{assy}\right)}{2\pi L_{eff} k_{ins}}$	$R_{ins} = 18.29$ W K^{-1}
$T_{amb} = 29.1^{o}$C (measured) $T_{ins,surf} = 31.33^{o}$C (solved iteratively)	$T_{air,film} = \frac{T_{amb} + T_{ins,surf}}{2}$	$T_{air,film} = 30.22^{o}$C
$T_{air,film} = 30.22^{o}$C $P_{amb} = 101$ kPa (assumed)	Air properties= $f\left(T_{air,film}, P_{amb}\right)$	$\beta = 0.00331$ K^{-1} $c_p = 1.007$ kJ kg^{-1} K^{-1} $k = 0.02663$ W m^{-1} K^{-1} $\nu = 1.612\times10^{-5}$ m^2 s^{-1} $\rho = 1.16$ kg m^{-3} Pr = 0.707
$T_{amb} = 29.1^{o}$C (measured) $T_{ins,surf} = 31.33^{o}$C (solved iteratively) $\mathrm{OD}_{ins} = 0.0889$ m $\beta = 0.00331$ K^{-1} $\nu = 1.612\times10^{-5}$ m^2 s^{-1} Pr = 0.707	$\mathrm{Ra}_{air} = \frac{g\cdot\left(T_{amb} - T_{ins,surf}\right)\cdot \mathrm{Pr}\cdot\beta\cdot \mathrm{OD}_{ins}^3}{\nu^2}$	$\mathrm{Ra}_{air} = 138219$
$k = 0.02663$ W m^{-1} K^{-1} Pr = 0.707 $\mathrm{Ra}_{air} = 138,219$ $\mathrm{OD}_{ins} = 0.0889$ m $L_{eff} = 0.1715$ m	Churchill and Chu (1975) $\mathrm{Nu}_{air} = \left(0.6 + \frac{0.387\cdot \mathrm{Ra}_{air}^{1/6}}{\left(1+\left(0.559/\mathrm{Pr}\right)^{9/16}\right)^{8/27}}\right)^2$ $\alpha_{conv,air} = \frac{\mathrm{Nu}_{air}\cdot k}{\mathrm{OD}_{ins}}$ $R_{assy,conv} = \frac{1}{\pi\cdot L_{eff}\cdot \mathrm{OD}_{ins}\cdot \alpha_{conv,air}}$	$\mathrm{Nu}_{air} = 8.46$ $\alpha_{conv,air} = 2.536$ W m^{-2} K^{-1} $R_{assy,conv} = 8.23$ K W^{-1}
$T_{amb} = 29.1^{o}$C (measured) $T_{ins,surf} = 31.33^{o}$C (solved iteratively) $\varepsilon = 0.85$ (assumed) $\mathrm{OD}_{ins} = 0.0889$ m $L_{eff} = 0.1715$ m	$\alpha_{rad,air} = \sigma\cdot\varepsilon\cdot\left(T_{ins,surf}^2 + T_{amb}^2\right)\left(T_{ins,surf} + T_{amb}\right)$ $R_{assy,rad} = \frac{1}{\pi\cdot L_{eff}\cdot \mathrm{OD}_{ins}\cdot \alpha_{rad,air}}$	$\alpha_{rad,air} = 5.38$ W m^{-2} K^{-1} $R_{assy,rad} = 3.88$ K W^{-1}
$R_{assy,conv} = 5.38$ K W^{-1} $R_{assy,rad} = 3.88$ K W^{-1}	$R_{assy,surf} = \left(\frac{1}{R_{assy,conv}} + \frac{1}{R_{assy,rad}}\right)^{-1}$	$R_{assy,surf} = 2.63$ K W^{-1}

Table A.2: NH_3 test section heat loss sample calculation – cont.

Sample Calculation: NH_3 , D = 1.44 mm, T_{sat} = 40, G = 150 kg m^{-2} s^{-1}, TestID: 143		
Inputs	**Equations**	**Results**
$R_{ref} = 0.01$ K W^{-1} $R_{assy,wall} = 0.047$ K W^{-1} $R_{ins} = 18.29$ K W^{-1} $R_{assy,surf} = 2.63$ K W^{-1} $T_{amb} = 29.1^{o}$C (measured) $T_{ref,avg} = 46.85^{o}$C	$\dot{Q}_{pre,loss} = \frac{T_{ref,avg} - T_{amb}}{R_{ref} + R_{assy,wall} + R_{ins} + R_{assy,surf}}$	$\dot{Q}_{post,loss} = 0.85$ W

Table A.3 NH_3 condensation heat transfer coefficient calculation

Sample Calculation: NH_3 , D = 1.44 mm, T_{sat} = 40, G = 150 kg m^{-2} s^{-1}, TestID: 143		
Inputs	**Equations**	**Results**
Calculation of Log-Mean Temperature Difference ΔT_{LM}		
$P_2 = 1569$ kPa (measured) $P_3 = 1561$ kPa (measured) $T_2 = 40.39^{o}$C (measured) $T_3 = 40.05^{o}$C (measured)	$T_{2,sat} = f\left(P_2\right)$ $T_{3,sat} = f\left(P_3\right)$	$T_{2,sat} = 40.32^{o}$C $T_{3,sat} = 40.13^{o}$C $\Delta T_{sat,2} = -0.07$ K $\Delta T_{sat,3} = 0.08$ K
$T_{2,sat} = 40.3^{o}$C $T_{3,sat} = 40.1^{o}$C $T_{w,i} = 37.5^{o}$C $T_{w,o} = 37.3^{o}$C	$\Delta T_{LM} = \frac{\left[T_{2,sat} - T_{w,o}\right] - \left[T_{3,sat} - T_{w,i}\right]}{\ln\left[\frac{T_{2,sat} - T_{w,o}}{T_{3,sat} - T_{w,i}}\right]}$	$\Delta T_{LM} = 2.8$ K
Calculation of Tube Wall Thermal Resistance R_{wall}		
$OD_i = 0.001651$ m $ID_i = 0.001435$ m $L_{ann} = 0.2489$ m $L_{red} = 0.0099$ m $k_{wall} = 13.68$ W m^{-1} K^{-1} (Stainless AISI316)	$R_{wall} = \frac{\ln\left(\frac{OD_i}{ID_i}\right)}{2 \cdot \pi \cdot \left(L_{ann} + 2 \cdot L_{red}\right) \cdot k_{wall}}$	$R_{wall} = 0.00607$ K W^{-1}
Calculation of Water-Side Thermal Resistance R_{water}		
$T_{w,avg} = 40.3^{o}$C (measured) $P_w = 1049$ kPa (measured)	Water properties= $f\left(T_{w,avg}, P_w\right)$	$k = 0.6273$ W m^{-1} K^{-1} $\rho = 993.6$ kg m^{-3} $\mu = 6.862 \times 10^{-4}$ kg m^{-1} s^{-1} Pr = 4.57
$ID_o = 0.00386$ m $OD_i = 0.001651$ m	$D_{H,ann} = ID_o - OD_i$ $r^* = \frac{OD_i}{ID_o}$ $A = \pi\left[\left(\frac{ID_o}{2}\right)^2 - \left(\frac{OD_i}{2}\right)^2\right]$	$D_{H,ann} = 0.00221$ m $r^* = 0.4277$ $A = 9.561 \times 10^{-6}$
$\dot{V} = 7.612 \times 10^{-5}$ m^3 s^{-1} (measured) $\rho = 993.6$ kg m^{-3}	$G_w = \rho \dot{V}$	$G_w = 7910$ kg m^{-2} s^{-1}
$D_{H,ann} = 0.00221$ m $\mu = 6.862 \times 10^{-4}$ kg m^{-1} s^{-1}	$Re_{ann} = \frac{G D_{H,ann}}{\mu}$	$Re_{ann} = 25,464$
$r^* = 0.4277$	$Re_{CL} = 2089.26 + 686.15 \cdot r^*$ $Re_{CU} = 2963.02 + 686.15 \cdot r^*$	$Re_{CL} = 2383$ $Re_{CU} = 3106$

Table A.3 NH_3 condensation heat transfer coefficient calculation – cont.

Sample Calculation: NH_3 , D = 1.44 mm, T_{sat} = 40, G = 150 kg m^{-2} s^{-1}, TestID: 143		
Inputs	**Equations**	**Results**
$D_{H,ann} = 0.00221$ m $OD_i = 0.001651$ m $L_{ann} = 0.2489$ m $r^* = 0.4277$ $Re_{ann} = 25,464$ $Pr = 4.57$ $k = 0.6273$ W m^{-1} K^{-1}	Garimella and Christensen (1995) $Nu_a = 0.025 Re_{ann}^{0.78} Pr^{0.48} r^{*-0.14}$ (turbulent) $\alpha_w = \frac{Nu_a \cdot k}{D_{H,ann}}$ $R_{ann} = \frac{1}{\pi \cdot \alpha_w \cdot OD_i \cdot L_{ann}}$	$Nu_a = 159.6$ $\alpha_w = 45,311$ W m^{-2} K^{-1} $R_{ann} = 0.01709$ K W^{-1}
$k = 0.6273$ W m^{-1} K^{-1}	$Ra^* << 100$ from Incropera and Dewitt (2002) $k_{eff} = k$	$k_{eff} = 0.6273$ W m^{-1} K^{-1}
$OD_i = 0.001651$ m $ID_{red} = 0.002$ m $L_{red} = 0.0099$ m $Re_{ann} = 25,464$ $k_{eff} = 0.6273$ W m^{-1} K^{-1}	$R_{red} = \frac{\ln\left(\frac{ID_{red}}{OD_i}\right)}{2 \cdot \pi \cdot L_{red} \cdot k_{eff}}$	$R_{red} = 4.9$ K W^{-1}
$R_{ann} = 0.01709$ K W^{-1} $R_{red} = 4.9$ K W^{-1}	$\frac{1}{R_{water}} = \frac{1}{R_{ann}} + 2\frac{1}{R_{red}}$	$R_{water} = 0.01698$ K W^{-1}
Calculation of Condensation Heat Transfer Coefficient α_{cond}		
$\dot{Q}_{cond} = 46.43$ W (see Table A.1) $\Delta T_{LM} = 2.8$ K $R_{water} = 0.01698$ K W^{-1} $R_{wall} = 0.00607$ K W^{-1} $ID_i = 0.001435$ m $L_{ann} = 0.2489$ m $L_{red} = 0.0099$ m	$R_{cond} = \frac{\Delta T_{LM}}{\dot{Q}_{cond}} - R_{wall} - R_{water}$ $\alpha_{cond} = \frac{1}{R_{cond} \cdot \pi \cdot (L_{ann} + 2 \cdot L_{red}) \cdot ID_i}$	$R_{cond} = 0.038$ K W^{-1} $\alpha_{cond} = 21,911$ W m^{-2} K^{-1}

Table A.4 NH_3/H_2O bulk mass fraction analysis

Sample Calculation: NH_3/H_2O , D = 1.44 mm, x_{bulk} = 40, G = 100 kg m^{-2} s^{-1}, TestID: 501		
Inputs	**Equations**	**Results**
$\dot{Q}_{pre} = 218.9$ W (measured) $\dot{Q}_{pre,loss} = 1.69$ W (see procedure in Table A.2) $T_1 = 26.12$ °C (measured) $T_2 = 101.2$ °C (measured) $P_1 = 1510$ kPa (measured) $P_2 = 1510$ kPa (measured) $\dot{m} = 1.583\times10^{-4}$ kg s^{-1} (measured)	$\dot{Q}_{pre} - \dot{Q}_{pre,loss} = \dot{m}\begin{bmatrix} h_2\left(T_2, P_2, x_{bulk,pre}\right) \\ -h_1\left(T_1, P_1, x_{bulk,pre}\right) \end{bmatrix}$ Solve iteratively for $x_{bulk,pre}$	$x_{bulk,pre} = 0.92$
$\dot{Q}_{post} = 113.4$ W (measured) $\dot{Q}_{post,loss} = 3.6$ W (see procedure in Table A.2) $T_3 = 57.4$ °C (measured) $T_4 = 146$ °C (measured) $P_3 = 1505$ kPa (measured) $P_4 = 1507$ kPa (measured) $\dot{m} = 1.583\times10^{-4}$ kg s^{-1} (measured)	$\dot{Q}_{post} - \dot{Q}_{post,loss} = \dot{m}\begin{bmatrix} h_4\left(T_4, P_4, x_{bulk,post}\right) \\ -h_4\left(T_4, P_4, x_{bulk,post}\right) \end{bmatrix}$ Solve iteratively for $x_{bulk,post}$	$x_{bulk,pre} = x_{bulk} = 0.91$

Table A.5 NH_3/H_2O condensation heat duty and average quality calculation

Sample Calculation: NH_3/H_2O , D = 1.44 mm, x_{bulk} = 40, G = 100 kg m^{-2} s^{-1}, TestID: 501		
Inputs	**Equations**	**Results**
Calculation of Condensation Heat Duty $\dot{Q}_{cond}$		
$T_1 = 26.1$ °C (measured) $P_1 = 1510$ kPa (measured) $x_{bulk} = 0.91$ (see Table A.4)	$h_1 = f(T_1, P_1, x_{bulk})$ (subcooled)	$h_1 = 54.69$ kJ kg^{-1}
$h_1 = 54.69$ kJ kg^{-1} $\dot{Q}_{pre} = 218.9$ W (measured) $\dot{Q}_{pre,loss} = 1.69$ W (see procedure in Table A.2) $\dot{m} = 1.583\times10^{-4}$ kg/s (measured)	$h_2 = \frac{\dot{Q}_{pre} - \dot{Q}_{pre,loss}}{\dot{m}} + h_1$	$h_2 = 1427$ kJ kg^{-1}
$T_4 = 146.2$ °C (measured) $P_4 = 1505$ kPa (measured) $x_{bulk} = 0.91$ (see Table A.4)	$h_4 = f(T_4, P_4, x_{bulk})$	$h_4 = 1690$ kJ kg^{-1}
$h_4 = 1690$ kJ kg^{-1} $\dot{Q}_{post} = 113.4$ W (measured) $\dot{Q}_{post,loss} = 3.55$ W (see Table A.2) $\dot{m} = 1.583\times10^{-4}$ kg/s (measured)	$h_3 = h_4 - \frac{\dot{Q}_{post} - \dot{Q}_{post,loss}}{\dot{m}}$	$h_3 = 996$ kJ kg^{-1}
$h_2 = 1427$ kJ kg^{-1} $h_3 = 996$ kJ kg^{-1} $\dot{m} = 1.583\times10^{-4}$ kg/s (measured)	$\dot{Q}_{cond} = \dot{m}(h_2 - h_3)$	$\dot{Q}_{cond} = 68.18$ W
Calculation of Average Test Section Quality q_{avg}		
$h_2 = 1427$ kJ kg^{-1} $P_2 = 1510$ kPa (measured) $x_{bulk} = 0.91$ (see Table A.4)	$q_2 = f(h_2, P_2, x_{bulk})$	$q_2 = 0.920$
$h_3 = 996$ kJ kg^{-1} $P_3 = 1507$ kPa (measured) $x_{bulk} = 0.91$	$q_3 = f(h_3, P_3, x_{bulk})$	$q_3 = 0.724$
$q_2 = 0.920$ $q_3 = 0.724$	$q_{avg} = \frac{q_2 + q_3}{2}$	$q_{avg} = 0.822$

Table A.6 NH_3 frictional pressure gradient calculation

Sample Calculation: NH_3 , D = 1.44 mm, T_{sat} = 40, G = 150 kg m^{-2} s^{-1}, TestID: 143		
Inputs	**Equations**	**Results**
Inlet and Outlet Minor Losses		
$D_1 = 17.8$ mm $D_2 = 8.8$ mm $D_3 = 3.2$ mm $D_4 = 1.44$ mm	$A = \pi\left(\frac{D}{2}\right)^2$	$A_1 = 2.50\times10^{-4}$ m^2 $A_2 = 6.01\times10^{-5}$ m^2 $A_3 = 8.04\times10^{-6}$ m^2 $A_4 = 1.62\times10^{-6}$ m^2
$A_2 = 6.01\times10^{-5}$ m^2 $A_3 = 8.04\times10^{-6}$ m^2 $A_4 = 1.62\times10^{-6}$ m^2 $\dot{m} = 2.46\times10^{-4}$ kg s^{-1} (measured)	$G_A = \frac{\dot{m}}{A_2}$ $G_B = \frac{\dot{m}}{A_3}$ $G_C = \frac{\dot{m}}{A_4}$	$G_A = 4.09$ kg m^{-2} s^{-1} $G_B = 30.5$ kg m^{-2} s^{-1} $G_C = 151$ kg m^{-2} s^{-1}
$A_1 = 2.50\times10^{-4}$ m^2 $A_2 = 6.01\times10^{-5}$ m^2 $A_3 = 8.04\times10^{-6}$ m^2 $A_4 = 1.62\times10^{-6}$ m^2	$A_{ratio,A} = \frac{A_2}{A_1}$ $A_{ratio,B} = \frac{A_3}{A_2}$ $A_{ratio,C} = \frac{A_4}{A_3}$	$A_{ratio,A} = 0.2404$ $A_{ratio,B} = 0.1338$ $A_{ratio,C} = 0.2015$
$G_A = 4.09$ kg m^{-2} s^{-1} $G_B = 30.5$ kg m^{-2} s^{-1} $G_C = 151$ kg m^{-2} s^{-1} $A_{ratio,A} = 0.2404$ $A_{ratio,B} = 0.1338$ $A_{ratio,C} = 0.2015$ $\rho_V = 12.14$ kg m^{-3} $\rho_L = 579$ kg m^{-3} $q_2 = 0.461$ (see Table A.1)	Hewitt *et al.* (1994) – Inlet Contractions (G is of smaller cross section) $\Delta P_{contraction} = \frac{G^2}{\rho_L}\left(1 - A_{ratio}^2 + \left[\frac{1}{C_c} - 1\right]^2\right)\psi_H$ where $C_C = \frac{1}{0.639\left[1 - A_{ratio}\right]^{1/2} + 1}$ $\psi_H = 1 + \left(\frac{\rho_L}{\rho_V} - 1\right)q$	$\Delta P_{contraction,A} = 0.41$ Pa $\Delta P_{contraction,B} = 24.5$ Pa $\Delta P_{contraction,C} = 582$ Pa
$\Delta P_{contraction,A} = 0.41$ Pa $\Delta P_{contraction,B} = 24.5$ Pa $\Delta P_{contraction,C} = 581$ Pa	$\Delta P_{inlet} = \Delta P_{contraction,A} + \Delta P_{contraction,B} + \Delta P_{contraction,C}$	$\Delta P_{inlet} = 606.7$

Table A.6 NH_3 frictional pressure gradient calculation – cont.

Sample Calculation: NH_3 , D = 1.44 mm, T_{sat} = 40, G = 150 kg m^{-2} s^{-1}, TestID: 143		
Inputs	**Equations**	**Results**
$G_A = 4.09$ kg m^{-2} s^{-1} $G_B = 30.5$ kg m^{-2} s^{-1} $G_C = 151$ kg m^{-2} s^{-1} $A_{ratio,A} = 0.2404$ $A_{ratio,B} = 0.1338$ $A_{ratio,C} = 0.2015$ $\rho_V = 12.14$ kg m^{-3} $\rho_L = 579$ kg m^{-3} $q_3 = 0.29$ (see Table A.1)	Hewitt *et al.* (1994) – Outlet Expansions (G is of smaller cross section) $\Delta P_{exp} = -\frac{G^2 A_{ratio}\left(1-A_{ratio}\right)\psi_s}{\rho_L}$ where $\psi_s = 1+\left(\frac{\rho_L}{\rho_V}-1\right)\left[0.25\cdot q\left(1-q\right)+q^2\right]$	$\Delta P_{expansion,A} = -0.03$ Pa $\Delta P_{expansion,B} = -1.39$ Pa $\Delta P_{expansion,C} = -47.6$ Pa
$\Delta P_{expansion,A} = -0.03$ Pa $\Delta P_{expansion,B} = -1.39$ Pa $\Delta P_{expansion,C} = -47.6$ Pa	$\Delta P_{outlet} = \Delta P_{expansion,A} + \Delta P_{expansion,B} + \Delta P_{expansion,C}$	$\Delta P_{outlet} = -48.98$ Pa
Momentum Pressure Change		
$q_2 = 0.461$ (see Table A.1) $q_3 = 0.29$ (see Table A.1) $\rho_V = 12.14$ kg m^{-3} $\rho_L = 579$ kg m^{-3} $\mu_L = 1.137\times10^{-4}$ kg m^{-1} s^{-1} $\mu_V = 1.034\times10^{-5}$ kg m^{-1} s^{-1}	Baroczy (1965) – Void Fraction $\varepsilon = \left(1+\left(\frac{1-q}{q}\right)^{0.74}\left(\frac{\rho_V}{\rho_L}\right)^{0.65}\left(\frac{\mu_L}{\mu_V}\right)^{0.13}\right)^{-1}$	$\varepsilon_2 = 0.8894$ $\varepsilon_3 = 0.8232$
$G = 152.5$ kg m^{-2} s^{-1} (measured) $q_2 = 0.461$ (see Table A.1) $q_3 = 0.29$ (see Table A.1) $\rho_V = 12.14$ kg m^{-3} $\rho_L = 579$ kg m^{-3} $\varepsilon_2 = 0.8894$ $\varepsilon_3 = 0.8232$	$\Delta P_{DECELERATION} = \begin{pmatrix} G^2\left[\frac{q_3^2}{\rho_V\cdot\varepsilon_3}+\frac{\left(1-q_3\right)^2}{\rho_L\cdot\left(1-\varepsilon_3\right)}\right] \\ -G^2\left[\frac{q_2^2}{\rho_V\cdot\varepsilon_2}+\frac{\left(1-q_2\right)^2}{\rho_L\cdot\left(1-\varepsilon_2\right)}\right] \end{pmatrix}$	$\Delta P_{DECELERATION} = -253$ Pa
Frictional Pressure Drop and Gradient		
$\Delta P_{exp} = 8080$ Pa (measured) $\Delta P_{inlet} = 606.7$ $\Delta P_{outlet} = -48.98$ Pa $\Delta P_{deceleration} = -253$ Pa	$\Delta P_{fric} = \Delta P_{exp} - \left(\Delta P_{inlet} + \Delta P_{outlet} + \Delta P_{deceleration}\right)$	$\Delta P_{fric} = 7.78$ kPa
$\Delta P_{fric} = 7.78$ kPa $L_{DP} = 0.381$ m	$\left(\frac{dP}{dz}\right)_{fric} = \frac{\Delta P_{fric}}{L_{DP}}$	$\left(\frac{dP}{dz}\right)_{fric} = 20.4$ kPa m^{-1}

APPENDIX B

UNCERTAINTY ANALYSIS

Uncertainty analyses were conducted for the calculated parameters of ammonia heat duty, heat transfer coefficient and frictional pressure drop, and ammonia/water bulk mass fraction, heat duty and frictional pressure gradient. These analyses were conducted using the built-in uncertainty propagation feature in the *Engineering Equation Solver* (Klein, 2012) platform, according to the method of Taylor and Kuyatt (1994). By assuming that the individual measurements are uncorrelated and random, the uncertainty in each quantity was calculated as follows:

$$U_Y = \sqrt{\sum_i \left(\frac{\partial Y}{\partial X_i} \right)^2 U_{X,i}^2} \tag{B.1}$$

The ammonia heat duty, heat transfer coefficient, and frictional pressure drop uncertainty procedures are illustrated in Sections B.1, B.2, and B.3, respectively, for a sample point with D = 1.44 mm, G = 150 kg m^{-2} s^{-1} and $\underline{T}_{sat}$ = 40°C. The ammonia/water condensation heat duty uncertainty procedure is illustrated in Section B.4 for a sample point with D = 1.44, G = 100 kg m^{-2} s^{-1} and x_{bulk} = 0.90.

B.1 Ammonia Condensation Heat Duty Uncertainty

As presented in Chapter 4, the ammonia condensation heat duty can be calculated from the following expression:

$$\dot{Q}_{cond} = \dot{m}\left(h_4 - h_1\right) - \dot{Q}_{pre} - \dot{Q}_{post} + \dot{Q}_{pre,loss} + \dot{Q}_{post,loss} \tag{B.2}$$

The resulting uncertainty in the heat duty can then be expressed as follows:

$$\left(U_{\dot{Q}_{\text{cond}}}\right)^2 = \left(\frac{\partial \dot{Q}_{\text{cond}}}{\partial \dot{m}} U_{\dot{m}}\right)^2 + \left(\frac{\partial \dot{Q}_{\text{cond}}}{\partial h_1} U_{h_1}\right)^2 + \left(\frac{\partial \dot{Q}_{\text{cond}}}{\partial h_4} U_{h_4}\right)^2$$
$$+ \left(\frac{\partial \dot{Q}_{\text{cond}}}{\partial \dot{Q}_{\text{pre}}} U_{\dot{Q}_{\text{pre}}}\right)^2 + \left(\frac{\partial \dot{Q}_{\text{cond}}}{\partial \dot{Q}_{\text{post}}} U_{\dot{Q}_{\text{post}}}\right)^2 + \left(\frac{\partial \dot{Q}_{\text{cond}}}{\partial \dot{Q}_{\text{pre,loss}}} U_{\dot{Q}_{\text{pre,loss}}}\right)^2 + \left(\frac{\partial \dot{Q}_{\text{cond}}}{\partial \dot{Q}_{\text{post,loss}}} U_{\dot{Q}_{\text{post,loss}}}\right)^2 \quad \text{(B.3)}$$

Differentiating Eq. (B.2) for each term yields the following:

$$\left(U_{\dot{Q}_{\text{cond}}}\right)^2 = \left((h_4 - h_1)U_{\dot{m}}\right)^2 + \left(\dot{m} \cdot U_{h_1}\right)^2 + \left(\dot{m} \cdot U_{h_4}\right)^2$$
$$+ \left(U_{\dot{Q}_{\text{pre}}}\right)^2 + \left(U_{\dot{Q}_{\text{post}}}\right)^2 + \left(U_{\dot{Q}_{\text{pre,loss}}}\right)^2 + \left(U_{\dot{Q}_{\text{post,loss}}}\right)^2 \quad \text{(B.4)}$$

The uncertainty in the measured mass flow was ±0.25% of reading, while the measurement uncertainty of pre- and post-heater power was ±0.2% of reading. The uncertainty of the calculated ambient loss was conservatively assumed to be ±50%. Finally, the uncertainties in the pre-heater inlet (h_1) and post-heater outlet (h_4) enthalpies were a function of the measured uncertainties in temperature (±0.2°C) and pressure (±2.62 kPa). Finally, the uncertainty in the condensation heat duty was calculated as follows:

$$\left(U_{\dot{Q}_{\text{cond}}}\right)^2 = \left(\left[1210.6 \times 10^3 \text{ J kg}^{-1}\right] \cdot \left[6.16 \times 10^{-7} \text{ kg s}^{-1}\right]\right)^2$$
$$+ \left(\left[2.47 \times 10^{-4} \text{ kg s}^{-1}\right] \cdot \left[0.957 \times 10^3 \text{ J kg}^{-1}\right]\right)^2$$
$$+ \left(\left[2.47 \times 10^{-4} \text{ kg s}^{-1}\right] \cdot \left[0.6439 \times 10^3 \text{ J kg}^{-1}\right]\right)^2$$
$$+ \left(0.284 \text{ W}\right)^2 + \left(0.408 \text{ W}\right)^2 + \left(0.098 \text{ W}\right)^2 + \left(0.423 \text{ W}\right)^2 \quad \text{(B.5)}$$

The calculated uncertainty was ±1.07 W or ±2.3% of measured value.

B.2 Ammonia Heat Transfer Coefficient Uncertainty

As presented in Chapter 4, the ammonia condensation thermal resistance was found from the following equation:

$$R_{\text{cond}} = \frac{\Delta T_{\text{LM}}}{\dot{Q}_{\text{cond}}} - R_{\text{water}} - R_{\text{wall}} \tag{B.6}$$

The uncertainty in $\dot{Q}_{\text{cond}}$ was calculated in the previous section (B.1). The uncertainty in the water-side thermal resistance was assumed to be a conservative ±25%, and the uncertainty in the wall thermal resistance was assumed negligible. The log-mean temperature was calculated as follows:

$$\Delta T_{\text{LM}} = \frac{\left[T_{\text{sat}}\left(P_2\right) - T_{\text{w,o}}\right] - \left[T_{\text{sat}}\left(P_3\right) - T_{\text{w,i}}\right]}{\ln\left[\dfrac{T_{\text{sat}}\left(P_2\right) - T_{\text{w,o}}}{T_{\text{sat}}\left(P_3\right) - T_{\text{w,i}}}\right]} \tag{B.7}$$

The uncertainty in ΔT_{LM} was calculated as follows:

$$\left(U_{\Delta T_{\text{LMTD}}}\right)^2 = \left(\frac{\partial \Delta T_{\text{LM}}}{\partial T_{\text{sat}}\left(P_2\right)}\right)^2 U_{T_{\text{sat}}(P_2)}^2 + \left(\frac{\partial \Delta T_{\text{LM}}}{\partial T_{\text{sat}}\left(P_3\right)}\right)^2 U_{T_{\text{sat}}(P_3)}^2 + \left(\frac{\partial \Delta T_{\text{LM}}}{\partial T_{\text{w,i}}}\right)^2 U_{T_{\text{w,i}}}^2 + \left(\frac{\partial \Delta T_{\text{LM}}}{\partial T_{\text{w,o}}}\right)^2 U_{T_{\text{w,o}}}^2 \tag{B.8}$$

The log-mean temperature difference was differentiated by replacing $\Delta T_1 = \left(T_{\text{sat}}\left(P_2\right) - T_{\text{w,o}}\right)$ and $\Delta T_2 = \left(T_{\text{sat}}\left(P_3\right) - T_{\text{w,i}}\right)$, to simplify Eq. (B.7):

$$
\begin{aligned}
\frac{\partial \Delta T_{\mathrm{LM}}}{\partial T_{\mathrm{sat}}\left(P_2\right)} &= \frac{1}{\ln\left(\dfrac{\Delta T_1}{\Delta T_2}\right)} - \frac{\Delta T_1 - \Delta T_2}{\ln\left(\dfrac{\Delta T_1}{\Delta T_2}\right)^2} \cdot \frac{1}{\Delta T_1} = 0.49 \\
\frac{\partial \Delta T_{\mathrm{LM}}}{\partial T_{\mathrm{sat}}\left(P_3\right)} &= \frac{-1}{\ln\left(\dfrac{\Delta T_1}{\Delta T_2}\right)} + \frac{\Delta T_1 - \Delta T_2}{\ln\left(\dfrac{\Delta T_1}{\Delta T_2}\right)^2} \cdot \frac{1}{\Delta T_2} = 0.51 \\
\frac{\partial \Delta T_{\mathrm{LM}}}{\partial T_{\mathrm{w,i}}} &= \frac{-1}{\ln\left(\dfrac{\Delta T_1}{\Delta T_2}\right)} - \frac{\Delta T_1 - \Delta T_2}{\ln\left(\dfrac{\Delta T_1}{\Delta T_2}\right)^2} \cdot \frac{1}{\Delta T_2} = -0.51 \\
\frac{\partial \Delta T_{\mathrm{LM}}}{\partial T_{\mathrm{w,o}}} &= \frac{1}{\ln\left(\dfrac{\Delta T_1}{\Delta T_2}\right)} + \frac{\Delta T_1 - \Delta T_2}{\ln\left(\dfrac{\Delta T_1}{\Delta T_2}\right)^2} \cdot \frac{1}{\Delta T_1} = -0.49
\end{aligned}
\tag{B.9}
$$

The water inlet and outlet temperature had measured uncertainties of ±0.2°C. The saturated inlet and outlet temperatures were functions of the uncertainty in the measured pressures (±2.62 kPa), yielding an uncertainty in saturation temperature of ±0.061°C. Thus, Eq. (B.8) was evaluated as follows:

$$
\left(U_{\Delta T_{\mathrm{LM}}}\right)^2 = (0.49)^2 (0.061\ \mathrm{K})^2 + (0.51)^2 (0.061\ \mathrm{K})^2 + (-0.51)^2 (0.2\ \mathrm{K})^2 + (-0.49)^2 (0.2\ \mathrm{K})^2 \tag{B.10}
$$

The resulting uncertainty in ΔT_{LM} was ±0.15 K. The uncertainty in R_{cond} was then expressed as:

$$
\begin{aligned}
\left(U_{R_{\mathrm{cond}}}\right)^2 &= \left(\frac{\partial R_{\mathrm{cond}}}{\partial \dot{Q}_{\mathrm{cond}}}\right)^2 \left(U_{\dot{Q}_{\mathrm{cond}}}\right)^2 + \left(\frac{\partial R_{\mathrm{cond}}}{\partial \Delta T_{\mathrm{LMTD}}}\right)^2 \left(U_{\Delta T_{\mathrm{LMTD}}}\right)^2 + \left(\frac{\partial R_{\mathrm{cond}}}{\partial R_{\mathrm{water}}}\right)^2 \left(U_{R_{\mathrm{water}}}\right)^2 + \left(\frac{\partial R_{\mathrm{cond}}}{\partial R_{\mathrm{wall}}}\right)^2 \left(U_{R_{\mathrm{wall}}}\right)^2 \\
\left(U_{R_{\mathrm{cond}}}\right)^2 &= \left(\frac{\Delta T_{\mathrm{LM}}}{\dot{Q}_{\mathrm{cond}}^2}\right)^2 \left(U_{\dot{Q}_{\mathrm{cond}}}\right)^2 + \left(\frac{1}{\dot{Q}_{\mathrm{cond}}}\right)^2 \left(U_{\Delta T_{\mathrm{LMTD}}}\right)^2 + \left(U_{R_{\mathrm{water}}}\right)^2 \\
\left(U_{R_{\mathrm{cond}}}\right)^2 &= \left(\frac{2.8\ \mathrm{K}}{[46.4\ \mathrm{W}]^2}\right)^2 (1.07\ \mathrm{W})^2 + \left(\frac{1}{46.4\ \mathrm{W}}\right)^2 (0.15\ \mathrm{W})^2 + \left(0.00431\ \mathrm{K\ W^{-1}}\right)^2
\end{aligned}
\tag{B.11}
$$

The resulting uncertainty in the condensation thermal resistance for the sample ammonia point was ±0.00556 K W^{-1}, or 14.8% of the measured value.

B.3 Zeotropic Mixture Condensation Heat Duty Uncertainty

The zeotropic mixture heat duty is calculated in the same manner as for pure ammonia (see Eq. (B.2)). The primary difference was that the uncertainty in the enthalpy of h_1 and h_4 for the mixture was also a function of the uncertainty in the bulk ammonia mass fraction ($x_{\text{bulk}} = 0.91 \pm 0.0024$):

$$\begin{aligned} h_1 &= f\left(T_1, P_1, x_{\text{bulk}}\right) = f\left(26.1\ ^{\circ}\text{C}, 1510\ \text{kPa}, 0.91\right) = 54.69 \pm 1.96\ \text{kJ kg}^{-1} \\ h_4 &= f\left(T_4, P_4, x_{\text{bulk}}\right) = f\left(146.2\ ^{\circ}\text{C}, 1505\ \text{kPa}, 0.91\right) = 1690 \pm 2.55\ \text{kJ kg}^{-1} \end{aligned} \tag{B.12}$$

As before, the uncertainty in the zeotropic heat duty can be expressed as follows:

$$\begin{aligned} \left(U_{\dot{Q}_{\text{cond}}}\right)^2 &= \left(\frac{\partial \dot{Q}_{\text{cond}}}{\partial \dot{m}} U_{\dot{m}}\right)^2 + \left(\frac{\partial \dot{Q}_{\text{cond}}}{\partial h_1} U_{h_1}\right)^2 + \left(\frac{\partial \dot{Q}_{\text{cond}}}{\partial h_4} U_{h_4}\right)^2 \\ &+ \left(\frac{\partial \dot{Q}_{\text{cond}}}{\partial \dot{Q}_{\text{pre}}} U_{\dot{Q}_{\text{pre}}}\right)^2 + \left(\frac{\partial \dot{Q}_{\text{cond}}}{\partial \dot{Q}_{\text{post}}} U_{\dot{Q}_{\text{post}}}\right)^2 + \left(\frac{\partial \dot{Q}_{\text{cond}}}{\partial \dot{Q}_{\text{pre,loss}}} U_{\dot{Q}_{\text{pre,loss}}}\right)^2 + \left(\frac{\partial \dot{Q}_{\text{cond}}}{\partial \dot{Q}_{\text{post,loss}}} U_{\dot{Q}_{\text{post,loss}}}\right)^2 \end{aligned} \tag{B.13}$$

Differentiating Eq. (B.2) for each term and substituting in the appropriate values for the zeotropic mixture yields the following:

$$\begin{aligned} \left(U_{\dot{Q}_{\text{cond}}}\right)^2 &= \left(\left(h_4 - h_1\right) U_{\dot{m}}\right)^2 + \left(\dot{m} \cdot U_{h_1}\right)^2 + \left(\dot{m} \cdot U_{h_4}\right)^2 \\ &+ \left(U_{\dot{Q}_{\text{pre}}}\right)^2 + \left(U_{\dot{Q}_{\text{post}}}\right)^2 + \left(U_{\dot{Q}_{\text{pre,loss}}}\right)^2 + \left(U_{\dot{Q}_{\text{post,loss}}}\right)^2 \end{aligned}$$

$$\begin{aligned} \left(U_{\dot{Q}_{\text{cond}}}\right)^2 &= \left(\left[1635 \times 10^3\ \text{J kg}^{-1}\right] \cdot \left[3.96 \times 10^{-7}\ \text{kg s}^{-1}\right]\right)^2 \\ &+ \left(\left[1.58 \times 10^{-4}\ \text{kg s}^{-1}\right] \cdot \left[1.96 \times 10^3\ \text{J kg}^{-1}\right]\right)^2 \\ &+ \left(\left[1.58 \times 10^{-4}\ \text{kg s}^{-1}\right] \cdot \left[2.55 \times 10^3\ \text{J kg}^{-1}\right]\right)^2 \\ &+ \left(0.438\ \text{W}\right)^2 + \left(0.227\ \text{W}\right)^2 + \left(0.845\ \text{W}\right)^2 + \left(1.775\ \text{W}\right)^2 \end{aligned} \tag{B.14}$$

The calculated uncertainty for the zeotropic mixture sample point was ±2.12 W or ±3.1% of measured value.

B.4 Frictional Pressure Drop Uncertainty

For the both the ammonia and ammonia/water data, frictional pressure drop was calculated as follows:

$$\Delta P_{\text{fric}} = \Delta P_{\text{measured}} - \left(\Delta P_{\text{inlet}} + \Delta P_{\text{outlet}} + \Delta P_{\text{deceleration}}\right) \tag{B.15}$$

The uncertainty in frictional pressure drop was expressed as follows:

$$\begin{aligned}\left(U_{\Delta P_{\text{fric}}}\right)^2 = &\left(\frac{\partial \Delta P_{\text{fric}}}{\partial \Delta P_{\text{measured}}}\right)^2 \left(U_{\Delta P_{\text{measured}}}\right)^2 + \left(\frac{\partial \Delta P_{\text{fric}}}{\partial \Delta P_{\text{inlet}}}\right)^2 \left(U_{\Delta P_{\text{inlet}}}\right)^2 \\ &+ \left(\frac{\partial \Delta P_{\text{fric}}}{\partial \Delta P_{\text{outlet}}}\right)^2 \left(U_{\Delta P_{\text{outlet}}}\right)^2 + \left(\frac{\partial \Delta P_{\text{fric}}}{\partial \Delta P_{\text{deceleration}}}\right)^2 \left(U_{\Delta P_{\text{deceleration}}}\right)^2\end{aligned} \tag{B.16}$$

Here, the uncertainty in the measured value was ±75 Pa, while a conservative uncertainty of ±50% was assigned to the inlet, outlet, and deceleration pressure changes. For the sample ammonia point, the uncertainty was calculated as:

$$\left(U_{\Delta P_{\text{fric}}}\right)^2 = \left(75 \text{ Pa}\right)^2 + \left(303.4 \text{ Pa}\right)^2 + \left(-24.5 \text{ Pa}\right)^2 + \left(-126.5 \text{ Pa}\right)^2 \tag{B.17}$$

For the sample ammonia point, the uncertainty in frictional pressure drop was 0.338 kPa or 4.3% of the calculated frictional pressure drop.

APPENDIX C

MODEL IMPLEMENTATION

The implementation of the ammonia condensation correlation (Table C.1) and zeotropic condenser design model (Table C.2) are introduced in this section. The steps correspond to equations and figures introduced in Chapter 6.

Table C.1: Implementation of NH_3 condensation correlation

Inputs	Equations	Results
Inlet Conditions and Dimensionless Parameters		
$D = 2.16$ mm $G = 100$ kg m^{-2} s^{-1} $T_{sat} = 40$ $q = 0.25$	Ammonia Saturated Properties = $f(T_{sat})$	$c_{p,L} = 4.93$ kJ kg^{-1} K^{-1} $h_{fg} = 1099$ kJ kg^{-1} $k_L = 0.443$ W m^{-1} K^{-1} $P_{sat} = 1555$ kPa $\mathrm{Pr}_L = 1.27$ $\rho_L = 579$ kg m^{-3} $\rho_V = 12.03$ kg m^{-3} $\mu_L = 1.14\times10^{-4}$ kg m^{-1} s^{-1} $\mu_V = 1.03\times10^{-5}$ kg m^{-1} s^{-1} $\sigma = 0.0164$ N m^{-1}
	$\mathrm{Re}_L = \frac{G\cdot(1-q)\cdot D}{\mu_L}$ $\mathrm{Re}_{LO} = \frac{G\cdot D}{\mu_L}$ $\mathrm{Re}_V = \frac{G\cdot q\cdot D}{\mu_V}$ $\mathrm{Ca}_L = \frac{\mu_L\cdot(1-q)\cdot G}{\rho_L\cdot\sigma}$ $j_G^* = \frac{G\cdot q}{\sqrt{D\cdot g\cdot\rho_V\cdot(\rho_L-\rho_V)}}$	$\mathrm{Re}_L = 1421$ (laminar) $\mathrm{Re}_{LO} = 1894$ $\mathrm{Re}_V = 5230$ (turbulent) $\mathrm{Ca}_L = 9.0\times10^{-4}$ $j_G^* = 2.079$ (non-annular)
	$j_L = \frac{G\cdot(1-q)}{\rho_L}$ $j_V = \frac{G\cdot q}{\rho_V}$ $j = j_L + j_V$	$j_L = 0.1294$ m s^{-1} $j_V = 2.078$ m s^{-1} $j = 2.207$ m s^{-1}

Table C.1: Implementation of NH_3 condensation correlation – cont.

Inputs	Equations	Results
Calculation of Martinelli Parameter X		
$\mathrm{Re_L} = 1421$ (laminar) $\mathrm{Re_V} = 5230$ (turbulent)	$f_\mathrm{L} = 16/\mathrm{Re_L}$ (liquid-phase laminar) $f_\mathrm{V} = 0.079 \cdot \mathrm{Re_V^{0.25}}$ (vapor-phase turbulent)	$f_\mathrm{L} = 0.01126$ $f_\mathrm{V} = 0.00929$
$D = 2.16$ mm $G = 100$ kg m^{-2} s^{-1} $q = 0.25$ $f_\mathrm{L} = 0.01126$ $f_\mathrm{V} = 0.00929$ $\rho_\mathrm{L} = 579$ kg m^{-3} $\rho_\mathrm{V} = 12.03$ kg m^{-3}	$\left(\frac{dP}{dz}\right)_\mathrm{L} = \frac{2 \cdot f_\mathrm{L} \cdot G^2 \cdot (1-q)^2}{\rho_\mathrm{L} D}$ $\left(\frac{dP}{dz}\right)_\mathrm{V} = \frac{2 \cdot f_\mathrm{V} \cdot G^2 \cdot q^2}{\rho_\mathrm{V} D}$	$\left(\frac{dP}{dz}\right)_\mathrm{L} = 101.2$ Pa m^{-1} $\left(\frac{dP}{dz}\right)_\mathrm{V} = 446.8$ Pa m^{-1}
$\left(\frac{dP}{dz}\right)_\mathrm{L} = 101.2$ Pa m^{-1} $\left(\frac{dP}{dz}\right)_\mathrm{V} = 446.8$ Pa m^{-1}	$X = \sqrt{\frac{(dP/dz)_\mathrm{L}}{(dP/dz)_\mathrm{V}}}$	$X = 0.476$
Calculation of Void Fraction, ε (Keinath, 2012) and film thickness δ		
$j_\mathrm{L} = 0.1294$ m s^{-1} $j_\mathrm{V} = 2.078$ m s^{-1}	$\beta = \frac{j_\mathrm{V}}{j_\mathrm{L} + j_\mathrm{V}}$	$\beta = 0.9414$
$X = 0.476$ $j = 2.207$ m s^{-1} $\mathrm{Ca_L} = 9.0 \times 10^{-4}$ $\rho_\mathrm{L} = 579$ kg m^{-3} $\rho_\mathrm{V} = 12.03$ kg m^{-3}	$\bar{V}_\mathrm{vj} = 0.336 \cdot X^{0.25} \cdot \mathrm{Ca_L}^{0.154} \cdot \left(\sqrt{\frac{\rho_\mathrm{L}}{\rho_\mathrm{V}}} - 1\right)^{0.81} \cdot j$	$\bar{V}_\mathrm{vj} = 0.8864$ m s^{-1}
$\beta = 0.9414$ $j = 2.207$ m s^{-1} $\bar{V}_\mathrm{vj} = 0.8864$ m s^{-1}	$\varepsilon = \frac{\beta}{\left(1 + \frac{\bar{V}_\mathrm{vj}}{j}\right)}$	$\varepsilon = 0.672$
$D = 2.16$ mm $\varepsilon = 0.672$	$\delta = \left(\frac{D}{2}\right) \cdot \left(1 - \sqrt{\varepsilon}\right)$	$\delta = 1.95 \times 10^{-4}$ m
Calculation of Annular Nusselt Number, Nu_a		
$q = 0.25$ $\varepsilon = 0.672$ $\rho_\mathrm{L} = 579$ kg m^{-3} $\rho_\mathrm{V} = 12.03$ kg m^{-3}	$\frac{U_\mathrm{V}}{U_\mathrm{L}} = \left(\frac{q}{1-q}\right)\left(\frac{\rho_\mathrm{L}}{\rho_\mathrm{V}}\right)\left(\frac{1-\varepsilon}{\varepsilon}\right)$	$\frac{U_\mathrm{V}}{U_\mathrm{L}} = 7.85$
$\frac{U_\mathrm{V}}{U_\mathrm{L}} = 7.85$ $\delta = 1.95 \times 10^{-4}$ m $\rho_\mathrm{L} = 579$ kg m^{-3} $\rho_\mathrm{V} = 12.03$ kg m^{-3} $\sigma = 0.0164$ N m^{-1}	$\Phi = \left(1 + 0.27\left(\frac{U_\mathrm{V}}{U_\mathrm{L}}\right)^{0.21} f_\mathrm{i}^{-0.46}\right)$ where $f_\mathrm{i} = \frac{(\rho_\mathrm{L} - \rho_\mathrm{V}) \cdot g \cdot \delta^2}{\sigma}$	$\Phi = 4.08$ $f_\mathrm{i} = 0.01289$

Table C.1: Implementation of NH_3 condensation correlation – cont.

Inputs	Equations	Results
$\mathrm{Re_{LO}} = 1894$ $\mathrm{Pr_L} = 1.27$ $\Phi = 4.08$	$\mathrm{Nu_a} = 0.023 \cdot \mathrm{Re_{LO}^{0.8}} \cdot \mathrm{Pr_L^{0.4}} \cdot \Phi$	$\mathrm{Nu_a} = 43.2$
Calculation of Wavy Nusselt Number, Nu_{wavy} (Cavallini et al. 2006)		
$\mathrm{Re_{LO}} = 1894$ $\mathrm{Pr_L} = 1.27$ $q = 0.25$ $\rho_L = 579\ \mathrm{kg\ m^{-3}}$ $\rho_V = 12.03\ \mathrm{kg\ m^{-3}}$ $h_{fg} = 1099\ \mathrm{kJ\ kg^{-1}}$ $k_L = 0.443\ \mathrm{W\ m^{-1}\ K^{-1}}$ $\mu_L = 1.14 \times 10^{-4}\ \mathrm{kg\ m^{-1}\ s^{-1}}$ $\mu_V = 1.03 \times 10^{-5}\ \mathrm{kg\ m^{-1}\ s^{-1}}$	$\mathrm{Nu_{wavy}} = \left[\left(1 + 0.741 \left[\frac{1-q}{q} \right]^{0.3321} \right)^{-1} \mathrm{Nu_{film}} + \mathrm{Nu_{pool}} \right]$ where $\mathrm{Nu_{film}} = \left(\frac{D}{k_L} \right) 0.725 \left(\frac{k_L^3 \rho_L (\rho_L - \rho_V) g h_{fg}}{\mu_L D (T_{sat} - T_{wall})} \right)^{0.25}$ $\mathrm{Nu_{pool}} = 0.023\, \mathrm{Re_{LO}^{0.8}}\, \mathrm{Pr_L^{0.4}} \left(1 - q^{0.087}\right)$	$\mathrm{Nu_{wavy}} = 49.28$ $\mathrm{Nu_{pool}} = 1.2$ $\mathrm{Nu_{film}} = 99.4$
Calculation of Non-Annular Nusselt, $Nu_{n\text{-}a}$, and Heat Transfer Coefficient α		
$\mathrm{Nu_a} = 43.2$ $\mathrm{Nu_{wavy}} = 49.28$ $j_G^* = 2.079$ (non-annular) $j_T = 2.5$	$\mathrm{Nu_{n\text{-}a}} = \left[\mathrm{Nu_a} \left(\frac{j_T}{j_G^*} \right)^{0.8} - \mathrm{Nu_{wavy}} \right] \left(\frac{j_G^*}{j_T} \right) + \mathrm{Nu_{wavy}}$	$\mathrm{Nu_{n\text{-}a}} = 49.85$
$\mathrm{Nu_{n\text{-}a}} = 49.85$ $k_L = 0.443\ \mathrm{W\ m^{-1}\ K^{-1}}$ $D = 2.16\ \mathrm{mm}$	$\alpha = \frac{\mathrm{Nu_{n\text{-}a}} \cdot k_L}{D}$	$\alpha = 10.2\ \mathrm{kW\ m^{-2}\ K^{-1}}$

Table C.2: Implementation of non-equilibrium film model

Sample Calculation: NH_3/H_2O, D = 0.98 mm, x_{bulk} = 0.90, G = 100 kg m^2 s^1, Segment #2		
Inputs	**Equations**	**Results (solved iteratively)**
Average Properties and Dimensionless Parameters		
Outlet conditions from previous segment $h_{in,T} = 1369$ kJ kg^{-1} $P_i = 1480$ kPa $q_i = 0.869$ $T_{v,i} = 109.1$ °C $T_{i,i} = 66.36$ °C $T_{L,i} = 74.2$ °C $x_{1,i} = 0.5868$ $x_{1,int,i} = 0.5868$ $y_{1,i} = 0.9358$ $y_{1,int,i} = 0.9949$ Solved Iteratively $q_o = 0.7868$ $T_{v,o} = 95.1$ °C $T_{i,o} = 58.2$ °C $T_{L,o} = 54.8$ °C $x_{1,o} = 0.6529$ $x_{1,int,o} = 0.6529$ $y_{1,o} = 0.9542$ $y_{1,int,o} = 0.9975$	$q_{avg} = \frac{q_i + q_o}{2}$ $T_{v,avg} = \frac{T_{v,i} + T_{v,o}}{2}$ $T_{L,avg} = \frac{T_{L,i} + T_{L,o}}{2}$ $x_{1,avg} = \frac{x_{1,i} + x_{1,o}}{2}$ $y_{1,avg} = \frac{y_{1,i} + y_{1,o}}{2}$	$q_{avg} = 0.8279$ $T_{v,avg} = 102.1$ $T_{L,avg} = 64.5$ $x_{1,avg} = 0.6199$ $y_{1,avg} = 0.945$
$T_{v,avg} = 102.1$ $T_{L,avg} = 64.5$ $x_{1,avg} = 0.6199$ $y_{1,avg} = 0.945$	Vapor Properties = $f(T_{v,avg}, y_{1,avg}, P)$ Liquid Properties = $f(T_{L,avg}, x_{1,avg})$	$c_{p,L} = 4.76$ kJ kg^{-1} K^{-1} $c_{p,V} = 2.51$ kJ kg^{-1} K^{-1} $D_{1-2,V} = 2.94\times10^{-6}$ m^2 s^{-1} $h_{fg} = 1301$ kJ kg^{-1} $k_L = 0.490$ W m^{-1} K^{-1} $k_V = 0.0369$ W m^{-1} K^{-1} $Pr_L = 3.20$ $Pr_V = 0.903$ $\rho_L = 783$ kg m^{-3} $\rho_V = 9.06$ kg m^{-3} $\mu_L = 3.26\times10^{-4}$ kg m^{-1} s^{-1} $\mu_V = 1.33\times10^{-5}$ kg m^{-1} s^{-1} $\sigma = 0.0229$ N m^{-1}

Table C.2: Implementation of non-equilibrium film model – cont.

Inputs	Equations	Results (solved iteratively)
	$\mathrm{Re_L} = \frac{G\cdot(1-q)\cdot D}{\mu_L}$ $\mathrm{Re_{LO}} = \frac{G\cdot D}{\mu_L}$ $\mathrm{Re_V} = \frac{G\cdot q\cdot D}{\mu_V}$ $\mathrm{Ca_L} = \frac{\mu_L\cdot(1-q)\cdot G}{\rho_L\cdot\sigma}$ $j_G^* = \frac{G\cdot q}{\sqrt{D\cdot g\cdot\rho_V\cdot(\rho_L-\rho_V)}}$	$\mathrm{Re_L} = 54.8$ (laminar) $\mathrm{Re_{LO}} = 318$ $\mathrm{Re_V} = 6481$ (turbulent) $\mathrm{Ca_L} = 3.32\times10^{-4}$ $j_G^* = 10.7$ (annular)
Vapor Sensible Heat Transfer		
$\mathrm{Re_V} = 6481$ (turbulent) $\varepsilon = 0$ (assumed)	$f_v = 8\cdot\left(\left(\frac{8}{\mathrm{Re_V}}\right)^{12} + \frac{1}{\left(\left(2.457\cdot ln\left(\frac{1}{(7/\mathrm{Re_V})^{0.9}+(0.27\cdot\varepsilon)}\right)\right)^{16}+\left(37530/\mathrm{Re_V}\right)^{16}\right)^{1.5}}\right)^{1/12}$	$f_V = 0.0351$
$f_V = 0.0351$ $\mathrm{Pr_V} = 0.903$ $\mathrm{Re_V} = 6481$ (turbulent)	$\mathrm{Nu_V} = \frac{\alpha_V D}{k_L} = \left(4.364^{10}+(B)^{-5}\right)^{1/10}$ $B = \frac{exp\left(\frac{2200-\mathrm{Re_V}}{365}\right)}{4.364^2} + \frac{1}{\left(6.3+0.079\cdot\left(\frac{f_V}{8}\right)^{0.5}\cdot\mathrm{Re_V}\cdot\frac{\mathrm{Pr_V}}{\left(1+\mathrm{Pr_V}^{0.8}\right)^{5/6}}\right)^2}$	$\mathrm{Nu_V} = 24$
$D = 0.98$ mm $k_V = 0.0369$ W m^{-1} K^{-1} $\mathrm{Nu_V} = 24$	$\alpha_V = \frac{\mathrm{Nu_V}\cdot k_V}{D}$	$\alpha_V = 906$ W m^{-2} K^{-1}
$\alpha_V = 906$ W m^{-2} K^{-1} $c_{p,V} = 2.51$kJ kg^{-1} K^{-1} $m'' = 0.1191$ kg m^{-2} s^{-1}	$\kappa = \frac{a}{1-\exp(-a)}$ where $a = \frac{m''\cdot c_{p,V}}{\alpha_V}$	$a = 0.3297$ $\kappa = 1.174$
$T_{v,i} = 109.1$ °C $T_{v,o} = 95.1$ °C $T_{int,i} = 66.4$ °C $T_{int,o} = 58.2$ °C	$\Delta T_{LM,V} = \frac{(T_{v,i}-T_{int,i})-(T_{v,o}-T_{int,o})}{\ln\left(\frac{T_{v,i}-T_{int,i}}{T_{v,o}-T_{int,o}}\right)}$	$\Delta T_{LM,V} = 39.73$ K

Table C.2: Implementation of non-equilibrium film model – cont.

Inputs	Equations	Results (solved iteratively)
$c_{p,V} = 2.51 \text{kJ kg}^{-1}\ \text{K}^{-1}$ $D = 0.98$ mm $\dot{m} = 7.97\times10^{-5}$ kg s^{-1} $L_{seg} = 0.01786$ m $\Delta T_{LM,V} = 39.73$ K $T_{v,i} = 109.1$ °C $T_{v,o} = 95.1$ °C $q_{avg} = 0.8279$	$\dot{Q}_{S,V} = \dfrac{\alpha_V \cdot \kappa \cdot \Delta T_{LM,V}}{\pi \cdot D \cdot L_{seg}}$ $\dot{Q}_{S,V} = \dot{m} \cdot q_{avg} \cdot c_{P,V} \cdot \left(T_{V,i} - T_{V,o}\right)$	$\dot{Q}_{S,V} = 2.319$ W
Vapor-Phase Mass Transfer and Condensing Flux		
$D_{1-2,V} = 2.94\times10^{-6}$ m^2 s^{-1} $\rho_V = 9.07$ kg m^{-3} $\mu_V = 1.33\times10^{-5}$ kg m^{-1} s^{-1}	$\text{Sc}_V = \dfrac{\mu_V}{\rho_V D_{1-2}}$	$\text{Sc}_V = 0.4964$
$\text{Nu}_V = 24$ $\text{Pr}_V = 0.903$ $\text{Sc}_V = 0.4964$	Chilton and Colburn (1934) $\text{Sh}_V = \text{Nu}_V \left(\dfrac{\text{Sc}_V}{\text{Pr}_V}\right)^{1/3}$ $\beta_V = \dfrac{\text{Sh}_V D_{1-2}}{D}$	$\text{Sh}_V = 19.72$ $\beta_V = 0.0593$ m s^{-1}
$\beta_V = 0.0593$ m s^{-1} $\rho_V = 9.07$ kg m^{-3} $\tilde{y}_{1,int,avg} = 0.9976$ $\tilde{y}_{1,avg} = 0.9479$	$\dot{N}_T = \dot{N}_1 + \dot{N}_2 = \beta_V \cdot C_{T,V} \cdot \ln\left(\dfrac{z - \tilde{y}_{1,int,avg}}{z - \tilde{y}_{1,avg}}\right)$ $z = \dfrac{\dot{N}_1}{\dot{N}_T}$	$\dot{N}_T = 0.0069$ kmol m^{-2} s^{-1} $\dot{N}_1 = 0.005303$ kmol m^{-2} s^{-1} $\dot{N}_2 = 0.001597$ kmol m^{-2} s^{-1} $z = 0.7686$
$\dot{N}_1 = 0.005303$ kmol m^{-2} s^{-1} $\dot{N}_2 = 0.001597$ kmol m^{-2} s^{-1} $MW_1 = 17.03$ kg kmol^{-1} $MW_1 = 18.02$ kg kmol^{-1}	$m_1'' = \dot{N}_1 \cdot MW_1$ $m_2'' = \dot{N}_2 \cdot MW_2$ $m'' = m_1'' + m_1''$	$m_1'' = 0.0903$ kg m^{-2} s^{-1} $m_2'' = 0.0288$ kg m^{-2} s^{-1} $m'' = 0.1191$ kg m^{-2} s^{-1}

Table C.2: Implementation of non-equilibrium film model – cont.

Inputs	Equations	Results (solved iteratively)
Overall Heat Transfer, $\dot{Q}_T$		
$T_{int,i} = 66.4\ ^{o}C$ $T_{int,o} = 58.2\ ^{o}C$ $T_{water} = 46.1\ ^{o}C$	$\Delta T_{LM,int} = \frac{\left(T_{int,i} - T_{water}\right) - \left(T_{int,o} - T_{water}\right)}{\ln\left(\frac{T_{int,i} - T_{water}}{T_{int,o} - T_{water}}\right)}$	$\Delta T_{LM,int} = 15.9\ K$
Calculated from procedure in Table C.1: $\alpha_L = 30.0\ kW\ m^{-2}\ K^{-1}$ $L_{seg} = 0.01786\ m$ $D = 0.98\ m$	$R_L = \frac{1}{\alpha_L \cdot \pi \cdot D \cdot L_{seg}}$	$R_L = 0.61\ K\ W^{-1}$
$R_{wall} = 0.169\ K\ W^{-1}$ (given) $R_{water} = 0.305\ K\ W^{-1}$ (given) $R_L = 0.61\ K\ W^{-1}$ $\Delta T_{LM,int} = 15.9\ K$	$\dot{Q}_T = \frac{\Delta T_{LM,int}}{R_L + R_{wall} + R_{water}}$	$\dot{Q}_T = 14.7\ W$
Phase Species and Energy Balance		
$m_1'' = 0.0903\ kg\ m^{-2}\ s^{-1}$ $m_2'' = 0.0288\ kg\ m^{-2}\ s^{-1}$ $A = 1.75\times10^{-5}\ m^2$ Outlet conditions from previous segment: $\dot{m}_{L,i} = 1.05\times10^{-5}\ kg\ s^{-1}$ $\dot{m}_{V,i} = 6.92\times10^{-5}\ kg\ s^{-1}$	$\dot{m}_{L,O} = \underbrace{\dot{m}_{L,i}}_{\text{Mass flow liquid in}} + \underbrace{m_1'' \cdot A}_{\text{Mass Flow } NH_3 \text{ condensed in}} + \underbrace{m_2'' \cdot A}_{\text{Mass Flow } H_2O \text{ condensed in}}$ $\dot{m}_{V,O} = \underbrace{\dot{m}_{V,i}}_{\text{Mass flow vapor in}} - \underbrace{m_1'' \cdot A}_{\text{Mass Flow } NH_3 \text{ condensed in}} - \underbrace{m_2'' \cdot A}_{\text{Mass Flow } H_2O \text{ condensed in}}$	$\dot{m}_{L,O} = 1.699\times10^{-5}\ kg\ s^{-1}$ $\dot{m}_{V,O} = 6.27\times10^{-5}\ kg\ s^{-1}$
$m_1'' = 0.0903\ kg\ m^{-2}\ s^{-1}$ $m_2'' = 0.0288\ kg\ m^{-2}\ s^{-1}$ $\dot{m}_{L,O} = 1.699\times10^{-5}\ kg\ s^{-1}$ $\dot{m}_{V,O} = 6.27\times10^{-5}\ kg\ s^{-1}$ $x_{1,i} = 0.5868$ $y_{1,i} = 0.9358$ $A = 1.75\times10^{-5}\ m^2$ Outlet conditions from previous segment: $\dot{m}_{L,i} = 1.05\times10^{-5}\ kg\ s^{-1}$ $\dot{m}_{V,i} = 6.92\times10^{-5}\ kg\ s^{-1}$	$x_{1,O}\dot{m}_{L,O} = \underbrace{x_{1,i} \cdot \dot{m}_{L,i}}_{\text{Mass Flow } NH_3 \text{ in}} + \underbrace{m_1'' \cdot A}_{\text{Mass Flow } NH_3 \text{ condensed in}}$ $y_{1,O}\dot{m}_{V,O} = \underbrace{y_{1,i} \cdot \dot{m}_{V,i}}_{\text{Mass Flow } NH_3 \text{ in}} - \underbrace{m_1'' \cdot A}_{\text{Mass Flow } NH_3 \text{ condensed out}}$	$x_{1,o} = 0.6529$ $y_{1,o} = 0.9542$

Table C.2: Implementation of non-equilibrium film model – cont.

Inputs	Equations	Results (solved iteratively)
$\dot{Q}_{\mathrm{T}} = 14.7$ W $\dot{m} = 7.97\times10^{-5}$ kg s^{-1} $h_{\mathrm{in,T}} = 1369$ kJ kg^{-1}	$h_{\mathrm{out,T}} = h_{\mathrm{in,T}} - \frac{\dot{Q}_T}{\dot{m}}$	$h_{\mathrm{out,T}} = 1185$ kJ kg^{-1}
$h_{\mathrm{out,T}} = 1185$ kJ kg^{-1} $\dot{m} = 7.97\times10^{-5}$ kg s^{-1} $\dot{m}_{\mathrm{L,O}} = 1.699\times10^{-5}$ kg s^{-1} $\dot{m}_{\mathrm{V,O}} = 6.27\times10^{-5}$ kg s^{-1} $P = 1480$ kPa $T_{\mathrm{L,O}} = 54.8$ °C $T_{\mathrm{V,O}} = 95.1$ °C $x_{1,\mathrm{o}} = 0.6529$ $y_{1,\mathrm{o}} = 0.9542$	$\dot{m}\cdot h_{\mathrm{out,T}} = \dot{m}_{\mathrm{V,O}} h_{\mathrm{V,O}} + \dot{m}_{\mathrm{L,O}} h_{\mathrm{L,O}}$ $h_{\mathrm{V,O}} = f\left(P, T_{\mathrm{V,O}}, y_{1,\mathrm{O}}\right)$ $h_{\mathrm{L,O}} = f\left(P, T_{\mathrm{L,O}}, x_{1,\mathrm{O}}\right)$	$h_{\mathrm{V,O}} = 1491$ kJ kg^{-1} $h_{\mathrm{L,O}} = 54.6$ kJ kg^{-1}

REFERENCES

Ackermann, G. (1937) Heat Transfer and Molecular Mass Transfer in the Same Field at High Temperatures and Large Partial Pressure Differences. *VDI-Forschungsheft*, **8**, pp. 1-10.

Afroz, H.M.M., Miyara, A., Tsubaki, K. (2008) Heat Transfer Coefficients and Pressure Drops During in-Tube Condensation of CO2/Dme Mixture Refrigerant. *International Journal of Refrigeration*, **31**, pp. 1458-1466.

Agarwal, A., 2006. Heat Transfer and Pressure Drop During Condensation of Refrigerants in Microchannels, GWW School of Mechanical Engineering. Georgia Institute of Technology, Atlanta, GA, USA, p. 373.

Agarwal, A., Bandhauer, T.M., Garimella, S. (2010) Measurement and Modeling of Condensation Heat Transfer in Non-Circular Microchannels. *International Journal of Refrigeration*, **33**, pp. 1169-1179.

Agarwal, A., Garimella, S. (2009) Modeling of Pressure Drop During Condensation in Circular and Noncircular Microchannels. *Journal of fluids engineering*, **131**, pp. 011302-011308.

Agarwal, A., Garimella, S. (2010) Representative Results for Condensation Measurements at Hydraulic Diameters Similar to 100 Microns. *Journal of Heat Transfer*, **132**, pp. 1-12.

Agarwal, A., Garimella, S. (2014a) Condensation Pressure Drop Experiments and Modeling at Hydraulic Diameters ~ 100 Microns. *International Journal of Heat and Mass Transfer*, **In preperation**.

Agarwal, A., Garimella, S. (2014b) Development of Model for Microchannel Condensation Heat Transfer of Synthetic Refrigerants. *International Journal of Heat and Mass Transfer*, **In preperation**.

Akbar, M.K., Plummer, D.A., Ghiaasiaan, S.M. (2003) On Gas-Liquid Two-Phase Flow Regimes in Microchannels. *International Journal of Multiphase Flow*, **29**, pp. 855-865.

Andresen, U., 2007. Supercritical Gas Cooling and near-Critical-Pressure Condensation of Refrigerant Blends in Microchannels, G.W.W. School of Mechanical Engineering. Georgia Institute of Technology, Atlanta, GA, USA, p. 261.

Armand, A.A. (1946) The Resistance During the Movement of a Two-Phase System in Horizontal Pipes. *Izv. Vses. Teplotekh. Inst.*, **1**, pp. 16–23 (AERE-Lib/Trans 828).

Baird, J.R., Fletcher, D.F., Haynes, B.S. (2003) Local Condensation Heat Transfer Rates in Fine Passages. *International Journal of Heat and Mass Transfer*, **46**, pp. 4453-4466.

Baker, O. (1954) Simultaneous Flow of Oil and Gas. *Oil and Gas Journal*, **53**, pp. 185-190.

Bandhauer, T.M., Agarwal, A., Garimella, S. (2006) Measurement and Modeling of Condensation Heat Transfer Coefficients in Circular Microchannels. *Journal of Heat Transfer*, **128**, pp. 1050-1059.

Barnea, D., Luninski, Y., Taitel, Y. (1983) Flow Pattern in Horizontal and Vertical Two Phase Flow in Small Diameter Pipes. *Canadian Journal of Chemical Engineering*, **61**, pp. 617-620.

Baroczy, C.J. (1965) Correlation of Liquid Fraction in Two-Phase Flow with Application to Liquid Metals. *Chemical Engineering Progress Symposium Series*, **61**, pp. 179-191.

Beattie, D.R.H., Whalley, P.B. (1982) A Simple Two-Phase Frictional Pressure Drop Calculation Method. *International Journal of Multiphase Flow*, **8**, pp. 83-87.

Bell, K.J., Ghaly, M.A. (1973) An Approximate Generalized Design Method for Multicomponent/Partial Condensers. *AIChE Symposium Series*, **69**, pp. 72-79.

Bird, R.B., Stewart, W.E., Lightfoot, E.N. (1960) *Transport Phenomena*. (Wiley, New York).

Blasius, P.R.H. (1913) Das Aehnlichkeitsgesetz Bei Reibungsvorgangen in Flüssigkeiten. *Forschungsheft*, **131**, pp. 1-41.

Braun, M., Renz, U. (1996) Multicomponent Diffusion Interactions During Condensation in Laminar and Turbulent Pipe Flow. *International Journal of Heat and Mass Transfer*, **40**, pp. 131-139.

Breber, G., Palen, J.W., Taborek, J. (1980) Prediction of Horizontal Tubeside Condensation of Pure Components Using Flow Regime Criteria. *Journal of Heat Transfer*, **102**, pp. 471-476.

Butterworth, D. (1983) *Film Condensation of Pure Vapor*, in: Schlunder, E.H. (Ed.), Heat Exchanger Design Handbook. (Hemisphere Publishing Co., Washington, D.C.

Carey, V. (2008) *Liquid-Vapor Phase-Change Phenomena*, 2nd ed. (Taylor & Francis Group, New York).

Cavallini, A., Censi, G., Del Col, D., Doretti, L., Longo, G.A., Rossetto, L. (2001) Experimental Investigation on Condensation Heat Transfer and Pressure Drop of New Hfc Refrigerants (R134a, R125, R32, R410a, R236ea) in a Horizontal Smooth Tube. *International Journal of Refrigeration*, **24**, pp. 73-87.

Cavallini, A., Censi, G., Del Col, D., Doretti, L., Longo, G.A., Rossetto, L. (2002a) Condensation of Halogenated Refrigerants inside Smooth Tubes. *HVAC&R Research*, **8**, pp. 429-451.

Cavallini, A., Censi, G., Del Col, D., Doretti, L., Longo, G.A., Rossetto, L. (2002b) A Tube-in-Tube Water/Zeotropic Mixture Condenser: Design Procedure against Experimental Data. *Experimental Thermal and Fluid Science*, **25**, pp. 495-501.

Cavallini, A., Del Col, D., Doretti, L., Matkovic, M., Rossetto, L., Zilio, C. (2005a) Condensation Heat Transfer and Pressure Gradient inside Multiport Minichannels. *Heat Transfer Engineering*, **26**, pp. 45-55.

Cavallini, A., Del Col, D., Doretti, L., Matkovic, M., Rossetto, L., Zilio, C., 2005b. A Model for Condensation in Minichannels, 2005 ASME Summer Heat Transfer Conference. ASME, San Francisco, pp. 297-304.

Cavallini, A., Del Col, D., Doretti, L., Matkovic, M., Rossetto, L., Zilio, C., Censi, G. (2006) Condensation in Horizontal Smooth Tubes: A New Heat Transfer Model for Heat Exchanger Design. *Heat Transfer Engineering*, **27**, pp. 31-38.

Cavallini, A., Del Col, D., Matkovic, M., Rossetto, L. (2009) Frictional Pressure Drop During Vapour-Liquid Flow in Minichannels: Modelling and Experimental Evaluation. *International journal of heat and fluid flow*, **30**, pp. 131-139.

Cavallini, A., Zecchin, R., (1974). A Dimensionless Correlation for Heat Transfer in Forced Convection Condensation, *Proc*. *5th International Heat Transfer Conference*, pp. 309-313.

Chato, J.C. (1962) Laminar Film Condensation inside Horizontal and Inclined Tubes. *ASHRAE Journal*, **4**, pp. 52-60.

Chen, S.L., Gerner, F.M., Tien, C.L. (1987) General Film Condensation Correlations. *Experimental Heat Transfer*, **1**, pp. 93-107.

Chilton, T.H., Colburn, A.P. (1934) Mass Transfer (Absorption) Coefficients Prediction from Data on Heat Transfer and Fluid Friction. *Industrial and Engineering Chemistry*, **26**, pp. 1183-1187.

Chisholm, D. (1967) A Theoretical Basis for the Lockhart-Martinelli Correlation for Two-Phase Flow. *International Journal of Heat and Mass Transfer*, **10**, pp. 1767-1778.

Chung, P.M.Y., Kawaji, M. (2004) The Effect of Channel Diameter on Adiabatic Two-Phase Flow Characteristics in Microchannels. *International Journal of Multiphase Flow*, **30**, pp. 735-761.

Churchill, S.W. (1977a) Comprehensive Correlating Equations for Heat, Mass and Momentum-Transfer in Fully Developed Flow in Smooth Tubes. *Industrial & Engineering Chemistry Fundamentals*, **16**, pp. 109-116.

Churchill, S.W. (1977b) Friction-Factor Equation Spans All Fluid-Flow Regimes. *Chemical Engineering*, **84**, pp. 91-92.

Churchill, S.W., Chu, H.H.S. (1975) Correlating Equations for Laminar and Turbulent Free Convection from a Horizontal Cylinder. *International Journal of Heat and Mass Transfer*, **18**, pp. 1049-1053.

Churchill, S.W., Usagi, R. (1974) A Standardized Procedure for the Production of Correlations in the Form of a Common Empirical Equation. *Industrial & Engineering Chemistry Fundamentals*, **13**, pp. 39-44.

Cioncolini, A., Thome, J.R., Lombardi, C. (2009) Unified Macro-to-Microscale Method to Predict Two-Phase Frictional Pressure Drops of Annular Flows. *International Journal of Multiphase Flow*, **35**, pp. 1138-1148.

Colburn, A.P. (1934) Calculation of Condensation with a Portion of Condensate Layer in Turbulent Motion. *Industrial and Engineering Chemistry*, **26**, pp. 432-434.

Colburn, A.P., Drew, T.B. (1937) The Condensation of Mixed Vapors. *Transactions of the American Institute of Chemical Engineers*, **33**, pp. 0197-0215.

Coleman, J.W., Garimella, S. (1999) Characterization of Two-Phase Flow Patterns in Small Diameter Round and Rectangular Tubes. *International Journal of Heat and Mass Transfer*, **42**, pp. 2869-2881.

Coleman, J.W., Garimella, S., 2000. Two-Phase Flow Regime Transitions in Microchannel Tubes: The Effect of Hydraulic Diameter, ASME Heat Transfer Division - 2000. American Society of Mechanical Engineers, Orlando, FL, pp. 71-83.

Coleman, J.W., Garimella, S. (2003) Two-Phase Flow Regimes in Round, Square and Rectangular Tubes During Condensation of Refrigerant R134a. *International Journal of Refrigeration*, **26**, pp. 117-128.

DeGrush, D., Stoecker, W.F., 1987. Measurements of Heat-Transfer Coefficents of Nonazeotropic Refrigerant Mixtures Condensing inside Horizontal Tubes. Oak Ridge National Laboratory.

Del Col, D., Cavallini, A., Thome, J.R. (2005) Condensation of Zeotropic Mixtures in Horizontal Tubes: New Simplified Heat Transfer Model Based on Flow Regimes. *Journal of Heat Transfer*, **127**, p. 221.

Del Col, D., Torresin, D., Cavallini, A. (2010) Heat Transfer and Pressure Drop During Condensation of the Low Gwp Refrigerant R1234yf. *International Journal of Refrigeration*, **33**, pp. 1307-1318.

Derby, M.M., Lee, H.J., Craft, R.C., Michna, G.J., Pelese, Y., Jensen, M.K., 2010. Exploration of Experimental Techniques to Determine the Condensation Heat Flux in Microchannels and Minichannels, 14th International Heat Transfer Confrence. ASME, Washington, DC.

DiPippo, R. (2004) Second Law Assessment of Binary Plants Generating Power from Low-Temperature Geothermal Fluids. *Geothermics*, **33**, pp. 565-586.

Dobson, M.K., Chato, J.C. (1998) Condensation in Smooth Horizontal Tubes. *Journal of Heat Transfer*, **120**, pp. 193-213.

Doerr, T.M., Eckels, S.J., Pate, M.B. (1994) In-Tube Condensation Heat Transfer of Refrigearnt Mixtures. *ASHRAE Transactions*, **100**, pp. 547-557.

Eckels, S.J., Unruh, B.J. (1999) Local Heat Transfer Coefficents During Condensation of R-22 and R-32/R-125 Mixtures. *HVAC&R Research*, **5**, pp. 59-76.

El Hajal, J., Thome, J.R., Cavallini, A. (2003) Condensation in Horizontal Tubes Part 1: Two-Phase Flow Pattern Map. *International Journal of Heat and Mass Transfer*, **46**, pp. 3349-3363.

Fenghour, A., Wakeham, W.A., Vesovic, V., Watson, J.T.R., Millat, J., Vogel, E. (1995) The Viscosity of Ammonia. *Journal of Physical and Chemical Reference Data*, **24**, pp. 1649-1667.

Fernández-Seara, J., Uhía, F.J., Sieres, J., Campo, A. (2007) A General Review of the Wilson Plot Method and Its Modifications to Determine Convection Coefficients in Heat Exchange Devices. *Applied Thermal Engineering*, **27**, pp. 2745-2757.

Friedel, L., (1979). Improved Friction Pressure Drop Correlations for Horizontal and Vertical Two Phase Pipe Flow (Paper E2), *Proc. European Two Phase Flow Group Meeting*.

Fronk, B.M., Garimella, S., 2010. Measurement of Heat Transfer and Pressure Drop During Condensation of Carbon Dioxide in Microscale Geometries, 14th International Heat Transfer Conference. ASME, Washington, DC.

Fujii, T., Uehara (1973) *Film Condensation Heat Transfer (in Japanese)*, Progress in Heat Transfer. (Yokendo Book Co., Tokyo), p. 1.

Furno, J.S., Taylor, R., Krishna, R. (1986) Condensation of Vapor Mixtures. 2. Comparison with Experiment. *Industrial & Engineering Chemistry Process Design and Development*, **25**, pp. 98-101.

Garimella, S. (2006) *Condensation in Minichannels and Microchannels*, in: Kandlikar, S. (Ed.), Heat Transfer and Fluid Flow in Minichannels and Microchannels (Elsevier, Amsterdam.

Garimella, S. (2014) *Condensation in Minichannels and Microchannels*, in: Kandlikar, S.G. (Ed.), Heat Transfer and Fluid Flow in Minichannels and Micochannels, 2nd ed. (Elsevier.

Garimella, S., Agarwal, A., Killion, J.D. (2005) Condensation Pressure Drop in Circular Microchannels. *Heat Transfer Engineering*, **26**, pp. 28-35.

Garimella, S., Bandhauer, T.M., 2001. Measurement of Condensation Heat Transfer Coefficients in Microchannel Tubes, 2001 ASME International Mechanical Engineering Congress and Exposition, 3 ed. American Society of Mechanical Engineers, New York, NY, United states, pp. 243-249.

Garimella, S., Christensen, R.N. (1995) Heat Transfer and Presure Drop Characteristics of Spirally Fluted Annuli: Part Ii - Heat Transfer. *Journal of Heat Transfer*, **117**, pp. 61-68.

Garimella, S., Killion, J.D., Coleman, J.W. (2002) An Experimentally Validated Model for Two-Phase Pressure Drop in the Intermittent Flow Regime for Circular Microchannels. *Journal of fluids engineering*, **124**, pp. 205-214.

Garimella, S., Killion, J.D., Coleman, J.W. (2003) An Expermentally Validated Model for Two-Phase Pressure Drop in the Intermittent Flow Regime for Noncircular Microchannels. *Journal of fluids engineering*, **125**, pp. 887-894.

Ghiaasiaan, S.M. (2008) *Two-Phase Flow, Boiling, and Condensation in Conventional and Miniature Systems*, 1st ed. (Cambridge University Press, New York).

Gnielinski, V. (1976) New Equations for Heat and Mass-Transfer in Turbulent Pipe and Channel Flow. *International Chemical Engineering*, **16**, pp. 359-368.

Govier, G.W., Omer, M.M. (1962) Horizontal Pipeline Flow of Air-Water Mixtures. *Canadian Journal of Chemical Engineering*, **40**, pp. 93-104.

Granryd, E.G., 1989. Heat Transfer in Flow Evaporation (and Condensation) of Mixtures. Oak Ridge National Laboratory, Oak Ridge, Tennessee.

Griffith, P., Lee, K.S. (1964) The Stability of an Annulus of Liquid in a Tube. *Journal of Basic Engineering*, **86**, p. 666.

Haraguchi, H., Koyama, S., Fujii, T. (1994a) Condensation of Refrigerants Hcfc22, Hfc134a and Hcfc123 in a Horizontal Smooth Tube (1st Report, Proposal of Empirical Expression for the Local Frictional Pressure Drop). *Transactions of the JSME (B)*, **60**, pp. 239-244.

Haraguchi, H., Koyama, S., Fujii, T. (1994b) Condensation of Refrigerants Hcfc22, Hfc134a and Hcfc123 in a Horizontal Smooth Tube (2nd Report, Proposal of Empirical Expressions for the Local Heat Transfer Coefficient). *Trans. JSME (Ser. B)*, **60**, pp. 245-252.

Hashimoto, R., Yanagi, K., Fujii, T. (1996) Condensation of Organic Binary Mixtures Flowing Downward inside a Vertical Tube. *Heat Transfer - Japanese Research*, **25**, pp. 362-381.

Hewitt, G.F., Roberts, D., 1969. Studies of Two-Phase Flow Patterns by Simultaneous X-Ray and Flash Photography. Atomic Energy Research Establishment, Harwell (England).

Hewitt, G.F., Shires, G.L., Bott, T.R. (1994) *Process Heat Transfer*. (CRC Press, New York).

Hibiki, T., Mishima, K. (1996) Approximate Method for Measurement of Phase-Distribution in Multiphase Materials with Small Neutron-Attenuation Using a Neutron Beam as a Probe. *Nuclear Instruments & Methods in Physics Research Section a-Accelerators Spectrometers Detectors and Associated Equipment*, **374**, pp. 345-351.

Ibrahim, O.M., Klein, S.A. (1993) Thermodynamic Properties of Ammonia-Water Mixtures. *ASHRAE Transactions*, **99**, pp. 1495-1502.

Incropera, F.P., Dewitt, D.P. (2002) *Fundamentals of Heat and Mass Transfer*, 5th ed. (John Wiley and Sons).

Jaster, H., Kosky, P.G. (1976) Condensation Heat-Transfer in a Mixed Flow Regime. *International Journal of Heat and Mass Transfer*, **19**, pp. 95-99.

Jiang, Y., McAuley, K.B., Hsu, J.C.C. (1997) Nonequilibrium Modeling of Condensed Mode Cooling of Polyethylene Reactors. *AIChE Journal*, **43**, pp. 13-24.

Jin, D.X., Kwon, J.T., Kim, M.H. (2003) Prediction of in-Tube Condensation Heat Transfer Characteristics of Binary Refrigerant Mixtures. *International Journal of Refrigeration*, **26**, pp. 593-600.

Jones, W.P., Launder, B.E. (1972) The Prediction of Laminarization with a Two-Equation Model of Turbulence. *International Journal of Heat and Mass Transfer*, **15**, pp. 301-314.

Kalina, A.I. (1984) Combined-Cycle System with Novel Bottoming Cycle. *Journal of Engineering for Gas Turbines and Power*, **106**, pp. 737-742.

Kalina, A.I., Leibowitz, H.M. (1989) Application of the Kalina Cycle Technology to Geothermal Power-Generation. *Geysers - Three Decades of Achievement : A Window on the Future*, **13**, pp. 605-611.

Kattan, N., Thome, J.R., Favrat, D. (1998) Flow Boiling in Horizontal Tubes: Part 1 - Development of a Diabatic Two-Phase Flow Pattern Map. *Journal of Heat Transfer*, **120**, pp. 140-147.

Kays, W.M., Leung, E.Y. (1963) Heat Transfer in Annular Passages: Hydrodynamically Developed Flow with Arbitrarily Prescribed Heat Flux. *International Journal of Heat and Mass Transfer*, **6**, pp. 537-557.

Keinath, B.L., 2012. Void Fraction, Pressure Drop and Heat Transfer in High Pressure Condensing Flows through Microchannels, G.W.W. School of Mechanical Engineering. Georgia Institute of Technology, Atlanta, GA, USA.

Kew, P.A., Cornwell, K. (1997) Correlations for the Prediction of Boiling Heat Transfer in Small-Diameter Channels. *Applied Thermal Engineering*, **17**, pp. 705-715.

Kim, B.J. (1998) A Model for the Condensation Heat Transfer of Binary Refrigerant Mixtures. *Ksme International Journal*, **12**, pp. 281-290.

Kim, S.M., Mudawar, I. (2012) Universal Approach to Predicting Two-Phase Frictional Pressure Drop for Adiabatic and Condensing Mini/Micro-Channel Flows. *International Journal of Heat and Mass Transfer*, **55**, pp. 3246-3261.

Kim, S.M., Mudawar, I. (2013) Universal Approach to Predicting Heat Transfer Coefficient for Condensing Mini/Micro-Channel Flow. *International Journal of Heat and Mass Transfer*, **56**, pp. 238-250.

Klein, S.A., 2012. Engineering Equation Solver, V9.199-3D ed. F-Chart Software.

Knudsen, J.G., Katz, D.L. (1958) *Fluid Dynamics and Heat Transfer*. (McGraw-Hill Book Company, New York).

Kogawa, K., 1993. An Experimental Study on Condensation of R134a/R123 Mixtures inside Horizontal Smooth and Micro-Fin Tubes. Kyushu University, Fukuoka.

Kotake, S. (1978) Film Condensation of Binary Mixture Flow in a Vertical Channel. *International Journal of Heat and Mass Transfer*, **21**, pp. 875-884.

Koyama, S., Dilao, C.O., Fujii, T., 1994. Condensation Heat Transfer of Refrigerant Mixtures inside Horizontal Tubes, WTPF, AFERC, POSTECH, pp. 175-190.

Koyama, S., Ju, J., Ishibashi, A. (1998) Condensation of Binary Refrigerant Mixtures in a Horizontal Tube. *Thermal Science and Engineering*, **6**, pp. 230-246.

Koyama, S., Kuwahara, K., Nakashita, K., Yamamoto, K. (2003) An Experimental Study on Condensation of Refrigerant R134a in a Multi-Port Extruded Tube. *International Journal of Refrigeration*, **26**, pp. 425-432.

Koyama, S., Miyara, A., Takamatsu, H., Fujii, T. (1990) Condensation Heat-Transfer of Binary Refrigerant Mixtures of R22 and R114 inside a Horizontal Tube with Internal Spiral Grooves. *International Journal of Refrigeration*, **13**, pp. 256-263.

Krishna, R. (1981) Ternary Mass Transfer in a Wetted-Wall Column Significance of Diffusional Interactions Part I. Stefan Diffusion. *Chemical Engineering Research and Design*, **59**, pp. 35-43.

Krishna, R. (1982) A Turbulent Film Model for Multicomponent Mass-Transfer. *Chemical Engineering Journal and the Biochemical Engineering Journal*, **24**, pp. 163-172.

Krishna, R., Standart, G.L. (1976) A Multicomponent Film Model Incorporating a General Matrix Method of Solution to the Maxwell-Stefan Equations. *AIChE Journal*, **22**, pp. 383-389.

Krishna, R., Standart, G.L. (1979) Mass and Energy-Transfer in Multicomponent Systems. *Chemical Engineering Communications*, **3**, pp. 201-275.

Lamourelle, A.P., Sandall, O.C. (1972) Gas Absorption into a Turbulent Liquid. *Chemical Engineering Science*, **27**, pp. 1035-1043.

Launay, P.F., 1981. Improving the Efficiency of Refrigerators and Heat Pumps by Using a Nonazeotropic Mixture of Refrigerants. Oak Ridge National Laboratory.

Lee, H.J., Lee, S.Y. (2001) Pressure Drop Correlations for Two-Phase Flow within Horizontal Rectangular Channels with Small Heights. *International Journal of Multiphase Flow*, **27**, pp. 783-796.

Lemmon, E.W., Jacobsen, R.T. (2004) Viscosity and Thermal Conductivity Equations for Nitrogen, Oxygen, Argon, and Air. *International Journal of Thermophysics*, **25**, pp. 21-69.

Lemmon, E.W., Jacobsen, R.T., Penoncello, S.G., Friend, D. (2000) Thermodynamic Properties of Air and Mixtures of Nitrogen, Argon, and Oxygen from 60 to 2000 K at Pressures to 2000 Mpa. *Journal of Physical and Chemical Reference Data*, **29**.

Lockhart, R., Martinelli, R. (1949) Proposed Correlation of Data for Isothermal Two-Phase, Two-Component Flow in Pipes. *Chemical Engineering Progress*, **45**, pp. 39-48.

Lolos, P.A., Rogdakis, E.D. (2009) A Kalina Power Cycle Driven by Renewable Energy Sources. *Energy*, **34**, pp. 457-464.

Lombardi, C., Carsana, C.G. (1992) A Dimensionless Pressure Drop Correlation for Two-Phase Mixtures Flowing Uphill in Vertical Ducts Covering Wide Parameter Range. *Heat Technology*, **10**.

Lu, D.C., Lee, C.C. (1994) An Analytical Model of Condensation Heat Transfer of Non-Azeotropic Refrigerant Mixtures in a Horizontal Tube. *ASHRAE Transactions*, **100**, pp. 721-731.

Mandhane, J.M., Gregory, G.A., Aziz, K. (1974) A Flow Pattern Map for Gas-Liquid Flow in Horizontal Pipes. *International Journal of Multiphase Flow*, **1**, pp. 537-553.

Martinelli, R.C., Nelson, D.B. (1948) Prediction of Pressure Drop During Forced-Circulation Boiling of Water. *Transactions of ASME*, **70**, pp. 695-702.

McAdams, W.H., Woods, W.K., Bryan, R.L. (1942) Vaporization inside Horizontal Tubes-Ii-Benzene-Oil-Mixtures. *Transactions of ASME 64*.

Meacham, J.M., 2002. An Integrated Experimental and Analytical Study of Ammonia-Water Absorption in Microchannel Geometries, Mechanical Engineering. Iowa State University, Ames, IA, USA.

Milkie, J.A., 2014. Condensation of Hydrocarbons and Zeotropic Hydrocarbon/Refrigerant Mixtures in Horizontal Tubes, Mechanical Engineering. Georgia Institute of Technology, Atlanta, GA.

Minkowycz, W.J., Sparrow, E.M. (1966) Condensation Heat Transfer in the Presence of Noncondensables, Interfacial Resistance, Superheating, Variable Properties, and Diffusion. *International Journal of Heat and Mass Transfer*, **9**, pp. 1125-1144.

Mishima, K., Hibiki, T. (1996) Some Characteristics of Air-Water Two-Phase Flow in Small Diameter Vertical Tubes. *International Journal of Multiphase Flow*, **22**, pp. 703-712.

Mlcak, H.A. (2002) Kalina Cycle Concepts for Low Temperature Geothermal. *Transactions - Geothermal Resources Council*, pp. 707-713.

Modine, A.D., 1963. Ternary Mass Transfer, Department of Chemical Engineering. Carnegie Institute of Technology, Pittsburgh, PA, USA.

Mohanraj, M., Muraleedharan, C., Jayaraj, S. (2011) A Review on Recent Developments in New Refrigerant Mixtures for Vapour Compression-Based Refrigeration, Air-Conditioning and Heat Pump Units. *International Journal of Energy Research*, **35**, pp. 647-669.

Müller-Steinhagen, H., Heck, K. (1986) A Simple Friction Pressure Drop Correlation for Two-Phase Flow in Pipes. *Chemical Engineering and Processing: Process Intensification*, **20**, pp. 297-308.

Nema, G., 2008. Flow Regime Transitions During Condensation in Microchannels, G.W.W School of Mechanical Engineering. Georgia Institute of Technology, Atlanta, GA, USA.

Nema, G., Garimella, S., Fronk, B.M. (2014) Flow Regime Transitions During Condensation in Microchannels. *International Journal of Refrigeration*, **40**, pp. 227-240.

Nusselt, W. (1916) Die Oberflächenkondensation Des Wasserdampfes. *VDI Zeitschrift*, **60**, pp. 541-546 and 569-575.

Oliemans, R., Pots, B., Trompe, N. (1986) Modelling of Annular Dispersed Two-Phase Flow in Vertical Pipes. *International Journal of Multiphase Flow*, **12**, pp. 711-732.

Onda, K., Sada, E., Takahashi, K. (1970) The Film Condensation of Mixed Vapour in a Vertical Column. *International Journal of Heat and Mass Transfer*, **13**, pp. 1415-1424.

Onda, K., Sada, E., Takahashi, K., Ito, K. (1968) Film Condensation in a Vertical Tube. *Kagaku Kogaku*, **32**, pp. 1215-1221.

Palen, J.W., Wang, Q., Chen, J.C. (1994) Falling Film Evaporation of Binary Mixtures. *AIChE Journal*, **40**, pp. 207-214.

Panchal, C.B., Kuru, W.C., Chen, F.C., Domingo, N., HuangFu, E.P., (1997). Experimental and Analytical Study of Condensation of Ammonia-Water Mixtures, *Proc. AICHE/ASME National Heat Transfer Conference*.

Philpott, C., Deans, J. (2004) The Condensation of Ammonia-Water Mixtures in a Horizontal Shell and Tube Condenser. *Journal of Heat Transfer*, **126**, pp. 527-534.

Price, B.C., Bell, K.J. (1974) Design of Binary Vapor Condensers Using the Colburn-Drew Equations. *AIChE Symposium Series*, **70**, pp. 163-171.

Revellin, R., Thome, J.R. (2007) Adiabatic Two-Phase Frictional Pressure Drops in Microchannels. *Experimental Thermal and Fluid Science*, **31**, pp. 673-685.

Rezkallah, K.S. (1996) Weber Number Based Flow-Pattern Maps for Liquid-Gas Flows at Microgravity. *International Journal of Multiphase Flow*, **22**, pp. 1265-1270.

Ribatski, G., Wojtan, L., Thome, J.R. (2006) An Analysis of Experimental Data and Prediction Methods for Two-Phase Frictional Pressure Drop and Flow Boiling Heat Transfer in Micro-Scale Channels. *Experimental Thermal and Fluid Science*, **31**, pp. 1-19.

Rose, J.W. (1969) Condensation of a Vapour in the Presence of a Non-Condensing Gas. *International Journal of Heat and Mass Transfer*, **12**, pp. 233-237.

Sami, S., Grell, J. (2000) Prediction of Two-Phase Condensation Characteristics of Some Alternatives to R-22 inside Air/Refrigerant Enhanced Surface Tubing. *International Journal of Energy Research*, **24**, pp. 1277-1290.

Sami, S.M., Maltais, H. (2000) Experimental Investigation of Two Phase Flow Condensation of Alternatives to Hcfc-22 inside Enhanced Surface Tubing. *Applied Thermal Engineering*, **20**, pp. 1113-1126.

Sardesai, R., Owen, R., Pulling, D. (1981) Flow Regimes for Condensation of a Vapour inside a Horizontal Tube. *Chemical Engineering Science*, **36**, pp. 1173-1180.

Serizawa, A., Feng, Z., Kawara, Z. (2002) Two-Phase Flow in Microchannels. *Experimental Thermal and Fluid Science*, **26**, p. 703.

Shah, M.M. (1979) A General Correlation for Heat Transfer During Film Condensation inside Pipes. *International Journal of Heat and Mass Transfer*, **22**, pp. 547-556.

Shah, M.M. (2009) An Improved and Extended General Correlation for Heat Transfer During Condensation in Plain Tubes. *HVAC&R Research*, **15**, pp. 889-913.

Shao, D.W., Granryd, E. (1998) Experimental and Theoretical Study on Flow Condensation with Non-Azeotropic Refrigerant Mixtures of R32/R134a. *International Journal of Refrigeration*, **21**, pp. 230-246.

Shao, D.W., Granryd, E.G. (2000a) Flow Pattern, Heat Transfer and Presssure Drop in Flow Condensation Part I: Pure and Azeotropic Refrigerants. *HVAC&R Research*, **6**, pp. 175-195.

Shao, D.W., Granryd, E.G. (2000b) Flow Pattern, Heat Transfer and Presssure Drop in Flow Condensation Part Ii: Zeotropic Refrigerant Mixtures (Narms). *HVAC&R Research*, **6**, pp. 197-209.

Sherwood, T.K., Pigford, R.L., Wilke, C.R. (1975) *Mass Transfer*. (McGraw-Hill, New York).

Silver, L. (1947) Gas Cooling with Aqueous Condensation. *Chemical Engineering Research and Design*, **25a**, pp. 30-42.

Smit, F.J., Meyer, J.P. (2002) R-22 and Zeotropic R-22/R-142b Mixture Condensation in Microfin, High-Fin, and Twisted Tape Insert Tubes. *Journal of Heat Transfer*, **124**, pp. 912-921.

Smit, F.J., Thome, J.R., Meyer, J.P. (2002) Heat Transfer Coefficients During Condensation of the Zeotropic Refrigerant Mixture Hcfc-22/Hcfc-142b. *Journal of Heat Transfer*, **124**, pp. 1137-1146.

Smith, L.W., Taylor, R. (1983) Film Models for Multicomponent Mass Transfer: A Statistical Comparison. *Industrial & Engineering Chemistry Fundamentals*, **22**, pp. 97-104.

Smith, S.L. (1971) Void Fraction in Two-Phase Flow: A Correlation Based Upon an Equal Velocity Head Model. *Heat Fluid Flow*, **1**, pp. 22-39.

Sparrow, E.M., Marschall, E. (1969) Binary, Gravity-Flow Film Condensation. *Journal of Heat Transfer*, **91C**, pp. 205-211.

Stewart, W.E., Prober, R. (1964) Matrix Calculation of Multicomponent Mass Transfer in Isothermal Systems. *Industrial & Engineering Chemistry Fundamentals*, **3**, pp. 224-235.

Stoecker, W.F., Kornota, E. (1985) Condensing Coefficents When Using Refrigerant Mixtures. *ASHRAE Transactions*, **91**, pp. 1351-1367.

Stoecker, W.F., McCarthy, C.I., 1984. The Simulation and Performance of a System Using and R-12/R-114 Refrigerant Mixture. Oak Ridge National Laboratory.

Su, Q., Yu, G.X., Wang, H.S., Rose, J.W. (2009) Microchannel Condensation : Correlations and Theory. *International Journal of Refrigeration*, **32**, pp. 1149-1152.

Suliman, R., Liebenberg, L., Meyer, J.P. (2009) Improved Flow Pattern Map for Accurate Prediction of the Heat Transfer Coefficients During Condensation of R-134a in Smooth Horizontal Tubes and within the Low-Mass Flux Range. *International Journal of Heat and Mass Transfer*, **52**, pp. 5701-5711.

Taitel, Y., Dukler, A.E. (1976) A Model for Predicting Flow Regime Transitions in Horizontal and near Horizontal Gas-Liquid Flow. *AIChE Journal*, **22**, pp. 47-55.

Tamir, A. (1973) Condensation of Binary Mixtures of Miscible Vapors. *International Journal of Heat and Mass Transfer*, **16**, pp. 683-685.

Tandon, T., Varma, H., Gupta, C. (1982) A New Flow Regimes Map for Condensation inside Horizontal Tubes. *Journal of Heat Transfer*, **104**, p. 763.

Tandon, T., Varma, H., Gupta, C. (1985a) Prediction of Flow Patterns During Condensation of Binary Mixtures in a Horizontal Tube. *Journal of Heat Transfer*, **107**, pp. 424-430.

Tandon, T.N., 1983. Forced Convection Condensation of Pure Refrigerants and Binary Mixtures inside a Horizontal Tube, Mechanical and Industrial Engineering Department. University of Roorkee, Roorkee, India.

Tandon, T.N., Varma, H.K., Gupta, C.P. (1985b) An Experimental Investigation of Forced-Convection Condensation During Annular Flow inside a Horizontal Tube. *ASHRAE Transactions,* **91**, pp. 343-355.

Tandon, T.N., Varma, H.K., Gupta, C.P. (1986) Generalized Correlation for Condensation of Binary Mixtures inside a Horizontal Tube. *International Journal of Refrigeration*, **9**, pp. 134-136.

Taylor, B.N., Kuyatt, C.E., 1994. Guidelines for Evaluating and Expressing the Uncertainty of Nist Measurement Results. National Institute of Standards and Technology, Washington, DC, USA, p. 15.

Taylor, R., Krishna, R. (1993) *Multicomponent Mass Transfer*. (Wiley, New York).

Taylor, R., Krishnamurthy, R., Furno, J.S., Krishna, R. (1986) Condensation of Vapor Mixtures. 1. Nonequilibrium Models and Design Procedures. *Industrial & Engineering Chemistry Process Design and Development*, **25**, pp. 83-97.

Thome, J.R., El Hajal, J., Cavallini, A. (2003) Condensation in Horizontal Tubes, Part 2: New Heat Transfer Model Based on Flow Regimes. *International Journal of Heat and Mass Transfer*, **46**, pp. 3365-3387.

Tillner-Roth, R., Harms-Watzenberg, F., Baehr, H. (1993) Eine Neue Fundamentalgleichung Für Ammoniak. *DKV TAGUNGSBERICHT*, **20**, pp. 167-181.

Toor, H.L. (1964) Solution of the Linearized Equations of Multicomponent Mass Transfer: I. *AIChE Journal*, **10**, pp. 448-455.

Traviss, D.P., Rohsenow, W.M. (1973) Flow Regimes in Horizontal Two-Phase Flow with Condensation. *ASHRAE Transactions*, **79**, pp. 31-39.

Traviss, D.P., Rohsenow, W.M., Baron, A.B. (1973) Forced-Convection Condensation inside Tubes: A Heat Transfer Equation for Condenser Design. *ASHRAE Transactions*, **79**, pp. 157-165.

Triplett, K., Ghiaasiaan, S., Abdel-Khalik, S., Sadowski, D. (1999) Gas–Liquid Two-Phase Flow in Microchannels Part I: Two-Phase Flow Patterns. *International Journal of Multiphase Flow*, **25**, pp. 377-394.

Tsotsas, E., Schlünder, E.U. (1987) Heat Transfer During Evaporation and Condensation of Binary Mixtures. *Chemical Engineering and Processing: Process Intensification*, **21**, pp. 209-215.

Tufeu, R., Ivanov, D.Y., Garrabos, Y., Le Neindre, B. (1984) Thermal Conductivity of Ammonia in a Large Temperature and Pressure Range Including the Critical Region. *Berichte der Bunsengesellschaft für physikalische Chemie*, **88**, pp. 422-427.

Ungar, E.K., Cornwell, J.D., (1992). Two-Phase Pressure Drop of Ammonia in Small Diameter Horizontal Tubes, *Proc. 17th Aerospace Ground Testing Conference*, AIAA.

van Es, J.P., Heertjes, P.M. (1956) On the Condensation of a Vapour of a Binary Mixture in a Vertical Tube. *Chemical Engineering Science*, **5**, pp. 217-225.

Vuddagiri, S.R., Eubank, P.T. (1998) Condensation of Mixed Vapors and Thermodynamics. *AIChE Journal*, **44**, pp. 2526-2540.

Wallis, G.B. (1969) *One-Dimensional Two-Phase Flow*, New York, McGraw-Hill).

Wang, H.S., Rose, J.W. (2005) A Theory of Film Condensation in Horizontal Noncircular Section Microchannels. *Journal of Heat Transfer*, **127**, pp. 1096-1105.

Wang, H.S., Rose, J.W. (2011) Theory of Heat Transfer During Condensation in Microchannels. *International Journal of Heat and Mass Transfer*, **54**, pp. 2525-2534.

Wang, W.-W., Radcliff, T.D., Christensen, R.N. (2002) A Condensation Heat Transfer Correlation for Millimeter-Scale Tubing with Flow Regime Transition. *Experimental Thermal and Fluid Science*, **26**, pp. 473-485.

Ward, D.J. (1960) How to Design a Multiple Component Partial Condenser. *Petro/Chem Engineer*, **32**, pp. C42-C48.

Webb, D.R., Fahrner, M., Schwaab, R. (1996) The Relationship between the Colburn and Silver Methods of Condenser Design. *International Journal of Heat and Mass Transfer*, **39**, pp. 3147-3156.

Webb, D.R., McNaught, J.M. (1980) *Condensers*, in: Chisholm, D. (Ed.), Developments in Heat Exchanger Technology-1. (Applied Science Publishers, London), pp. 71-126.

Webb, D.R., Sardesai, R.G. (1981) Verification of Multicomponent Mass Transfer Models for Condensation inside a Vertical Tube. *International Journal of Multiphase Flow*, **7**, pp. 507-520.

Wen, M.-Y., Ho, C.-Y., Hsieh, J.-M. (2006) Condensation Heat Transfer and Pressure Drop Characteristics of R-290 (Propane), R-600 (Butane), and a Mixture of R-290/R-600 in the Serpentine Small-Tube Bank. *Applied Thermal Engineering*, **26**, pp. 2045-2053.

Yaws, C.L. (1999) *Chemical Properties Handbook*. (McGraw-Hill).

Zhao, L., Rezkallah, K.S. (1993) Gas-Liquid Flow Patterns at Microgravity. *International Journal of Multiphase Flow*, **19**, pp. 751-763.